

PHOTO-ASSISTED WET (PAW) ETCHING FOR LASER FABRICATION

By

EUN-HYEONG YI

A Dissertation submitted to the

Graduate School-New Brunswick

Rutgers, The State University of New Jersey

in partial fulfillment of the requirements

for the degree of

Doctor of Philosophy

Graduate Program in Electrical and Computer Engineering

written under the direction of

Professor Michael A Parker, Ph. D

and approved by

New Brunswick, New Jersey

October, 2009

©2009

Eun-Hyeong Yi

ALL RIGHTS RESERVED

ABSTRACT OF THE DISSERTATION

PHOTO-ASSISTED WET (PAW) ETCHING FOR LASER FABRICATION

By Eun-Hyeong Yi

Dissertation Director:

Professor Michael A. Parker

Modern day technology uses discrete optical components including laser diodes and integrated electronic circuits. Fabricating an etched mirror laser is one of the major tasks to realize integrated optics. While dry etching is the most widely accepted process to fabricate optoelectronic devices, wet etching has potential advantages including lower cost, smoother surfaces, and faster etching rate. However typical wet etching does not provide a viable alternative for the demanding process of fabricating vertical side walls with low lateral etch rates. The application of the wet etching to the production of vertical sidewalls has been a significant problem for several decades.

The primary accomplishments of the research consists of developing processes, apparatus, and models for the Photo-Assisted Wet (PAW) etching that uses light directed perpendicular to the surface of a wafer in order to alter the typical crystal-plane etching and thereby control the sidewall profile. The new techniques demonstrate integrated laser mirrors in III-V laser heterostructure. These mirrors achieve as high as 93% of the reflectance of the cleaved mirror with negligible dependence on the crystal orientation.

The research explores the PAW etching process using both coherent (lasers) and incoherent (LEDs) illumination for different types of materials including bulk GaAs and III-V

laser heterostructure. The effects of different wavelengths, intensities and wafer masking structures are investigated. Specific combinations control the sidewall profile and etching characteristics to produce on-demand etch-stop layers and sidewall angles ranging from 0 to 90°. Laser heterostructure etched with coherent illumination shows unexpected results for heterostructure including non-uniform etch depth linked to the masking materials and surface density of excess carriers.

New apparatus was designed and applied to the PAW etching for the fabrication of III-V devices. The apparatus has in-situ, real-time systems including (i) an optical system to expand, filter and dither the etching beam, (ii) a pulsed-laser wet etch monitor to determine the etch depth, rate, formation of surface microstructure and transition layers in a preselected region of the sample (iii) a steady-state photoluminescence (PL) monitor with CCD array and Photo Detector (PD) to provide (2-D) spatially-resolved and integrated measurements of PL during the etching.

Acknowledgements

First of all, I am especially grateful to my advisor, Dr. Michael A. Parker, for his support, encouragement, and guidance. During my research at Rutgers University, many of the faculty and staff members have aided me. I thank all of those in the solid state and control groups including as well as those on my dissertation committee Dr. Z. Gajic, Dr. S. McAfee, Dr. Yicheng Lu, and Dr. M. Caggiano. I appreciate their words of support and advice. I thank the out-side committee Dr. Sigel for his kindness.

I would like to thank my family and friends who have believed in me through my research. In particular, I would like to thank my husband Chang Ho Yu for his constant care, friendship and support. I would like to thank my parents and my grandmother, who is living in my memory, for their love, wisdom and prayers.

And finally, I appreciate the great moviemakers and musicians. Their works of art give me new strength to overcome obstacles for many years.

Table of Contents

Abstract of the Dissertation.....	ii
Acknowledgements.....	iv
Table of Contents.....	v
List of Tables.....	ix
List of Figures.....	x
Chapter 1 Introduction	1
Chapter 2 Theory of Electrochemistry.....	12
2.1 Electrochemical System.....	13
2.1.1 Electrolyte and Energy Level.....	14
2.1.2 Energy Band Fluctuations.....	18
2.1.3 Solid-Liquid Interface.....	21
2.2 Charge Transfer.....	28
2.2.1 Kinetics of Charge Transfer	29
2.2.2 Charge Transfer in the Dark and Illumination	35
2.3 Semiconductor Dissolution.....	40
2.3.1 Anodic Dissolution	41
2.3.2 Electroless Dissolution	46
2.3.3 Chemical Dissolution.....	51
2.4 Summary	52
Chapter 3 LED Photo-Assisted Wet (PAW) Etch Test.....	54
3.1 Experimental Set-up and Sample Preparation.....	55
3.1.1 Experimental Set-up.....	55
3.1.2 Light Sources.....	56

3.1.3 Etch Masks.....	57
3.1.4 Sample Preparation	60
3.2 LED Photo-Assisted Wet (PAW) Etching.....	63
3.2.1 LED-PAW Etching of Bulk GaAs Materials.....	65
3.2.2 Simple Model for Bulk GaAs.....	68
3.2.3 LED-PAW of Epitaxial AlGaAs Layer.....	72
3.2.4 LED-PAW of Laser Heterostructure.....	76
3.3 Summary.....	82
Chapter 4 Laser Fabrication and Photo-Assisted Wet (PAW) Etch Tests.....	86
4.1 Design of Laser PAW Etching.....	88
4.1.1 Fabrication Step and Mask Design.....	88
4.1.2 Etch Mask Design and Designation.....	91
4.1.3 Laser Photo-Assisted Wet (PAW) Etching Set up.....	92
4.1.4 The Reflectometer Etch Monitor.....	96
4.1.5 Photoluminescence Measurement.....	101
4.1.6 Sample Layers and Preparation.....	102
4.2 Laser-PAW Etching.....	105
4.2.1 Reflectometer and PL Signals in Laser-PAW Etching.....	107
4.2.2 EPI samples: Waveguide Etch Tests.....	113
4.2.2.1 Result from Both-PR Mask for Waveguide Etching...	120
4.2.2.2 Result from Both-Blank Mask for Waveguide Etching.....	122
4.2.2.3 Result from Both-Metal Mask for Waveguide Etching.....	124
4.2.2.4 Summary for Waveguide Etch Test of EPI.....	126

4.2.3 EPI samples: Mirror Etch Test.....	129
4.2.3.1 Results for Mirror Etching Using Both-PR Mask.....	132
4.2.3.2 Results for Mirror Etching Using the Both-Blank Mask	136
4.2.3.3 Results for Mirror Etching Using the Both-Metal Mask.....	139
4.2.3.4 Summary for Mirror Etch Test of EPI.....	140
4.2.4 M1 Samples: Waveguide and Mirror Etch Test.....	142
4.3 Laser Fabrication to Evaluate PAW Etching.....	148
4.4 Discussion.....	155
Chapter 5 Test of Photo-Assisted Wet (PAW) Etched Mirror Laser.....	161
5.1 Basic Equations Used to Compare Laser Operation.....	163
5.2 Laser Test Setup.....	166
5.3 Evaluation of the PAW Etched Laser.....	168
5.3.1 Comparison of Lasers with Various Etched-Ridge Heights.....	170
5.3.2 Comparison of Deep-Etched Lasers.....	177
5.3.3 Deep Etched Lasers: One Side Etched Mirror.....	185
5.3.4 Fabrication and Tests of 852nm Lasers.....	188
5.4 Multimode Behavior of CE-D and CL2-D Lasers.....	191
5.4.1 Modes Observations.....	191
5.4.2 End View of the Single Mode.....	193
5.5 Discussion.....	195
Chapter 6 Summary and Conclusions	198
Appendix A: $\text{Al}_x\text{Ga}_{1-x}\text{As}$ Complex Refractive Index.....	212

Appendix B: GaAs/AlGaAs Heterostructure Wafer Specs.....	217
Appendix C: R_{\perp}/R_{\parallel} Versus R_{\parallel} Plot.....	221
Appendix D: Pictures of Experimental Set-up.....	222
Appendix E: Ridge-Waveguide Laser Masks.....	225
Appendix F: CCD-Based Holographic Etch Monitor.....	230
F.1 Introduction.....	230
F.2 Background Review.....	232
F.3 HEMC System Overview.....	235
F.4 Example Calibration Plot.....	240
F.5 Example Results.....	241
Appendix G: 1-D Lens Calculations for Transforming a Gaussian Beam into a Uniform Intensity Profile.....	244
G.1 Lens Equations.....	245
G.2 Example Results.....	248
Appendix H: Vibrating Mirror for the PAW etching.....	249
H.1 Simple Mirror Model.....	249
H.2 The Transfer Function for the Mirror Angle and Beam Deflection.....	250
H.3 Open-Terminal Transfer Functions.....	251
H.4 Determine the Parameters.....	252
H.5 Mirror Response.....	254
References.....	256
Curriculum Vita.....	265

List of Tables

Table 4.1 Definitions for the etching masks.....	92
Table 4.2 Approximate values for laser parameters at the position of the sample (with typical size 5mm × 5mm).....	95
Table 5.1 Laser Parameter of CL2-S and CL2-D Lasers.....	176
Table 5.2 Parameters of CL2-D and CE-D lasers.....	184
Table 5.3 Comparison of Etched Mirror Reflectance [111, 113- 115, 123-125].....	196
Table 5.4 Summaries of Etched TIR mirrors [14, 126-128].....	196
Table 6.1 Definitions for the Etching Masks.....	202
Table A.1 Refractive Index of $\text{Al}_x\text{Ga}_{1-x}\text{As}$ (Real Part) [107].....	208
Table A.2 Refractive Index of $\text{Al}_x\text{Ga}_{1-x}\text{As}$ (Imaginary Part) [107].....	209
Table B.1 EPI-1179 Wafer Specs	213
Table B.2 EPI-1179 Wafer Layer Structure.....	214
Table B.3 EPI-179 Wafer Layer Structure.....	215
Table B.4 M1-5 Wafer Layer Structure.....	216
Table B.5 M1-3 Wafer Layer.....	217
Table H.1 Partial List of symbols.	255

List of Figures

Figure 1.1 Summary of the thesis work.....	7
Figure 2.1 Solvated ion structure for (a) negative ion and (b) positive ion. Circle (i) represents the inner shell, and circle (ii) represents the outer shell [Modified from 68, 69].....	16
Figure 2.2 Electron energies (negative upwards) of a redox system vs. density of states: (a) standard condition (same concentration of <i>Ox</i> and <i>Red</i> species), (b) different concentration [modified from 32].....	20
Figure 2.3 Model of the surface state distributions on the (110) GaAs surface [73].....	22
Figure 2.4 (a) illustration of the surface layers at the n type semiconductor and solution interface and (b) the corresponding energy diagram. HL and GL represent Helmholtz double layer and Gouy layer, respectively [modified from 32, 31, 54].....	24
Figure 2.5 Energy band bending of the space charge region at the semiconductor/solution interface at equilibrium: (a) showing the Fermi levels for both n- and p-type semiconductors approaching contact with the redox system, (b) after contact of n-type semiconductor with redox system at equilibrium and (c) after contact of p-type semiconductor with redox system at equilibrium. $E_{F,n}$ and $E_{F,p}$ indicates Fermi level of the n and p-type semiconductor, respectively.....	25
Figure 2.6 Three types of space charge region for the n-type semiconductor depending on the external potential: (a) depletion, (b) flat-band and (c) accumulation condition.....	27

Figure 2.7 Anodic (j^a) and Cathodic current (j^c) versus applied potential (ϕ_{ex}) (i) in the dark and (ii) under illumination. Note that curve (i) approaches zero near point ‘a’ while curve (ii) extends from the anodic to cathodic regimes. Corresponding energy band bending for three potential points are marked in the plot: a. equilibrium (electron depletion), b. flat-band, and c. negative (electron accumulation). The E axis represents electron energy (negative) [modified from 32, 54].....	36
Figure 2.8 Position of energy bands of various semiconductors at the surface in the dark (d) and in light (l) with respect to the electrochemical scale. The vertical lines marked by an energy indicate the band gap of the semiconductor while the small horizontal lines indicate the edges of the conduction and valence band edges [modified from 75, 76].....	39
Figure 2.9 Typical current-potential curve of semiconductor electrode: (a), p-type and (b) n-type semiconductor; (i) in the dark and (ii) under illumination [54].....	43
Figure 2.10 Energy band diagrams of GaAs in the contact with acidic H_2O_2 solution for either an n-type or p-type semiconductor. (a) The bands and Fermi level before contact between the semiconductor and electrolyte. (b) and (c) shows energy band diagram after contact for n-type and p-type semiconductor and electrolyte, respectively.....	48
Figure 2.11 Current potential curves of (a) p-type GaAs and (b) n-type GaAs in the dark in a solution of pH=0 containing a strong oxidizer. (i) and (ii) indicates the estimated cathodic and anodic current, respectively. (iii) represents sum of the cathodic and anodic current [54].....	49
Figure 3.1 Experiment set up for the photo-assisted semiconductor dissolution.....	56

Figure 3.2 Different mask types and corresponding charge flow under illumination: (a) type 0, PR only mask, (b) type 1, metal only mask, (c) type 2, silica and metal mask and (d) type 3, silica, metal and PR mask.....	59
Figure 3.3 Layer structures of samples from (a) EPIQ9501179 and (b) M1-5 laser heterostructure wafer.....	61
Figure 3.4 Detailed formation steps for all of the samples.....	62
Figure 3.5 Photo-Assisted Wet (PAW) etching of bulk GaAs material with different light sources (UV, green and dark): (a)-(g) SEM pictures of the etched side profiles; (g) etch profile in the dark for all types of materials and masks; (h) the relative etch rate (R_{VR}) and (i) the ratio of horizontal-to-vertical etch depth (H/V) for n and p type bulk materials with two different types of masks.....	66
Figure 3.6 Etch rate ($\mu\text{m}/\text{min}$) and relative etch rate (R_{VR}) versus optical intensity. Lines refer to (a) n-type GaAs in the dark, (b) n-type GaAs with illumination, and (c) Relative etch rate (R_{VR}) for n-type GaAs in the $\text{H}_2\text{SO}_4:\text{H}_2\text{O}_2:\text{H}_2\text{O}$ (4:1:25) etchant system. The sidewall angles under illumination appear next to the measured points [64].....	68
Figure 3.7 (a) Sidewall angles from data (regression) and from three different empirical models and (b) comparing the normalize lateral etch rate for the three simplest models. Plot (i), (ii), (iii) and (iv) denotes Data regression, Fermi, Exponential and Linear model, respectively.....	70

Figure 3.8 photo-assisted semiconductor dissolution of epitaxial AlGaAs with different masks (Type 1 and 2) and light sources (UV, green, red and dark) (a)-(i) SEM pictures of etched side profiles; (i) EPIN, EPIP and MIN material with both types of masks in dark, EPIP-2 material with all colors of LED or EPIN-1 and MIN-2 with red LED. (j) the relative etch rate (R_{VR}) and (k) ratio of horizontal-to-vertical etch rate (H/V) vs. light source of n and p type epitaxial AlGaAs layer with two different types of masks. V in the picture indicate vertical etch depth of the sample..	73
Figure 3.9 Etched profile of laser heterostructure materials in the dark for all types of the masks (a) M1 and (b) EPI material.....	77
Figure 3.10 LED-PAW etched profile of laser heterostructure materials for metal masked M1 samples with (a) backside covered and (b) exposed case.....	78
Figure 3.11 LED-PAW etched side profile of laser heterostructure material (M1 samples) with different masks (Type 1, 2 and 3) and light sources (UV, green, red and dark) (a), (b) and (c): M1-1 with UV, Green and Red LED, respectively, (d) M1-3 with UV LED, (e) M1-3 sample with green or red LED, (f) M1-2 sample with UV, green or red LED.....	79
Figure 3.12 Photo-assisted semiconductor dissolution of laser heterostructure material (EPI) with different masks (Type 1, 2 and 3) and light sources (UV, green, red and dark) (a)-(h) SEM pictures of etched side profile of EPI samples; (f) EPI-2 or EPI-3 with red LED, and (g) EPI-3 with UV or Green LED applied to the samples.....	80
Figure 3.13 The relative vertical etch rate (R_{VR}) vs. wavelength of light source for EPI and M1N samples. Wavelength of UV: 395nm, Green: 530nm, and Red: 625nm.....	81

Figure 4.1 Ridge-waveguide lasers having either two cleaved mirrors (CL2) or one cleaved and one etched mirror (CE).....	88
Figure 4.2 Fabrication steps for etched mirror lasers with PAW etching. Note that the features are not drawn to scale, and the etched and cleaved mirrors would be at opposite ends of the cavity.....	89
Figure 4.3 Laser PAW etch set up. EM PD: Photodetector for Etch Monitor, EM laser: laser probe beam (670nm, 1mW pulsed) for Etch Monitor, PAW laser: controllable-power green laser (532nm, up to 100mW) for PAW, GT: Galilean Telescope.....	93
Figure 4.4 (a) Aluminum concentration as a function of depth into the M1-5 laser heterostructure wafer. (b) The fringe pattern obtained during a chemical dissolution. Points A, B, C and D indicate sudden changes in aluminum composition. Dotted line represents primary reflected signal.....	97
Figure 4.5 Block diagram for the pulsed-laser wet etch monitor [106].....	100
Figure 4.6 Wafer layer structures of (a) EPI-1179 (U/D) and (b) EPI-179 (n+).....	102
Figure 4.7 Reflectometer signal of EPI-179 sample during the dark wet etching. The large ‘active layer’ includes the quantum wells as well as the graded index region for optical confinement.....	103
Figure 4.8 (a) EPI(U/D) and (b) EPI(n+) Wafer layer structure.....	104
Figure 4.9 Layer structures of (a) M1-5(892nm) and (b) M1-3 (854nm).....	104
Figure 4.10 EPI-179 samples (a) Reflectometer patterns in dark and (b) high power PAW etching form EPI-179 samples and (c) Photoluminescence Intensity during the PAW with high power green laser ($P_{PAW} \geq 70\text{mW}$). Active layer includes graded layer and quantum walls (Q.Ws).....	108

Figure 4.11 M1 sample: (a) reflectometer signal for dark wet etching and (b) reflectometer signal and (c) PL signal during the PAW with high power green laser ($P_{PAW} \geq 70\text{mW}$). Active layer includes graded layer and quantum walls (Q.Ws).....	109
Figure 4.12 (a) Typical reflectometer signal during the laser PAW etching of the M1 sample, (b) reflectometer signal and (c) corresponding photoluminescence intensity in the boxed area from (a) where the anomaly occurs. Etching stops four times for a rinse in DI water during the anomalous behavior of the reflectometer signal. The reflectometer signal returns to the identical level as before the rinse indicating a relatively stable surface layer.....	111
Figure 4.13 Reflectometer signal versus PAW laser power for M1-3: (a) Dark, (b) $P_{PAW} \leq 5\text{mW}$, (c) $P_{PAW} \sim 10\text{mW}$, (d) $P_{PAW} \sim 30\text{mW}$, (e) $P_{PAW} \sim 70\text{mW}$ and (f) $P_{PAW} \sim 100\text{mW}$. The plots have been displace along the vertical axis and therefore, the absolute magnitude does not correlate with reflectance.....	112
Figure 4.14 Initial-Mask for waveguide: (a) Overall patterned sample and (b) details of ridge-waveguide pattern near the mirror pattern. A sample includes three device patterns; Serpentine waveguide, ridge-waveguide laser and TIR laser. See Appendix E for details of ridge-waveguide pattern.....	114
Figure 4.15 (a) Reflectometer and (b) PL signal measured using PD for EPI material etched with high power green laser ($P_{PAW} \sim 100\text{mW}$) . (c) shows corresponding CCD images of the sample. For size reference, the thin strip in the center is about $100\mu\text{m}$ wide.....	116
Figure 4.16 Reflectometer signal of waveguide masked EPI sample with high power PAW laser ($P_{PAW} \sim 100\text{mW}$). Gray color boxed reason shows etch rate delay at the n-GaAs and n-AlGaAs layer interface.....	117

Figure 4.17 Waveguide etched side profile of (a) EPI with high power green laser PAW ($P_{PAW} \sim 100\text{mW}$) and (b) dark.....	118
Figure 4.18 Microscope picture of the post-etched serpentine waveguide pattern of EPI sample with laser PAW etching ($P_{PAW} \sim 100\text{mW}$).The width of the figure corresponds to approximately 1.7 mm.....	119
Figure 4.19 (a) Both-PR case surface condition after waveguide etching and (b) corresponding microscope pictures of positions A and B. Pictures A and B span an approximate horizontal distance of 1.3mm.....	120
Figure 4.20 (a) overall illustration of the post-etched surface of EPI samples and (b) microscope pictures of area A and B. Both-Blank mask but with some PR patterns in the side strips. The horizontal width of the Figures A and B span approximately $900\mu\text{m}$	123
Figure 4.21 Both-Metal sample surface of EPI sample with both side metal covered waveguide pattern (a) before etching, (b) after etching and (c) microscope pictures of corresponding areas. Picture A shows rough surface and rough metal after etching. Figure C spans a horizontal distance of approximately 0.9 mm based on the largest width waveguide of $20\mu\text{m}$	125
Figure 4.22 Relative vertical etch rate (R_{VR}) variation of the patterns depends on the conditions at the side strips: (a) with Initial-Mask for waveguide, (b) Both-PR (PR covers both sides of the waveguide pattern), (c) Both-Blank (most of the side area leaves as blank) and (d) Both-Metal (metal layers area deposited on the both side of the sample).....	128
Figure 4.23 Initial-Mask for Mirror etch (a) overall sample illustration and (b) mirror window pattern at the etched mirror side of the ridge-waveguide laser.....	130

Figure 4.24 SEM pictures of mirror after PAW etching using the Initial-Mask with high power green laser for EPI sample. (a) mirror window pattern on the sample near the center of the sample and (b) patterns near the edge of the sample.....	131
Figure 4.25 PAW etched PI sample with Both PR mask: (b) PAW etched sample surface and microscope pictures at the blank surface and mirror pattern and (a) Reflectometer and PL signal during the etching and corresponding video capture. Picture A spans approximately 1.3mm and picture B spans a width of approximately 350 μ m.....	133
Figure 4.26 Etched-mirror profile for the EPI sample and Both-PR mask using high-power PAW laser. (a) and (b) shows scanning position on the sample and the profile across the mirror pattern, respectively. The arrow in (a) represent profilometer scanning and the grey area (20 μ m wide) in (b) indicate the actual mirror area.....	135
Figure 4.27 PAW etch results for the EPI sample with the Both-Blank mask: (a) Reflectometer signal during the etching and corresponding video capture, (b) PAW etched sample surface and microscope pictures of five different areas on the sample and (c) simplified profilometer profile across the mirror pattern. The grey area in (b) represents the actual mirror area. Pictures I, IV and V span a horizontal distance of approximately 1.3 mm and II and III span a horizontal distance of 400 μ m.....	137
Figure 4.28 Microscope pictures of mirror patterns with mostly exposed EPI sample after (a) PAW etching and (b) dark. ($P_{PAW} \geq 70mW$). The scale is set by the waveguide width; the widest waveguide is 20 μ m.....	139

Figure 4.29 Mirror etch test using the Both-Metal mask on the EPI sample: (a) PL monitoring CCD image captured during the PAW etching and (b) post-etched surface illustration and microscope pictures of 4 different positions.....	140
Figure 4.30 Relative vertical etch rate (R_{VR}) of the patterns depends on the conditions at the side strips. Both-PR: PR covers the side-strips straddling the waveguide pattern, Both-Blank: Side-strips expose semiconductor to light and etchant, Both-Metal: metal layers deposited on the side-strips.....	141
Figure 4.31 Waveguide etched side profile of (a) M1 with green laser PAW and (b) dark. ($P_{PAW} \geq 70\text{mW}$).....	142
Figure 4.32 Microscope pictures of post-etched M1 samples with high power PAW etching. (a) and (b) shows the pictures of the mirror patterns near the center and edge, respectively. (c) shows laser and PD pattern and (d) present magnified picture of the circled area in the picture. Picture (b) spans a horizontal distance of approximately $640\text{ }\mu\text{m}$ while (c) spans approximately 1.2 mm	143
Figure 4.33 SEM pictures of M1 sample with (a) and (b) high power PAW etched, (c) and (d) dark wet etched samples.....	145
Figure 4.34 M1 mirror etch with the Both-Blank mask (a) post-etched surface under PAW, (b) dark etched sample surface with same mask and (c) Reflectometer and PL signal of the upper blank area of the sample during the high power PAW etching. I and II represent reflectometer and PL signal, respectively in (c). The distance scales in the pictures can be determined based on the widest waveguides of $20\mu\text{m}$	146
Figure 4.35 Fabrication process for laser devices with metal-only mask.....	150

Figure 4.36 High power PAW etched M1 sample with metal-only mask (a) Overall etched sample surface. The gray area represents dark surface, (b) and (c) microscope picture of the sample surface corresponds to the area A and B, respectively. ($P_{PAW} \geq 70mW$). Picture (b) spans a horizontal distance of approximately 900 μm while Picture (c) spans 350 μm based on the widest waveguide of 20 μm	151
Figure 4.37 Comparison of side profiles of (a) Laser and (b) LED PAW etching. Both have the same masking conditions and same M1 material type. The quantum well (QW) layer has a position above the etch steps.....	152
Figure 4.38 High power green laser PAW etched side profile variations on the etch depth of M1 samples with Metal-Only mask; etch depth about (a) 2.16 μm , (b) 4.33 μm and (c) 8.15 μm . While dotted line indicates the active layer in figure (a), (b) and (c).....	154
Figure 5.1 Fabre-Perot cavity with length, L and gain, g with two different mirrors 1 and 2. R_1 and R_2 denote the reflectance of mirror 1 and 2. P_1 and P_2 indicates power output from mirror 1 and 2.....	165
Figure 5.2 P-I test set-up for CW and pulsed current operations. CW: Continuous Wave, PD: Photo Detector.....	167
Figure 5.3 Optical power measured from one mirror versus bias current (P-I plots): (a) and (b) present pulsed and CW operation of shallow etched 10 μm wide laser etched in low power PAW etching, respectively, (c) and (d) show P-I of pulsed and CW operation of deep etched 5 μm wide laser etched in 70mW PAW, respectively.....	168

Figure 5.4 Ridged Waveguide Lasers with either two cleaved mirrors (CL2) or one cleaved and one etched mirror (CE). (a) The CL2-S laser has a shallow ridge that does not extend to the active region. (b), (c) The CL2-D and CE-D lasers have deep etched waveguides that have ridge depths past the active layer.....	169
Figure 5.5 Optical power measured from one mirror versus pulsed bias current for shallowly etched waveguide lasers (CL2-S); (a) and (b) present P-I plots corresponding to the waveguide etched using PAW etch powers of about 60mW and 0mW, respectively.....	171
Figure 5.6 Optical Power measured from one mirror versus bias current (P-I) plot of shallow and deep etched waveguide lasers with mask width of 10 μ m and sidewall pictures; (a) and (b) presents P-I plots of the shallow etched waveguide laser with two cleaved mirrors (CL2-S) using PAW etch laser powers of approximately 60mW and 0mW, respectively. (c), (d) and (e) present P-I plots of deep etched waveguide lasers (CL2-D) with PAW powers of 0mW, 5mW and 70mW, respectively. Laser operation measured with pulsed input bias current. (f) and (g) shows the microscope pictures of side profile correspond to the dark and low PAW power etched laser (plot (c) and (d)) and high PAW power etched laser. (e), respectively. Gray dotted line in Figure (f) and (g) indicates the active layer.....	173
Figure 5.7 Optical Power measured from one mirror versus bias current density (P-J) plot of shallow and deep etched laser waveguides (10 μ m wide); (a) and (b) presents P-J plots of the shallow etched waveguide laser with two cleaved mirrors (CL2-S) using PAW etch powers of about 60mW and 0mW, respectively. (c), (d) and (e) present P-J plots of deep-etched waveguide lasers (CL2-D) with PAW laser powers of 0mW, 5mW and 70mW, respectively. Laser operation measured with pulsed bias current.....	175

Figure 5.8 Sidewall profile versus PAW laser power. (a), (b), (c) and (d) show microscope pictures of the etched sidewall of 5 μ m, 10 μ m, 15 μ m and 20 μ m wide metal contacted pattern with low power (i.e. lower than 5mW) PAW etching, respectively. (e), (f), (g), and (h) shows etched sidewall of 5 μ m, 10 μ m, 15 μ m and 20 μ m wide metal contacted pattern with high power (i.e. higher than 70mW) PAW etching, respectively. The post-etched widths and depths written on the figures are average values.....	178
Figure 5.9 Optical Power measured from one mirror versus bias current (P-I) plot for deep-etched 15 μ m wide laser using low power PAW etching. P-I measured in pulsed operation: (a) and (b) show both CL2-D lasers etched in dark and low power PAW etch laser, respectively. (c) and (d) shows CE-D laser etched in dark and with low power PAW, respectively.....	179
Figure 5.10 Optical power measured from one mirror versus input bias current from (a) CL2-D etched in dark, (b) CL2-D etched with high-power PAW, (c) etched-mirror on CE-D etched in low power PAW, (d) etched-mirror on CE-D etched in high power PAW, (e) cleaved-mirror on CE-D etched in high-power PAW. Example optical spectrums of CE-D lasers: (f) $P_{PAW} \sim 100\text{mW}$, CE-D laser, 5 μ m Wide, $I_{Bias} = 39.2\text{mA}$, $P_{out} = 8.97\text{mW}$, (g) $P_{PAW} \sim 100\text{mW}$, CE-D laser, 20 μ m Wide, $I_{Bias} = 36.8\text{mA}$, $P_{out} = 3.24\text{mW}$	180
Figure 5.11 Schematics of CE-D laser. R_e and R_c indicate etched and cleaved mirror reflectance. P_e and P_c represent power output from etched and cleaved mirror side.....	181
Figure 5.12 P-I plot of CE-D lasers with high power PAW etching ($P_{PAW} \geq 70\text{mW}$) placed (a) near the edge and (b) center of the sample.....	186

Figure 5.13 Optical power measured from one mirror versus bias current (P-I) plot for CE-D type lasers: (a) single laser without a second laser optically coupled through etched mirrors, and (b) two lasers optically coupled through the etched mirrors. (c) and (d) illustrate lasers measured (a) and (b), respectively. The laser (a) is about 230 μm long and (b) is approximately 249 μm long with same width.....	187
Figure 5.14 Optical power measured from one mirror versus bias current (P-I) plot of 852nm lasers. (a) and (b) presents both cleaved mirror laser (CL2-D) etched in high power PAW and Dark. (c) and (d) shows one etched (CE-D) lasers fabricated with high power PAW and Dark. (e), (f) and (g) shows laser spectrum of CE-D lasers; (e) high power PAW Etched 5 μm wide and 256.9 μm long, $I_{\text{Bias}}=18.2\text{mA}$, (f) high power PAW Etched 20 μm wide and 256.9 μm long, $I_{\text{Bias}}=38.8\text{mA}$ and (g) with Dark Etched 15 μm wide and 273.6 μm long, $I_{\text{Bias}}=60\text{mA}$	189
Figure 5.15 Threshold current and slope versus etching power for lasers with two cleaved mirrors and deep-etched waveguides (CL2-D). Pictures show typical (a) Dark Wet etched and (b) PAW etched side profiles.....	190
Figure 5.16 Microscope pictures of CL2-D laser (20 μm wide, 256 μm long) with two 12 μm probe tips. (a) shows overall device picture with $I_{\text{Bias}} = 0\text{mA}$. Microscope pictures of one laser device with different bias current (b) $I_{\text{Bias}} = 15\text{mA}$, (c) $I_{\text{Bias}} = 16\text{mA}$, (d) $I_{\text{Bias}} = 17.6\text{mA}$, (e) $I_{\text{Bias}} = 20\text{mA}$, (f) $I_{\text{Bias}} = 24\text{mA}$, (g) $I_{\text{Bias}} = 25.8\text{mA}$, front mirror and (h) $I_{\text{Bias}} = 25.8\text{mA}$, back mirror.....	192
Figure 5.17 Microscope picture taking set up for laser emits at a 45° angle with respect to the optical axis of the microscope.....	194

Figure 5.18 Microscope pictures of CL2-D laser front with different bias current (a) $I_{Bias} = 0mA$, (b) $I_{Bias} = 11.2mA$, (c) $I_{Bias} = 15.2mA$, (d) $I_{Bias} = 15.6mA$, (e) $I_{Bias} = 20.2mA$ and (f) $I_{Bias} = 27mA$	194
Figure A.1 Real and imaginary refractive index versus aluminum mole fraction [107].....	214
Figure A.2 Imaginary refractive index versus aluminum mole fraction for incident light wavelengths of (a) $\lambda = 395$, (b) $\lambda = 532nm$ and (c) $\lambda = 625nm$	215
Figure A.3 Absorption length for the $Al_xGa_{1-x}As$ with incident wavelength (a) $\lambda = 395$, (b) $\lambda = 532nm$ and (c) $\lambda = 625nm$. (y scale from 0 to $10\mu m$).....	215
Figure A.4 Absorption length for the $Al_xGa_{1-x}As$ with incident wavelength (a) $\lambda = 395$, (b) $\lambda = 532nm$ and (c) $\lambda = 625nm$. (y scale from 0 to $1\mu m$).....	216
Figure C.1 Simulation of R_e/R_c (Ratio of etched and cleaved mirror reflectance) versus R_c (Cleaved mirror reflectance) for different P-I slope. z represents ratio of slopes of P-I (optical power versus bias current) from etched and cleaved mirror (M_e/M_c) above threshold current. R_e : reflectance of etched mirror and R_c : reflectance of cleaved mirror.....	221
Figure D.1 Laser PAW etch set up: (a) overall set up, (b) control part and (c) optical elements and detectors.....	222
Figure D.2 Cleaving stage.....	223
Figure D.3 Laser test set up: (a) Laser power versus current test set up and (b) Optical spectrum measurement set up.....	223
Figure D.4 High power LED for LED PAW etch test: (a) high power LED mounted on the cooling fan and (b) magnified picture of the LED.....	224
Figure E.1 Ridge-Waveguide Laser Mask: Metal Layer.....	225
Figure E.2 Ridge-Waveguide Laser Mask: PR Layer.....	226

Figure E.3 Ridge-Waveguide Laser Mask: Mirror Windows.....	227
Figure E.4 Masks for Ridge-Waveguide Etching: PR layer (Figure E.2) covers Metal waveguide patterns (Figure E.1) for minimizing lateral etching and protect mirror wells.....	228
Figure E.5 Masks for Mirror Etching: Mirror window pattern (Figure E.3) is deposited over waveguides.....	229
Figure F.1 Electromagnetic Fields in a multi-layer structure.....	232
Figure F.2 Interference pattern and etch rate for a diffusion limited wet etch. (a) and (b) denotes reflectometer signal and etch rate, respectively. The spacing between fringes corresponds to approximately 100 nm.....	234
Figure F.3 Block diagram for the HECM. BP: Band Pass.....	236
Figure F.4 A CCD calibration system. AMP: Amplifier.....	237
Figure F.5 Basic flow chart for custom EMC analysis software.....	239
Figure F.6 Example calibration plot for the CCD array. Vertical: brightness, horizontal: Optical power in arbitrary units.....	240
Figure F.7 Example sample with three small white selection rectangles for software analysis.....	241
Figure F.8 Fringe patterns for 3 small regions on an etching sample.....	242
Figure F.9 Example full fringe patterns using the CCD array.....	243
Figure G.1 Concept diagram for beam shaping lens. Z represents the thickness of the lens at any vertical point y.....	244
Figure G.2 Ray trajectory and definition of parameters.....	245
Figure G.3 Definition of angles for the lens surface.....	246
Figure G.4 Example lens contour for transforming a Gaussian beam in to a uniform one.....	248

Figure H.1 Small mirror attached to the axel of a motor with a spring return.....	249
Figure H.2 A function generator drives a shunt resistor R_2 and the mirror motor.	
The symbols are defined in the table at the back.....	250
Figure H.3 Relaxation oscillations for open-terminal mirror assembly.....	253
Figure H.4 (a) response of mirror for 15Hz and (b) voltage input signal.....	254

Chapter 1 Introduction

Modern day technology uses discrete optical components including laser diodes, photodiodes, and hybrid or monolithically integrated electronic circuits. The integration of optical and electronic devices is needed to realize higher performance with increased functionality, smaller size, lower cost, and higher reliability. Due to the successes in the fiber optics, speed and bandwidth in communication are significantly improved by transferring data via light. However, without the ability to generate, transmit, process and detect broadband high-frequency optical signals in optoelectronic systems and to interface these optoelectronic circuits to external elements, one cannot take full advantage of the high speed and large bandwidth of an optical fiber [1].

There are challenges to overcome such as reducing the height differences among the integrated devices (i.e., planar processes), integrating non-cleaved laser mirrors with other components, and simplifying the fabrication process for integrated optoelectronic devices [2]. The light source (laser) should operate with low power to minimize thermal effects and power dissipation. The integrated systems require good optical and electrical isolation between optical and electronic devices, or between optical and optical devices. To minimize the power requirement and heat from active optical elements, the device should be operated at low current and voltage levels. For semiconductor lasers as the optical source, low power requires low threshold current that, in part, depends on the quality of the mirror (angle and the surface smoothness of the mirror facet) [3].

Fabricating a laser without cleaved mirrors is one of the major tasks to realize integrated optics and optoelectronics. Vertical etches must maintain good control of lateral etching to prevent undercutting of metal contacts and increase the degree of integration. In addition to the vertical side wall for integrated laser mirrors, other integrated optical devices also require many

other etch characteristics including etched-sidewall profiles and angles ranging from shallow etched-slopes for electrical contacts to vertical flat smooth surfaces for integrated laser mirrors.

Generally, device fabrication requires either dry or wet etching processes. Dry etching is the most widely accepted process to fabricate optoelectronic devices [4-9] since it can easily produce vertical mirror facets for active optical elements. However, it can be expensive, slow, and most importantly, it generates rough surfaces which lead to increased optical loss for the device [10-16]. The surface condition of the mirror facet plays an important role in determining the threshold current of the laser [3, 9]. Also, the monolithic integration of electrical and optical elements often requires non-vertical sidewall angles that cannot be conveniently produced by dry etching.

On the contrary, wet etching has potential advantages over dry etching [11, 12, 14, 17] including lower cost, smoother surfaces, and faster etch speed. It has been reported that the wet-etched laser has smoother sidewall surface than the dry etched one [18-20]. However, conventional wet etching has a couple of drawbacks for laser fabrication such as producing uncontrollable non-vertical sidewall profile and deep lateral etching. The sidewall profiles obtained from wet chemical etching normally depend on the etching solution and the material crystal direction [21-25]. For example, an isotropic etching solution produces a rounded sidewall profile while the anisotropic type produces about 55° sidewalls in GaAs. Furthermore, the sidewall angle of wet etching also depends on the type of the etching solution [23-25] and the crystal direction of the material, which makes it difficult to produce angles other than that corresponding to the natural crystal direction. Also, from the experiments in this work, conventional wet etching (wet chemical etching in the dark) often shows multi-angled side profile in heterostructure material due to the etch rate differences for each layer. In general, the application of wet etching to the fabrication of vertical sidewalls and integrated semiconductor lasers has been an outstanding problem for decades.

It is important to understand the wet chemical etch mechanism to develop and apply the

PAW etching to the actual device fabrication. Wet etching can be described as the electrochemical dissolution of the solid in an etching solution (i.e., electrolyte). Semiconductor dissolution in the electrolyte occurs via electrochemical reactions between the solid (semiconductor) and the electrolyte (etching solution). Charge transfer at the interface leads to current flow that can be experimentally measured. The rate of the process, i.e., charge transfer rate, is one of the important factors to determine the solid dissolution. Several research groups have suggested electrochemical models of the charge transfer at the solid/electrolyte including the kinetic model by Memming [26], energy band model by Gerischer [27], and quantum mechanical model by Levich [28] and Dogonadze [29]. The Gerischer model is the most convenient for the semiconductor/solution interface since the model uses energy band diagrams to explain electron (charge) transfer at the solid/liquid interface. [30-32].

The Gerischer model [27] for the solid/electrolyte interface has analogy to the solid-to-solid interface such as a PN junction. According to the model, equilibrium at the solid-etchant interface occurs when the electrochemical potential of a redox system (i.e., electrolyte) coincides with that for the solid that maintains charge neutrality of the system in the equilibrium [27, 33]. Details of the theories are introduced in Chapter 2. However, the charge transfer theories are for very simple redox systems and not directly applicable to the general etching system. Also, the theory assumes there aren't any surface states at the solid (semiconductor) surfaces and the material has only one layer (bulk semiconductor material). Any energy applied from outside of the system cause changes in the system. At the semiconductor/electrolyte interface, electron transfer across the interface occurs via the energy bands [32]. Therefore any variation in the energy bands, such as band bending or shifting, plays a very important role in the charge transfer process. The energy band diagram at the interface depends on various factors such as the type of doping of the semiconductor, the Fermi energy level of the redox system, the ion concentration in the redox system, and any electrical potential applied to the solid.

The application of the models to etching and the fabrication process must necessarily

focus on the role of charge carriers. According to the bonding theory, the solid dissolution (etching) proceeds by consuming holes at the solid/etching solution interface [31-35], which is related to the current flow at the semiconductor/solution interface. Holes at the surface of the solid remove electrons from the bonds and thereby reduce the bonding energy of the surface atoms, which weakens the bonds [36, 37]. Consequently, the accessibility of holes and electrons at the surface can be determining factors of the solid dissolution rate. The carrier (electron and hole) flow at the surface can be controlled by many factors in the dissolution system including the Fermi level difference between the two phases (solid and the etching solution). It has been noticed that one can increase or decrease the dissolution rate by applying potentials or photons to the many kinds of semiconductors including Ge [35, 38], ZnO [39], LiN [40], InP [41, 42], GaN [43-45], SiC [46], and GaAs [35, 47-53].

Applying electrical potential or light to the etching system can lead to variations of the electrochemical parameters for the two phases (semiconductor and electrolyte) [31, 32, 54]. The experiments for this dissertation indicate that the Photo-Assisted Wet (PAW) etching is more readily applicable to the semiconductor fabrication since the system does not require the complicated system apparatus normally used for electro-chemical etching systems with externally applied potentials [54]. Photo-Assisted Wet (PAW) etching has been at the center of attention due to the scientific interests and many possible applications especially for the maskless etching. Other application include the generation of groove patterns without using an etch mask by applying laser-generated interference patterns [41, 50, 55-57] and directly carving various patterns onto bulk n-type GaAs or AlGaAs using a focused high-power laser [52, 53, 58, 59]. It is reported that illumination can accelerate or inhibit semiconductor dissolution process [60-63].

The experiments for this dissertation indicate that PAW etching provides control over not only the dissolution rate but also the sidewall angle by using the proper photon energy. Previous PAW etching experiments for bulk GaAs material performed in our laboratory [64] potentially expands the fabrication options offered by wet etching using UV light to alter the normal crystal-

plane directional etching and thereby providing control over the sidewall profiles with angles ranging from several degrees to 90° while retaining many favorable wet-etching properties for n-type GaAs material. The PAW etching demonstrates control of the sidewall profile and etch rate in bulk n-type GaAs with a metal mask by illuminating the wafer with UV light (395nm) from a LED (optical power density $\sim 64 \text{ mW/cm}^2$).

The literature suggests dissolution mechanisms for simple cases such as bulk n- and p-type GaAs material [65] and materials with a couple GaAs/AlGaAs layers [63, 66] whereby photo-generated carriers control the dissolution rate. The reported studies focus on the dissolution rate (vertical etch rate) rather than the variation of sidewall angle or the horizontal dissolution. However, the study of the photo-dissolution of the multi-layered materials applicable to device fabrication such as GaAs/ $\text{Al}_x\text{Ga}_{1-x}\text{As}$ heterostructure has not been reported. In the study of heterostructure, difficulties arise in part due to the variation of the energy band edge vs. depth, as a result of the various doping and aluminum concentrations in the epitaxial layers that affect the carrier movement in the material. From the experiments shown in this work using a laser with total intensity larger than 70mW, the etching of heterostructure material varies by layer structure and masking material.

The semiconductor wafers used in the fabrication of optical devices consist of many different layers in order to tailor the band gaps (i.e., band gap engineering) and to especially provide the quantum wells used for many optoelectronic devices. The study of the PAW etching of the heterostructure material opens new fabrication (etch) methods for optical devices. The illumination can control the semiconductor dissolution characteristics including the dissolution rate and the side profile of the pattern. The full mechanism of the PAW etching is not yet fully understood and little research has been reported for semiconductors with more than one layer. A general model that can be applied to both bulk and multi-layered materials has not been reported. Using such a model, one could easily apply the PAW system to GaAs/ $\text{Al}_x\text{Ga}_{1-x}\text{As}$ heterostructure for optical device fabrication.

Complexities arise in applying the PAW etching to heterostructure in part due to the variation of the energy band edge vs. depth as a result of the various doping and aluminum concentrations in the epitaxial layers that affect the carrier movement in the material. The laser has the basic structure of a p-n diode where the most common material for in-plane lasers has top layers consisting of p-type material while the bottom layers grown on the substrate consist of n-type material. A typical laser heterostructure has the following layers: (i) a p-type GaAs layer for electrical contacts; (ii) an $\text{Al}_{0.6}\text{Ga}_{0.4}\text{As}$ cladding layer with p-type doping; (iii) a graded index layer that transitions the refractive index and band gap for waveguiding and to inhibit the injection of hot carriers to the quantum wells; (iv) a set of quantum wells and barriers for efficient carrier recombination and the subsequent production of photons; (v) a lower graded index region; (vi) a lower n-type cladding layer made of $\text{Al}_{0.6}\text{Ga}_{0.4}\text{As}$; and (vii) an n-type epitaxial layer grown most often on an n-type substrate. The doping does not extend into the modal volume (consisting of a portion of the graded index region and the quantum wells, sometimes termed ‘active region’ in the present work) to minimize free-carrier absorption of optical energy. The present research uses a variety of heterostructure as will be presented in ensuing chapters. Some wafers use an undoped substrate (i.e., semi-insulating) so as to provide electrical isolation between the integrated devices (assuming proper fabrication) and between the devices and external systems in contact with the substrate. The PAW etching experiments for the present work use laser heterostructure with similar structure except in some cases, as detailed in the ensuing chapters, the n-layers are grown above the active layers and the p-type epitaxial layers.

As an overview, this work on PAW etching can be classified as a ‘scientific study’ and as ‘semiconductor processing’ as shown in Figure 1.1. The scientific study consists of (i) observing electrochemical reactions of different materials with various layer structures and masks under different light sources including high power LEDs with different wavelengths and a green laser (~532nm) with optical intensities ranging from 0 to 100mW (total laser power) and (ii)

understanding the interplay between the possible electrochemical reactions at the semiconductor/etching solution interface and the photo-carrier dynamics.

The PAW etching has attractive potential application for semiconductor device fabrication such as to control the sidewall angle, reduce the lateral etching and provide ‘on demand’ selective etching. Fabricating and testing optical devices such as lasers and waveguides provide techniques to evaluate the sidewall quality of the photo-dissolved pattern. As shown in Figure 1.1, the work designs a new laser fabrication system as an application of the PAW etching which entails the following: (i) constructing a system capable of controlling the etching while measuring the steady-state photoluminescence (PL) and the etch characteristics that includes the etch depth, rate, and the formation of surface microstructure and transition layers, (ii) designing fabrication steps and masks for PAW etched optical devices and (iii) appraising the PAW etching of the heterostructure semiconductor by fabricating and testing the optical devices such as laser and waveguide.

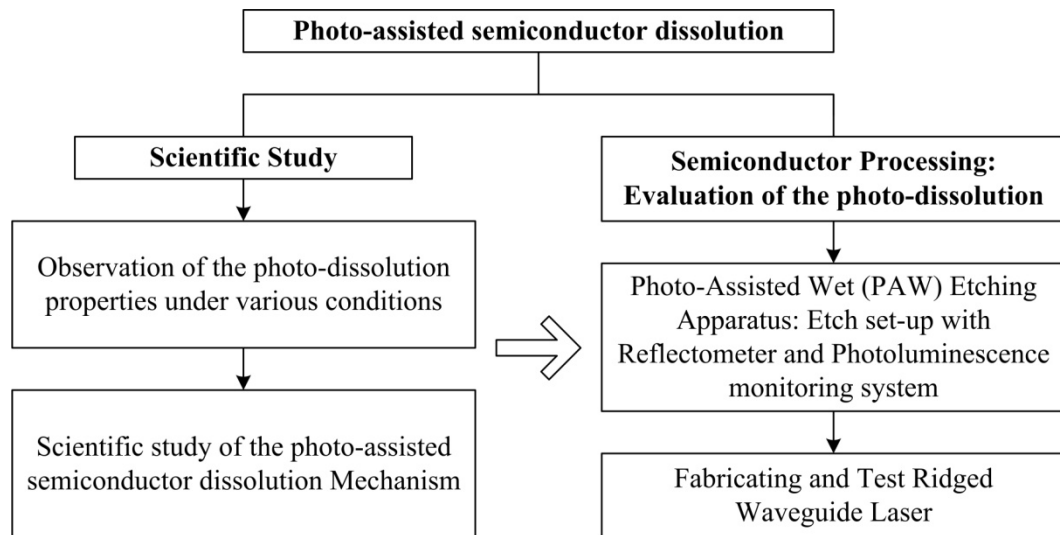


Figure 1.1 Summary of the thesis work.

The first goal for the thesis work is to extend the present understanding of the PAW etching by observing the photo-dissolution of the heterostructure material under various conditions. The second goal is to evaluate the quality of the photo-dissolution of the heterostructure material. Fabricating and testing lasers with integrated mirrors and ridge waveguides by using the PAW can indicate the quality of the process. The laser threshold current provides a sensitive operational method to determine the photo-dissolution quality for surfaces associated with the mirrors and waveguide. The mirror quality depends on its angle with respect to the body of the waveguide and its roughness, which can include uneven etching of the GaAs-AlGaAs layers near the quantum wells (active region).

The sidewall angle can be determined from SEM measurements and in some cases, by diffraction limited optical measurements. The optical scattering in a laser ridge waveguide is sensitive to both the planar and sidewall roughness near the semiconductor-air interfaces that determine the effective refractive index for lateral waveguiding (i.e., near the intersection of the ridge and etch-plane of the semiconductor). The roughness depends on the etch quality and on any “optical smoothing” provided by possible passivation layers. The operating characteristics (threshold current) for the etched-mirror integrated laser can be compared with that for the cleaved-mirror laser fabricated under the same conditions; this comparison provides one metric for the success of the PAW etching. To compare the mirror reflectivity of the cleaved and etched cases, all the other parameters of the laser design such as total length, the width of the laser and material growth should be kept constant.

The lateral confinement of the wave (transverse to the length of the laser body but parallel to the planar surface) can be controlled by the depth of the waveguide etched into the surface. Generally, shallowly-etched ridge-waveguides require the etching be stopped when the etching surface comes to within approximately $0.1\mu\text{m}$ of the quantum wells to minimize optical loss at the waveguide [67]. An optical reflectometer developed in conjunction with this dissertation is incorporated into the system to monitor in real-time the etch depth, rate, and

roughness caused by surface micro-structure, and the formation of surface transition layers. The dissolution depth can be controlled by the reflectometer etch monitor; consequently the laser threshold can be optimized with respect to the confinement factor. Microstructure formed on the planar surface during the etching affects one's ability to accurately access specific layers since the variation can exceed the thickness of the layer. The smooth surface produced by wet chemical dissolution minimizes the variation and thereby reduces the scattering for nearby propagating optical waves. Surface roughness on post-etch sidewalls affect optical scattering losses and can be anticipated to have significantly larger effects for narrow electron wave guides. The reflectometer monitors the planar roughness in real time as the material dissolves.

As described, the work consists of applying and advancing the relevant models for PAW etching, investigating the effects of optical power and wavelength on bulk and heterostructure GaAs with a variety of mask types using incoherent light, designing and constructing an etching system using a coherent light source (so the system can accommodate monitoring equipment), measuring the effectiveness and quality of the PAW etching using fabricated integrated quantum well lasers. These phases of the research are divided as follows.

Chapter 2 presents theoretical background for the thesis work including electrochemistry, wet and photo-chemical etch mechanisms. Experimental results and discussions continue in Chapter 3, 4, and 5. Chapter 3 presents PAW etching results using several different high power LEDs as light sources. In the chapter, PAW etching properties are found to depend on the etching conditions such as the layer structure of the materials, wavelengths of light and masking materials. By changing these PAW etching conditions, one can achieve the desired etch properties. For laser mirror applications, laser heterostructure samples show promising etch results under green or UV illumination. However for laser device fabrication, the LED PAW etch setup needs to be modified by including equipment to monitor the process and by providing better control over the optical source. For these reasons, the modifications employ a laser source rather the LEDs.

Chapter 4 discusses the use of a green laser as a light source instead of the LED and the design and construction of an optical reflectometer and photoluminescence (PL) monitoring system. The reflectometer and PL monitor display changes of the surface condition, etch rate and carrier densities in real time. For PAW etched laser fabrication, new fabrication steps and corresponding masks need to be designed. PAW etch experiments performed using total lasers power larger than 70mW uncovers a couple of issues for the laser-based PAW system: (i) the etch depth becomes non-uniform and (ii) the etch rate depends on the masking material and size of the opening on the mask. With higher than 70mW and using laser heterostructure material, the etch depth near the patterned area varies by the mask pattern design and the material. Etch inhibition occurs at the metal-photoresist patterned region thereby causing difficulty to etch mirror wells. The etch depth of the material varies according to the mask patterns used on the sample. For the laser heterostructure material, the quantum well and junction region as well as any semi-insulating substrate can block the current flow from the surface to the back-side of the sample. As a result, most of the photo-generated carriers are distributed on the etching surface and affect the material dissolution. Therefore, the etch depth can significantly vary across the surface which requires improved etch monitoring for measurement. Simple ridge waveguide lasers with deep etched waveguides and mirror facets are fabricated to evaluate PAW etching.

Chapter 5 discusses the measurements of optical power versus bias current (P-I) and the emission spectra of the ridge waveguide lasers fabricated using the laser PAW process. As an evaluation of the PAW etching, three different types of ridge waveguide lasers are tested. The first type has shallow etched waveguides which are formed by stopping the etch just before the active layer and then cleaving two mirrors (CL2-S). The second type has deep etched waveguides and two cleaved mirrors (CL2-D). The third type also has a deep-etched waveguide but has one etched mirror and one cleaved mirror (CE-D). The typical ridge waveguide laser has a shallow etched waveguide and two cleaved mirrors. Laser parameters including mirror reflectivity,

internal loss and differential quantum efficiencies are calculated from PI curves and used to compare cleaved and etched laser mirror quality.

PAW etching improves both mirror and waveguide quality by reducing the lateral etching and improving the side profile. The distributed losses (i.e., optical scattering) and the mirror reflectance can be obtained and compared for the various cases. Chapter 5 displays the dependence of the threshold and external differential efficiency on the various PAW etch powers. For comparison of the effects of PAW etching on the waveguides, lasers with shallowly etched waveguides are fabricated under illumination intensity ranging from dark conditions to 100mW (total laser power) 532nm laser illumination. Further, the shallowly etched waveguide lasers are compared with deep etched waveguide lasers (CL2-S and CL2-D) with various PAW laser power. When the waveguide is etched deeper than the active layer, the laser performance becomes more sensitive to the sidewall quality. The etch properties depend on the PAW laser power (P_{PAW}) and wavelength. This chapter examines the etched mirror lasers (CE-D) with difference powers of PAW lasers. CE-D (etched mirror with deep etched waveguide) lasers are also compared to the CL2-D (both cleaved mirror with deep etched waveguide) lasers.

Chapter 6 summarizes the dissertation research and discusses future works needed to improve the PAW etching system. Mass charge flow of the excess photo-generated carriers on the surface may cause the regional non-uniformity of the etch depth. Detailed research on current flow and modeling on the PAW etch mechanism needs to be continued. For device fabrication, the reflectometer can be improved by monitoring the etch depth at the patterned layer during the etch process. Further research on the surface current flow lead to the solution of the etch depth problem for the high power PAW etching (total laser power larger than 70mW).

Chapter 2 Theory of Electrochemistry

Solid dissolution can be classified as electrochemical and chemical processes between a solid and an etching agent. For wet etching, the agent consists of a acidic solution that can include an oxidizer (i.e., electrolyte). The chapter discusses the three basic wet etching mechanisms: (i) anodic etching that applies a voltage to induce current flow to control etching in the electrolyte without an oxidizing agent, (ii) electroless etching requires charge transfer to the etching surface without the use of externally applied voltages and (iii) chemical etching that uses an acid and oxidizer supply all the necessary resources for etching and does not use charge transfer. Both anodic and electroless etching depends on the charge transfer at the solid/electrolyte interface which is defined as the electrochemical process while chemical etching does not depend on the externally applied potential and charge transfer. Anodic and electroless etching can be classified as electrochemical process which constitutes the main interest of this dissertation. Illumination also alters the charge transfer and therefore the etch rate of the system for anodic and electroless etching.

In electrochemical solid dissolution, the charge transfer between the solid and etching solution plays a major role. By applying electrical potential or light to the system, one changes the electrochemical parameters, and thereby alters the etch properties. Gas and liquid electrochemical systems have very different thermodynamic properties. Therefore, it is important to introduce the theoretical background of electrochemistry to study photo-assisted semiconductor dissolution mechanisms especially for the electrochemical etching (photo-assisted solid dissolution) as the focus of this dissertation. Section 2.1 presents a brief review of the electrochemical system (electrolyte and solid) including the electrochemical potential and energy states, electric double layer generation at the electrolyte/solid interface and the band bending due to the Fermi level differences of two different phases (solution and solid). The kinetics of charge transfer is introduced in the subsequent section (Section 2.2). In the last section (Section 2.3),

electrochemical models for three different semiconductor dissolution mechanisms (anodic, electroless and chemical etching) are reviewed for the general bulk material case.

2.1 Electrochemical System

Wet etching proceeds through the electrochemical reactions at the solid-liquid interface by immersing the solid (semiconductor) into the etching solution (electrolyte), which consists of a mixture of the oxidizing agent such as hydrogen peroxide and reduction agent such as sulfuric acid with de-ionized (DI) water. In some cases such as anodic etching, the etching solution consists of a diluted acidic solution. The solid-electrolyte interface is somewhat similar to the solid-solid junction in a PN junction. However, there are some important distinctions between the solid-liquid system and the solid-solid junction due to the electrochemical characteristics of the liquid. The present chapter shows how (i) the semiconductor Fermi level and surface band-bending and (ii) the solution Fermi level and the oxidation/reduction states determine the interfacial current flow and in particular, the etching as a non-equilibrium process. Illumination can increase the interfacial hole concentration (especially for etching n-type semiconductors) and thereby increase the etch rate including those situations that do not use an oxidizer.

The first topic (Section 2.1.1) introduces chemical and electrical definitions and properties of the electrolyte. The Fermi level for the electrolyte is derived in this section. The electrolyte reviewed in this chapter is a very simple case with only one redox system (for example, a mixture of sulfuric acid and DI water). The electrochemical systems for semiconductor fabrication (etching solution) generally contain two or more redox systems which make the system more complicated. However, the basic theories for the simple case with one redox system are still applicable for more complicated cases. Section 2.1.2 shows how the redox energy states expand into “energy bands” due to water dipole fluctuations. Section 2.1.3 discusses the energy band formation at the liquid-solid interface and the role of electrons and holes in the material dissolution. Section 2.1.3 also briefly reviews bonding theories and energy bands at the

semiconductor surface before introducing double-layer generation and the energy band bending at the semiconductor/electrolyte interface in Section 2.1.4.

2.1.1. Electrolyte and Energy Level

An electrolyte is defined as a substance that dissociates into free ions when dissolved to produce an electrically conductive medium [68]. Etching solutions such as Hydrogen peroxide (H_2O_2)/Sulfuric acid (H_2SO_4)/Water (H_2O) can be generally categorized as an electrolyte. In solids such as metals and semiconductors, the carrier (electron or hole) movement generates current. On the contrary, in the liquid electrolyte, the current is primarily carried by ions. The electrical properties of the ions such as charge and mobility (and hence conductivity) play an important role to determine the material dissolution characteristics.

The conductivity σ of the electrolyte can be defined similar to that for the semiconductor conductivity. For more than one type of ion in the electrolyte, the conductivity has the form [32].

$$\sigma \propto F \sum z_i \mu_i c_i \quad (2.1)$$

where z_i is the charge number for specie i , μ_i is the mobility of each type of ions, c_i is the concentration of the ion in mole/cm³, and F is the Faraday constant that is defined as the amount of electric charge in one mole of electrons and given by $F = e \cdot N_A$ where N_A is Avogadro's number and $e > 0$ (magnitude of electron) represents the elementary charge as usual on one electron [68]. The mobility of the ion in the solution is related to the velocity v and the electric field E in which an ion is moving. The corresponding electric force, $F = |z_i|eE$, accelerates the ion until the frictional force counterbalances the electric force. The frictional force can be approximated from Stokes' law as $6\pi\eta r v$, in which η is the viscosity of the solution, r the radius of the ion and v the velocity. As a note, the application of Stokes' law approximates the ion as a small spherical object in a continuous viscous fluid. The mobility than can be expressed as follows [32].

$$\mu_i = \frac{v}{E} = \frac{|z_i|e}{6\eta r} \quad (2.2)$$

And the diffusion constant of species i , denoted by D_i , is related to the mobility by Einstein relation as follow

$$D_i = \frac{kT}{e} \mu_i \quad (2.3)$$

From Equations (2.2) and (2.3), it is clear that the mobility of the ions relates to both the conductivity and the diffusion constant, and therefore the reaction rate of the etching must be dependent on the viscosity of the solution. This result leads to the general classification of etching solutions in terms of their viscosity: diffusion rate limited and reaction rate limited etching solutions [23, 25]. The mobility of most ions in the solutions are about 5-6 orders of magnitude smaller than the mobility of electrons and holes in a semiconductor; the carrier velocity in the solution is smaller than the carrier velocity in the solid [31, 32]. The solution parameters (e.g., conductivity and mobility) vary depending on the ion concentration in the solution (i.e., pH of the solution).

Ion movement in the solution does have certain similarities with the carrier movement in the solid. However, in the aqueous solution, the ions interact with other ions and solvent molecules that leads to the formation of a relatively strong bound shell around any given ion; this bond shell travels though the solution with the ion. In common usage, the term ‘solvation’ refers to this overall interaction while ‘hydration’ refers to the case when the solvent consists of water. [68, 69]. Ions are unstable in solutions without solvation [68]. Electrostatic ion-dipole forces or chemical forces can cause thermodynamic interactions between ions and the polar solvent molecules.

Figure 2.1 schematically illustrates the structure of a solvated ion. The solvent structure around the ions depends on the charge of the ion (ionic strength and the size). The disturbance among the solvent molecules caused by the ions becomes weaker with increasing distance and

with increasing temperature. The solvated ion structure changes during or after an electron transfer; its primary structure is distorted where the ion is located, and its molecules undergo reorganization (reorientation) within a certain volume around the ion. Such “rearrangement” or “reorganization” of the solvent molecules and the corresponding energy change plays an important role in the theory of electron transfer.

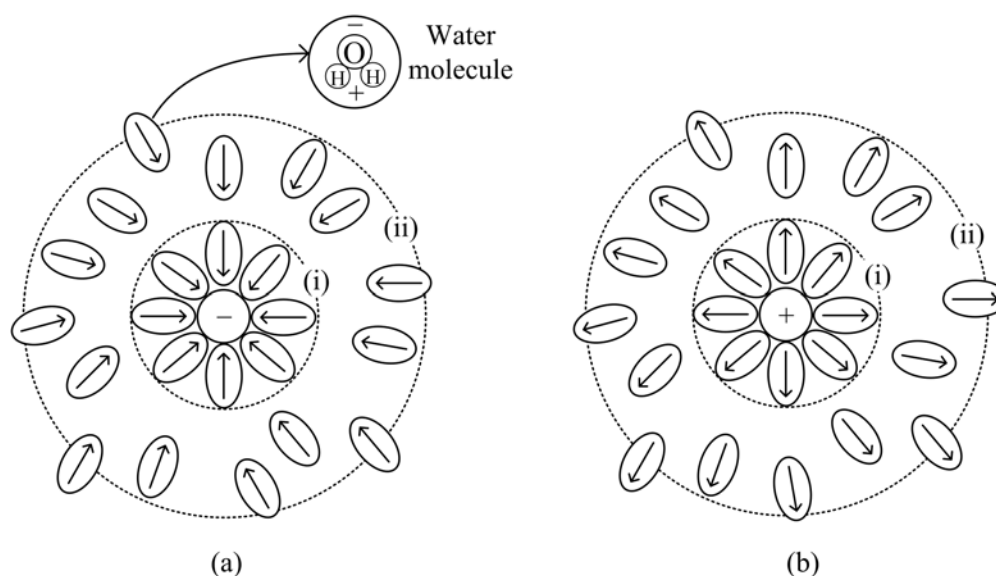


Figure 2.1 Solvated ion structure for (a) negative ion and (b) positive ion. Circle (i) represents the inner shell, and circle (ii) represents the outer shell [Modified from 68, 69].

When a solid (such as metal or semiconductor) is placed in the electrolyte, ‘redox couples’ are formed by molecules or ions in the solution that can be reduced and oxidized by an electron transfer. The two components of the redox couple do not need to bond to each other but one must be capable of being ‘reduced’ (receive an electron) by the oxidation (removal of an electron) of the other. A reduced state (*Red*) forms by adding an electron to an oxidation state (*Ox*). The corresponding chemical reaction for the redox system is given by [34]



In an electrochemical reaction both *Red* and *Ox* species remain in the solution and only the

electron is transferred between the redox system and the electrode. Assume only the redox couple dissolves in an electrolyte without any electrode, the electrochemical potential $\bar{U}_{e,redox}$ of this electron is given by

$$\bar{U}_{e,redox} = \bar{U}_{red} - \bar{U}_{ox} \quad (e^- \Leftrightarrow Red - Ox) \quad (2.5)$$

where the electrochemical potential of reducing, \bar{U}_{red} , and oxidizing, \bar{U}_{ox} , species are defined as follow [32]

$$\bar{U}_{red} = U_{red}^0 + RT \ln(c_{red}/c_{red}^0) + zF\phi^{sol} \quad (2.6)$$

$$\bar{U}_{ox} = U_{ox}^0 + RT \ln(c_{ox}/c_{ox}^0) + (z+1)F\phi^{sol} \quad (2.7)$$

where ' c_{ox} ' and ' c_{red} ' represent the concentration of ions in units of moles/cm³.

By substituting Equations (2.5) and (2.6) into (2.4), the electrochemical potential will be

$$\bar{U}_{e,redox} = \bar{U}_{redox}^0 - RT \ln(c_{ox}/c_{red}) \quad (2.8)$$

where

$$\bar{U}_{redox}^0 = U_{red}^0 - U_{ox}^0 + zF\phi^{sol} - (z+1)F\phi^{sol} \quad (2.9)$$

The superscript "0" represents the 'standard condition' ($c_{ox} = c_{red}$) of the solution.

Since the electrochemical potential of electrons in a metal or a semiconductor is called the Fermi level E_F , neglecting differences due to temperature, the electrochemical potential of a redox system, $\bar{U}_{e,redox}$, can be termed the Fermi level ($E_{F,redox}$) as first introduced by Gerischer [34].

$$E_{F,redox} = E_{F,redox}^0 + k_B T \ln\left(\frac{c_{ox}}{c_{red}}\right) \quad (2.10)$$

where k_B is Boltzmann constant and $E_{F,redox}^0$ is Fermi level of the redox system at the standard condition ($c_{ox} = c_{red}$).

Under equilibrium conditions, the Fermi energy level of both phases ($E_{F,solid}$ for solid and $E_{F,redox}$ for solution) coincide at the interface which maintain overall charge neutrality [34].

$$E_{F,solid} = E_{F,redox} \quad (2.11)$$

2.1.2 Energy Band Fluctuations

In the previous section, it is shown that the electrochemical potential in the redox system can be considered as a Fermi level as in a solid. Under equilibrium, Fermi levels of both phases should be the [34, 35]. The theory of the solid/electrolyte contact has analogy to the solid-to-solid contact such as the PN junction or the metal/semiconductor junction. However, there is a substantial difference between the two cases due to the dipole fluctuation in the electrolyte, which is caused in-part by the random transfer of thermal energy between the dipole and its environment to maintain or approach equilibrium.

Consider a solid surface in contact with fluctuating dipoles. As the dipoles fluctuate, the electrical potential at the surface varies as does also the electronic energy level of the surface states. Such fluctuations, however, can only affect electron transfer from (or to) the solid if the dipole fluctuations are slower than. If the fluctuations are faster than the electron transfer, they will average out during the process. A slow dipole fluctuation ‘freezes’ the surface state energy during the electron transfers. The Frank-Condon principle states that electron transfer to or from an energy level is faster than the dipole fluctuation at the solid/electrolyte interface [31].

In the case of a typical redox system, a solvation shell surrounds the ion as illustrated in Figure 2.1. As a definition, the “reorganization energy” λ represents the change in the energy of the polar medium (aqueous solution) due to reorientation (reorganization) of dipoles following the process of electron transfer to or from the surface. For example, the reorganization energy is necessary to change the dipole arrangement surrounding ions when the ion changes from negative to positive by electron transfer. The dipole reorientation causes a shift in energy levels, a “Frank-Condon splitting” of the mean occupied state (reduced state) from/to the mean unoccupied energy level (Oxidized state) [31] as shown in the Figure 2.2. The electrochemical potential of the electrons or the standard Fermi level of the redox system $E_{F,redox}^0$ occurs from the energy differences due to the reorganization of the dipoles.

$$E_{F,red}^0 - \lambda = E_{ox}^0 + \lambda = E_{F,redox}^0 \quad (2.12)$$

The values of E are negative for electrons and therefore a plot of energy has more negative values upwards (and $\lambda > 0$). It is found that λ can vary within a broad range between 0.3 and 1.6eV depending on the type of solid material and the composition of the solution [70-72].

The probability distribution function for the “thermally broadened” oxidized and reduced solvation states $W_{ox}(E)$ and $W_{red}(E)$, respectively, depends on the electronic energy E as follow [34];

$$W_{ox}(E) = \frac{1}{\sqrt{4kT\lambda}} \exp \left[-\frac{(E - E_{F,redox}^0 + \lambda)^2}{4kT\lambda} \right] \quad (2.13a)$$

$$W_{red}(E) = \frac{1}{\sqrt{4kT\lambda}} \exp \left[-\frac{(E - E_{F,redox}^0 - \lambda)^2}{4kT\lambda} \right] \quad (2.13b)$$

Equation (2.13a) and (2.13b) are a Gaussian probability density functions for finding the empty and occupied electronic states, respectively, at the energy E . The band width 2σ (twice the standard deviation) depends on the temperature T of the solution as expected through $\sigma = \sqrt{2kT\lambda}$. This temperature dependence can make etching quite sensitive to temperature. Since the Gerischer model concerns only one electron, the fluctuation functions ($W_{red}(E)$ and $W_{ox}(E)$) describe the distribution of the occupied and empty electronic levels for only one electron. The energy distribution for all of the electrons can be found by multiplying the concentration of the species (c_{red} and c_{ox}) with the distribution function for a single electron (W_{ox} and W_{red}).

$$D_{ox}(E) = c_{ox}W_{ox}(E) \quad (2.14a)$$

$$D_{red}(E) = c_{red}W_{red}(E) \quad (2.14b)$$

where the ion distribution D represents a type of density-of-states and provides the fraction of oxidation or reduction states at a given energy E and has the units of (mole/ $V \cdot E$) where V and E denotes volume and energy.

Figure 2.2(a) and 2.2(b) illustrate the energy band splitting and the distribution of the simple redox system in the standard ($c_{ox} = c_{red}$) and non-standard ($c_{ox} \neq c_{red}$) condition, respectively. In the Figure 2.2, E_{red} and E_{ox} indicates the most probable energy for the occupied level (reduced state) and unoccupied level (oxidized state), respectively.

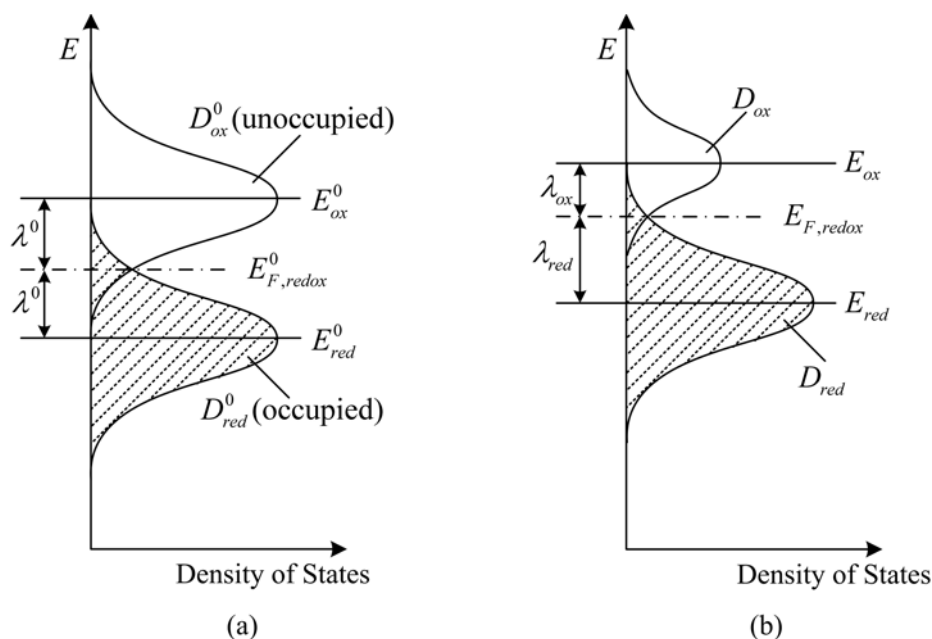


Figure 2.2 Electron energies (negative upwards) of a redox system vs. density of states: (a) standard condition (same concentration of Ox and Red species), (b) different concentration [modified from 32].

The superscript “0” in the Figure 2.2(a) denotes that the redox system is in the standard condition. The E^0_{red} (and E_{red}) is at a lower energy (i.e., $\lambda > 0$) than E^0_{ox} (and E_{ox}) as a result of the reorganization of the dipoles in the aqueous solutions (Franck-Condon splitting). λ^0 (a positive quantity) represents reorganization energy under standard conditions. According to the fluctuation functions W for the oxidized and reduced states in Equation (2.13), the ion concentrations in the redox system are important factors to the distributions D of each state. In the case with same concentration of the reduced and oxidized species ($c_{ox} = c_{red}$), the corresponding energy distributions are same as shown in the Figure 2.2(a). Generally for a diluted electrolyte,

the two distribution functions overlap and have equal value at the standard electrochemical potential of the redox couple (standard Fermi level $E_{F,redox}^0$) [31, 32].

For unequal concentrations of the two species in the redox system ($c_{ox} \neq c_{red}$), the energy distribution functions of the redox system, D_{ox} and D_{red} , are different from each other (Equation (2.14)). Also, the Fermi level of the redox system is shifted according to the Equation (2.10). For example, when the concentration of the oxidation species is smaller than the reduction species, ($c_{ox} < c_{red}$), the Redox Fermi level shifts upward as shown in the Figure 2.2(b). The Fermi level moves downward in case of $c_{ox} > c_{red}$. However, still, two energy distributions overlap with equal values $E = E_{F,redox}$.

The Gerischer model described in this section has analogy with the semiconductor case, which makes the model ready to apply at the solid/liquid interfacial interaction. The time-fluctuating energy levels in the Figure 2.2 can generally be considered as bands of energy levels similar to the conduction and valence bands in the solid. However, as Morrison has pointed out [31], these “bands” arise from the fluctuation of the solvent dipoles and they have different properties from the fixed bands in solids. In the solid case, electron-phonon interactions cause a fluctuation of electronic energy in a static distribution of levels. On the other hand, in the redox system, it is ion-phonon interactions that cause a fluctuation of the energy levels themselves.

2.1.3 Solid-Liquid Interface

Gallium-Arsenide(GaAs), Gallium (Ga) and Arsenic (As) have 4 covalent bonds in a tetrahedral arrangement to form a crystal. At the (1 1 0) surface, for example, one of the four covalent bonds of GaAs is broken and three remain (see Figure 2.3). A surface As atom has approximately five valence electrons whereas Ga would have approximately three (Ga is in group III and As is in V group). Each type of surface atom contributes three electrons to the covalent bonds. This leaves each surface As with two excess electrons which forms a filled surface band

lying below the top of the valence band (under ideal conditions at zero Kelvin in the dark) as shown in Figure 2.3. All three Ga electrons are taken up in the covalent bond leaving none to populate surface states; thus, the empty surface band (surface state without electrons) is formed primarily from the Ga states [73].

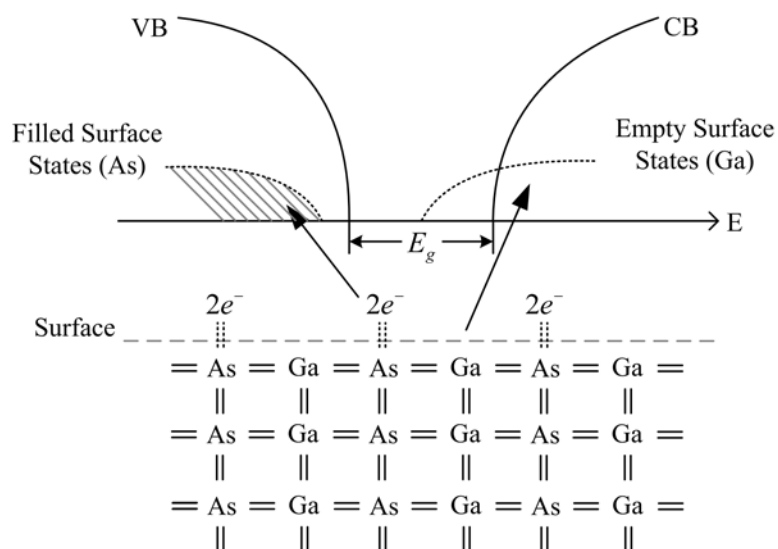


Figure 2.3 Model of the surface state distributions on the (110) GaAs surface [73].

This model of the surface has the result that the interaction between neighboring atoms in the surface becomes weak when an electron becomes excited from a bonding state in the valence band to an antibonding state in the conduction band. The surface atoms can gain energy by interacting with electrons of a suitable reagent, the energy states of which are in a range above this unoccupied level in the surface and which fulfill the necessary symmetry conditions. In one model, 'Nucleophilic' reagents [34] can supply two electrons and can rearrange the bonds at the surface by creating new quantum states and substituting for other surface bonds/atoms. As a result of nucleophilic interactions, a new set of electronic quantum states can be formed at the surface with more favorable energies than previously available. In this way, a new chemical bond can be obtained between a nucleophilic reagent and one surface atom [34]. The nucleophilic

bonds substitute for the bonds of the surface atom with its neighboring atoms in the semiconductor. One model [34] indicates that oxygen with its large electronegativity also creates favorable quantum states that ‘ruptures’ the surface bonds in favor of an oxygen bond.

When a solid (metal, semiconductor or insulator) makes contact with an electrolyte, a complex structure of charge layers forms resulting in charge transfer between phases (solid and liquid), adsorption of positive and negative ions, and orientation of molecules with permanent dipole moments. The layers due to the charge distribution in the interface are called electrical double layers. There are two different types of the electrical double layers depending on the charge distribution and the potential across the interface region: the Helmholtz double layer and Gouy double layer (see Figure 2.4). Surface layers (i.e., space charge layers) form on the solid side of the surface, due to the surface charge accumulated in the electric double layer. The space charge layer also strongly depends on the applied potential and illumination. The Helmholtz double layer plays a major role in the electrochemical processes. For most of the interfaces between an aqueous solution and a solid consisting of either metal or semiconductor, the potential across the Gouy layer is negligible [31, 32, 54]. This double layer arises between the charged solid and the solution ions of opposite sign attracted to the neighborhood of the solid to neutralize its charge, i.e., adsorption/desorption of ions.

Figure 2.4 illustrates (a) the double layer and (b) the corresponding energy diagram at the n type semiconductor and solution interface. As shown in the figure, the space charge region appears in the solid while the Helmholtz and Gouy layers form in the solution. In the solid, potential drop occurs across the space charge region indicated as $e\phi_{sc}$ with thickness of $d_{sc,n}$. On the solution side, Helmholtz potential $e\phi_H$ occurs across the Helmholtz double layer with thickness of d_H . The Gouy layer extends into the solution and shows relatively low potential drop. At the semiconductor/solution interface, the actual Helmholtz double layer, d_H , is much thinner than the space charge region $d_{sc,n}$ in the semiconductor.

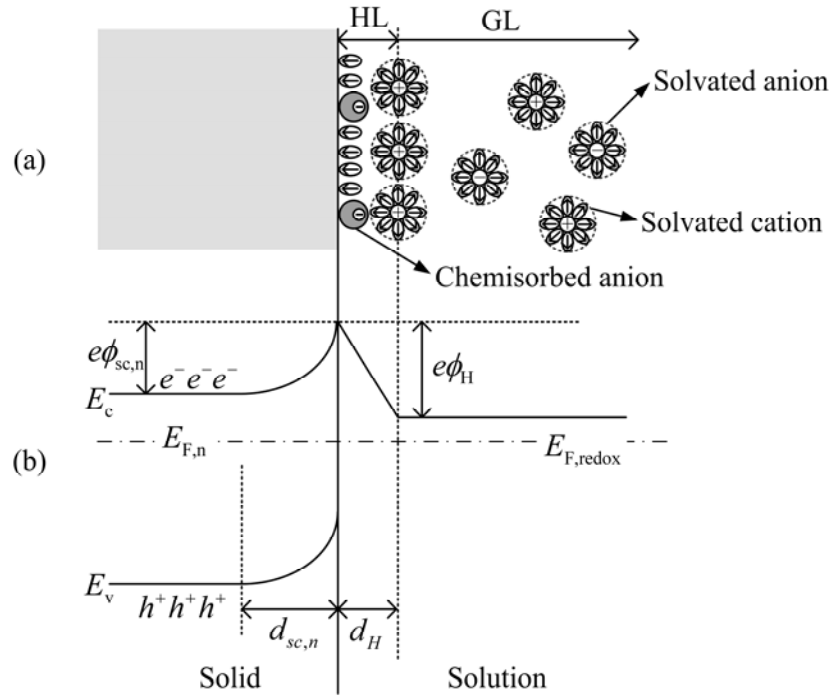


Figure 2.4 (a) illustration of the surface layers at the n type semiconductor and solution interface and (b) the corresponding energy diagram. HL and GL represent Helmholtz double layer and Gouy layer, respectively [modified from 32, 31, 54].

For a metal/electrolyte interface, most of the potential drop occurs at the Helmholtz double layer since there is no space charge region in the metal side due to the very high electron concentration. At a metal/liquid interface, the Helmholtz double layer potential is determined by the energy levels of the ions in the solution. The space charge region in the metal is very thin due to the high carrier (electron) concentration in the metal. Therefore, the potential across the metal/liquid interface exists mostly on the Helmholtz double layer. On the other hand, at the semiconductor/electrolyte interface, both the space charge region in the solid and the Helmholtz double layer in the electrolyte side should be considered since electron exchange and adsorption/desorption of ions must come to equilibrium.

The Helmholtz double layer forms by the accumulated adsorbed/desorbed ions from the solution side of the solid/solution interface. The space charge region develops to achieve the net rate of electron transfer equal to zero between the band and the redox couple in the electrolyte.

However, the Helmholtz double layer is not sensitive to the charge transfer at the semiconductor/electrolyte interface because the space charge layer in the semiconductor is much thicker than the Helmholtz double layer (on the order of 100X to 1000X) [74]. Often, the Helmholtz double layer can be ignored in the band bending model of the semiconductor/solution interface. If charge is transferred from the bulk to the surface, giving a potential change, most of the potential appears across the space charge region in the semiconductor.

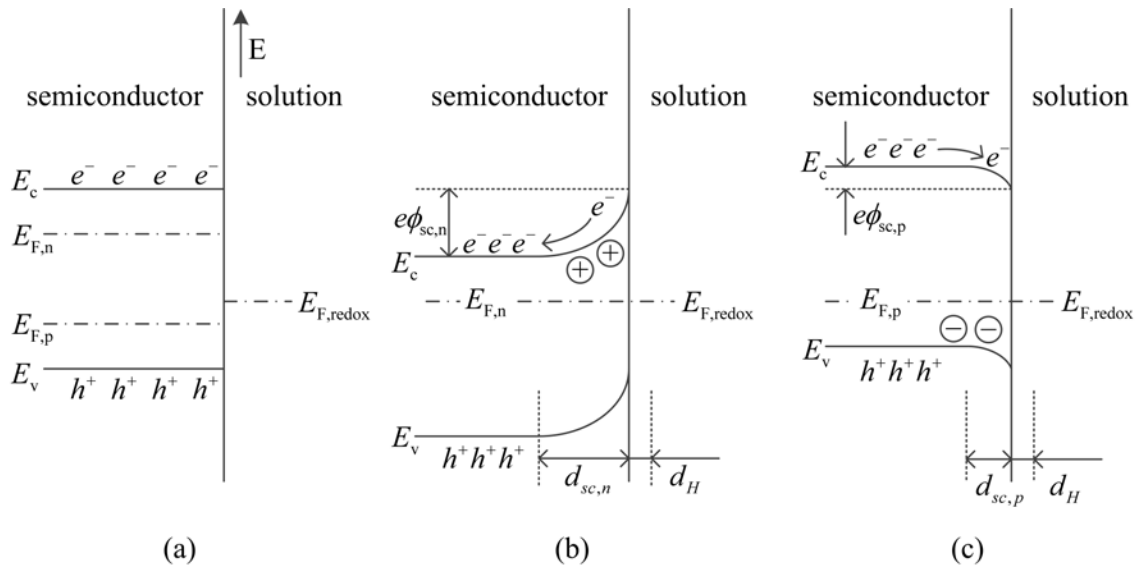


Figure 2.5 Energy band bending of the space charge region at the semiconductor/solution interface at equilibrium: (a) showing the Fermi levels for both n- and p-type semiconductors approaching contact with the redox system, (b) after contact of n-type semiconductor with redox system at equilibrium and (c) after contact of p-type semiconductor with redox system at equilibrium. $E_{F,n}$ and $E_{F,p}$ indicates Fermi level of the n and p-type semiconductor, respectively.

The symbols in Figure 2.5 have the following meanings. \oplus represents the ionized immobile donor atoms, e^- and h^+ respectively represent the mobile electrons (negative charges) and holes (positive charges), and $E_{F,redox}$ symbolizes the Fermi level in solution (redox system). The symbols $d_{sc,n}$, $d_{sc,p}$, and d_H represent the thickness of the space charge layer in the n type, p

type semiconductor and the Helmholtz Double layer, respectively. $\phi_{sc,n}$ and $\phi_{sc,p}$ are the potential across the space charge region in the n type and p type semiconductor.

As an example, Figure 2.5 (b) and (c) presents the energy band bending of an n- and p-type semiconductor in contact with the Redox system at Equilibrium. The figure includes both n and p-type semiconductors in one figure for illustration purposes. The Redox Fermi level ($E_{F,redox}^0$) is placed higher than the Fermi level of the p-type ($E_{F,p} < E_{F,redox}^0$) but lower than the Fermi level of the n-type ($E_{F,n} > E_{F,redox}^0$) semiconductor. The energy band diagram of the semiconductor and redox system before contact appears in Figure 2.5(a), which for convenience, shows two Fermi-levels while only one applies depending on the type of material. As the solution and solid (n-type for example, Figure 2.5(b)) approach thermal equilibrium after contact, electrons transfer from the semiconductor to the solution/surface and cause the Fermi levels to approach coincidence. The transferred electrons leave behind uncompensated immobile ionized donors within the semiconductor, which thereby form a space charge layer. For either type of semiconductor, the band bending in the space charge region depends on the Fermi energy difference in the solid and the electrolyte – charges can either accumulate or deplete in the semiconductor. The Fermi energy levels depend on the doping (or majority carrier types and concentration) in the solid, and on the oxidizing and reduction ion concentrations in the solution as shown in the Figure 2.2 [54].

For the n type semiconductor case, the energy band bends upward in the space charge region and therefore, electrons are depleted in the layer and leave ionize immobile donor atoms behind (Figure 2.5(b)). The electron accumulation layer (energy bands bend down) arises with p type semiconductors in same redox system (Figure 2.5(c)).

When a potential ϕ_{ex} is applied to the semiconductor, the semiconductor is no longer in equilibrium with the solution. The Fermi level in the solid changes with respect to that in the solution by an amount related to the external potential according to

$$E_F - E_{F,redox} = e\phi_{ex} \quad (2.15)$$

In the general non-degenerate semiconductor case, the external potential distributes over both the space charge region and the Helmholtz double layer and can be expressed as the sum of potential variations with respect to the potential at the equilibrium over the two layers.

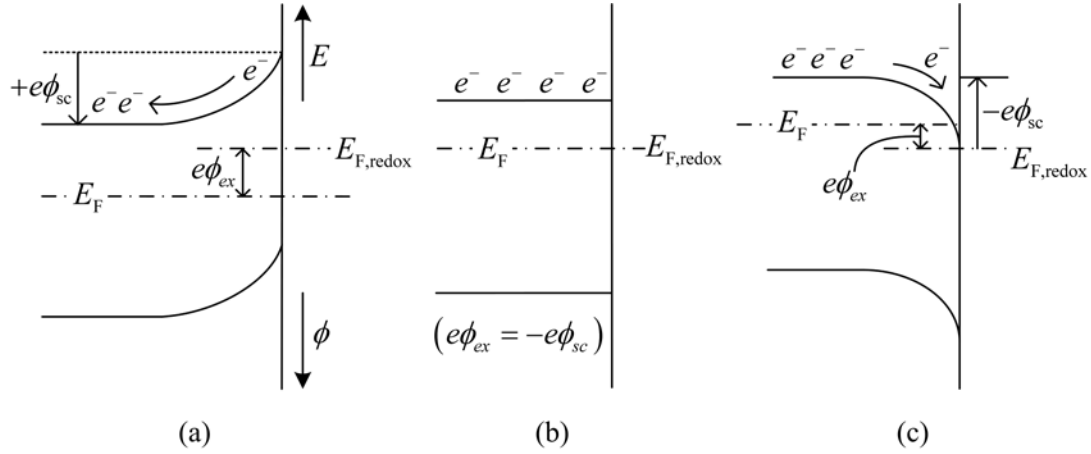


Figure 2.6 Three types of space charge region for the n-type semiconductor depending on the external potential: (a) depletion, (b) flat-band and (c) accumulation condition.

The space charge region can be distinguished by three cases (i.e., depletion, flat-band and accumulation) depending on the band bending in the space charge region. Figure 2.6 illustrates how the three kinds of the space charge regions depend on the applied potential for the n-type semiconductor as an example. When the n-type semiconductor comes into contact with a more negative redox Fermi energy level than the semiconductor Fermi level ($E_{F,n} > E_{F,redox}^0$), under equilibrium conditions, the energy bands bend upward as illustrated in Figure 2.5(b). When positive potential (anodic polarization) is applied to the semiconductor (with respect to the solution) from the outside source, the energy bands bend further upward and the depletion layer (space charge region) expands more toward the bulk semiconductor as shown in the Figure 2.6(a). As the thickness of the space charge layer ($d_{sc,n}$) increases, the total variation of the potential due

to the external potential appears mostly across the space charge region. The inversion of the semiconductor surface may occur in this condition.

On the other hand as shown by the sequence in Figure 2.6, as negative potential (cathodic polarization) is applied to the semiconductor, the energy band starts to bend more downward relative to the equilibrium condition illustrated in the Figure 2.5(a). Consequently, the space charge layer decreases with increasing negative external potential, and at a certain potential value, the energy band achieves the flat-band condition as illustrated in the Figure 2.6(b). In this condition, there is no potential drop ($\phi_{sc} = 0$) thus there is no space charge within the solid. The flat-band potential ϕ_{fb} , is defined as an external potential that can make the energy bands flat in the solid.

If the applied potential at the n-type semiconductor is made negative with respect to the flat-band potential ϕ_{fb} , the bands bend further downward and the electrons start to accumulate at the solid surface. In this condition, the electron concentration at the surface is higher than in the bulk of the semiconductor. This accumulation of majority carriers at the surface is accompanied by a considerable increase in the space charge capacitances. Under strong accumulation, the semiconductor becomes degenerate and shows quasi-metallic behavior and the potential drop occurs almost exclusively over the Helmholtz layer. P-type semiconductor cases have analogy with n type cases.

2.2 Charge Transfer

The transfer of electrons and the holes from the semiconductor to the surface can be interpreted as either forming or breaking the bonds of the surface atoms, respectively [36]. Therefore, the dissolution processes can often be considered as electrochemical reactions in which mobile charge carriers are exchanged between the solid and solution. To understand such charge transfer processes it is necessary to consider the energy levels of redox systems in the

solution. The kinetics of the charge transfer is derived in the first section (Section 2.2.1). Section 2.2.2 introduces charge transfer models under various condition such as depends on the potential and concentrations of the redox system in the dark and illumination. Under illumination, changes in the current flow at the interface are due to variations in the minority carrier density in the semiconductor. This case only concerns band-to-band reaction, (i.e electron-hole pair generation) by the light, which is the simplest case. Other light effects including energy band shifts in the semiconductor and surface state effects under illumination may occur in the electrochemical system.

2.2.1 Kinetics of Charge Transfer

The previous sections review the energy band mechanisms in the electrolyte and the solids when the two phases come into a contact. Experimentally, the current across the interface is due to the charge transfer between the solid and solution ions [30, 31]. The charge transfer at the surface plays a major role in the material dissolution by the redox system.

In the case of a semiconductor/electrolyte interface, electron transfer across the interface occurs via the energy bands. Therefore any variations in the energy band, such as band bending or shifting, play very important roles in the charge transfer process. There may also be electron transfer through the interfacial states by capturing an electron from the conduction band or a hole from the valence band. The electrons and holes will eventually be transported via one of the energy bands. The energy band diagram at the interface depends on various factors such as doping type of the semiconductor and Fermi energy level of the redox system, external potentials applied to the solid, and to the ion concentration in the redox system. As a comment, assuming the existence of well defined bands near the interface is a simplifying assumption (since the periodicity of the crystal is interrupted there) and remains an area of research.

Charge transfer at the interface leads to current flow that can be experimentally measured. The charge transfer rate determines the current flow although it can be a very uncertain factor.

Many researchers try to calculate the transfer rate using different approaches such as electrochemical models and quantum mechanical models. [75, 76]

Marcus [77,78] derives the electron transfer rate using a thermodynamic approach. However, the Marcus model only can be applied to the interface with small reorganization energy, which is not appropriate for the semiconductor/solution interface with relatively high reorganization energy [32]. The Gerischer model uses energy band diagrams to explain electron (charge) transfer at the solid/liquid interface. It is more convenient for the semiconductor/solution interface since the model uses energy bands and the state model for the solution [30, 31, 32].

At the interface, the reduction of an oxidizing agent (Ox^+) in solution can take place either by electron transfer (e^-) via the conduction band of the semiconductor



or via hole (h^+) transfer from the oxidizing agent into the valence band



In the ideal case without surface states at the interface, electron transfer occurs at the energy of the conduction band edge without any loss of energy (Frank-Condon principle) which means that the charge transfer between a semiconductor and a redox system in solution can occur between levels of equal energy [26, 27].

Gerischer et al suggest electron and hole transfer rate as shown below in Equations (2.18a) and (2.18b) respectively. The Gerischer model expresses the current densities (induced by the charge transfer) in terms of a rate constant and the redox density functions, D_{ox} and D_{red} . The transfer functions depend on the carrier density in the solid and energy distribution functions of the solid and the electrolyte [27, 30, 35, 54]. Therefore the transfer functions are essentially determined by the relative position of energy states on both sides of the interface [75]. The electron and hole transfer rates, k_e and k_h respectively, can be written as

$$k_e \propto \int f(E)\rho(E)W_{ox}(E)dE \quad (2.18a)$$

$$k_h \propto \int (1 - f(E))\rho(E)W_{red}(E)dE \quad (2.18b)$$

where $f(E)$ is the Fermi function for the electron and $\rho(E)$ is the density of states in the solid. $W_{ox}(E)$ and $W_{red}(E)$ are the distribution of the oxidizing (unoccupied) and reducing (occupied) states in the redox system derived previously in Equation (2.13a) and (2.13b)). Equation (2.18a) can be interpreted as follows. Large electron transfer rates k_e from the semiconductor states to the ‘empty’ (i.e., ‘Ox’) redox states can be expected to be large when the number of electrons in the semiconductor at energy E is large and when the number of empty solution states is large. The number of semiconductor electrons is large when the number of semiconductor states $\rho(E)$ is large (regardless of conduction or valence states) and when those states have large occupancy through the Fermi function $f(E)$. Similarly Equation (2.18b) shows the hole transfer rate k_h from the semiconductor to the solution is large when there are a large number of semiconductor states through $\rho(E)$ that are mostly empty $(1 - f(E))$ and there is a large number of states capable of receiving the hole through W_{red} . Equation (2.18b) has the alternative interpretation of an electron transferring from the reduced levels to the semiconductor.

The transfer rates in Equations (2.18) depend on position within the semiconductor since the bands bend in the vicinity of the surface in contact with the solution. As a result, Equations (2.18) should be applied to the surface region. The electron transfer rates can then be expressed in terms of the surface charge densities and the distribution functions of the redox species as

$$k_e \propto \int n_s W_{ox}(E)dE \quad (2.19a)$$

$$k_h \propto \int p_s W_{red}(E)dE \quad (2.19b)$$

where

$$n_s = f(E)\rho(E) \quad (2.20a)$$

$$p_s = (1 - f(E))\rho(E) \quad (2.20b)$$

At the semiconductor/electrolyte interface, the electron transfer via valence band or conduction band processes can occur. The current induced by electron transfer can also be classified according to the direction of the charge flow. The electron transfer from the solid to the redox system classified as “cathodic current” (or as reduction current since it reduces the redox) while the opposite direction of charge flow, electron transfer from the redox to the semiconductor, is classified as “anodic current” (or oxidizing current). The same currents can be restated for hole transfer if needed. For example, reduction current can also be interpreted as hole transfer from the redox to the solid.

As a result of the two types of semiconductor charge carriers and the fact that charge transfer can only occur via energy states in the solid and the redox system, four different kinds of current densities can be defined as: (i) cb cathodic current density j_{cb}^c which consists of electron transfer to the redox system via the conduction band), (ii) vb cathodic current density j_{vb}^c for the transfer of holes from the redox solution to the semiconductor valence band, (iii) cb anodic current density j_{cb}^a that describes electron transfer from the redox system to the semiconductor conduction band, vb anodic current density j_{vb}^a corresponding to the transfer of holes from the valence band to the redox system via the semiconductor valence band.

Based on the definitions, the four types of current density can be expressed in terms of ion concentration and charge transfer rates as follow;

$$j_{cb}^c = F \cdot c_{ox} \cdot k_{cb}^c \quad (2.21a)$$

$$j_{vb}^c = F \cdot c_{ox} \cdot k_{vb}^c \quad (2.21b)$$

$$j_{cb}^a = F \cdot c_{red} \cdot k_{cb}^a \quad (2.21c)$$

$$j_{vb}^a = F \cdot c_{red} \cdot k_{vb}^a \quad (2.21d)$$

where F is the Faraday constant, c_{ox} and c_{red} is the concentration of oxidizing (Ox^+) and the reducing species (Red^-) in the redox system, k_{cb}^c , k_{vb}^c is the cathodic transfer rate for an electron

from the solid to the redox system via conduction and valence band and k_{cb}^a, k_{vb}^a is the anodic transfer rate for an electron from the redox system to the solid via conduction and valence band, respectively. The subscript represents the band ('cb' for conduction band and 'vb' for the valence band) involved and the superscript indicates the direction ('c' for cathodic and 'a' for anodic current density) of the charge transfer. For example, k_{cb}^c and k_{vb}^c in Equations (2.18) correspond to k_e in Equation (2.18a) when 'cb' and 'vb' refers to the conduction band and valence bands, respectively.

To derive a useable current density, the charge (electron or hole) transfer rates must be determined in terms of accessible quantities such as the voltage. For example, from Equation (2.19a), the electron transfer rate from conduction band of the semiconductor to the empty states (oxidizing states) in the redox system Equation (2.21a) can be defined as follow;

$$k_{cb}^c \propto \int_{E_c}^{\infty} n_s W_{ox}(E) dE \quad (2.22)$$

The integration term in this transfer rate equation reflects the dependency of the charge transfer rate, and therefore the current density, on the relative position of the energy states in the semiconductor (conduction band and valence band) and the redox energy distributions ($W_{ox}(E)$ and $W_{red}(E)$). When the band edges at the semiconductor/electrolyte interface are fixed and the electron density at the surface n_s is not a function of energy, E ,

$$\int_{E_c}^{\infty} W_{ox}(E) dE = K_{cb}^c \quad (2.23)$$

where K_{cb}^c is a constant (note the use of capital letters). Therefore, the electron transfer rate of cathodic current via conduction band is

$$k_{cb}^c = K_{cb}^c \cdot n_s \quad (2.24)$$

and where

$$n_s = n_0 \exp \left[\frac{-e\phi_{sc}}{kT} \right] \quad (2.25)$$

Here ϕ_{sc} is a potential across the semiconductor space charge region and n_0 represents the electron density in the semiconductor bulk.

From Equations (2.21a), (2.22) and (2.23), the cathodic current density via the conduction band can be expressed as

$$j_{cb}^c = F \cdot c_{ox} \cdot K_{cb}^c \cdot n_0 \cdot \exp \left[\frac{-e\phi_{sc}}{kT} \right] \quad (2.26a)$$

Similary, the other three currents can be derived as

$$j_{vb}^c = F \cdot c_{ox} \cdot N_v \cdot K_{vb}^c \quad (2.26b)$$

$$j_{cb}^a = F \cdot c_{red} \cdot N_c \cdot K_{cb}^a \quad (2.26c)$$

$$j_{vb}^a = F \cdot c_{red} \cdot K_{vb}^a \cdot p_0 \cdot \exp \left[\frac{e\phi_{sc}}{kT} \right] \quad (2.26d)$$

where

$$k_{vb}^c \propto \int_{-\infty}^{E_v} N_v W_{ox}(E) dE = N_v \cdot K_{vb}^c \quad (2.27)$$

$$k_{cb}^a \propto \int_{E_c}^{\infty} N_c W_{red}(E) dE = N_c \cdot K_{cb}^a \quad (2.28)$$

$$k_{cb}^a \propto \int_{-\infty}^{E_v} p_s W_{red}(E) dE = K_{cb}^a \cdot p_s \quad (2.29)$$

and N_v and N_c represents the density of filled and empty state in the valence and conduction band in the semiconductor, respectively. From Equation (2.26a) and (2.26d), the cathodic current via conduction band (j_{cb}^c) and the anodic current via valence band (j_{vb}^a) strongly depend on the potential across the space charge layer. From Equation (2.26), j_{cb}^c increases exponentially as one applies more negative potential to the semiconductor (with respect to the redox system) and for the j_{vb}^a case it is opposite. On the other hand, the other two kinds of currents (j_{vb}^c and j_{cb}^a) are independent of the potential variations at the semiconductor/electrolyte interface since the states are essentially filled.

2.2.2 Charge Transfer in the Dark and Illumination

As derived in Section 2.2.1, the charge transfer between the semiconductor and the redox system depends on the overlap of the energy bands and the band bending which depends on the Fermi level of the redox system, the applied potential, and the concentration of the ions. Also, illumination can vary the charge transfer by generating extra electron-hole pairs on the surface.

The potential variation at the interface (i.e. applying external potential) leads to corresponding changes of the potential across the space charge layer and therefore of the band bending. As an example, typical current-potential curves of n-type GaAs in a solution of 0.5 mole H_2SO_4 and corresponding energy diagrams appear in Figure 2.7. The Fermi level of the redox system locates close to the valence band of the semiconductor [54].

As shown in Figure 2.7(a), the energy band bends upward due to the Fermi level differences of two phases (n type GaAs and 0.5 mole H_2SO_4) at equilibrium. Under this condition, almost no current can flow at the interface (Figure 2.7 (a)). As one applies negative external potential, the energy band starts to bend in the opposite direction. For more negative potential than the flat-band potential (Figure 2.7 (c)), the energy band bends downward and electrons drift to the solid surface due to the electric field formed in the space charge region. Therefore, electron transfer occurs from the solid to the empty band in the redox system ('Ox' state), which induces cathodic current (Figure 2.7 (b) and (c)).

The cathodic current due to the electron transfer via the conduction band (j_{cb}^c) depends strongly on the potential across the space charge region (or extra potential applied) as derived in Equation (2.25a). As one applies more negative potential to the semiconductor, the cathodic current increases exponentially (Figure 2.7 (b) and (c)). Current variations according to the potential for the p-type semiconductor have analogy to the n-type case. In the example, electron transfers occur mostly via the conduction band due to the low hole concentration in the valence band even with the good overlap between the 'Red' state (filled state in the redox system) and the valence band (filled band in the semiconductor).

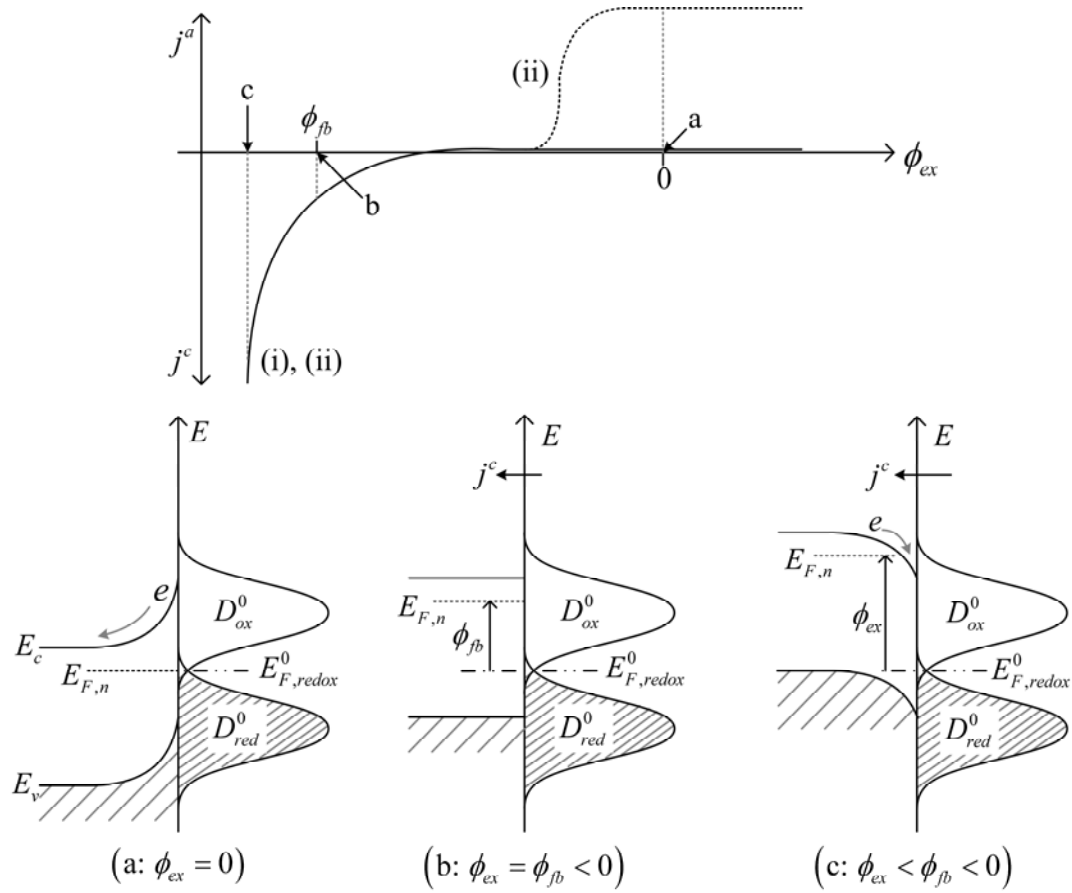


Figure 2.7 Anodic (j^a) and Cathodic current (j^c) versus applied potential (ϕ_{ex}) (i) in the dark and (ii) under illumination. Note that curve (i) approaches zero near point 'a' while curve (ii) extends from the anodic to cathodic regimes. Corresponding energy band bending for three potential points are marked in the plot: a. equilibrium (electron depletion), b. flat-band, and c. negative (electron accumulation). The E axis represents electron energy (negative). [modified from 32, 54]

The current flow at the semiconductor/solution interface is closely related with the carrier concentration at the surface. Curve (i) in Figure 2.7 represents the dark current flow versus applied potential ϕ_{ex} , which is an increment of potential applied to the semiconductor with respect to the solution. The dark cathodic current increases with more negative potential as the surface bands tend toward a flat condition whereas the dark cathodic current approaches zero for more positive potentials that produce a diode reverse bias condition. Illumination incident on the semiconductor with energy larger than the energy gap of the material generates electron-hole

pairs in the material that can contribute to the current. In all light-induced reactions, the minimum photon energy required for excitation corresponds to the band gap of the semiconductor. Figure 2.7 (ii) presents the anodic and cathodic current versus potential under illumination for the n- type semiconductor. Under illumination, cathodic current increases with negative potential and essentially coincides with the dark cathodic current as the current due to band bending dominates (essentially a forward biased diode); the two currents (Figure 2.7 (i) and (ii)) overlap in the plot. Anodic current increases with illumination (Figure 2.7 (ii)) unlike with the dark case. In the dark, only majority carriers contribute to the current flow at the interface. However, under illumination, minority carriers also can increase the current density due to the electron-hole pair generation in the semiconductor.

The current flow can be an indication of the material dissolution. As will be discussed later, material dissolution occurs when holes are available at the semiconductor surface. Consequently, the dissolution primarily occurs under hole accumulation (electron depletion) when the energy bands bend upward. For n-type semiconductor shown in Figure 2.7, the energy band bends upward at equilibrium (Figure 2.7(a)); this bending depletes electrons at the semiconductor surface. For dark conditions, due to the low hole concentration in the valence band, only negligible current flows as indicated by the right-hand portion of curve (i) in Figure 2.7. Consequently in the dark, the semiconductor cannot be anodically dissolved in inert electrolytes (without adding strong oxidizing agent such as Hydrogen Peroxide (H_2O_2)). When negative potential is applied to the semiconductor with respect to the solution, the energy band bends downward and electrons start to accumulate on the surface. The cathodic dark current increases dramatically in the vicinity of flat band potential due to the electron transfer from the semiconductor CB to the oxidizing states in the redox system (reduction reaction). However, the cathodic current, again, cannot contribute to the dissolution of the GaAs because of the hole depletion at the surface.

With illumination having photon energy larger than the energy gap of the semiconductor, anodic current increases (region (ii), Figure 2.7) due to the photo-generated holes in the valence band and so does the dissolution of the semiconductor (curve (ii), Figure 2.7). The current becomes independent of the applied electrode potential at more positive values and the light intensity limits the photocurrent. Electrons in the conduction band of the n-type semiconductor can easily recombine with the photo-generated holes. As shown in the Figure 2.7, the photo-anodic dissolution does not start right after the flat-band potential due to recombination of electrons and holes at moderate band bending. [54, 79]

The currents are also related to the wavelength of the light source. The electron hole pair generation depth (absorption depth of the light) is closely related to the wavelength of the incident light. For example, short wavelength (Blue or UV light for AlGaAs structures) has smaller absorption depth and light with longer wavelength absorbs deeper in the bulk (Figure A.4 in Appendix A). Also, the generation rate of the carriers is a function of the wavelength. For the case of an n-type semiconductor, when the minority carriers (holes) are generated deeper than the space charge region, the carrier has to diffuse to the space charge region without recombination to participate in the chemical reaction on the solid surface. The maximum distance that the minority carrier can diffuse without recombination is defined by the diffusion length L_p [80]. Only the carriers created within an approximated range of $d_{sc} + L_p$ can reach the interface (where d_{sc} represents the thickness of the space charge region) and contribute to the interfacial charge transfer and therefore to the interfacial current density.

The Fermi level of the redox system also varies depending on the wavelength and intensity of illumination due to mechanisms associated with the semiconductor. The electrochemical potentials of various redox systems (H_2/H^+ , OH^-/O_2 , H_2O_2/OH^-) with energy band of the semiconductor materials (GaP, SiC, CdS and GaAs) forming the interface surface are illustrated for the dark and illuminated cases in Figure 2.8.

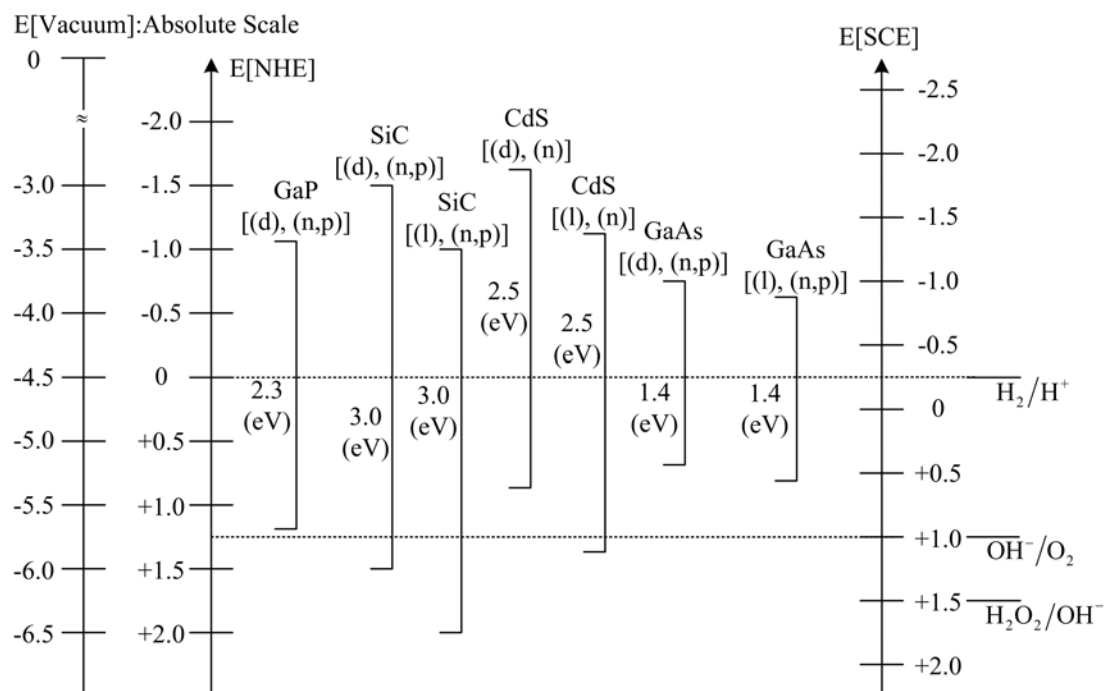


Figure 2.8 Position of energy bands of various semiconductors at the surface in the dark (d) and in light (l) with respect to the electrochemical scale. The vertical lines marked by an energy indicate the band gap of the semiconductor while the small horizontal lines indicate the edges of the conduction and valence band edges [modified from 75, 76].

As shown in Figure 2.8, the energy levels of the semiconductors are shifted under illumination; therefore, the electrochemical characteristics of the system also change with light. The illumination however, affects the electrochemical system differently than does the applied external potential. So far, only the photo-effects for electron transfers due to the band-to-band semiconductor transitions are considered – assuming there aren't any surface states. Photons with energy greater than the bandgap energy of the semiconductor can be absorbed by the semiconductor and can induce other types of electron processes such as transitions to or from an adsorbate of the ions from the solution or an equivalent surface state, or transitions to or from energy levels in the forbidden gap region in the bulk material.

Surface states can act as a recombination centers. Photo-excited charge carriers can be captured in surface states and are available for transfer across the interface. However, it is not

clear how many surface states exist on a semiconductor prepared using standard cleaning processes or during the semiconductor fabrication processes. Also, it is very difficult to obtain direct experimental information about the surface states. Also, when light with higher energy than the energy bandgap is absorbed by the semiconductor, photogenerated electron-hole pairs with excess kinetic energy are created. These hot carriers can dissipate their excess kinetic energy and cool to the lattice temperature through electron-phonon interactions. Still, the photo-effect including the hot carrier process is not fully understood for the semiconductor [75, 76]. However, from the references for photo-assisted dissolution of semiconductors [51, 81], the etch rates increase as the wavelength of the light decreases for the bulk semiconductor material. There has been speculation [76] on the role of hot carriers in the dissolution process but the question remains open at present.

2.3 Semiconductor Dissolution

The previous sections review basic terms for the electrochemical models, i.e. the variations of energy states in the solid and the electrolyte when two phases are brought into contact including the mechanisms for surface layer generation, energy band bending and charge transfer. The electrochemical reactions of the solid and electrolyte have many applications such as for solar cells or semiconductor fabrication. The dissolution of the solid can be the most useful for the semiconductor fabrication process.

The semiconductor dissolution can occur through three different mechanisms: anodic dissolution, electroless dissolution and chemical dissolution. Anodic dissolution and electroless dissolution involve with charge transfer between the solid and electrolyte. The dissolution mechanisms depend on the potential or illumination applied to the system. In contrast to electroless dissolution, the chemical etch supplies all the necessary resources (such as charge) and does not rely on that from the semiconductor surface. As a result, if one limits etching to

chemical etching then the etch rate is not influenced by the charge concentration at the semiconductor surface. This dissolution rate is potential-independent over a wide potential range.

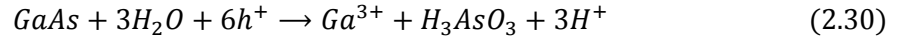
The anodic and electroless dissolution of semiconductor occurs through electrochemical process. The III-V semiconductors, such as GaAs and InP, have the zinc-blende structure [80]. For this type of solid, the surface atoms are triply bonded to three underlying atoms by means of valence electrons [34]. When such a crystal is dissolved, the bonding electrons are removed from the semiconductor surface (valence band of the semiconductor) which means holes are required to break bonds (dissolve solid). GaAs requires six holes per atom to dissolve the material. The solid dissolution rate can be enhanced or suppressed according to whether holes are supplied or extracted from the material.

Therefore, the electrochemical dissolution mechanisms are closely related to the charge transfer in Section 2.2. As shown in section 2.2.1, the charge transfer rate depends on the potential and redox system. The reaction also depends on the pH and composition of the electrolyte. In the case with strong oxidation agent such as H_2O_2 in the acidic electrolyte, different mechanisms should be applied to explain the electrochemical system, i.e. electroless dissolution. Pure chemical dissolution may occur with a strong oxidizing agent (H_2O_2 or Br_2) independent of charge transfer at the interface. Illumination has a major effect on the dissolution process regardless of the oxidizer content. Anodic dissolution (without an oxidizing agent, i.e. H_2O_2) is reviewed in Section 2.3.1. The next section introduces the electroless dissolution mechanisms for the semiconductor (GaAs) within the acidic solution with oxidizing agent (H_2O_2). Section 2.3.3 summarizes chemical dissolution.

2.3.1 Anodic Dissolution

Anodic dissolution refers to the situation where electrolyte does not contain an oxidizer (such as H_2O_2) but material dissolution can only occur by applying an electrical potential (and/or illumination) to the acid-solid system. Without the oxidization agent, the semiconductor can be

dissolved in electrolyte with externally applied potential [54]. The etching proceeds by charge transfer at the surface. A typical dissolution reaction for removing As from a GaAs surface in contact with an acidic solution can be expressed as follow:



From the equation, dissolution of a GaAs molecule requires six holes to transfer from the solution to the valence band of the semiconductor. The etch rate can be enhanced or suppressed according to whether holes are supplied or extracted from the material. Therefore, the electrochemical etching presents high selectivity between materials with different types of doping. For example, in the dark, p-type GaAs dissolves in the anodic condition (as next described) and n-type can be dissolved in the cathodic condition.

Anodic etching connects the III-V semiconductor in an electrolyte to the positive terminal and a metal electrode in the electrolyte to the negative terminal of the voltage source. When the potential of the anode is sufficiently positive, a current starts to flow and the semiconductor starts to oxidize and the material dissolves into the acidic solution. The anodic etching rate depends on the applied potential and electrical type of the material. With III-V samples connected to the negative terminal of the voltage source, cathodic dissolution may occur.

Dissolution occurs when current flows across the solid/electrolyte interface and holes accumulate at the solid surface as expected from the reaction equations above. The current flow at the semiconductor/solution interface is closely related to the carrier concentration at the surface. Illumination on the semiconductor with energy larger than the energy gap of the material generates electron-hole pairs in the material that can contribute to the increment of the current. In all light-induced reactions, the minimum photon energy required for excitation corresponds to the band gap of the semiconductor. A schematic representation of the anodic and cathodic current versus potential for the n- and p-type semiconductor is plotted in the Figure 2.9. In the dark, only majority carriers contribute to the current flow at the interface. However, under illumination,

minority carriers also can increase current density due to the electron-hole pair generation in the semiconductor.

The current flow can be an indication of the material dissolution. As shown in the Equation (2.30), material dissolution occurs when holes are available at the semiconductor surface. Consequently, the dissolution can only occur under hole accumulation (electron depletion) when the energy bands bend upward.

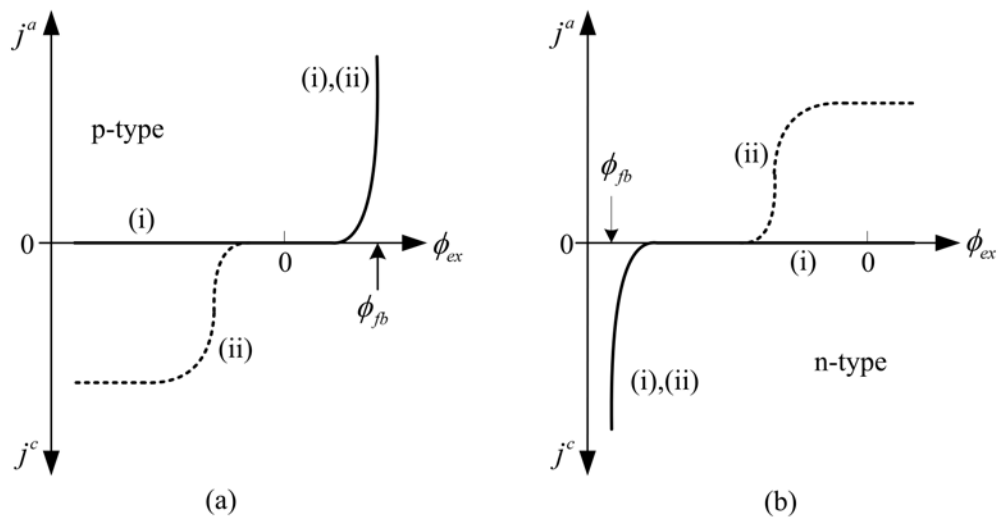


Figure 2.9 Typical current-potential curve of semiconductor electrode: (a), p-type and (b) n-type semiconductor; (i) in the dark and (ii) under illumination [54].

For p-type materials, holes are present in the valence band and anodic dissolution can occur when holes are available at the solid surface – here, anodic dissolution refers to positive potential applied to the semiconductor. From the current-potential curve of a p-GaAs electrode in H_2SO_4 solution in Figure 2.9 (a), in the dark (curve (i)) the current is almost zero at zero potential (equilibrium condition). Without external potential, due to the Fermi level differences between the p-type semiconductor and the redox system, the energy bands bend down and electrons accumulate at the surface. Therefore not many holes can contribute to solid dissolution for these conditions at equilibrium. The current stays low with negative (cathodic) potential with respect to

the standard electrode [32]. since the band bends more downward with negative external potential and the hole depletion occurs at the electrode surface. When positive potential is applied to the semiconductor, the energy bands start to bend upward. After the flat band potential, holes accumulate at the surface. Consequently, anodic dissolution starts close to the flat band potential and the current increases exponentially at positive potentials.

When light of a wavelength corresponding to the band-gap of the semiconductor is applied to the p-type semiconductor, electron-hole pairs are generated. In this case, due to the high hole concentration in the valence band, the hole density is not significantly affected by the illumination but the electron density in the conduction band does significantly increase. Due to the large band bending downward for cathodic potentials, these photo-generated electrons accumulate at the electrode surface and transfer to the redox system (oxidizing state, or empty state) and cathodic current can flow in the negative potential region (electron accumulation region). However, increasing the cathodic current does not mean that the material dissolution occurs at this potential range. The electron transfer rate increases but does not contribute to the dissolution process. They can inhibit material dissolution since more electrons imply stronger bonding. The plateau current in curve (ii) is determined by the light intensity. With anodic potential larger than the flat-band potential, the current is almost the same with the dark condition since there are already enough holes in the valence band before e-h pair generation and the majority carrier density stays almost the same. In this region of potential, material dissolution occurs at the surface and the dissolution rate is almost the same as the dark case since the photo-generated holes do not significantly change the hole density (i.e. majority carrier concentration)

For an n-type semiconductor, the energy band bends upward as one increases the positive (anodic) potential (of the semiconductor with respect to the redox system) so as to deplete electrons at the semiconductor surface. Under the dark condition, due to the low hole concentration in the valence band, only small current flows in this range as shown by curve (i) of the Figure 2.9(b). Consequently, the semiconductor cannot be dissolved anodically in the dark.

When cathodic (negative) potential is applied, the cathodic dark current increases dramatically in the vicinity of flat band potential due to the electron transfer from the semiconductor CB to the oxidizing state in the redox system (reduction reaction). However in this case, the cathodic current, again, cannot contribute to the dissolution of the GaAs because of the hole depletion at the surface. Therefore, no anodic dissolution occurs for n-type GaAs in the dark.

With illumination, anodic current increases and so does the dissolution of the semiconductor (curve (ii), Figure 2.9(b)). The current becomes independent of the applied electrode potential at more positive values where the light intensity limits the photocurrent. The photo-anodic dissolution does not start right after the flat-band potential due to recombination of electrons and holes at moderate band bending. In the potential range with deep band bending, most of the photo-generated holes within the space charge region and up to a diffusion length from that region, transfer to the semiconductor surface and are consumed in GaAs dissolving process. [54, 79, 82]

It is reported that the anodic dissolution rates does not depend on the GaAs crystal direction [34, 35] (no difference for the Ga(111) face and the As ($\bar{1}\bar{1}\bar{1}$) face contacting the electrolyte, yielding no difference in dissolution rate). On the other hand, the flat-band potential and the onset potential of the photocurrent do depend on the crystal faces. Accordingly, the Helmholtz layer is different for the two surfaces.

The rate of anodic dissolution of GaAs depends on the pH of the electrolyte [54, 83, 84] with or without illumination. In general, dissolution is observed at the high (alkaline) or low (acidic) pH. The anodic oxidation of GaAs in acidic solutions is, in general, not accompanied by film formation, unless oxide-promoting agents are added to the electrolyte. In the intermediate pH range, surface passivation occurs due to the oxide film generation, which generally inhibits the material dissolution. The charged intermediates might be formed during oxidation of the solid. A build up of positive charge at the surface should influence the potential distribution over the

semiconductor/electrolyte interface, which affects the position of the band-edges at the surface and, consequently, the kinetics of hole injection.

Although it is inconvenient for technological applications to etch semiconductors anodically with an externally applied potential, the electrochemical etching can be applied to the selective etching of different electronic types of the material and doping concentration of the semiconductor. However, it is inconvenient to etch semiconductors anodically with an externally applied potential for technological applications since the electrode can limit the device design.

2.3.2 Electroless Dissolution

In general, the redox Fermi energy level for diluted acidic solution has a value between that of the conduction band and the valence band of the GaAs. Consequently, the anodic dissolution of the semiconductor in the dilute acidic solution depends on the availability of holes at the semiconductor surface and is strongly influenced by an externally applied potential (band bending). The actual etching solutions usually include more than one redox system such as the sulfuric acid and hydrogen peroxide used for the experiments for this dissertation. Also, the oxidizer eliminates the need for electrodes and applied electrical potential.

Electroless etching occurs with the addition of a strong oxidation agent such as Br₂ (Bromine) or H₂O₂ so that the semiconductor can be decomposed under open-circuit conditions (without electrode). The electroless dissolution mechanism is based on two separate electrochemical reactions, which take place simultaneously on the same surface, the anodic oxidation of the semiconductor in which holes are consumed and the reduction of an oxidizing agent, which supplies these holes.



The Ox^+ (Oxidizing agent) can be reduced either via the conduction band or via the valence band, depending on the relative position of the Fermi level of two phases.

Electroless etching, by definition, requires hole transfer from the solution to the semiconductor surface (valence band) without the application of an external voltage. As a comment, electroless dissolution can simultaneously proceed with photo-dissolution whereby the photo-holes produced in the semiconductor transfer to the reaction site. According to the GaAs dissolution model from Gerischer [34, 35], these injected holes weaken (i.e., break) surface bonds in order to dissolve GaAs. The charge transfer is only possible when the distribution function of the oxidizing agent (D_{ox}) overlaps with the valence band of the semiconductor. The degree of overlap determines the rate of hole injection which affects dissolution rate. For example, in the case when H_2O_2 (Hydrogen Peroxide), an oxidizing agent with a very positive redox potential, is added to the electrolyte (acidic solution), the distribution function of the oxidizing agent, D_{ox} , overlaps very well with the valence band of the semiconductor at the equilibrium condition as shown in Figure 2.10.

The oxidizing agent with a very positive redox potential bends the semiconductor conduction and valence bands more than would the single redox system with its Fermi level between the conduction and valence band edges. Figure 2.10 shows (a) the situation before-contact for either an n or p-type semiconductor (GaAs), (b) after contact between the solution and n-type semiconductor (GaAs), and (c) after contact between the solution and a p-type semiconductor. The electrolyte is a mixture of H_2O_2 and acid. The addition of the H_2O_2 to the single redox systems (acid) shifts the solution distributions to more positive electron energy (downward in the figure). Therefore before contact (Figure (2.10a), for this example), the redox Fermi energy level of H_2O_2 is placed lower than the valence band edge of the GaAs.

One can now see the effect of the oxidizer in Figure 2.10. When the solid is immersed in the electrolyte, the Fermi levels in the semiconductor and electrolyte move to the same energy under equilibrium conditions. The energy band bending depends on the Fermi level differences in the semiconductor and electrolyte. Since the Fermi energy level $E_{redox}^{H_2O_2}$ in H_2O_2 in this case, is

lower than the Fermi energy level of both n-type $E_{F,n}$ and p-type $E_{F,p}$ GaAs, the semiconductor energy bands bend upward (Figure 2.10 (b) and (c)). The bands produce larger electron barriers and deeper hole wells for the n-type semiconductor and electrolyte interface than for the p-type semiconductor.

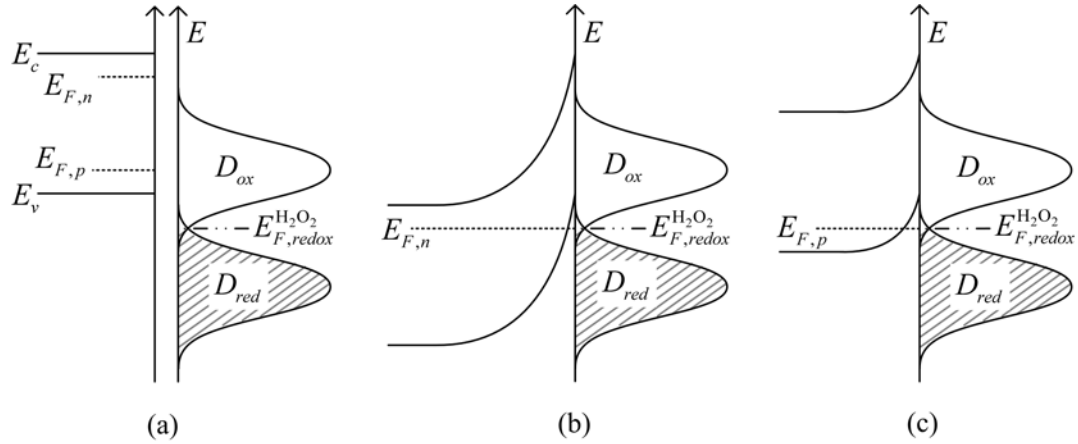


Figure 2.10 Energy band diagrams of GaAs in the contact with acidic H_2O_2 solution for either an n-type or p-type semiconductor. (a) The bands and Fermi level before contact between the semiconductor and electrolyte. (b) and (c) shows energy band diagram after contact for n-type and p-type semiconductor and electrolyte, respectively.

The electroless dissolution mechanism is based on the two distinct electrochemical reactions of reduction and oxidation. Electroless etching can be described by the Mixed Potential Theory [85] and proceeds at the mixed potential (ϕ_r) at which the partial oxidation (or anodic) current (j^+) must be equal to the partial reduction (or cathodic) current (j^-). Since anodic oxidation depends on the surface hole concentration, the etch rate in these solutions can be changed by applying an external potential. Figure 2.11 presents the current-potential curves of p- and n-type GaAs in a solution of pH=0 containing strong oxidization agent (H_2O_2).

According to the mixed potential theory, [104] the total measured current at the semiconductor/solution interface consists of the two partial currents, the reduction and oxidation currents, which are assumed independent of each other [54, 86]. From the current derived in the

Equation (2.25b), the reduction current induced by the reduction process via the valence band (electron transfer from the valence band of the semiconductor to the Ox species) is independent of the applied potential over a broad range of potential for both p- and n-type GaAs. Hole injection occurs from “Red” species in the redox system to the valence band of the semiconductor. The injection rate (and the oxidation current via valence band) strongly depends on the applied potential and therefore the total current also depends on the externally applied potential. In the Figure 2.11, a solid line represents the measured total current and the dotted lines (i) and (ii) indicates the estimated cathodic and anodic current, respectively.

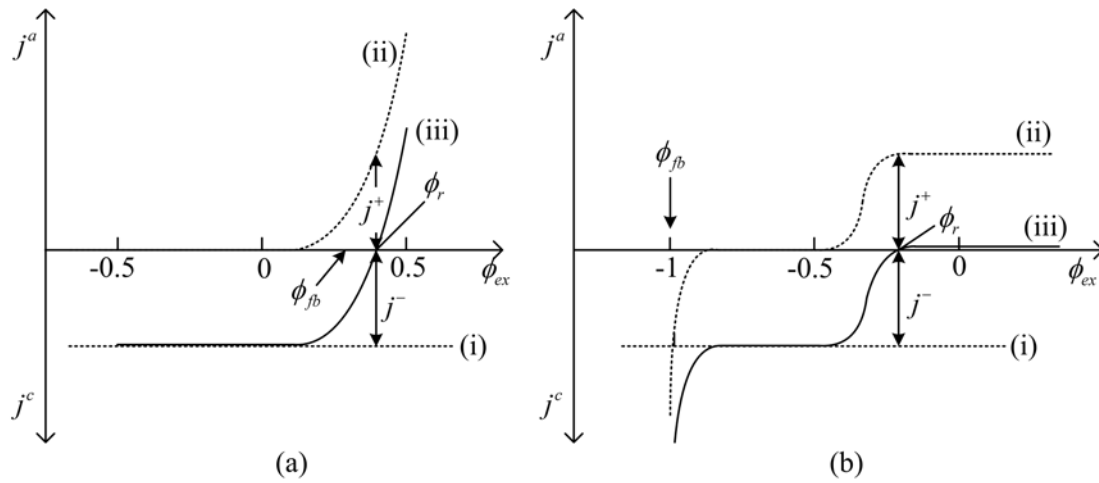


Figure 2.11 Current potential curves of (a) p-type GaAs and (b) n-type GaAs in the dark in a solution of pH=0 containing a strong oxidizer. (i) and (ii) indicates the estimated cathodic and anodic current, respectively. (iii) represents sum of the cathodic and anodic current [54].

In the p-type GaAs, the dissolution can occur in the positive potential range due to the high hole concentration in the valence band in the dark. During semiconductor dissolution in the acidic H_2O_2 solution, a mixed potential (ϕ_r) is established at which the reduction and oxidation reactions occur at the same rate. For the mixed potential, two partial current densities, oxidation and reduction current, represented by j^+ and j^- respectively, must be equal ($j^+ = j^-$), as

indicated in Figure 2.11. During etching under electroless conditions at the mixed potential (ϕ_r), no external current flows.

The same reactions occur at the corresponding n-type semiconductor as shown in the Figure 2.11 (b). For n-type GaAs the electroless mechanism is somewhat more complex since the injected holes are now minority charge carriers. In the dark, the holes are not created by light but are injected by the oxidizing agent (and neglecting thermal generation within the semiconductor). From the energy band diagram in Figure 2.10, with positive potentials, the injected holes accumulate at the semiconductor surface due to the band bending and the current is independent of the potential. The holes dissolve GaAs in the dark. Unlike the p-type GaAs case in the Figure 2.11(a), n-type GaAs shows another plateau in the negative potential region due to the recombination of injected holes with electrons from the conduction band (Figure 2.11(b)-(ii) and (iii)).

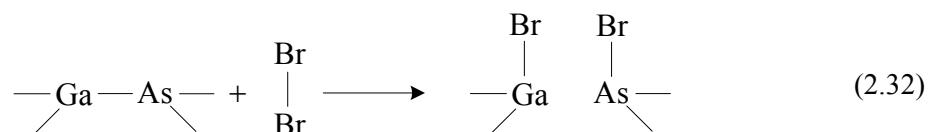
Oxide formation also affects the semiconductor dissolution by influencing the rate of hole injection from the solution. It is reported that anodic oxidation of the semiconductor is often accompanied by oxide formation. The growth of oxides causes changes to the band bending within the semiconductor since the oxides can drop significant amounts of voltage. In addition, the oxides can trap surface charge as well as slow the reactions. In particular for the case shown, the semiconductor band-edges are shifted downwards towards positive potentials during dissolution. When an oxide layer is formed during this reaction, these intermediates induce a much larger potential drop over the oxide layer, as the capacitance of this layer is significantly smaller than that of the Helmholtz layer. Consequently, the shift of the semiconductor band-edges is much larger under oxide-forming conditions. Since the hole injection rate depends on the degree of overlap between the D_{ox} function and the valence band, these shifts can markedly influence the kinetics of electroless dissolution of GaAs. Both oxide formation and surface/interface charging effects may influence the cathodic reduction of the oxidizing agent and electroless etching at the open-circuit potential(ϕ_r).

2.3.3 Chemical Dissolution

Assume the dissolution of a Ga-As pair is equivalent to the transfer of six charge carriers to the solution, the current–potential curve (such as in Figure 2.9) can be interpreted as an etch rate–potential curve. For both n- and p-type GaAs, increasing the cathodic currents leads to decreasing of the etch rate whereas anodic current leads to the dissolution of the material. Without an oxidizing agent (H_2O_2), p-type GaAs dissolution does not occur with negative potential and positive potential for n-type GaAs. With strong oxidation agent, such as H_2O_2 , the etching can be described by the partial anodic and cathodic current-potential curves [85]. The dissolution rate can be changed by means of an externally applied potential.

Gerischer et al. found the etch rate of n-type germanium (Ge) in an acidic H_2O_2 solution to be potential-independent over the potential range for which Ge is not anodically dissolved. They proposed a distinction between an ‘electroless’ and a ‘chemical’ mechanism for the dissolution of Ge. They also found similar potential-independent etching of GaAs in Bromine solution [34].

For the chemical dissolution of GaAs in these solutions they proposed a coordinated reaction sequence involving the rupture of Ga-As and Br-Br bonds and the simultaneous formation of Ga-Br and As-Br bonds represented as follows [34]. It is also found that GaAs is also etched by a chemical mechanism in acidic and alkaline H_2O_2 solutions [23-25].



In contrast to electroless dissolution, the chemical etch rate is not influenced by the surface hole concentration in the valence band of the semiconductor. The rate is potential-independent over a wide potential range. It is reported that ‘bifunctional etching-species’ are involved in the chemical dissolution. The bifunctional molecules are capable of forming two new bonds with the semiconductor surface in a synchronous mechanism. These species were found to

be either symmetrical, e.g. H_2O_2 , Cl_2 , Br_2 and I_2 , or asymmetrical, such as OCl^- , HCl and HBr . A dissolution reaction occurs by direct chemical attack of these bifunctional etching species at the semiconductor surface. Dissolution is initiated by an exchange of bonds between the solid and the etchant. Since direct chemical attack of the semiconductor is necessary, chemical etching stops when an oxide is formed on the surface. However, electron tunneling can still occur when the oxide layer is thin.

2.4 Summary

Photo-assisted dissolution of semiconductors in aqueous solutions especially offers attractive possibilities in device fabrication. Device applications of the photo-assisted material dissolution are reported [53, 87-91]. Photo-assisted electroless dissolution systems (no externally applied potential) are of particular interest since they are more likely compatible with the existing device technology. However, the mechanism is very complicated and researchers are suggesting new models of the dissolution system [51, 52, 62, 92]. Material dissolution by supplying holes to the valence band through electron-hole pair generation model is the most widely accepted in a manner identical to that for electrochemical etching [26, 31-34, 70, 93]. The other mechanism uses the thermal energy from the light source (such as laser) to melt oxide [94]. However, there is no temperature increasing during the etching with moderate power of light [64].

It is clear that illumination and external potential influences semiconductor dissolution due to the charge density changes at the surface and energy band bending or shift. This work is most interesting for semiconductor dissolution with light. Basically, photo-assisted solid dissolution can be classified as electrochemical etching. However, the mechanism is more complicated than electrochemical etching in the dark. With an oxidization agent in the electrolyte, the mechanism becomes even more complex. In the etching solution such with strong oxidization agent, experimental results show that there is a complex interrelation between electrochemical and chemical processes. The etch system can be expected to be affected by density and flow of

the photo-generated charges at the surface. Chapter 3 and 4 examine the photo-assisted dissolution of GaAs and GaAs/AlGaAs multilayer materials with LEDs and Lasers under various conditions.

Chapter 3 LED Photo-Assisted Wet (PAW) Etch Test

One of the primary goals of the research on Photo-Assisted Wet (PAW) etching consists of developing methods and apparatus to produce the first wet-etched integrated heterostructure laser mirrors with characteristics independent of the relative orientation between the integrated laser and crystal. The initial tests and apparatus are designed to extend early observations on the photo-etching of bulk-like GaAs including those related to selective etching [17, 63, 66, 92, 95] and changes to the etched side profile [61, 64, 96]. However, the dissolution mechanism of the semiconductor, especially the photo-assisted dissolution, is not yet fully understood. The literature has few reports on the photo-dissolution characteristics of bulk and double layered semiconductors and no reports on the multilayered heterostructure and quantum well laser material. Developing photo-assisted III-V material dissolution processes requires investigation of the dissolution characteristics of the semiconductor with respect to the masking material, wavelength of the light source and target material. The electrochemical reaction of the semiconductor and the etching solution (redox system) under illumination can be influenced by many factors in the system such as light source, layer structure of the target material and the masking material deposited on the sample.

This chapter presents Photo-Assisted Wet (PAW) etching using the incoherent illumination from multi-element light-emitting-diodes (LEDs) as light sources. Section 3.1 discusses the experimental set-up and the methods for preparing the test material. Next, Section 3.2 investigates the photo-dissolution of the bulk GaAs and various structures of GaAs/AlGaAs materials including laser heterostructure using different types of the mask patterns and light sources. A simple photo-dissolution model is presented in section 3.2.2 for bulk GaAs. The heterostructure materials add complexity to the photo-dissolution model. Sections 3.2.3 and 3.2.4 discuss Photo-Assisted Wet (PAW) etching of epitaxial AlGaAs layers and laser heterostructure. The etch profile of the photo-dissolution depends not only on the light wavelength and intensity,

but also on the electrical type of the mask and layer structure of the material. The photo-dissolution of the laser heterostructure samples using green and UV LEDs produces smooth vertical sidewalls suitable for integrated semiconductor lasers.

3.1 Experimental Set-up and Sample Preparation

Section 3.1 presents the experimental set-up and the method for preparing the test material for LED-PAW etch tests. Sections 3.1.1 and 3.1.2 review the LED-PAW etch setup and light sources for the PAW etch test. Three different high-power LEDs are used to compare photo-electrochemical dissolution under different wavelengths of the light. The LEDs produce UV (395 nm, 3.14 eV), green (530 nm, 2.33 eV) and red (625 nm, 2.00 eV) and optical power density of approximately $64\text{mW}/\text{cm}^2$ ($\pm 10\text{mW}/\text{cm}^2$). The PAW etching characteristics depend on the wavelength of the light through the absorption length and photo-carrier energy (i.e., hot carriers). Sections 3.1.3 and 3.1.4 discuss sample preparation and investigate the effects of masking.

3.1.1 Experimental Set-up

The experimental set-up for the LED-PAW etching is illustrated in Figure 3.1. The first set of experiments use an LED as a light source since the emitted light has a broad, uniform spatial distribution that provides excellent coverage of the target sample. However, the LED optical power incident on the sample quickly decreases as the distance between the sample and the light source increases. To apply maximum optical intensity, the target sample needs to be placed as close to the light source as possible. In the experimental set-up, the target sample is placed within approximately 5mm from the bottom of a clear Pyrex[®] dish with the LED illumination passing through the bottom. Metal should not be introduced into the etching solution since it can interfere with the electrochemical system [24, 25]. Instead, Teflon[®]-insulated tweezers suspend the target sample (face-down) in the etching solution. The backsides of the samples remain unmasked so as to expose the back sides of the semiconductors to the etchant.

The etching solution consists of sulfuric acid (H_2SO_4), hydrogen peroxide (H_2O_2) and DI (De-Ionized) water (H_2O) [21-23] in the volumetric ratio of 4:1:25 based on previous promising results from our lab for the bulk n-type GaAs case [64]. The mixture of the sulfuric acid (H_2SO_4) and water (H_2O) generates heat during solvation. The temperature easily rises higher than 80°C . It is necessary to cool the etching solution to room temperature for stability/reproducibility. The temperature of the etching solution is maintained at $23^\circ\text{C} \pm 2^\circ\text{C}$. Temperatures are measured before and after the etching and the differences are within 1°C .

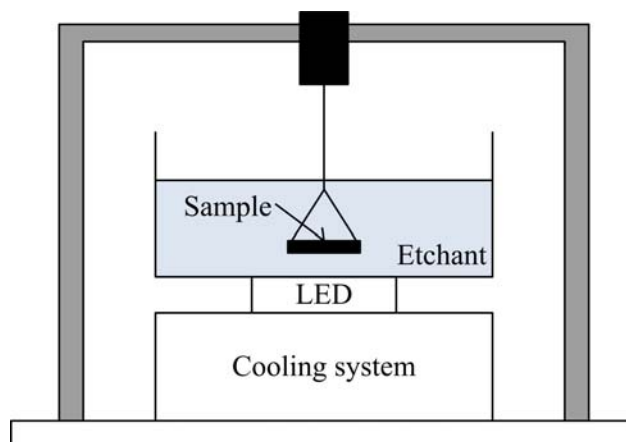


Figure 3.1 Experiment set up for the photo-assisted semiconductor dissolution.

3.1.2 Light Sources

For the photo-assisted semiconductor dissolution experiments, the illumination should cover the whole sample in order to promote uniform etching across the surface. High power multi-element LEDs (upto 70mW of optical power with approximate emission areas of 1 cm^2 , optical power density $\sim 70\text{ mW/cm}^2$) provide good control over the intensity. Three different colors of high-power LEDs are used to compare photo-electrochemical dissolution under different wavelengths of the light. The LEDs produce UV (395 nm, 3.14 eV), green (530 nm, 2.33 eV) and red (625 nm, 2.00 eV) and absorbed optical power density of approximately

64mW/cm² (± 10 mW/cm²) at the position of the sample depending on slight variations in separation between the sample and LED, the material refractive index, and the wavelength. Light with wavelength 395nm, 530nm, and 625nm has calculated (power) absorption lengths of 15nm, 90nm, 191nm in GaAs, respectively, and 29nm, 179nm, and more than 40000nm in Al_{0.5}Ga_{0.5}As (see Appendix A Figure A.4). The LEDs have a full-width-half-maximum (FWHM) optical bandwidth of 45 nm for green and 20 nm for UV and red. The optical power of LED is measured using Newport optical power meter with about 1cm \times 1cm photodetector (PD). For an exact power measurement, the photodetector is placed at the same position as the sample. The size of the photodetector is approximately 1cm \times 1cm. The spatial distribution is found to be uniform within 10% across a 5mm sample by scanning a photodetector masked with a pin-hole across the illumination.

3.1.3 Etch Masks

Electrochemically, the dissolution system can be considered as an electric circuit consisting of the target semiconductor, the masking pattern and the electrolyte [97]. The observations focus on the electrochemical reaction with different electrochemical environments using different types of masks and target materials.

Masks can be distinguished by four different types depending on their electrical properties. The Type 0 and 1 masks consists solely of photoresist (AZ 5214-E) and e-beam evaporated metal, respectively. The photoresist (PR) transmits light with a wide range of wavelengths (UV through IR). Therefore, a 1.5 μ m thick PR mask (Type 0) only blocks the contact of the semiconductor with the electrolyte (etching solution) and not the illumination. The metal layers used in these experiments are the typical p-contacts (Titanium (Ti, 400 Å) –Platinum (Pt, 200 Å) –Gold (Au, 3000 Å)) for the laser device. The same metal type is applied to both n- and p-type sample surface (for the LED experiments) in order to maintain the same metal-

solution interface. The metal type may alter the charge flow at the semiconductor-metal interface due to the barrier difference at the interface. However, the experiments with coherent illumination to produce actual lasers use both n and p-type metals as appropriate for the layer structures. Type 1 masks block both the etching solution and light. However, the charge may flow from/to the solid through the metal. Based on the electrochemical etch mechanisms discussed in Chapter 2, charge transfer at the solid/etching solution interface determines the dissolution rate and etch characteristics.

Type 2 masks consist of silica (SiO_2 , 1000 Å) in direct contact with the semiconductor, which is then covered with metal layers (Chromium (Cr, 400 Å) - Titanium (Ti, 400 Å) - Platinum (Pt, 200 Å) – Gold (Au, 3000 Å)). Chromium (Cr) is used as an adhesion enhancement agent on the oxide before depositing a subsequent metal layer. The silica layer is intended to electrically isolate the semiconductor from the metal and therefore block the electron and hole movement from the sample to the etching solution.

To study the photo-assisted semiconductor dissolution with “non-metallic” light-blocking masks, type 3 masks employ three layers in the order of silica (on the semiconductor), followed by metal (Cr-Ti-Pt-Au) and then topped with photoresist (AZ 5214-E). Photoresist (PR) can be spun-on and then patterned to cover the metal and thereby provide electrical isolation between the metal layer and the etching solution. Figure 3.2 illustrates the four different mask types and corresponding charge flow under illumination.

With a type 0 mask (Figure 3.2 (a)), light passes through the mask and generates electron-hole pairs everywhere on the surface including under the mask. With this mask, one may not see the photo-assisted dissolution effect. The type 0 masks are not included in the actual experiments since the preliminary tests with ‘type 0 masked’ bulk GaAs shows the same etch characteristics as for dark etching. With opaque masks such as type 1, 2 and 3, the electron-hole pairs can only be generated where the surface is exposed to the etching solution. The charge

density distributions induce potential at the material surface which results in charge flow at the surface. As etching continues, holes are consumed by the etching at the non-masked area while electrons move toward the masked area. The charge flow may vary by the mask types. With type 1 masks (Figure 3.2 (b)), electrons in the dark area may flow to the metal. For metal masks isolated from the semiconductor surface, such as type 2 and 3 masks in Figure 3.2 (c) and (d), electrons can accumulate under the masked area and at the sidewalls of the pattern as the etching continues.

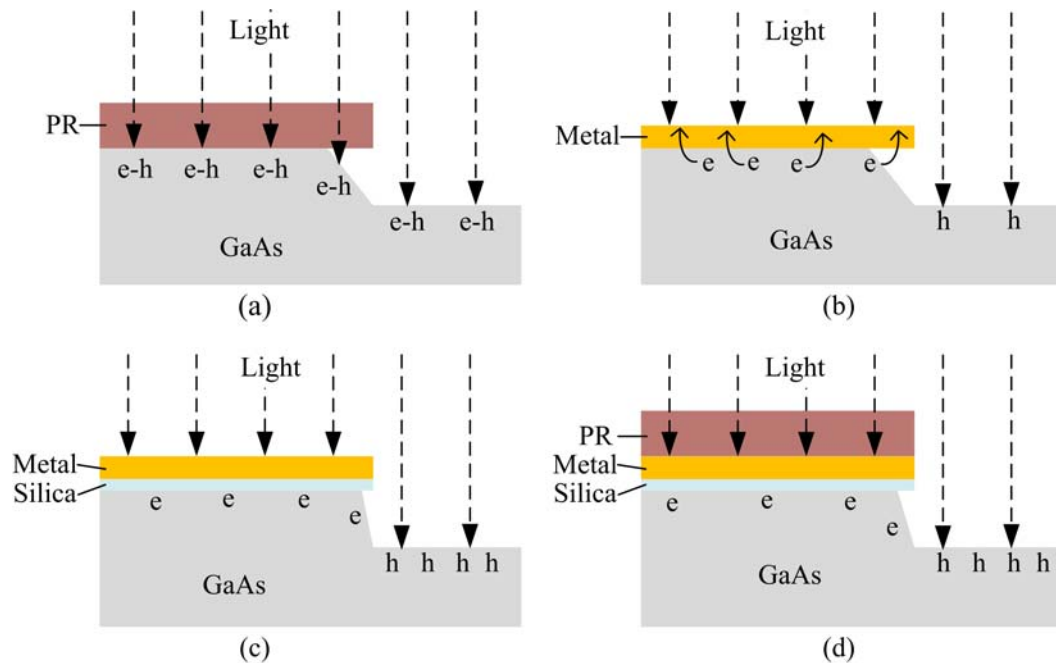


Figure 3.2 Different mask types and corresponding charge flow under illumination: (a) type 0, PR only mask, (b) type 1, metal only mask, (c) type 2, silica and metal mask and (d) type 3, silica, metal and PR mask.

Electron accumulation affects the solid dissolution near the dark area i.e. sidewall of the pattern. In addition, some of the charges may transfer toward the back of the semiconductor. For the bulk material, excess electrons can easily flow toward the back of the material. For the heterostructure case, identical masking produces different results since the current flow can be

affected by (i) the doping and energy band gap of the layers, (ii) the p-n junction region, and (iii) the quantum wells where the carriers can efficiently recombine carriers. Various conditions including different mask types and material structures are tested in this chapter.

3.1.4 Sample Preparation

The photo-dissolution of three different types of the materials is tested: bulk GaAs, GaAs/AlGaAs multilayer with different structures, and laser heterostructure. Most of the samples, except the bulk n- and p-type GaAs, are generated from two types of laser heterostructure material. Figure 3.3 shows the layer structure of the original materials used in these experiments. The material with in-house number EPI-1179 (see Figure 3.3(a)) has several thin GaAs/ $\text{Al}_x\text{Ga}_{1-x}\text{As}$ layers (forming a Field Effect Transistor (FET)) followed by a laser structure with top n-type layers. Another wafer with in-house number M1-5 (see Figure 3.3(b)) has p-type layers on top, indium added to the quantum wells for 894 nm emission, and n-type AlGaAs grown on an n-type GaAs substrate.

The laser has the basic structure of a p-n diode where the most common material for in-plane lasers has top layers consisting of p-type material while the bottom layers grown on the substrate consist of n-type material as shown in Figure 3.3b. The various layers include: (i) a highly-doped p-type GaAs cap layer for electrical contacts; (ii) an $\text{Al}_{0.6}\text{Ga}_{0.4}\text{As}$ cladding layer with p-type doping; (iii) a graded index layer that transitions both the refractive index for waveguiding and the band gap to inhibit the injection of hot carriers to the quantum wells; (iv) a set of quantum wells and barriers for efficient carrier recombination and the production of photons; (v) a lower graded index region; (vi) a lower n-type cladding layer made of $\text{Al}_{0.6}\text{Ga}_{0.4}\text{As}$; and (vii) an n-type epitaxial layer grown most often on an n-type substrate. The doping does not extend into the modal volume (consisting of a portion of the graded index region and the quantum wells) to minimize free-carrier absorption of optical energy. While the quantum wells represent the actual active region, sometimes in the course of the present dissertation, the term ‘active

region' will refer to the quantum wells and a portion of the graded-index region for convenience. The graded band edge improves the efficiency of the radiative recombination process at the quantum wells since a step-like grade causes an increase in the kinetic energy of the carriers as they transport from the high to low band gap region and thereby potentially overshoot the wells. The grade allows the carriers to come to thermal equilibrium with respect to their band. The present research uses a variety of heterostructures. Some wafers use an undoped substrate (i.e., semi-insulating) so as to provide electrical isolation between the integrated devices (assuming appropriate fabrication steps), and between the devices and external systems in contact with the substrate.

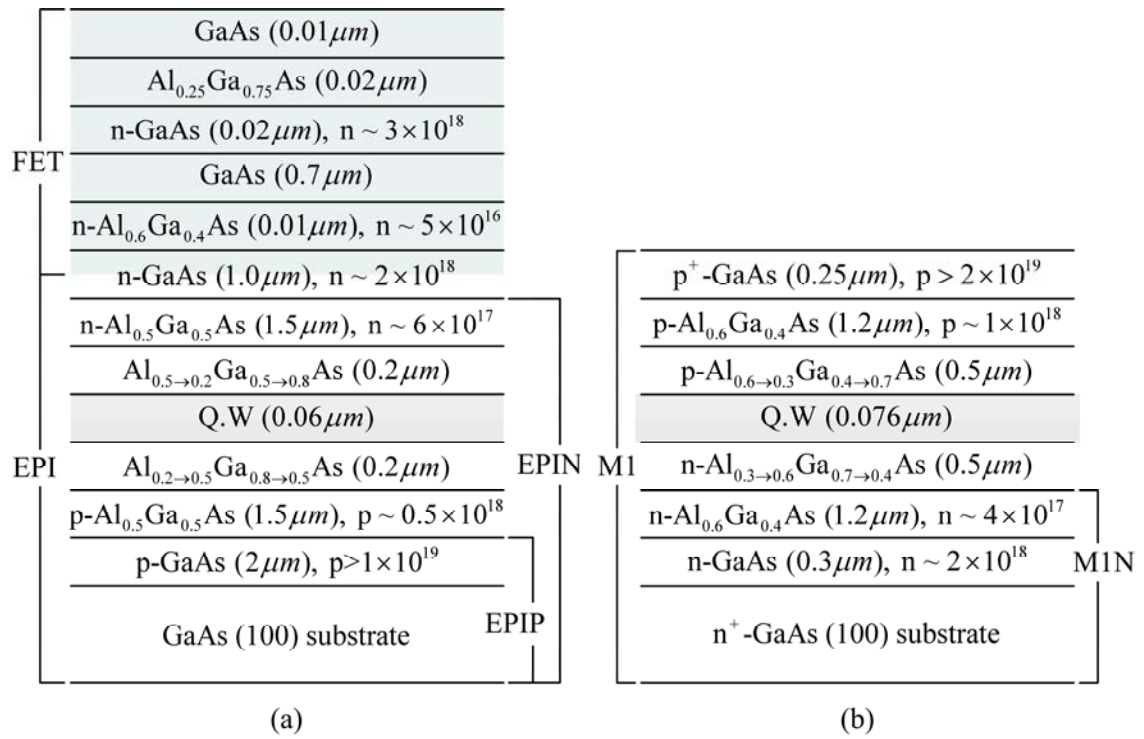


Figure 3.3 Layer structures of samples from (a) EPIQ9501179 and (b) M1-5 laser heterostructure wafer.

The samples for the photo-assisted semiconductor dissolution are generated from the heterostructure shown in the Figures 3.3. In particular, Figure 3.4 schematically summarizes the

sample preparation. In the text, the samples are labeled by material and mask type for simplicity. For example, the bulk GaAs case, GaAsN-1 and GaAsP-2 in the Figure 3.4 indicates n-type bulk GaAs with type 1 mask (metal mask) patterned on the sample and p-type bulk GaAs with type 2 mask, respectively. In label “M1N-2”, the M1 refers to the M1 wafer (i.e., M1-5), the N symbolizes the n-type AlGaAs epitaxial layer and the “-2” indicates the type 2 silica-metal masking on top. Similarly in “EPI-1,” the EPI refers to the EPI-1179 wafer and the “-1” indicates the type 1 metal mask.

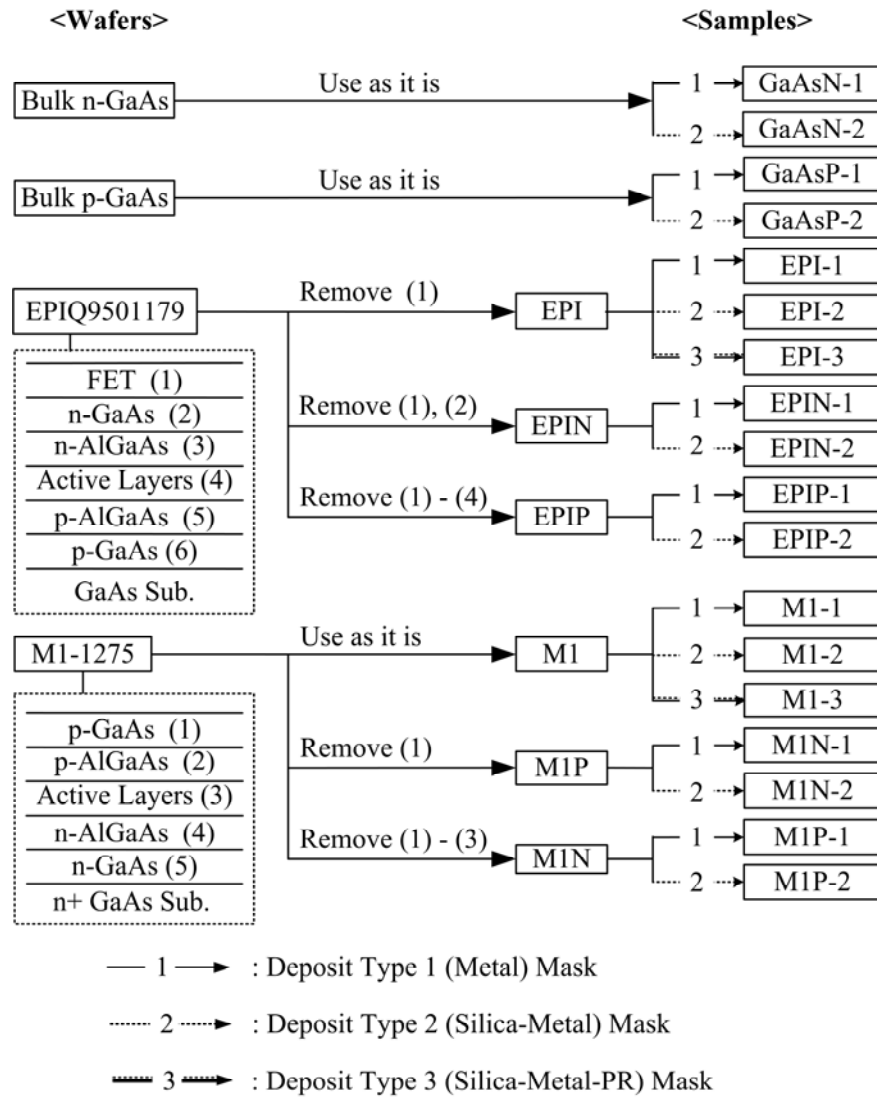


Figure 3.4 Detailed formation steps for all of the samples.

For the photo-assisted semiconductor dissolution for multilayered material, various layers of the materials are generated from two layer heterostructure wafers, EPI-1179 and M1-5 (Figure 3.3) by using a diffusion-rate-limited phosphoric acid (7:3:3, H_2PO_4 : H_2O_2 : H_2O) etching system. The etching system can dissolve both GaAs and AlGaAs layers and leave a polished surface after etching [22-25]. The GaAs/AlGaAs multilayered sample from EPI-1179 and M1-5 wafer is denoted as EPI and M1, respectively. For the EPI sample, the top FET (Field Effect Transistor) layers are chemically removed from the EPI-1179 wafer. Samples with various layer structures can be generated by chemical dissolution of certain layers in the laser heterostructure wafer. For example, EPIN sample is obtained by removing the first two layers from the top of the EPI-1179 wafer (FET and n-type GaAs layer) and has n-type AlGaAs layer on top [98].

As illustrated in the Figure 3.4, EPIN-1 and EPIN-2 denotes EPIN sample with type 1 and 2 mask deposited on it, respectively. The same methods produce the other samples. The EPIP samples expose a p-type AlGaAs layer while the M1N samples expose an n-type AlGaAs layer to the etchant during the photo-assisted semiconductor dissolution process. Wet etching the EPI-1179 wafer (using the diffusion-rate-limit phosphoric acid and the reflectometer) down past the quantum wells exposes the p – $\text{Al}_{0.5}\text{Ga}_{0.5}\text{As}$ layer – these samples are denoted as type EPIP. Similarly, an n – $\text{Al}_{0.5}\text{Ga}_{0.5}\text{As}$ layer is obtained from heterostructure M1-5 by etching past the quantum wells – these samples are denoted by M1N. The correct layers are obtained by using a reflectometer [98] to monitor the etch depth and the surface quality.

3.2 LED Photo-Assisted Wet (PAW) Etching

The experiments investigate the etch characteristics of the various types of multi-layered GaAs/AlGaAs materials and bulk GaAs materials using three types of masks and three illumination wavelengths. A simple model of the angle variation versus light source intensity is presented for the bulk GaAs.

After cleaving the wafer, all the samples receive a standard cleaning process (TCE (ClCH = CCl₂) – Acetone (C₃H₆O) – Methanol (CH₃OH) – Isopropanol (C₃H₈O) – DI water (H₂O)) followed by photolithography and mask deposition. Oxygen plasma then removes any remaining photoresist from the photolithography that would otherwise interfere with the etching. Immediately prior to the photo-dissolution, the samples are dipped in Buffered Hydrofluoric acid (BHF) for 30 seconds to remove possible surface oxides from the oxygen plasma. All samples are etched for 7 minutes.

After the photo-dissolution of the sample, a Dektak 3030 profilometer provides a measure of the vertical etch depth, V. The reflectometer cannot be used with the LED-PAW etching due to the LED and proximity to the etching surface (see Figure 3.1). The samples are then cleaved and mounted on-end for SEM pictures of the etch profile. The SEM pictures provide an estimation of the horizontal etch depth, H, in order to calculate the ratio of horizontal-to-vertical etch depth define as follows:

$$\left(\frac{H}{V} = \frac{\text{Horizontal Etch Depth}}{\text{Vertical Etch Depth}}\right) \quad (3.1)$$

The ratio of horizontal-to-vertical etch depth (H/V) provides one metric to characterize the etching. For a second metric, define the relative (vertical) etch rate (R_{VR}) as

$$R_{VR} = \frac{R_{LV} - R_{CV}}{R_{CV}} \times 100 \quad (3.2)$$

where R_{LV} and R_{CV} represent the vertical etch rates with light and without light, respectively. In the dark, only the chemical dissolution processes operate. The relative etch rate R_{VR} compares the light-induced vertical etch rate (R_{LV} – R_{CV}) with the dark chemical etch rate R_{CV} [64]. The relative etch rate can be negative when light inhibits the etching.

The experiments show that not only the electrical properties of the mask, but also doping type and concentration, as well as the energy gap of each layer, and the band bending [62, 63]

may have an effect on the photo-carrier dynamics to control the light induced etch characteristics of multi-layered materials.

3.2.1 LED-PAW Etching of Bulk GaAs Materials

The photo-assisted semiconductor dissolution experiments on n-GaAs (Si doped, $n > 5 \times 10^{17}$) bulk material in this work show that control over the etched sidewall angle requires either a robust native oxide on the semiconductor or a deposited silica layer to provide electrical isolation between the semiconductor and metal. Also, as the optical intensity approaches 64mW/cm^2 (for both UV and green), the sidewall angle becomes independent of the etching direction (011) and (01 $\bar{1}$) unlike the results for dark-chemical etching [21-24]. Figure 3.5 presents etched sidewall profiles for the (011) crystal direction of bulk n- and p- type GaAs under various conditions. The etched sidewall angle depends on the mask type under same wavelength of light as can be seen.

In Figure 3.5, with the same UV LED illumination, n-type GaAs with metal masking (GaAs N-1: Figure 3.5(a)) presents a different side profile than n-type GaAs with type 2 masking (GaAs N-2: Figure 3.5 (b)). The same results are obtained with Green LED illumination as shown in the Figures 3.5 (c) and (d). All of the dark-etched bulk GaAs, regardless of the type of doping, display the same sidewall profile for the (011) etch direction and the sulfuric 4:1:25 etching system as shown in Figure 3.5 (g). Without light, the n- and p-type bulk GaAs samples have the same etch characteristics (profile and rate) independent of the mask type. Also, even with light, samples with type 0 mask (PR mask) show identical etch characteristics with dark etching.

Figure 3.5 (h) and (i) display the R_{VR} (relative etch rate) and the H/V (ratio of horizontal-to-vertical etch depth) versus the light sources (UV and green LED), respectively. The n-type GaAs material with type 2 mask, which has the silica isolation layer between the semiconductor and the metal, provides the larger profile angle (compare SEM pictures in Figure 3.5 (a) and (b)

for UV and (c) and (d) for green) with low horizontal etching but approximately the same R_{VR} (Figure 3.5 (h)) with type 1 masked sample.

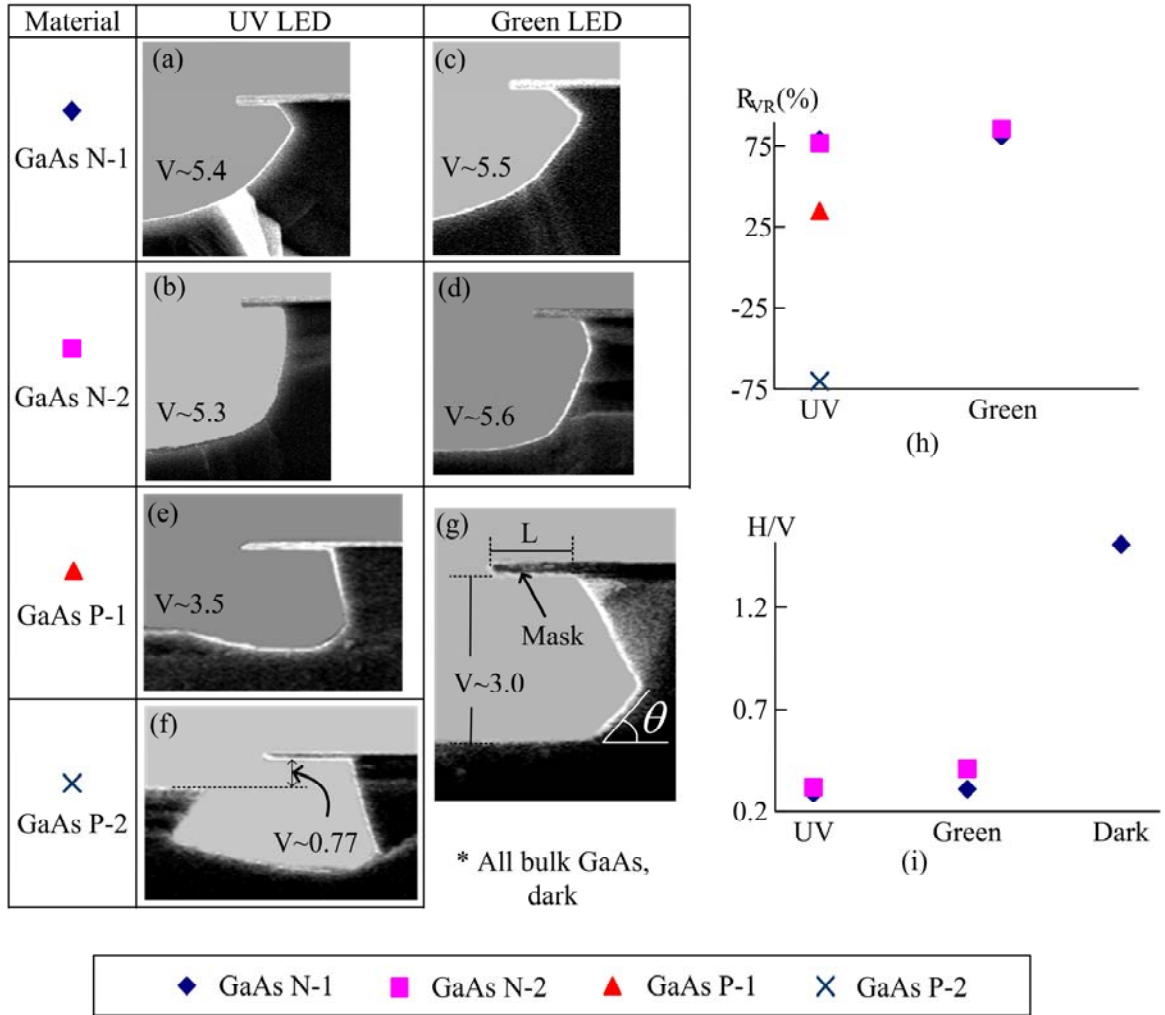


Figure 3.5 Photo-Assisted Wet (PAW) etching of bulk GaAs material with different light sources (UV, green and dark): (a)-(g) SEM pictures of the etched side profiles; (g) etch profile in the dark for all types of materials and masks; (h) the relative etch rate (R_{VR}) and (i) the ratio of horizontal-to-vertical etch depth (H/V) for n and p type bulk materials with two different types of masks.

The SEM pictures of n-GaAs bulk materials corresponding to the UV LED (Figure 3.5 (a) and (b)) show an angle of approximately 49° for type 1 (metal mask) sample, while type 2

(silica-metal) mask presents 83° . The R_{VR} has the value of approximately 76% for both mask types as seen in Figure 3.5 (h). The photo-assisted semiconductor dissolution with the green LED shows similar improvement in sidewall angle for the type 2 (silica-metal) mask. The type 1 metal mask produced 55° and type 2 (silica-metal) produced 70° (See Figure 3.5 (c) and (d)) and yet the relative etch rate (R_{VR}) remained approximately the same for both masks (Figure 3.5 (h)). For both UV and green photo-assisted semiconductor dissolution, the ratio of horizontal-to-vertical etch depth H/V remains relatively small at approximately 0.3 which can be compared with the ratio of horizontal-to-vertical etch depth in dark ($H/V \sim 1.4$) in Figure 3.5 (i). Apparently, the illumination can change the etch profile and also reduce the horizontal etch depth while etching to the desired vertical depth.

The photo-dissolution characteristics for the p-GaAs bulk materials also depend on the mask type. The present research (see Figure 3.5 (h)) shows that the R_{VR} increases by 35% with type 1 metal masks and decreases by -75% with type 2 silica-metal masks where the UV light strikes the sample. The SEM pictures in the Figure 3.5 (e) and (f) show clear differences for the etched sidewall profiles between the two mask types. Although the vertical etch rate changes under UV illumination, the sidewall angle under the masked area remains approximately the same as for the dark etch (compare Figure 3.5 (e) and (f) with (g)). Furthermore, the UV light inhibits etching for the p-GaAs with type 2 silica-metal mask (Figure 3.5 (f)) whereas the vicinity of the masked area displays an etch rate approximately the same as the dark rate.

In summary, type 2 (silica-metal) mask provides more vertical side angle than the type 1 (metal) mask. The change in the etch characteristics of both n- and p-GaAs bulk samples for the different mask types suggests that the carrier flow through the etching system (semiconductor-mask-etchant (redox system)) plays a key role in determining not only the etch rate but also the sidewall profile.

3.2.2. Simple Model for Bulk GaAs

From experimental data presented in the Section 3.2.1, there is a relationship between the sidewall angle of the semiconductor and the light source (intensity and wavelength). For the n-type GaAs case, the vertical etch rate increases with the intensity of the UV illumination and at the same time, the horizontal etch rate and the sidewall change. Figure 3.6 presents etch rate and relative etch rate (R_{VR}) for different optical power density.

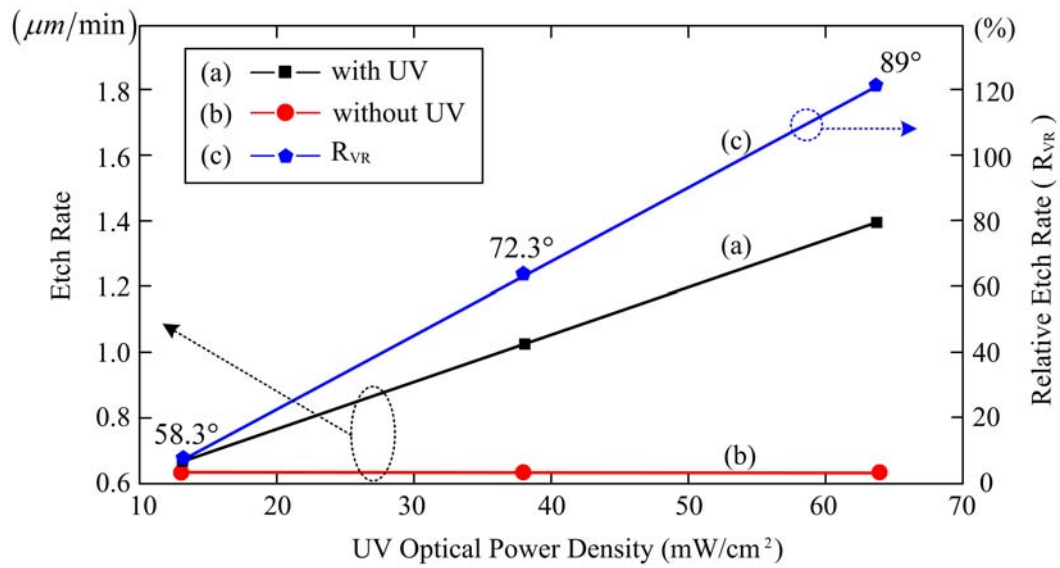


Figure 3.6 Etch rate ($\mu\text{m}/\text{min}$) and relative etch rate (R_{VR}) versus optical intensity. Lines refer to (a) n-type GaAs in the dark, (b) n-type GaAs with illumination, and (c) Relative etch rate (R_{VR}) for n-type GaAs in the $\text{H}_2\text{SO}_4:\text{H}_2\text{O}_2:\text{H}_2\text{O}$ (4:1:25) etchant system. The sidewall angles under illumination appear next to the measured points [64].

The combination of greater vertical etch rate and inhibit horizontal etch rate increases the sidewall angle θ . A rough estimate of the optical power required to photo-etch a 0.25 cm^2 area at a rate of $1\text{ }\mu\text{m}/\text{min}$ can be obtained by assuming fully surface absorbed illumination (i.e., all holes enter the reaction) and assuming 4 valence electrons per atom. The optical power density would need to be at least approximately $42\text{ mW}/\text{cm}^2$ for 390 nm wavelength. Therefore, the initial LED experiments used approximately $64\text{ mW}/\text{cm}^2$; however, the actual photo-etch rate

was approximately $0.5 \mu\text{m}/\text{min}$ (at most). This calculated estimate does not account for a variety of effects [60, 61] including interfacial recombination, absorption length, band bending, oxidation-reduction mechanisms and hot electrons.

The relative importance of photo-dissolution compared with the (dark) chemical dissolution can be describe by the relative etch rate R_{VR} previously defined in Equation (3.2). Related work [64] found the dependence of the sidewall angle on the relative etch rate for n-type bulk GaAs using upto $64\text{mW}/\text{cm}^2$ illumination (UV LED, 395 nm). The experiments include changing the UV intensity and the oxidizer content. The linear regression for the data appears in Figure 3.7 (a) given by

$$\theta = 32.5 \left(\frac{R_{VR}}{100} \right) + 55^\circ \quad (3.3)$$

The n-type GaAs produces nearly vertical sidewalls for a variety of UV intensities.

A simple model in connection with the present work defines a sidewall angle in terms of the etch rates as

$$\text{Tan}\theta = \frac{R_{LV}}{R_{LH}} \quad (3.4)$$

with R_{LV} and R_{LH} respectively representing the vertical etch rate in the presence of light (which includes both the photo and chemical dissolution rates) and the horizontal (lateral) etch rate under the optical mask. The “dark” angle is approximately $\theta_0 = 55^\circ$ for the (011) etch plane in GaAs. The simplest relation for the vertical etch rate (with light) can be written as

$$R_{LV} = R_{CV} + AP_{PAW} \quad (3.5)$$

where R_{CV} , A , and P_{PAW} respectively represent the chemical vertical etch rate, a proportionality factor and the optical power of PAW etching. The horizontal etch rate with light R_{LH} (beneath an opaque optical mask) can be written as

$$R_{LH} = R_{CH} - BP_{PAW} \quad (3.6)$$

or more generally as

$$R_{LH} = R_m + (R_{CH} - R_m)F \quad (3.7)$$

where F represents a function of optical power, and R_m represents the minimum observed etch rate (which can be zero for intense illumination) [99]. Whereas the optical power P_{PAW} increases the vertical etch rate (Equation (3.5)) through the participation of photo-holes (represented by '+ AP_{PAW} '), it inhibits the lateral etch rate (Equation (3.6) or (3.7)) by electron diffusion to the sidewalls (represented by '- AP_{PAW} '). The linear model (Equation (3.6)) obtains from the more general form by setting $F = 1 - P_{PAW}/\sigma_P$ so that $B = (R_{CH} - R_m)/\sigma_P$.

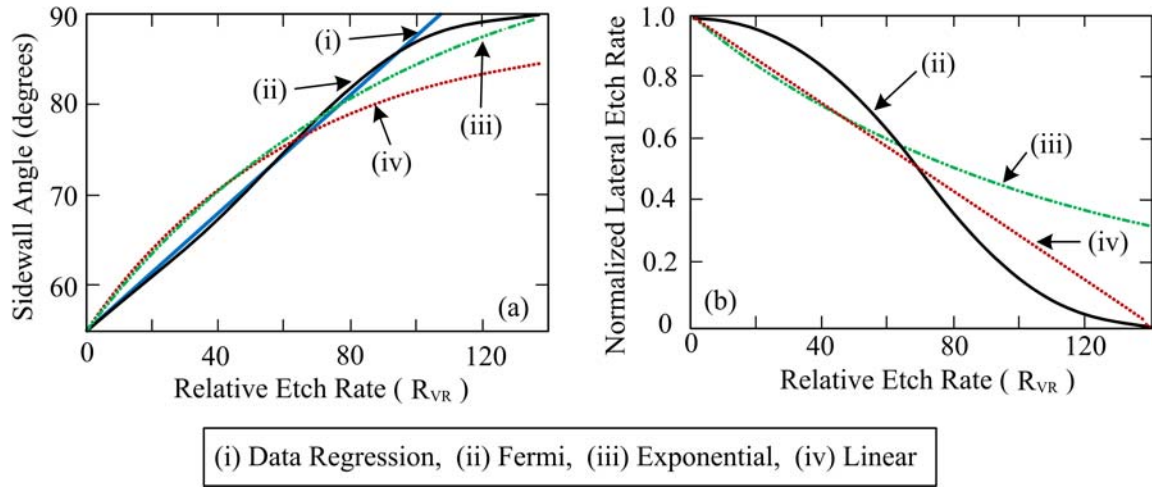


Figure 3.7 (a) Sidewall angles from data (regression) and from three different empirical models and (b) comparing the normalized lateral etch rate for the three simplest models. Plot (i), (ii), (iii) and (iv) denotes Data regression, Fermi, Exponential and Linear model, respectively.

The simplest linear model in Equations (3.5) and (3.6) produces a sidewall angle given by

$$\tan\theta = \frac{\tan\theta_o \left(1 + \frac{R_{VR}}{100}\right)}{1 - \frac{B}{A} \tan\theta_o \left(\frac{R_{VR}}{100}\right)} \quad (3.8)$$

where A and B can differ since more holes might be available at the reaction interface than electrons reaching the sidewall. The regression results in Figure 3.7 (a) provides the overall best ratio of $B/A \sim 0.5$ and for low light levels provides $B/A \sim 0.2$. Equation (3.8) predicts that the

sidewall angle should approach 90° . However, the linear model does not well predict the regression results over the entire range of R_{VR} for the n-GaAs especially near the asymptote. The linear model produces a non-physical negative etch rate for sufficiently large optical power, which suggests that a nonlinear set of equations would be more appropriate (also observe the pole due to the denominator of Equation (3.8)).

A better fit to the regression results in Figure 3.7 (a) can be obtained using the function

$$F = \left[1 + \text{Exp} \left(\frac{P_{PAW} - \mu_P}{\sigma_P} \right) \right]^{-1} \quad (3.9)$$

denoted “Fermi” in Figure 3.7(a) [99]. For comparison, an approximation to Equation 3.9 produces an intermediate case $F = \text{Exp}[-P_{PAW}/\sigma_P]$ (denoted by “Exponential” in Figure 3.7 (a)). The linear function represents a Taylor approximation to the exponential. In all cases, the function F decreases with optical power. Figure 3.7 (b) shows how the lateral (horizontal) etch rate differs for the three models. The Fermi model shows a sharp “switching” action (i.e., “sharp” decrease in the lateral etch rate in Figure 3.7 (b)) that suggests the reduction of a barrier for the n-type bulk GaAs material. Low relative etch rates (low photon density) produce lateral etch rates similar to the dark. However, as the relative etch rate (R_{VR}) increases, the electrons alter/surmount the sidewall barrier and decrease the lateral etch rate.

The Fermi-style function F suggests the photo-electrons (for n-GaAs) reduce or surmount an interfacial barrier. The literature [32, 54] points out that the relative positions of the Fermi-level in the etchant and semiconductor should produce electron depletion at the interfaces (bands bend upward near equilibrium). Illuminating the n-GaAs (532 nm green light) produces electron-hole pairs within the optical (power) absorption length of $\sim 0.2\mu\text{m}$. Assuming only moderate changes to the local band profile, the electrons should drift to the bulk and the holes to the reaction site at the interface [33]. Further assuming the sidewalls have approximately the same “no-light” surface band bending (upward), then one must infer greater numbers of holes at the sidewall than in the bulk. Electrons diffusing toward the sidewall should recombine with holes there and lower the

barrier, which in-turn should further increase the electron transport to the surface. As a result, the lateral etch rate would be non-linear in the photo-carrier generation rate.

The models predict that the sidewall angle should approach 90° depending on the participation of electrons at the sidewall and holes at the reaction region. Varying the relative etch rate (R_{VR}) by either increasing the optical power or changing the oxidizer content should influence the sidewall angle (and vertical etch rate). The simplest model (Equations (3.5) and (3.6)) offers some insight, but produces a non-physical negative etch rate for sufficiently large optical power; however, the other 2 models do not have the same drawback. The models correlate with experimental data for n-type bulk GaAs but not with the cases consisting of the more complicated layer structures of semiconductor material presented in the next two sections (Section 3.2.3 and 3.2.4). The model has the same drawbacks in that it does not incorporate the various electrochemical factors such as material absorption coefficient, surface recombination rate that alters the bond occupancy, surface band bending that affects transport of holes to the reaction area or provides a background supply of holes, doping and the redox mechanisms. The extension of the model for more realistic results needs to be a primary focus for the research. However, first one must uncover the relevant parameters controlling the process. The investigation of the controlling factors forms the main focus for the present dissertation.

3.2.3. LED-PAW of Epitaxial AlGaAs Layer

In the photo-dissolution experiment of n- and p-type GaAs bulk material, the photo-electrochemical properties show strong dependence on the type of the masking material. To observe the electrochemical properties of the AlGaAs material, the experiments examine the etch characteristics of $Al_xGa_{1-x}As$ as a top layer (see Figure 3.3 for the layer structure and Figure 3.4 for the sample forming process). Figure 3.8 displays the etched sidewall profile of each case. Figure 3.8 (j) and (k) show the relative etch rate (R_{VR}) and the ratio of horizontal to vertical etch rate (H/V) for the three different colors of light (UV, green and red), respectively.

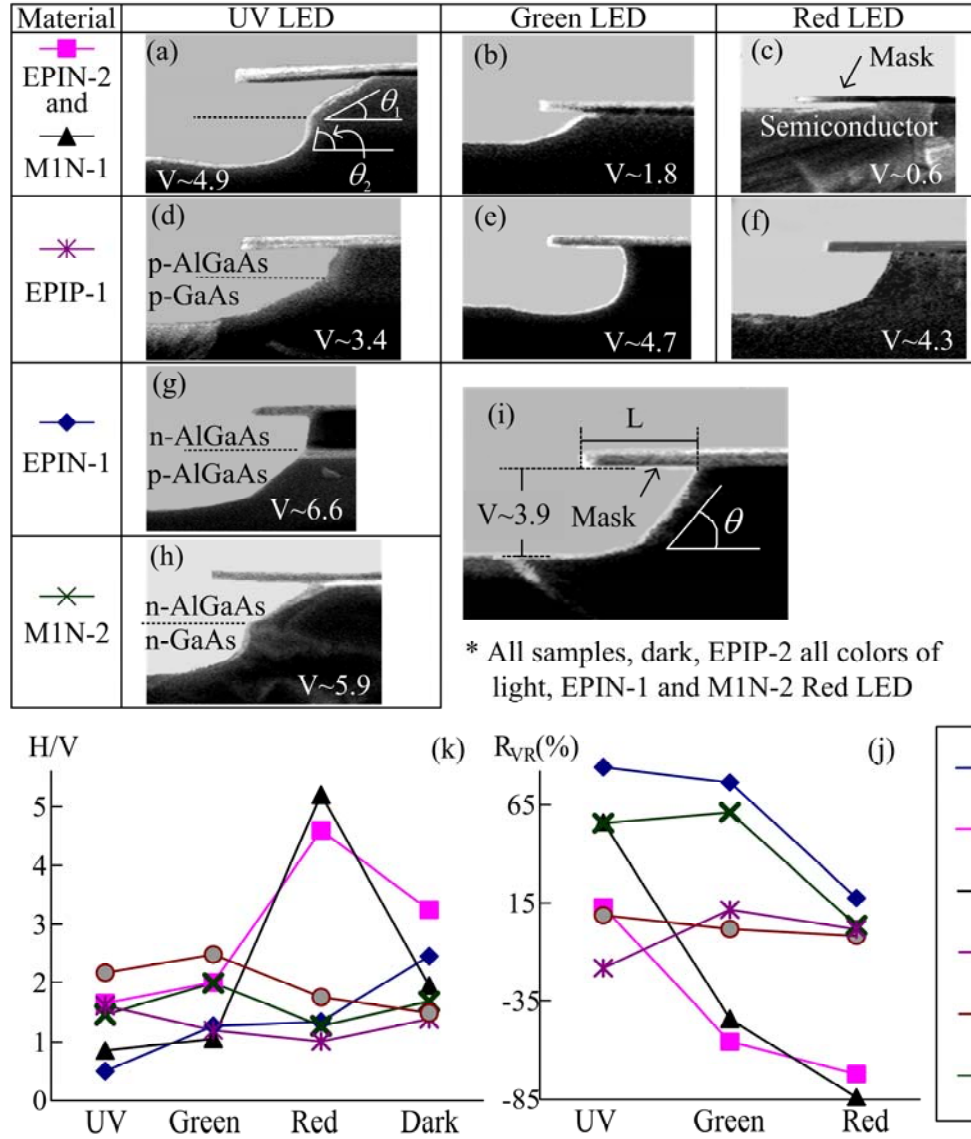


Figure 3.8 photo-assisted semiconductor dissolution of epitaxial AlGaAs with different masks (Type 1 and 2) and light sources (UV, green, red and dark) (a)-(i) SEM pictures of etched side profiles; (i) EPIN, EPIP and MIN material with both types of masks in dark, EPIP-2 material with all colors of LED or EPIN-1 and MIN-2 with red LED. (j) the relative etch rate (R_{VR}) and (k) ratio of horizontal-to-vertical etch rate (H/V) vs. light source of n and p type epitaxial AlGaAs layer with two different types of masks. V in the picture indicate vertical etch depth of the sample.

These experiments for AlGaAs on multilayer materials show that the photo-dissolution characteristics depend not only on the mask type and the material, but also on the underlying

layer structure. For example, the EPIN-1 (Figure 3.8 (g)) and M1N-1 (Figure 3.8 (a)) samples produce distinct etched-sidewall profiles even though they have similar n-AlGaAs layer doping and aluminum concentration (Figure 3.3), identical type 1 metal contacts, and illumination. On the other hand, the M1N-1 sample shows the same photo-dissolution characteristics with EPIN-2 sample for all colors of light (Figure 3.8 (a), (b) and (c)). In the Figure 3.8 (a), EPIN with type 2 silica-metal mask (EPIN-2) has a shallow angle ($\theta_1 = 36^\circ$) for the top n – Al_{0.5}Ga_{0.5}As and a vertical sidewall ($\theta_2 = 86^\circ$) for the bottom p – Al_{0.5}Ga_{0.5}As. In this case, switching both the layer structure and the mask type produces the same etch profile and R_{VR} (Figure 3.8 (j)). Both the M1N-1 and EPIN-2 samples have overall UV etch rates larger than the dark (positive relative etch rate, R_{VR}) but the longer wavelengths tend to inhibit the etching (negative relative etch rates; $R_{VR} \sim -45\%$ with green and $R_{VR} \sim -85\%$ with red) as shown in Figure 3.8 (a), (b), and (c) and (j) for UV, green and red LED, respectively.

Switching the layer structure and the mask type produces similar decreases in R_{VR} with increasing wavelength (see Figure 3.8 (j)). In the EPIN-1 and MIN-2 case, for either green or red illumination, both contact types have identical etch profiles to that obtained under dark conditions as shown in the Figure 3.8 (i) but not with UV (see Figure 3.8 (g) and (h)). For a type 1 metal mask on an EPIN sample (EPIN-1) under UV LED, the top n – Al_{0.5}Ga_{0.5}As shows a nearly vertical sidewall of approximately $\theta_1 = 86^\circ$ whereas the bottom p – Al_{0.5}Ga_{0.5}As shows a shallow angle of approximately $\theta_2 = 42^\circ$ (Figure 3.8 (g)). The vertical etch rate is larger than the dark ($R_{VR} \sim 80\%$). However, under UV, M1N-2 has approximately the same etched sidewall profile as the EPIN-2/M1N-1 pair.

For the EPIN-2/M1N-1 pair, interesting results occur for the longer wavelengths such as for red. One might speculate that UV should affect the etching more than long-wavelength illumination since the UV should generate electron-hole pairs at the surface where the chemical reaction occurs. The red LED is expected to have negligible effect on the etching of

$\text{Al}_{0.5}\text{Ga}_{0.5}\text{As}$ since the red has photon energy similar to the band gap energy ($E_g=2.0\text{eV}$) of the bulk $\text{Al}_{0.5}\text{Ga}_{0.5}\text{As}$ and the light should therefore be absorbed deep within the bulk (more than 40000nm from Figure A.4). Therefore, the red dissolution rate of AlGaAs material is expected to be almost the same as for the dark. However, the photo-dissolution with red (and green in Figure 3.8) does not strictly support this hypothesis and in addition, the profiles depend on the mask type. Figure 3.8 (b) and (c) show the photo-dissolution with the green and red for the EPIN-2/M1N-1 pair. The vertical etch rate decreases by a factor of 2 to 4 compared with the dark vertical etch rate while the horizontal etch rates remain comparable. Therefore the change in the vertical etch rate primarily accounts for the change in the H/V in Figure 3.8 (k). Interestingly, ‘surface absorbed’ green light, which has a calculated (power) absorption length of approximately 290 nm in AlGaAs, produces a sidewall profile intermediate to that produced by red and UV illumination.

The p – $\text{Al}_{0.5}\text{Ga}_{0.5}\text{As}$ layers in the EPI material (EPIP) produce the photo-dissolution profiles in Figure 3.8 (d), (e), (f) and (i). The sidewall angle can be controlled by the mask type and wavelength of the light source but the R_{VR} and H/V of the EPIP material are relatively independent of the mask type and the wavelength (see Figure 3.8 (j) and (k)). For example, type 1 metal-masked EPIP material (EPIP-1) under green illumination produces a nearly 90° sidewall angle throughout the p-AlGaAs and p-GaAs layers. With other wavelengths, the SEM pictures show two different sets of sidewall angles for the AlGaAs layer (top layer, $\theta_1 \sim 79^\circ$ with UV and $\theta_1 \sim 76^\circ$ with red) and p-GaAs (the second layer, $\theta_2 \sim 24.5^\circ$ with UV and $\theta_2 \sim 55^\circ$ with red). All other cases show approximately the same 40° angle. On the other hand, regardless of the illumination wavelength, the EPIP-2 samples (EPIP with type 2 silica-metal mask, not separately shown in Figure 3.8) have the same etch profile as for the dark case shown in Figure 3.8 (i). Unlike the samples with n-AlGaAs as a top layer (EPIN and MIN samples), the R_{VR} and H/V for the p-AlGaAs layers have approximately the same values as for the dark ($R_{VR} \sim 0$ and $H/V \sim 1.5$) regardless of the light color as shown in Figure 3.8 (j) and (k), respectively.

For all cases of AlGaAs epitaxial layer samples, the etch profile depends on the various factors; the light source, mask and layer structure. The photo-dissolution properties change depending on the other layers above or below the target material. For example, the photo-dissolution with the green LED for the EPIN sample with type 1 mask (EPIN-1) has an average R_{VR} of 76%, which would produce a sidewall angle of approximately 80° in n-GaAs with the top silica layer. However, the SEM pictures show about the same side angle as for the dark-etched sample ($0\sim 30^\circ$). On the contrary, the green photo-assisted semiconductor dissolution for the EPIP-1 (type 1 metal mask) has a light etch rate almost the same as in the dark (R_{VR} about 11%) but produces a nearly vertical side profile ($0\sim 90^\circ$). These results suggest that the side profiles are determined not only by the relative etch rate (R_{VR}) but involve other electrochemical factors so that the photo-dissolution of the multilayer semiconductor becomes very complicated.

3.2.4. LED-PAW Etching of Laser Heterostructure

As demonstrated above, the PAW etching of a semiconductor depends on the electrochemical conditions of the system such as layer structure of the target material, mask type and the light source. The present work studies two types of laser heterostructure materials (M1: p-type layers on top with n+ GaAs substrate and EPI: n-type layers on top with undoped GaAs substrate). Both types of laser heterostructure offer the possibility of new fabrication processes for light-controlled mirror surfaces and etch-stop layers.

Figure 3.9 shows the etch profiles of the laser heterostructure samples (M1 and EPI) in the dark. The detailed layer structures appear in the Figure 3.3. First, consider the M1 sample, which has a multi-angled sidewall profile in the dark as shown in the Figure 3.9(a); p-type layers above the quantum wells (Q.Ws) exhibit about $\theta_1 \sim 80^\circ$ of sidewalls while the n-layers below the quantum well show angles θ_2 of approximately 35° . The side angle varies under illumination according to the wavelength light source and the mask type.

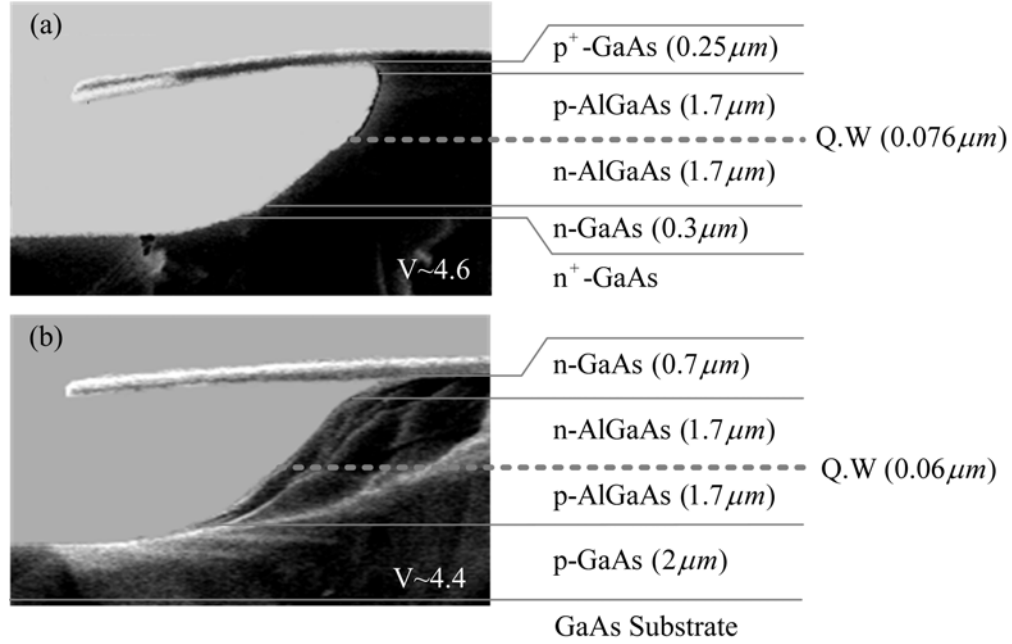


Figure 3.9 Etched profile of laser heterostructure materials in the dark for all types of the masks (a) M1 and (b) EPI material.

In the LED-PAW setup, the backside of the sample is exposed to the etching solution by suspending the sample (face-down) Teflon[®]-insulated tweezers in the etching solution. Van de van et. al. reports that, for bulk GaAs material, exposing the sample backside produces higher front illuminated-surface etch rates than does electrically insulating the backside since the exposed backsides allows excess electrons to be removed [100]. As discussed previously, the electron at the surface inhibits etching while hole promotes the process. The GaAs bulk materials examined for this work agree with the report. However for the laser heterostructure case (both EPI and M1 samples), the LED-PAW shows the same results as the backside-covered samples which indicates the back-side condition does not affect the etch properties. This suggests that the active layer also functions as barriers for photo-carrier transfer to the substrate. Figure 3.10 compares typical LED PAW etched side profile of laser heterostructure material (M1-5 samples) with backside exposed and covered cases. The samples are etched about 4 μm deep and the width of the pattern is 5 μm. The LED-PAW etching presents similar side profile for both cases. For

comparison, etching conditions are same (same mask type and LED power and type) except the backside conditions.

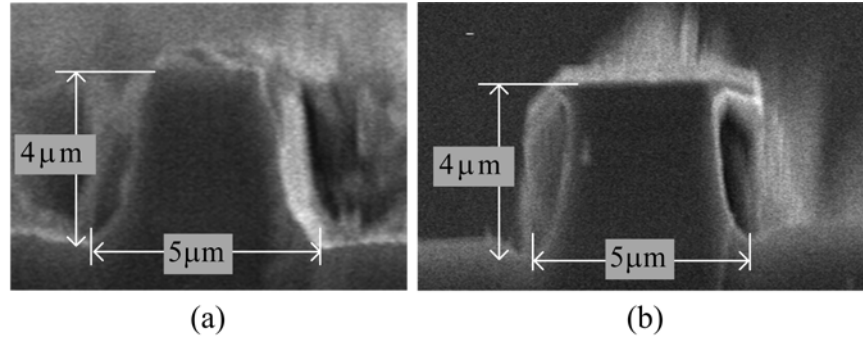


Figure 3.10 LED-PAW etched profile of laser heterostructure materials for metal masked M1 samples with (a) backside covered and (b) exposed case.

Figure 3.11 shows the photo-dissolved side profile of laser heterostructure material (M1 samples) with different masks (type 1, 2 and 3) and light sources (UV, green, red and dark). Both M1-1 (M1 material with type 1 metal masks) with UV LED (Figure 3.11 (a)) and the M1-3 (M1 material with type 3 silica-metal-PR masks) with green and red LED (Figure 3.11 (e)) show almost vertical ($\theta_1 \sim 90^\circ$) sidewalls above the active layer (p-type GaAs/AlGaAs layer) and a slow angle ($\theta_2 \sim 12^\circ$) in the layer below active region (n-type AlGaAs/GaAs). M1-1 with red illumination has very deep horizontal etching that undercuts the metal contact; additionally, the SEM pictures show the etched sidewall profile has a very shallow angle ($\theta_2 \sim 5^\circ$) in the second layer (n type AlGaAs-GaAs layers) and $\theta_1 \sim 48^\circ$ in the first layer (p type GaAs-AlGaAs layers) (Figure 3.11 (c)). The 2 μm thickness of the top-etched layer matches the combined thickness of the top p-GaAs and AlGaAs layers as shown in the layer structure in the Figure 3.3 (b) and 3.11 (a), which suggests the photo-dissolution system with red LED rapidly etches the p-layers and almost stops etching at the n-AlGaAs layer past the quantum wells (QW). The photo-dissolution with the red LED of the n- and p-AlGaAs epitaxial layers with type 1 mask (M1-1) appears in Figure 3.11 (c) and (f). In either case, the photo-dissolution with the red LED of AlGaAs with

high horizontal and low vertical etch rates might be useful to selectively remove a layer adjacent to the AlGaAs layer or possibly use the AlGaAs layer as a buried etch-stop layer in multi-layered material.

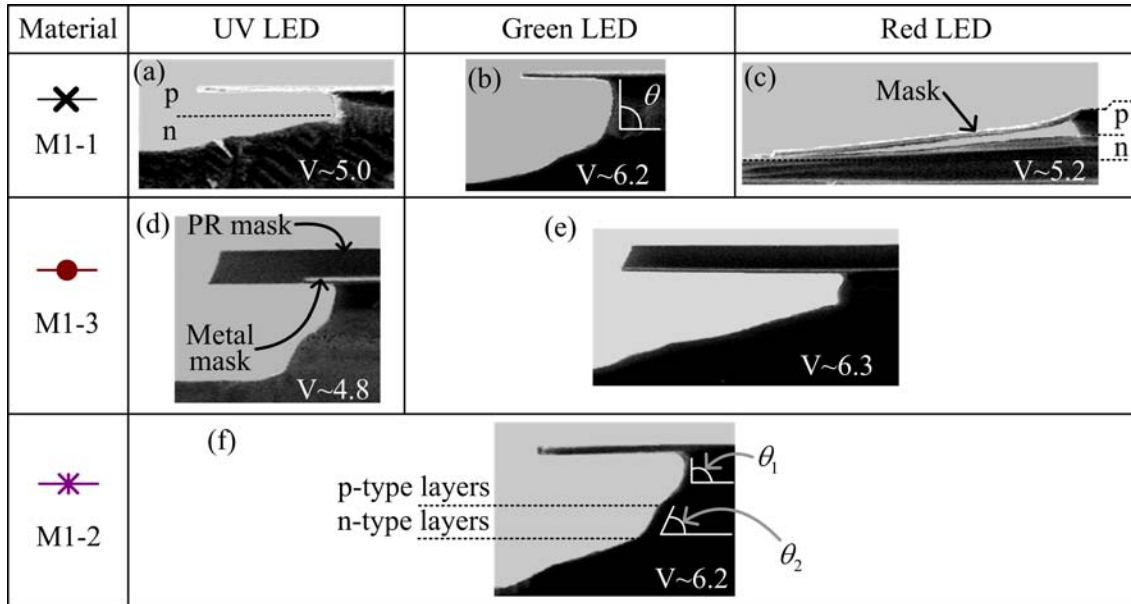


Figure 3.11 LED-PAW etched side profile of laser heterostructure material (M1 samples) with different masks (Type 1, 2 and 3) and light sources (UV, green, red and dark) (a), (b) and (c): M1-1 with UV, Green and Red LED, respectively, (d) M1-3 with UV LED, (e) M1-3 sample with green or red LED, (f) M1-2 sample with UV, green or red LED.

Contrary to the M1-1 with the red LED, the M1-1 samples (M1 sample with type 1 metal mask) with green illumination show a vertical sidewall angle ($\theta \sim 90^\circ$) throughout all epitaxial layers including the quantum wells (Figure 3.11 (b)), which suggest attractive possible application for the optical device fabrication such as integrated optics. The photo-dissolution of all M1-2 samples (M1 material with type 2 silica-metal mask) and the M1-3 samples (M1 material with type 3 silica-metal-PR mask) under UV show approximately $\theta_1 \sim 90^\circ$ in the top layer (with rounded corners) and $\theta_2 \sim 60^\circ$ in the second layer independent of wavelength (Figure 3.11 (d) and (f)) which is similar profile to the dark etching.

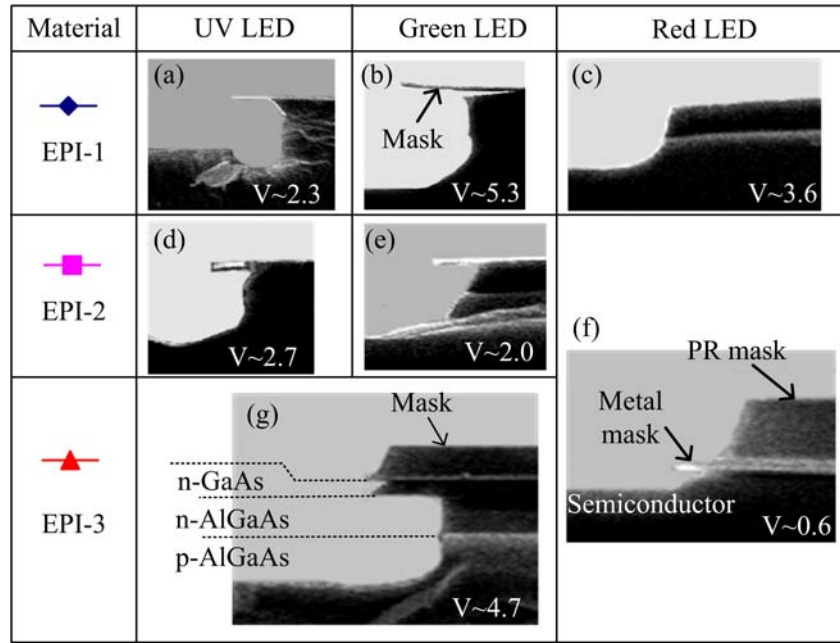


Figure 3.12 Photo-assisted semiconductor dissolution of laser heterostructure material (EPI) with different masks (Type 1, 2 and 3) and light sources (UV, green, red and dark) (a)-(h) SEM pictures of etched side profile of EPI samples; (f) EPI-2 or EPI-3 with red LED, and (g) EPI-3 with UV or Green LED applied to the samples.

In the dark, the side profile of the EPI sample is displayed in the Figure 3.9 (b) and corresponding layer structures are marked on the picture. The EPI samples exhibit various photo-dissolution properties depending on the mask types and the light source. The EPI samples show vertical sidewall angles under a number of etching conditions. For the EPI-3 sample with either UV or green (Figure 3.12 (g)), the sidewall angle appears nearly vertical over all of the epitaxial layers ($\sim 4.7\mu\text{m}$) (for comparison, the M1 samples present vertical sidewalls with type 1 metal mask using green illumination as shown in the Figure 3.11 (b)). A smooth vertical sidewall etch of this depth would be appropriate for a semiconductor laser mirror. Interestingly, the relative etch rate (R_{VR}) remained about 5% (Figure 3.13). The photo-dissolution of EPI-1 sample with green illumination (Figure 3.12 (b)) shows similar vertical etch profiles as for the UV or Green photo-dissolution of EPI-3 (Figure 3.12 (g)) except for the top n-GaAs layer; this behavior includes the n- and p-type layers past the active layer. The EPI-1 (Figure 3.12 (b)) shows very

deep horizontal etch at the top layer but the EPI-3 (Figure 3.12 (g)) shows the opposite – very little horizontal etch in the n-GaAs layer.

The photo-dissolution rate can decrease under certain conditions. UV-etched EPI samples with other mask types (type 1 and 2) show nearly vertical sidewalls as well (Figure 3.12 (a) and (d)). However, the vertical etch rate of the EPI samples decreases for metal masks (type 1) or silica-metal masks (type 2) unlike with silica-metal-PR masks (type 3). Figures 3.12 (a) and (d) for EPI-1 (metal-only) and EPI-2 (silica-metal mask) with UV, respectively, show a reduced etch rate in the illuminated region compared with under the mask; this situation corresponds to the approximate value of -45% for R_{VR} (Figure 3.13) with etch depth about 2.57 μm for 7min.

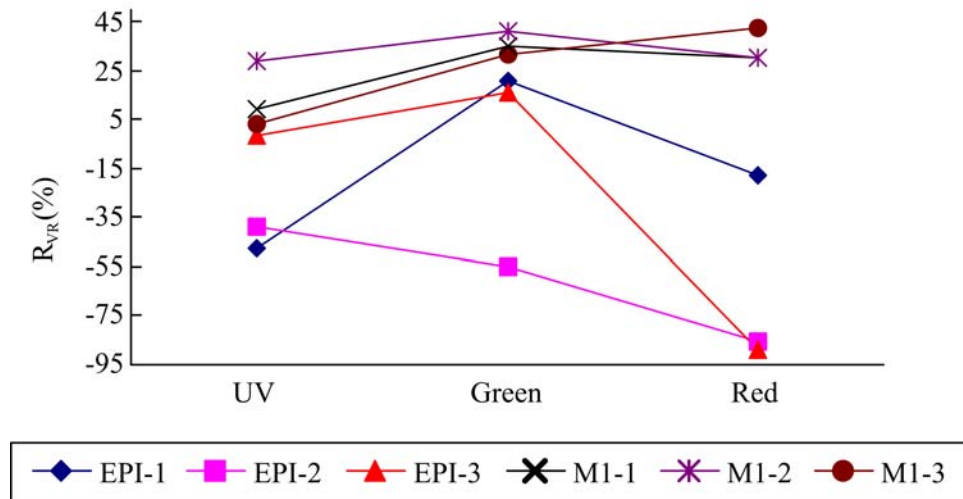


Figure 3.13 The relative vertical etch rate (R_{VR}) vs. wavelength of light source for EPI and M1N samples. Wavelength of UV: 395 nm, Green: 530 nm, and Red: 625 nm.

The photo-dissolution with green illumination of EPI-2 produces an etch depth of approximately 2 μm for 7 minutes of etching which indicates that either the etching stops near the active (quantum well (QW)) layers or the etch rate is low in the top n-layers (Figure 3.12 (e)). These EPI-2 results are consistent with the photo-dissolution tests of the n-type AlGaAs epitaxial layer of the EPI-1179 wafer where (1) the photo-dissolution with the red LED stops near the n-

type AlGaAs layers in EPIN material with type 2 silica-metal masks (EPIN-2) (Figure 3.8 (c)) and (2) the etch rate decreases ($R_{VR} \sim -50\%$) for the green photo-dissolution (Figure 3.8 (b) and (j)). Similar behavior occurs for the EPI-2 heterostructure where the photo-dissolution with green illumination decreases by about 55% ($R_{VR} \sim -55\%$) (Figure 3.12 (e) and Figure 3.13) and most significantly, the semiconductor dissolution almost stops for the red LED with a relative etch rate of $R_{VR} \sim -85\%$ (Figure 3.12 (f) and Figure 3.13). The remaining case for the EPI-3 sample (PR-silica mask) stops etching at the top n-AlGaAs layer with red illumination.

3.3 Summary

The experiments investigate the photo-dissolution of the various types of multi-layered GaAs/AlGaAs materials and bulk GaAs materials using four types of masks and wavelengths. From the experiment, it is obvious that the electrochemical reaction of the semiconductor and the etching solution (redox system) under illumination can be influenced by many factors in the system such as light source, layer structures of the target material and the masking material deposited on the sample. The experiments suggest possible applications for the photo-dissolution of the GaAs and GaAs/AlGaAs multilayer material to the device fabrication and can be summarized as follow. (1) Control over the sidewall angles in n-GaAs bulk material requires an oxide layer and the etch mask plays an important role in the photo-dissolution. (2) The experiments show that the aluminum concentration, illumination wavelength and layer structure of the multi-layered material affect the photo-dissolution of a heterostructure (vertical and horizontal etch rate and sidewall angle). For example, applying red LED illumination to semi-insulating laser heterostructure with n type material next to a silica-metal-PR or silica-metal contact almost completely stops the etching on the $n - \text{Al}_{0.5}\text{Ga}_{0.5}\text{As}$ layer. (3) The photo-dissolution with green and UV LED of the semi-insulating laser heterostructure with silica-metal-PR mask for EPI (laser heterostructure with n-type layers on top) and green LED with metal mask for M1 (laser heterostructure with p-type layers on top) sample produce a smooth vertical

sidewall suitable for integrated semiconductor lasers. For the LED-PAW setup, the backside of most of the sample is exposed to the etching solution. Van de van et. al. reports that, for bulk GaAs material, exposing the sample backside produces higher front illuminated-surface etch rates than does electrically insulating the backside since the exposed backsides allows excess electrons to be removed [100]. Electrons at the surface inhibit the semiconductor dissolution while holes promote it. The GaAs bulk materials examined for this work agree with the report. However for the laser heterostructure case (both EPI and M1 samples), the LED-PAW shows the same results as the backside-covered samples which indicates the back-side condition does not affect the etch properties. This suggests that the active layer also functions as barriers for photo-carrier transfer to the substrate.

The etch profile of the photo-dissolution depends not only on the light wavelength and intensity, but also on the electrical type of the mask and layer structure of the material. For the n-GaAs, the excess holes move to the etching solution/semiconductor interface to increase the oxidation rate and thereby increase the vertical etching rate. On the other hand, some of the photogenerated electrons transport to the dark region such as under the mask or etched sidewall while others move to the backside of the sample or recombine with holes. The data for the present work suggests that the type 1 metal-only mask removes excessive electrons from the solid by collecting the electrons from the same surface. However, the type 2 silica-metal mask blocks the flow through the metal and appears to increase the electron density at the etching sidewall which inhibits oxidation, alters the horizontal etch rate, and thereby changes the etch profile. Based on the data for the p-type GaAs bulk case, one might conjecture a similar mechanism operates but with the photo-generated electrons moving to the etching solution-semiconductor reaction region to decrease the vertical etch rate. The dark area (under the mask) can still show deep etching.

The photo-dissolution of multi-layered samples add more complexity to the system and according to the experiments, the results do not directly correlate with the relative etch rate and the types of the mask. The experiments show that not only the electrical properties of the mask,

but also doping type and concentration, and the energy gap of each layer, and the band bending may have an effect on the photo-carrier dynamics to control the photo-dissolution characteristics of multi-layered materials. Only very simple structures of the multilayered semiconductors [63, 92] have been investigated and have not produced an understanding of the mechanisms.

The model of the sidewall angle dependency of the photo-assisted semiconductor dissolution for bulk GaAs is suggested. Improvement of the model is necessary for the multi-layered material and includes various photo-dissolution characteristics observed in the experiments.

There is a disadvantage with the current etch set-up for use with laser fabrication. The distance between target sample and the LED light source has to be maintained within 5mm to get most of the optical power to the target. Laser fabrication requires delicate control of the etch depth for the waveguides. With typical wet chemical etching, it is difficult to control the etch depth since the chemical reaction and the dissolution rate are very sensitive to the etching conditions. The reflectometer etch monitor developed in this lab can be utilized for etch depth control. Also, using the reflectometer, the dissolution rate and the surface condition variations can be observed in real time. However, this requirement on the maximum separation distance makes it difficult to incorporate the reflectometer monitoring system into the photo-dissolution set-up.

The dissolution system for device fabrication uses semiconductor lasers rather than a high-power LED. The intensity of a semiconductor laser can be easily adjusted through the bias current. The low divergence laser beam allows the laser to be backed away from the sample, and thereby provide additional space for optics to combine multiple laser beams and to facilitate the installation of the etch monitor. The laser provides good control over the wavelength, polarization and coherence. Unlike the LED however, the laser cannot uniformly cover large sample areas as a result of the intrinsically low divergence of the beam and in addition, the laser can produce a speckle pattern in the etching surface.

Chapter 4 presents the laser-PAW etching set-up and fabricates test lasers with 894 and 852nm laser materials. The PAW etching apparatus includes reflectometer and photoluminescence (PL) monitoring systems. The apparatus includes beam expanders and an XY optical scanner driven by a circuit in order to “dither” the beam and eliminate the speckle. For optical device fabrication and PAW etch evaluation, fabrication processes and masks are designed. Chapter 5 measures the properties of the fabricated lasers including threshold current, P-I and spectrums and compares the laser with cleaved mirrors.

Chapter 4 Laser Fabrication and PAW Etch Tests

PAW etching characteristics such as the dissolution rate, sidewall angle, and surface microstructure depend on the PAW system including the material layer structure, masking material and wavelength of the light source. One of the important applications would be the integration of optical devices in laser heterostructure using vertically etched sidewalls. Unlike the dissolution rate and top surface condition, the sidewall condition cannot be measured directly using the optical profilometer. Instead, it can be indirectly determined by fabricating optical devices such as a laser and measuring the device properties. The quality of the typical ridge-waveguide laser (and therefore, the threshold current) is closely related to the construction of the cavity including the mirror reflectance and the optical scattering losses.

The present chapter experiments with the PAW etching to develop an understanding of the interplay among surface masking, heterostructure and illuminations intensity in order to develop the laser fabrication sequence required to produce quality laser mirrors and waveguides. The mirror quality depends on its angle with respect to the body of the waveguide and its roughness, which can include uneven etching of the GaAs-AlGaAs layers near the quantum wells (active region). The sidewall angle can be determined from SEM measurements. The optical scattering in a ridge-waveguide is sensitive to sidewall roughness near the semiconductor-air interfaces that determine the effective refractive index for lateral waveguiding (i.e., near the intersection of the ridge and etched plane of the semiconductor).

The primary focus for Chapter 4 consists of (i) designing and implementing a new PAW etching system that includes surface and photoluminescence monitors, (ii) investigating the effects of material and masking types on the PAW etching, (iii) fabricating PAW etched-mirror lasers. The chapter presents PAW etching using coherent illumination from a green 532nm laser, which will be termed laser-PAW etching, rather than the incoherent illumination from LEDs as in the previous chapter. Chapter 4 estimates the quality of laser-PAW etched surfaces and sidewalls

and evaluates the results for potential application to the laser device fabrication. Section 4.1 designs a new laser-PAW set up and fabrication process. Section 4.1.1 designs mask and fabrication steps for etched laser device. The laser-PAW etch setup includes reflectometer and PL apparatus for real-time measurements of the etch depth and surface conditions (Section 4.1.2). Section 4.1.3 and 4.1.4 reviews the reflectometer and PL monitoring systems, respectively. The experiments for the laser-PAW etching investigate the effects of different layer structures, by using different laser heterostructures. Wafers with numbers EPI-1179 and EPI-179 have n-type layers grown over the active layer while wafers M1-5 and M1-3 have the reverse structure.

Section 4.1.5 presents details on the layer structures and the sample preparation process. To maintain analogy with the layer structures for EPI and M1 samples, the FET layers in EPI-1179 and EPI-179 are removed using wet chemical etching and the reflectometer etch monitor. In the chapter, ‘EPI’ indicates the EPI-1179 and EPI-179 wafers but with the FET layers removed. M1 represents M1-5 and M1-3 samples. Even with different substrates, laser-PAW etching of the two EPI materials produces the same characteristics. M1-5 and M1-3 samples have identical layer structures except at the active layer which results in different emission wavelengths (852nm and 892nm) for lasers fabricated with the materials.

Section 4.2 tests PAW etching using a “high-power” laser, defined as having total optical power larger than 70mW, on the EPI and M1 samples with waveguide and mirror patterns described above. Section 4.2.1 examines the reflectometer and PL monitoring system for high-power laser-PAW etching of the EPI and M1 samples. It should be noted that this chapter defines “high power PAW” as the case when the total PAW laser has power $P_{PAW} \geq 70\text{mW}$. Subsequent sections (from section 4.2.2 to 4.2.4) present PAW etch test results for EPI and M1 samples.

Section 4.3 modifies the initial design for the M1 material with Metal-Only mask from Section 4.1.1 so as to circumvent ‘unexpected etch properties’ encounter in the work for Section 4.2. The Metal-Only mask simplifies the fabrication steps and the M1 sample shows vertical sidewall with low lateral etching for the Metal-Only mask using the LED in Chapter 3. The

section reviews PAW characteristics of M1 samples with Metal-Only masks. PAW etching with modified processes successfully fabricates etched mirror lasers with high power laser ($P_{PAW} \geq 70\text{mW}$). The laser properties are tested in Chapter 5.

4.1 Laser-PAW Etching Process and Setup

4.1.1 Fabrication Step and Mask Design

Different types of optical devices including laser with etched mirror [101], serpentine waveguides [14] with turning mirrors and integrated laser-photodetector pairs [102] can be used to evaluate the PAW etching properties for integrated optics. The present work fabricates and tests the simplest ridge-waveguide lasers having either one etched and one cleaved mirror, or else two cleaved mirrors. In either case the waveguide is laser-PAW etched.

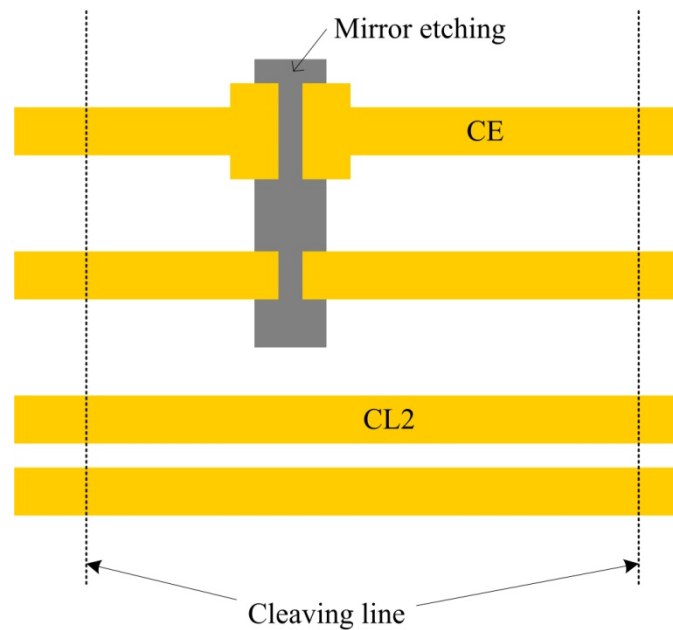


Figure 4.1 Ridge-waveguide lasers having either two cleaved mirrors (CL2) or one cleaved and one etched mirror (CE).

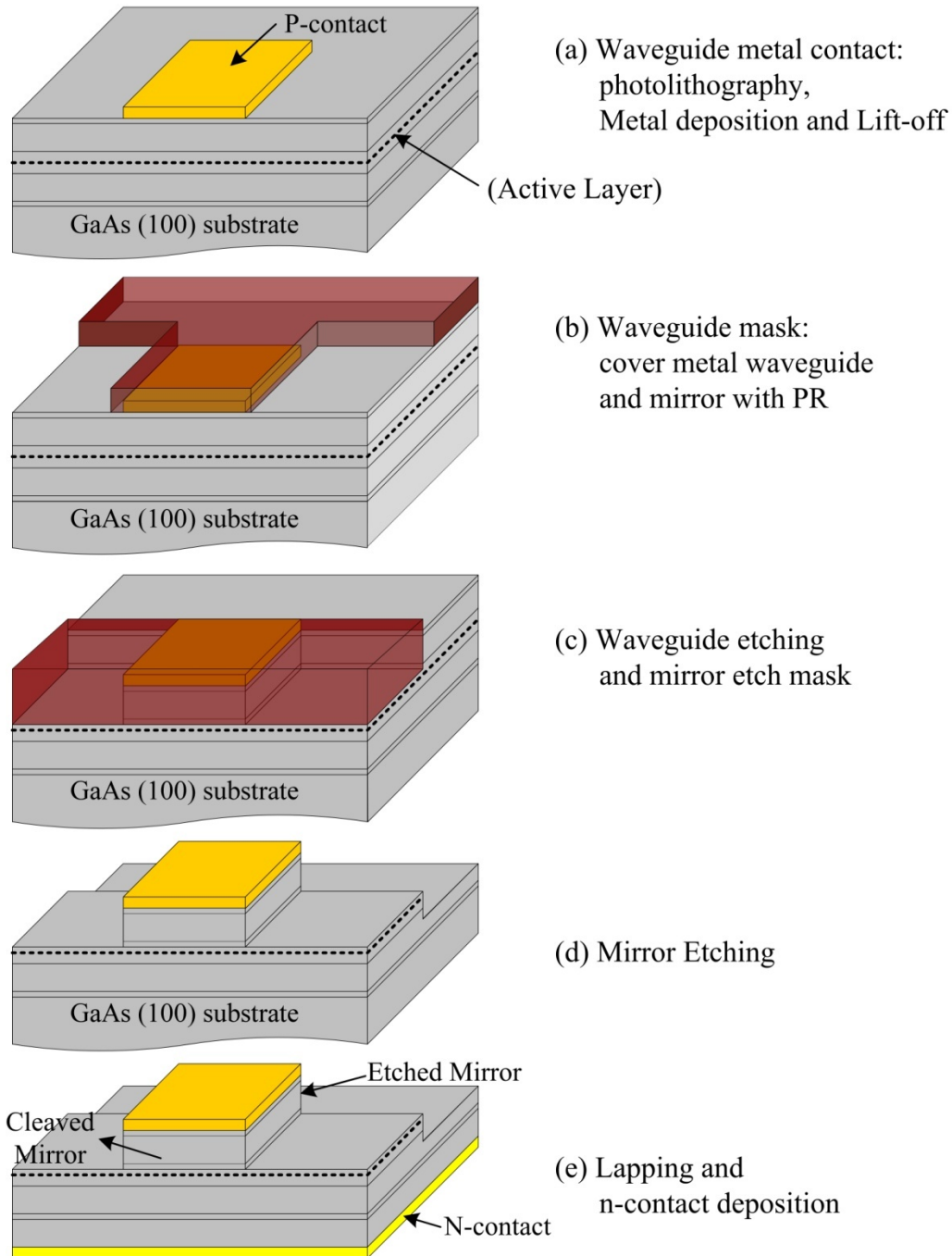


Figure 4.2 Fabrication steps for etched mirror lasers with PAW etching. Note that the features are not drawn to scale, and the etched and cleaved mirrors would be at opposite ends of the cavity.

For more exact comparison, the two types of lasers are fabricated in the same wafer next to each other as shown in Figure 4.1. Denote by CL2 those lasers that have two cleaved mirrors

and by CE those that have one etched and one cleaved mirror. Figure E.1, E.2 and E.3 in Appendix E presents the detailed ridge-waveguide laser patterns of Initial-Masks. The fabrication steps for the PAW etched lasers are similar to those used for lasers with dry-etched mirrors [12, 14]. Figure 4.2 illustrates the designed fabrication steps for both CE and CL2 lasers. The fabrication process can be justified based on the PAW etching properties.

First, metal is electron-beam (E-beam) evaporated to define the laser contact and waveguide pattern after image-reversal photolithography. A lift-off step removes unwanted metal (see Figure 4.2 (a)). The metal consists of either Nickel (Ni, 100 Å) – Germanium (Ge, 400 Å) – Gold (Au, 800 Å) for the n-type top layer on the EPI material, or else Titanium (Ti, 400 Å) – Platinum (Pt, 200 Å) – Gold (Au, 3000 Å) for the p-type top layer on the M1 samples. Usually, the waveguide metal contact serves as a etch mask as it is. In Figure 3.11 (g) in Chapter 3, EPI samples show the best etch characteristics with silica-metal-PR mask (type 3). For simplicity of the laser fabrication process, only the Metal-PR layer (without silica) is used for the etch mask in this work. A PR layer (second photolithography step) covers the metal waveguide contact based on the results from the LED-PAW etch test for laser-PAW waveguide etching (Figure 4.2 (b)).

The PR mask extends 2µm beyond each edge of the top metal layer for easier alignment and less lateral etching. The PR mask also protects the mirror area. Next, PAW etching defines the waveguide. For mirror definition, a mirror window is opened in the PR by another photolithography step – the PR covers all the other parts of the sample to protect waveguide pattern (Figure 4.2 (c)). At this point, another PAW etching defines the mirrors (Figure 4.2 (d)). Next, the sample is lapped to about 150µm thick followed by metal deposition at the back side for contact after the mirror etching (Figure 4.2 (e)). At the backside of the device, either p or n-type metal contacts are e-beam evaporated depending on the layer structure of the material. Typical p-type (Titanium (Ti, 400 Å) – Platinum (Pt, 200 Å) – Gold (Au, 3000 Å)) and n-type

(Nickel (Ni, 100 Å) – Germanium (Ge, 400 Å) – Gold (Au, 800 Å)) contacts are used in this work. The samples are 5mm × 5mm in size for the consistency of the experiment.

4.1.2 Etch Mask Design and Designation

PAW etch tests with laser power higher than 70mW show unexpected results (i.e., results that differ from that produced by the LEDs in Chapter 3) using the mask designed in Section 4.1.1 as will be discussed below in Section 4.2. The original mask distributes the features across the surface with fairly uniform density as described in Section 4.1.1.

The original mask design is modified to three different types to study the relation between semiconductor dissolution and masking conditions under illumination. The term “Initial-Mask” denotes the originally designed masks as detailed in Section 4.1.1 and summarized in the Table 4.1. Appendix E presents details of the Initial-Masks for waveguide and mirror etching. The Modified-Mask can take one of three forms depending on the masking conditions of the right-most and left-most 1mm wide region of semiconductor (termed ‘side-strips’). In all cases, patterns for ridge-waveguide laser are deposited in the middle area of the sample. The Both-Blank mask leaves blank approximately 1mm wide side-strips on the left and right edges of the sample (without PR or metal). The Both-PR mask has PR covering the edge strips. The Both-Metal mask has metal rather than photoresist covering the 1 mm wide strips on either edge of the sample. The masks change the photo-carrier movement by varying the electrical characteristics at the interface of the sample surface and etching solution. Each configuration has a different mask for the waveguide and mirror definitions and they have different surface exposure. The Both-PR mask exposes about 40% and 20% of the sample surface for the waveguide and mirror, respectively, with insulator (PR) that blocks the electrochemical reaction at the interface. For the Both-Blank mask, about 70% and 50% of the surface for waveguide and mirror mask is exposed to the etching solution so that photo-carriers can transfer between the solid and solution at the interface. For the Both-Metal mask, the metal protects the sample surface from the etching solution (about

40% and 20% of the surface exposed to the etching solution for waveguide and mirror mask) but carrier transfer can occur at the interface through the conducting metal mask. From the PAW experiments using different masks, it is found that mask materials such as PR or metal affect the etch characteristics under strong illumination (PAW laser power higher than 70mW).

Table 4.1 Definitions for the etching masks.

Mask Name	Description			
Initial-Mask	Uniformly distributed patterns across the sample surface with a 2mm blank region for the reflectometer probe. Processing steps detailed in Section 4.1.1. Appendix E shows detailed mask designs.			
	Waveguide	PR covers metal waveguide patterns. 60% of the surface exposed. (See Section 4.2.2 for detail)		
	Mirror	PR covers all the sample surface except mirror window. 30% of the surface exposed. (see Section 4.2.3 for detail)		
Modified	Defines two regions “side strips” approximately 1mm wide on either side of the sample at the edge. These strips can be given PR or Metal coatings, or left blank as necessary. The specific configurations are denoted by Both-PR, Both-Blank, and Both-Metal.			
	Both-PR	The side-strips are covered with PR. Light can be absorbed but the PR provides electrical isolation and masks the surface from the etchant.	Waveguide	40% exposure, (Section 4.2.2.1)
			Mirror	20% exposure, (Section 4.2.3.1)
	Both-Blank	The side-strips are left blank and surface exposed to etchant and light. Charge can transfer between solid and etchant.	Waveguide	70% exposure, PR-only patterns are still on the blank area. (Section 4.2.2.2)
			Mirror	50% exposure, (Section 4.2.3.2)
	Both-Metal	The side-strips are covered with metal. Charge can flow through the metal but the mask isolates the surface from light and etchant.	Waveguide	40% exposure, PR patterns are under the metal covered area. (Section 4.2.2.3)
			Mirror	20% exposure, PR patterns are under the metal covered area. (Section 4.2.3.3)

4.1.3 Laser Photo-Assisted Wet (PAW) Etching Set up

Recall Chapter 3 studied the PAW etch characteristics of the heterostructure semiconductor under various conditions using incoherent broad-area illumination from LEDs. The experiments showed interesting results for the variation of the sidewall angle and the

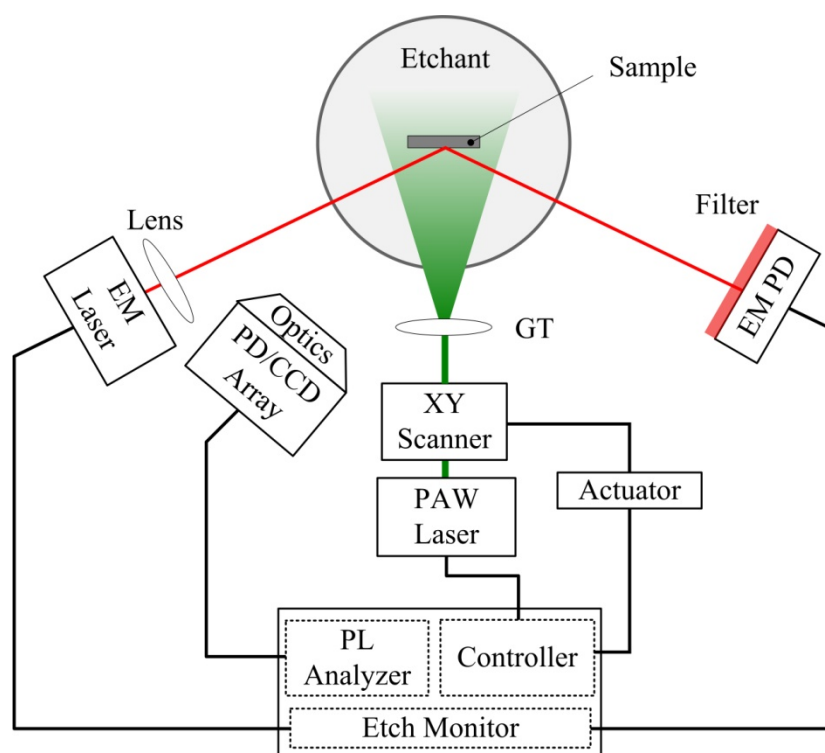


Figure 4.3 Laser PAW etch set up. EM PD: Photodetector for Etch Monitor, EM laser: laser probe beam (670nm, 1mW pulsed) for Etch Monitor, PAW laser: controllable-power green laser (532nm, up to 100mW) for PAW, GT: Galilean Telescope.

For laser device fabrication, it is preferred to have precise control of the etch depth for the waveguides. With wet chemical etching, it is difficult to control the etch depth since the chemical reaction and the dissolution rate are sensitive to the etching conditions. The reflectometer etch monitor developed as part of this research can be utilized for etch depth control.

The reflectometer can monitor in real-time the dissolution rate, etch depth, surface roughness, and the formation of surface nanostructure and surface transition layers.

The PAW etch apparatus for laser fabrication includes the reflectometer and PL monitors (Figure 4.3). The system suspends the target sample in a transparent etching vessel (clear Pyrex[®] dish) containing an etching solution consisting of sulfuric acid (H_2SO_4), hydrogen peroxide (H_2O_2), and DI water (H_2O) in the volumetric ratio of 4:1:25. After achieving the specified etch depth, the sample on its supporting arm swings to a DI water vessel which stops the etching.

For laser-PAW etching developed here, the backside of the sample is attached to a glass slide using photoresist (PR) for the laser-PAW etching. From LED experiment in Chapter 3, the backside condition does not effect on the etch characteristics. A controllable-power green laser (up to 100mW of optical power with wavelength of 532nm) provides a source of illumination for Photo-Assisted Wet (PAW) etching (denoted as ‘PAW Laser’ in Figure 4.3). The laser has significantly lower beam divergence than the LED as well as smaller full-width half-maximum (FWHM) for the range of wavelengths in the emission and greater optical power.

A Galilean telescope (beam expander) denoted as GT in Figure 4.3, expands the beam to ensure the coverage of the sample (beam diameter of approximately 1.5cm at the waist of the Gaussian beam). An electrically controlled mirror deflects the laser beam a small fraction (approximately 10%) of its waist diameter to randomize the “speckle” pattern that would otherwise transfer to the surface during etching. The laser with its low divergence beam makes it possible to introduce optical measurement instrumentation since the laser can be backed away from the sample. Table 4.2 summarizes the applicable laser parameters at the position of the etching wafer. For this dissertation, the laser intensity will be referenced by the total power in the beam (0, 5, 70, 100mW) and the table can be used to convert to an approximate intensity or total power incident on the etching wafer. Further, the terms ‘low power’ and ‘high power’ will refer to the cases $P_{\text{PAW}} \leq 5\text{mW}$ and $P_{\text{PAW}} \geq 70\text{mW}$, respectively.

Table 4.2 Approximate values for laser parameters at the position of the sample (with typical size $5\text{mm} \times 5\text{mm}$).

Parameter	Value	Details
Beam profile	Gaussian	Waist $\sim 1.5\text{cm}$ (diameter) (Waist radius determined by the position where the peak intensity drops by e^2) $\text{Variance} = (\text{Waist}/4)^2$
Power: total	0, 5, 70, 100 mW	Power in full beam, not all incident on etching sample
Intensity: Peak	0, 5.8, 82, 117 mW/cm^2	Intensity at center of Gaussian
Intensity: Average	0, 5, 70, 100 mW/cm^2	Average across a 5mm wide sample
Intensity: Edge	0, 4.6, 65, 93 mW/cm^2	Intensity at sample edge (2.5mm from center)
Power Incident on Sample	0, 1.2, 17, 25 mW	Power = Average Intensity \times Sample area

As mentioned, the setup incorporates a unique pulsed-laser optical reflectometer developed as part of the present research to determine the etch rate, etch depth, surface roughness and formation of surface transition layers during the photo-assisted dissolution process [98, 103, 104]. In operation, the etch monitor laser (EM laser in Figure 4.3) emits a pulsed beam (670nm , $<1\text{mW}$, $<1\text{mm}$ diameter) to the etching surface which reflects into a filtered photodetector (EM PD in Figure 4.3). Pulsing the EM laser prevents the monitor from interfering with the etching by reducing the energy delivered to the surface. The primary reflected signal consists of the average optical power reflected from the surface of the wafer as it etches (i.e., averages out the fringes as seen for example as the dotted curve in Figure 4.4b) thereby indicating the surface reflection coefficient for the surface exposed to the etchant (or for any layers produced on the surface during the etching process). A secondary detected signal consists of the interference between the light reflecting from the exposed surface and the buried heterostructure interfaces. For GaAs/AlGaAs heterostructure, the “distance between fringes” represent approximately $0.1\mu\text{m}$ of etch depth, which also provides the etch rate by dividing by the time between fringes.

The experimental setup uses another new in-situ technique to monitor real-time steady-state photoluminescence (PL) from the wafer during the photo-assisted dissolution. The use of PL has well known applications for determining the carrier and defect density [105]. The PL intensity measurements use a CCD-array with 510×492 pixels and a bandpass filter for infra-red (IR) with wavelengths larger than approximately 700nm. Magnification optics allow viewing of the entire sample during the etch process as well as spatially resolved measurements of IR intensity. In-house custom software measures the PL intensity in selected regions of the sample that can be correlated with the reflectometer data in real time. The optical reflectometer monitors do not interfere with the etching and the PL measurements.

4.1.4 The Reflectometer Etch Monitor

The optical non-contact etch monitor [98, 104, 106] ascertains in real-time (a) the material dissolution depth, (b) the dissolution rate, (c) the formation of nanostructure and the quality of the semiconductor surface [104], and (d) the formation of transition layers [98]. To utilize this method, one must correlate the optical power reflected from the $\text{Al}_x\text{Ga}_{1-x}\text{As}$ heterostructure with its composition. The aluminum mole fraction x and hence, the index of refraction n varies with the depth z from the initial top surface (Figure 4.4 (a)).

During the etch, TE-polarized laser emission (<1 mm diameter, <1 mW, 670nm), denoted EM Laser in Figure 4.3, reflects from the wafer to a silicon photodetector (PD) as power P_o . The primary signal consists of the optical power reflected from the surface of the wafer as it etches (average level of the fringe signals). Since the signal depends on the refractive index of the material surface, the reflectometer primarily signal indicates the type of material being etched at the time the signal is recorded. A secondary detected signal consists of the interference between the light reflecting from the exposed surface and the buried heterostructure interfaces. The fringe width and height provides information on the material dissolution rate and the surface condition, respectively.

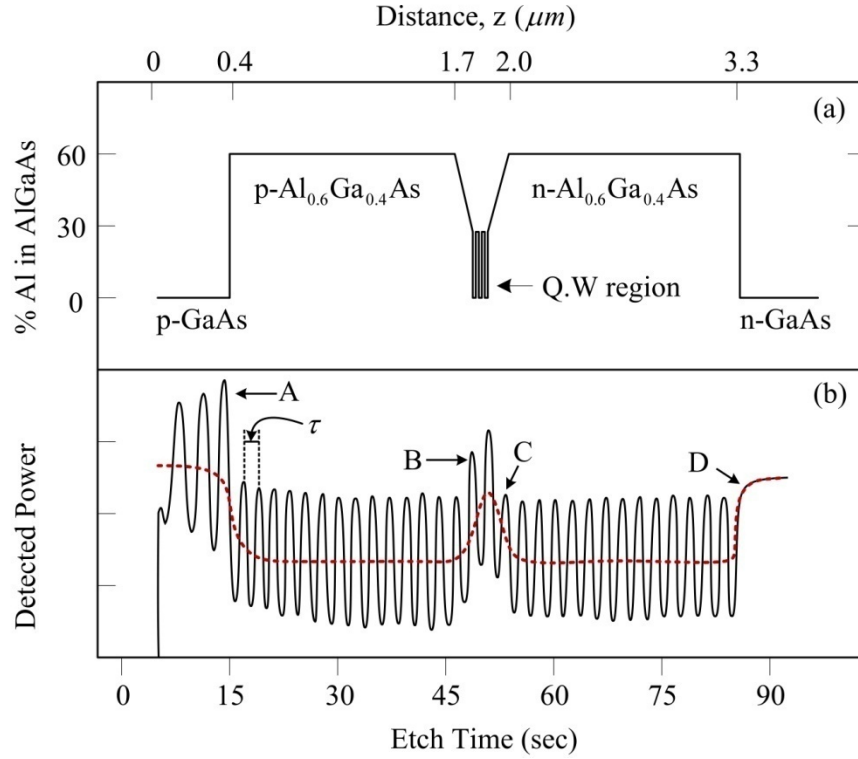


Figure 4.4 (a) Aluminum concentration as a function of depth into the M1-5 laser heterostructure wafer. (b) The fringe pattern obtained during a chemical dissolution. Points A, B, C and D indicate sudden changes in aluminum composition. Dotted line represents primary reflected signal.

The total detected power P_o is a superposition of the primary and secondary signals and constitutes a reflectivity-versus-depth map (see results in Figure 4.4 (b) for example) for the entire epitaxial structure. A simple two-layer model proves adequate for this heterostructure. The effective reflection coefficient $R_{eff} = P_o/P_{inc}$ (where P_{inc} is the incident power) can be written as [98, 106]

$$R_{eff} = \left| \frac{r_1 e^{-jk_2 z} + r_2 e^{jk_2 z}}{e^{-jk_2 z} + r_1 r_2 e^{jk_2 z}} \right|^2 \cong R_s + 2r_1 r_2 \cos(2k_2 z) \quad (4.1)$$

where the surface reflectance is

$$R_s = r_1^2 = \frac{(n_2 - n_{etch})^2}{(n_2 + n_{etch})^2} \quad (4.2)$$

n_2 and n_{etch} represents refractive index of the $\text{Al}_x\text{Ga}_{1-x}\text{As}$ and etching solution, respectively.

The absorption length L_{abs} for the electric field in a material with mole fraction x can be calculated from the imaginary index, n_{im} , using $L_{\text{abs}} = \lambda_o / (2\pi n_{\text{im}})$ where λ_o is the wavelength of the incident laser beam. Table A.1 and A.2 in Appendix A presents real and imaginary refractive index according to the aluminum mole fraction x [107], respectively. The photodiode detects the surface reflected signal superposed with the signal reflected from an internal interface as indicated by Equation (4.1). The cosine term (the secondary signal) produces oscillations centered on the average reflectance indicated by Equation (4.2). The surface reflectance (the primary signal) R_s maps out the composition of the material during the dissolution while the internally reflected beam and the resulting oscillations provide the interferometric accuracy for the etch monitor. Equation (4.1) produces fringes in the data plotted versus time with peaks corresponding to distances

$$z(t)|_{\text{max}} = \frac{m\pi}{k_2} = \frac{m\lambda_2}{2}, \quad m = 0, 1, 2, \dots, \quad \lambda_2 = \frac{\lambda_o}{2} \quad (4.3)$$

The etch depth between any two adjacent maximum or minimum interference fringes can be expressed as follow

$$\Delta z = \frac{\lambda_o}{2n_2} \quad (4.4)$$

For the $\text{Al}_{0.6}\text{Ga}_{0.4}\text{As}$ with $\lambda_o = 670\text{nm}$, Δz corresponds to approximately $0.1\mu\text{m}$ etch depth. The calculated etch depth of $0.1\mu\text{m}$ varies by at most 4% for angles of incidence in the range of $\pm 45^\circ$ and at most 8% over $\pm 90^\circ$ since (a) the value depends on the wavelength of light in the material as it propagates between the etching surface and an internal interface and (b) Snell's law gives a critical angle of approximately 23° for the sample in the etchant for which the cosine has the value of 0.92. The etch rate R can be determined by calculating

$$R = \frac{\Delta z}{\tau} \quad (4.5)$$

where Δz denotes etch depth during the time corresponding to one fringe width τ .

Surface roughness due to the formation of nanostructure during the etching necessarily decreases the coherence between the surface and internally reflected signals and therefore decreases the fringe amplitude. However, only very significantly rough surfaces (micron level roughness and more) affect the surface reflected signal (primary signal) through R_s . The coherence effects are embodied in the Secondary Modulation Ratio (SMR) defined as the ratio of the peak-to-peak Fabry-Perot interference signal (Cosine in Equation (4.6)) to its average value [104].

$$\text{SMR} = C_f \langle \cos(2knz) \rangle \quad (4.6)$$

where $C_f = 4r_1r_2/R_s$ denotes peak to peak divided by average.

For a perfect surface, the SMR is just C_f without rest. As expected from Equation (4.1), the superposed signal oscillates about an average value set by the surface reflectance. Equation (4.1) predicts the ratio between the peak-to-peak fringe height and the average value (in the $\text{Al}_{0.6}\text{Ga}_{0.4}\text{As}$ for example) to be approximately $C_f \cong 0.52$, which is in good agreement with experiment results.

As part of the definition, the average in Equation (4.6) applies to the variation in depth z in that area of the surface illuminated by the probe beam (EM Laser); that is, the area of the probe beam on the surface is the same as the area for the average. The SMR can be correlated with the surface nanostructure and the consequential roughness. Figure 4.4 (b) shows the fringe pattern for an almost perfectly smooth surface with an SMR of 0.5. The sensitivity for the surface roughness can be as low as 50-100 Å.

The reflectometer monitors the etch characteristics in real time, which for convenience has been reduced to hand-held size during the course of the research. The optical monitor includes a display, laser and photodetector (PD), one microcontroller for pulse and synchronization control, a second microcontroller for data reduction, data storage and transfer,

and graphics on a touch screen. Figure 4.5 illustrates the block diagram of the hand-held etch monitor.

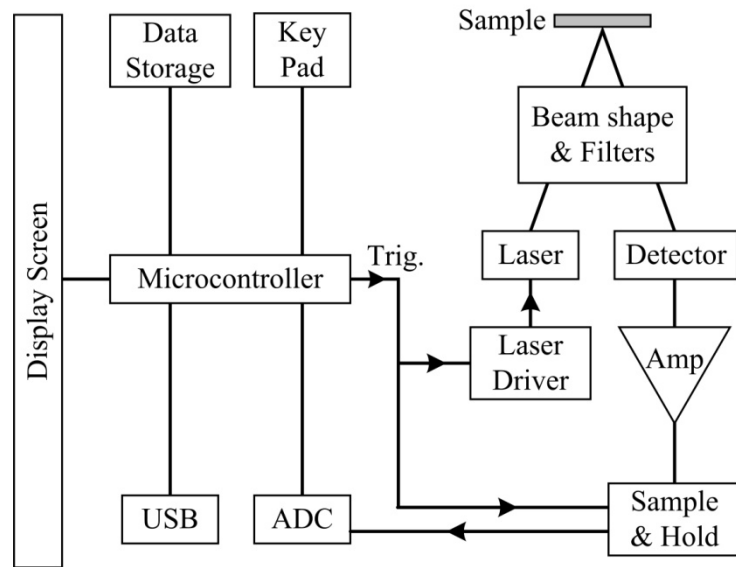


Figure 4.5 Block diagram for the pulsed-laser wet etch monitor [106].

The etch monitor pulses the probe laser and detects the optical signal reflected from the etching surface. The photodetector produces a corresponding photocurrent pulse with large signal-to-noise levels suitable for an analog-to-digital converter ADC (as opposed to using low quasi-CW light levels with slow lock-in amplifiers). A microcontroller synchronizes the laser pulses with a sample and hold circuit. The laser-detector module mounts near the etch vessel (Figure 4.3). The microcontroller transfers the data from the analog-to-digital converter (ADC) and displays the results on the display screen. The microcontroller can be programmed to control the photo-assisted semiconductor dissolution lasers as well as remove the sample at some predetermined time. The display presents fringe patterns similar to that depicted in the Figure 4.4 (b) during the etching of the laser heterostructure material. The most recent version of the etch monitor (to be published) uses a CCD array to map the reflections from the entire surface as it

etches. This provides real-time etch depth, rate and roughness monitoring at each point on the surface.

4.1.5 Photoluminescence Measurement

One would like to observe the surface deconstruction and the associated molecular and electronic processes (in real-time) without interfering with the measurements. For these purposes, an optimal choice would be to use electroless optical monitors and measurement apparatus including steady-state and transient photoluminescence (PL), Raman spectroscopy and optical interference methods. The photo-dissolution process uses intense illumination and can withstand slight perturbations to the optical intensity. Steady state monitors such as for photoluminescence (PL) do not require the application of further optical illumination. Time-resolved measurements do not significantly alter the steady state so long as the pulse duration and intensity remain relatively small and thereby minimize the energy delivered to the surface. The use of spatially-resolved measurements would be highly advantageous in providing a more complete picture of the carrier drift/diffusion and recombination centers. Time-resolved multi-parameter imaging (wavelength, intensity, position) would ideally view etch surfaces (and sidewalls), and internal optically-active regions such as near quantum wells or near the surface “dead” layers proposed in the literature [26-30]. Further, observations of PL fluctuations can be correlated with the ebb-and-flow of carriers, the time evolution of current loops in the etchant, and with the observed formation of surface microstructure.

For PL monitoring, software records the signal from a CCD camera and another photodetector (PD) that measures emission from the sample during the etching (Figure 4.3). A computer combines the PL signal with that from the reflectometer. The setup in Figure 4.3 places the PD in front of the etch vessel to measure PL emission from sample during the etching while CCD camera records the 2-D PL emission from the sample. In the first version for this dissertation, the PD integrates the PL across the surface while the CCD image provides detailed

spatial PL emission on the sample surface. Red filters prevent the green PAW laser reflections from scattering to the CCD camera and PD.

4.1.6 Sample Layers and Preparation

Four different laser heterostructure materials are used in this chapter; EPI-1179, EPI-179, M1-5 and M1-3 wafers. Among those wafers, EPI-1179 and EPI-179 wafers have almost same layer structure as M1-5 and M1-3 wafers. EPI-1179 and EPI-179 wafers have n-type layers above the active layers and p-type below it (Figure 4.6) while M1-5 and M1-3 wafers essentially reverse those layer structures (Figure 4.9). M1-5 and M1-3 wafers have essentially the same layer structures except for the active layers that provide the distinct laser emission wavelength. Samples from both wafers are indicated as M1 samples since both wafers show same PAW etch properties from the experiments.

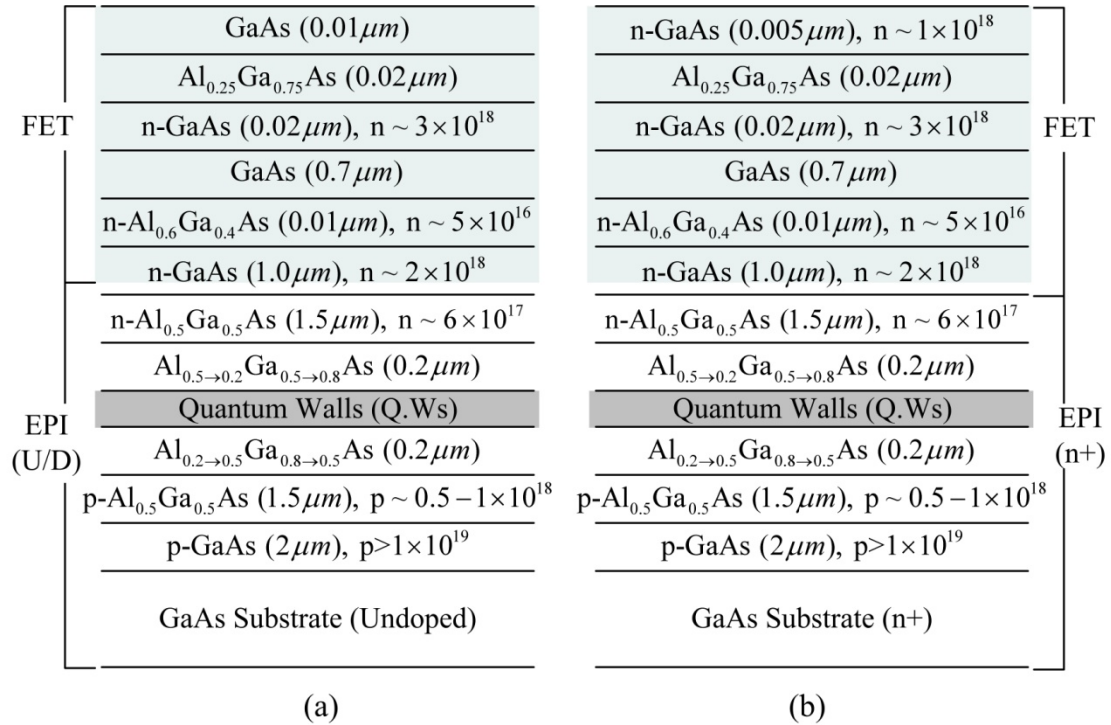


Figure 4.6 Wafer layer structures of (a) EPI-1179 (U/D) and (b) EPI-179 (n+)

EPI-1179 and EPI-179 have undoped (i.e., semi-insulating SI) and n⁺-type GaAs as substrates, respectively. Unlike M1-5 and M1-3 wafers, EPI-1179 and EPI-179 wafers have FET layers grown over the laser structures. For more direct comparison between two different layer structures of the laser material, the EPI-1179 and EPI-179 wafers receive pre-treatment to retain only laser layers by removing FET layers.

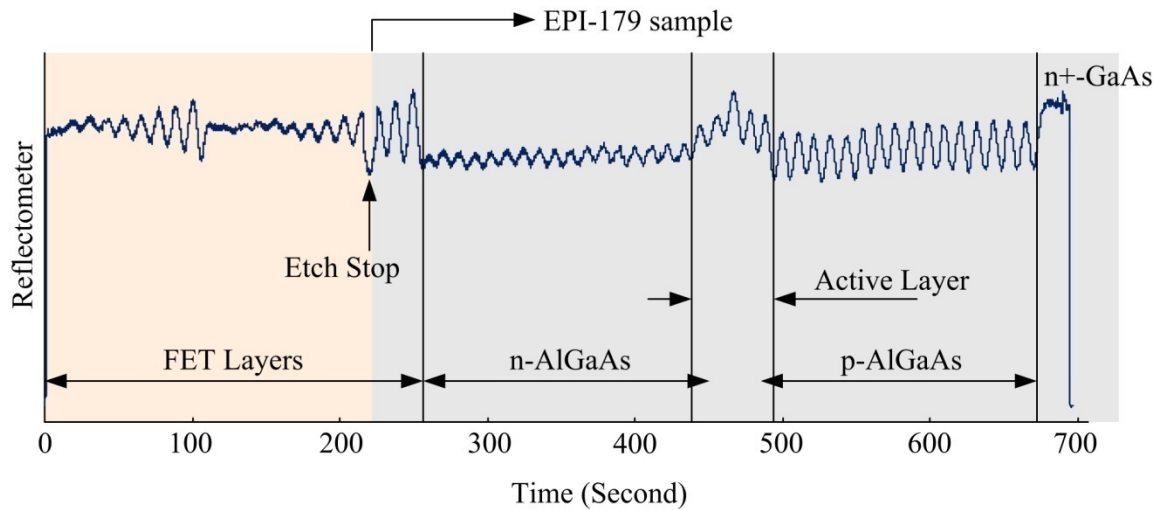


Figure 4.7 Reflectometer signal of EPI-179 sample during the dark wet etching. The large ‘active layer’ includes the quantum wells as well as the graded index region for optical confinement.

Figure 4.8 illustrates the layer structures of the EPI-1179 and EPI-179 wafer, denoted as EPI(U/D) and EPI(n⁺), respectively, after removing the top FET. EPI samples have similar structure with M1 samples (GaAs-AlGaAs-Active layer-AlGaAs-GaAs) except reversed material types. From the PAW etching experiments in the following sections, both EPI (U/D) and EPI (n⁺) samples show identical results throughout the experiments despite the different substrates. From the layer structure of the two samples (Figure 4.8), EPI(U/D) and EPI(n⁺) have semi-insulating and n⁺ GaAs as a substrate, respectively. This suggests that the electrical properties of the substrate have negligible effect on the PAW etching that can in part be attributed to all of the backsides being mounted to glass slides which provides electrical isolation. In contrast to the bulk

material, it is also found that the backside condition of the sample (whether exposed to the etching solution or not) does not affect the etch properties of the laser heterostructure. ‘EPI’ is used to denote both the EPI (U/D) and EPI (n+) since they show similar behavior despite the different substrates.

n-GaAs ($\sim 0.2\mu m$), $n \sim 2 \times 10^{18}$	n-GaAs ($\sim 0.2\mu m$), $n \sim 2 \times 10^{18}$
n-Al _{0.5} Ga _{0.5} As ($1.5\mu m$), $n \sim 6 \times 10^{17}$	n-Al _{0.5} Ga _{0.5} As ($1.5\mu m$), $n \sim 6 \times 10^{17}$
Al _{0.5→0.2} Ga _{0.5→0.8} As ($0.2\mu m$)	Al _{0.5→0.2} Ga _{0.5→0.8} As ($0.2\mu m$)
Quantum Walls (Q.Ws)	Quantum Walls (Q.Ws)
Al _{0.2→0.5} Ga _{0.8→0.5} As ($0.2\mu m$)	Al _{0.2→0.5} Ga _{0.8→0.5} As ($0.2\mu m$)
p-Al _{0.5} Ga _{0.5} As ($1.5\mu m$), $p \sim 0.5 - 1 \times 10^{18}$	p-Al _{0.5} Ga _{0.5} As ($1.5\mu m$), $p \sim 0.5 - 1 \times 10^{18}$
p-GaAs ($2\mu m$), $p > 1 \times 10^{19}$	p-GaAs ($2\mu m$), $p > 1 \times 10^{19}$
GaAs Substrate (Undoped)	GaAs Substrate (n+)

(a) (b)

Figure 4.8 (a) EPI(U/D) and (b) EPI(n+) Wafer layer structure

p ⁺ -GaAs ($0.2\mu m$), $p > 2 \times 10^{19}$	p ⁺ -GaAs ($0.15\mu m$), $p \sim 8 \times 10^{19}$
p ⁺ -GaAs ($0.05\mu m$), $p \sim 1 \times 10^{18}$	p ⁺ -GaAs ($0.05\mu m$), $p \sim 1 \times 10^{19}$
p-Al _{0.6} Ga _{0.4} As ($1.2\mu m$), $p \sim 1 \times 10^{18}$	p-Al _{0.6} Ga _{0.4} As ($1.2\mu m$), $p \sim 1 \times 10^{18}$
p-Al _{0.6→0.3} Ga _{0.4→0.7} As ($0.5\mu m$), $p \sim 5 \times 10^{17}$	p-Al _{0.6→0.3} Ga _{0.4→0.7} As ($0.2\mu m$), $p \sim \text{low} \times 10^{17}$
Quantum Walls (Q.Ws)	Quantum Walls (Q.Ws)
n-Al _{0.3→0.6} Ga _{0.7→0.4} As ($0.5\mu m$)	Al _{0.3→0.6} Ga _{0.7→0.4} As ($0.2\mu m$)
n-Al _{0.6} Ga _{0.4} As ($1.2\mu m$), $n \sim 4 \times 10^{17}$	n-Al _{0.6} Ga _{0.4} As ($1.2\mu m$), $n \sim 4 \times 10^{17}$
n-GaAs ($0.3\mu m$), $n \sim 2 \times 10^{18}$	n-GaAs ($0.3\mu m$), $n \sim 2 \times 10^{18}$
n ⁺ -GaAs (100) substrate	n ⁺ -GaAs (100) substrate

(a) (b)

Figure 4.9 Layer structures of (a) M1-5(892nm) and (b) M1-3 (854nm)

Figure 4.9 illustrates the layer structures of M1-5 and M1-3. Both wafers have similar layer structures but different laser emission wavelength. In this work, samples from both wafers are indicated as M1 samples since both wafers show the same PAW etch properties from the experiments. In contrast to the EPI sample, the M1 samples have p-type layers over the active layers.

4.2 Laser-PAW Etching

Before the actual laser device fabrication, the PAW etching process is tested using a high-power laser source using prepared samples (EPI and M1) and the Initial-Mask for waveguides and mirrors following the fabrication steps in Figure 4.2. From the LED-PAW etch tests in Chapter 3, the etch characteristics depend on the mask materials, layer structure of the material and PAW light source. Green LED-PAW produces a smooth vertical sidewall suitable for laser mirrors when the samples have silica-metal-PR (type 3) masks for EPI samples, and Metal-Only (type 1) masks for M1 samples (Figure 3.10 and 3.11). From the Chapter 3 data, a PAW laser fabrication process would work better for EPI samples and it may need to be modified for the M1 sample. The LED-PAW tests suggests that EPI samples with type 3 masks have more suitable side profile – less lateral etching and better sidewall profile – for laser devices than M1 samples due to the n-type layers above the active layer.

In this section, the laser fabrication process is first tested on EPI samples prior to the actual laser fabrication. The results from the EPI material suggests that a couple of issues need to be addressed including non-uniform etch depth and the fact that the variation of etch depth across the surface depends on the mask conditions. PAW tests using the same masks are continued with M1 samples for how different layer structures of the material change the etch properties under the same condition. With laser-PAW, the post-etched wafer has distinct characteristics compared with the LED cases. High power laser-PAW ($P_{PAW} \geq 70\text{mW}$) etching produces non-uniform etch depth depending on the mask pattern and the position of the unmasked region while the

LED-PAW shows no such characteristics. The reflectometer signal also shows an unexpected pattern for the high power laser ($P_{PAW} \geq 70\text{mW}$). Section 4.2.1 discusses (i) the observed reflectometer signal for dark and high power PAW using blank samples and (ii) the PL signal during the etching. In Section 4.2.2 and 4.2.3, waveguides and mirrors are etched using the originally designed fabricated steps (i.e., the ‘Initial-Mask’ type IM) and EPI samples.

Section 4.2.2 tests PAW etching of EPI-base waveguides. The PAW etchings with the “Initial-Mask” shows non-uniform etch rates over the sample surface. The surface charge current may cause the etch depth variation in which case, the arrangement of the mask pattern (size and the position of the unmasked regions) and the mask material type (and beam uniformity) all have an effect on the PAW etching. In order to study the effects of the size of the unmasked regions and the type of materials used as an etch mask, laser and mirror patterns are placed near the center of the sample while approximately 1mm strips near the edges of the wafers (termed ‘side strips’) are processed in accordance with one of the three alternate masks Both-Blank, Both-PR or Both-Blank as defined in Table 4.1.

The testing of laser-PAW etching on mirror patterns appears in Section 4.2.3. The mirror etching is the most important step in the fabrication of the laser. From the LED-PAW experiments, the laser etching is expected to produce vertical sidewall profiles when the EPI sample has a metal-PR mask. However, the laser-PAW inhibits the etching near the mirror window for the EPI sample using the Initial-Mask. Similar to the waveguide etch tests, the mirror patterns are only deposited in middle of the sample and three different mask conditions are applied to 1mm wide strips near the edge of the samples corresponding to the three alternate masks Both-PR, Both-Metal, and Both-Blank as defined in Table 4.1.

Section 4.2.4 and 4.2.5 test both the waveguide and mirror patterns for M1 samples. Waveguide etching of the M1 sample with the Initial-Mask for the waveguide agrees with the LED-PAW etch properties of the silica-metal-PR (type 3) mask for M1 material from Chapter 3. The etched pattern has almost the same amount of lateral etching as the dark etched one. The

mirror etching shows different laser-PAW etch properties with the Initial-Mask for mirror. Laser-PAW promotes the etching at the mirror for high power PAW ($P_{PAW} \geq 70\text{mW}$) for M1 material while it inhibits etching at the mirror window for the EPI material. Unlike the waveguide etch tests, the etching forms deep trenches along the edge of the mask (at the edge of the mirror window) and in addition produces large lateral etching for M1 samples. The PAW mirror etching does not produce the desired mirror facet for either the EPI or M1 sample. For practical application of the laser-PAW etching to device fabrication, it is necessary to further investigate the relation among (i) mask configuration, (ii) masking material, (iii) heterostructure types, and (iv) the fabrication sequence and processes.

4.2.1 Reflectometer and PL Signals in Laser-PAW Etching

With high power laser-PAW ($P_{PAW} \geq 70\text{mW}$), the reflectometer signal shows very different patterns than the dark case. Figure 4.10 and 4.11 compares the reflectometer signals and corresponding PL of EPI-179 (before removing the FET layers) and M1 samples during dark and PAW etching.

Figure 4.10 (a) shows a standard reflectometer signal of the sample during dark etching. Figure 4.10 (b), shows that the etch rate for the EPI-179 sample (the one with n-type materials over the active layer) does not increase with illumination in the top FET layers (undoped and n-GaAs). In the n-GaAs layer, the etch rate decreases. The etch rate of the layers in the heterostructure does not agree to the previous experiments using bulk GaAs. In the LED experiment in the Chapter 3.2.1, bulk n-GaAs etch rate increases about 75% under illumination (Figure 3.5 (h)) regardless of mask types.

The sample shows strong PL at the beginning (thin layers of n-GaAs, AlGaAs and n-GaAs, upto about 10 seconds) and then weaker PL at the undoped GaAs layer. The PL intensity slightly increases at the n-type GaAs layer (110-290 seconds) and drops at the n-AlGaAs layer (Figure 4.10 (c), near 290 secs).

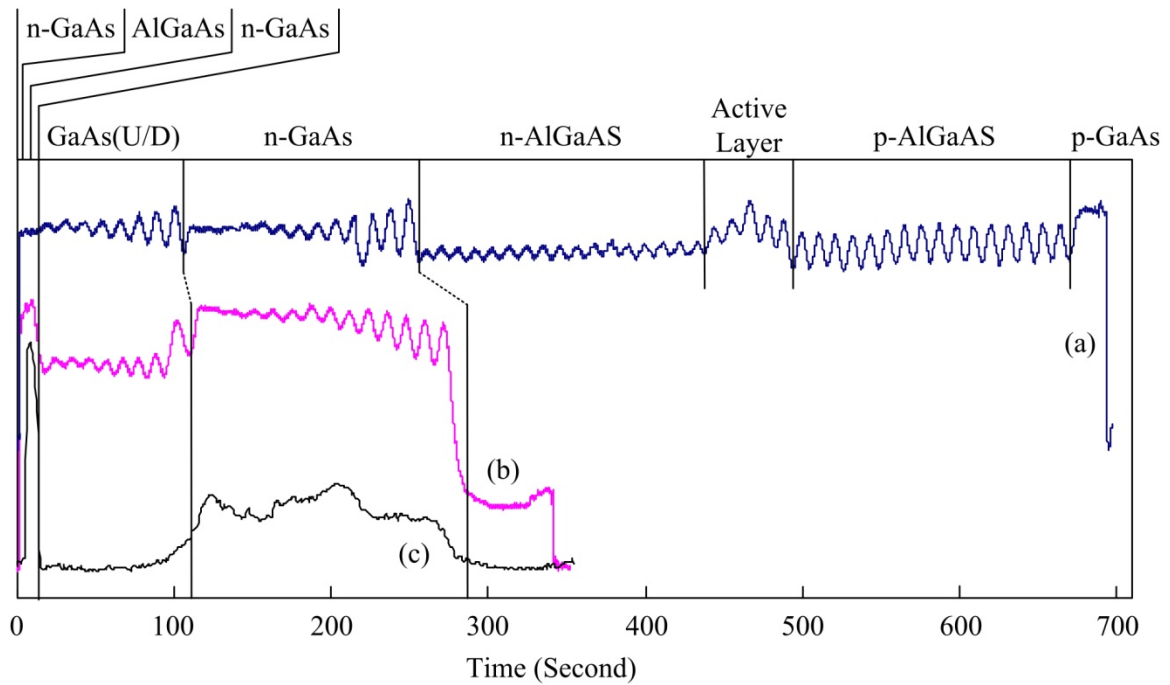


Figure 4.10 EPI-179 samples (a) Reflectometer patterns in dark and (b) high power PAW etching form EPI-179 samples and (c) Photoluminescence Intensity during the PAW with high power green laser ($P_{PAW} \geq 70\text{mW}$). Active layer includes graded layer and quantum walls (Q.Ws).

Similarly, the reflectometer signal decreases slightly at the undoped GaAs laser and recovers the original level at the n-type GaAs layer. The signal shows a very pronounced and unusual “dip” in the n-AlGaAs layer and the fringe of the signal is either reduced in height or expanded in time (i.e., low etch rate) at the ‘dip’ (Figure 4.10 (b)). The observed increase in fringe height in the FET layers and the GaAs region near the top is caused by the absorption of 670nm light in those two regions (the absorption length is approximately 170nm which appears to be doubled for the present situation). The M1 sample shows similar characteristics with the EPI sample for the reflectometer signal and PL (Figure 4.11). M1 also shows the “dip” in the n-AlGaAs layer from the reflectometer signal and the drop in PL intensity at the same layer. For both EPI and M1 samples, the PL intensity correlates with the primary signal of the reflectometer. Since the PL intensity does not interfere with the reflectometer signal detection, the dip suggests

the laser illumination alters the surface of the n- type AlGaAs layer. The reflectometer and PL signal for the M1 samples are clearer than for the EPI samples. The signal maintains clear fringes where the ‘dip’ occurs which make it possible to deduce the etch depth in the region. For the M1 sample, the reflectometer signal shows faster etch rate through out all the layers including p-GaAs, p-AlGaAs and n-AlGaAs from the reflectometer signal.

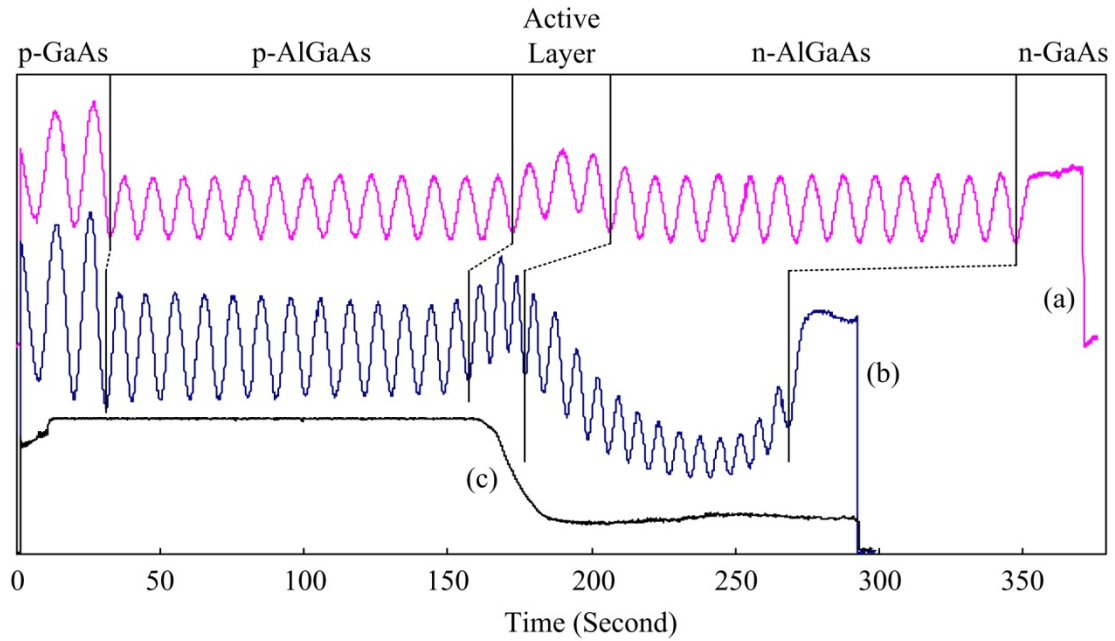


Figure 4.11 M1 sample: (a) reflectometer signal for dark wet etching and (b) reflectometer signal and (c) PL signal during the PAW with high power green laser ($P_{PAW} \geq 70\text{mW}$). Active layer includes graded layer and quantum wells (Q.Ws).

The high-power PAW etching shows narrower fringe width in Figure 4.11(b) compared with that for standard dark etching thereby indicating greater etch rate for the higher power case. With PAW laser power of 100mW, the fringe width reduces at both p and n-type AlGaAs layers by approximately 20% and 60% compared with the dark etching signal of the p and n-type AlGaAs layer, respectively. The reflectometer signal implies that the etch rate increases by about 20% and 60% at the p and n-type AlGaAs layer with high power laser ($P_{PAW} \geq 70\text{mW}$). The

result does agree with the bulk results in chapter 3. The bulk p and n-type GaAs etch rate increases by approximately 35% and 75% with high power UV and green LED (Figure 3.5 (h)).

The reflectometer signal of the M1 sample under illumination (Figure 4.11 (b)) shows a reflectance dip in the n-type AlGaAs layer and the reflectivity recovers to the initial level when the etching surface reaches the n-GaAs layer at the substrate. In the ‘dip’ for the M1 sample, the reflectometer signal maintains the fringe height with the p-type layers, which indicates the surface remains smooth in the ‘dip’ layer. The PL has high intensity at the p-AlGaAs layer and suddenly drops after the active layer where reflectometer signal shows the ‘dip’ and did not recovered back to the initial level of PL.

The reflectometer plot using the weakly absorbed 670nm probe laser appears normal until the active layers. Based on the fringe spacing in the p – $\text{Al}_{0.6}\text{Ga}_{0.4}\text{As}$, the etch rate has the approximate value of 10nm/sec. The ratio of the “fringe peak-to-peak” and the “average reflected” signals for the p – $\text{Al}_{0.6}\text{Ga}_{0.4}\text{As}$ layer of 51% represents a smooth surface (at the position of the 1mm probe beam, standard deviation < 20nm); the theoretical limit on the ratio is approximately 53%. After the active layer (corresponding to the “ledge” seen in Figure 4.11(c) for etching into the n-type material), the reflectometer signal starts to drop to approximately 50% of the proper height for $\text{Al}_{0.6}\text{Ga}_{0.4}\text{As}$ while the ratio of “the peak-to-peak fringe height to the average” decreases only slightly to 43%. The signal recovers to the original state at the substrate. Apparently, high power PAW etching modifies the surface layer (reflectance) without significantly affecting the surface microstructure during the etching of the n-type AlGaAs layer.

Initial research for these etching experiments [98] has shown similar anomalous reflectometer dips for the p-type layer of the GaAs/AlGaAs laser materials in diffusion-rate-limited phosphoric acid (dark) etches (7:3:3 volumetric ratio of Phosphoric Acid (H_2PO_4), Hydrogen Peroxide (H_2O_2) and DI water (H_2O)). With the thick phosphoric acid system, the interference pattern level recovers to the normal level when the sample is pulled out from the etching solution, DI rinsed and then re-inserted into the etching solution. A camera system shows

the dip is due to viscous etch byproduct with mass density larger than that of the etchant. However, for the present case, the “dip” in the n-type AlGaAs layer is not affected by agitation of the etching solution or rinsing of the sample.

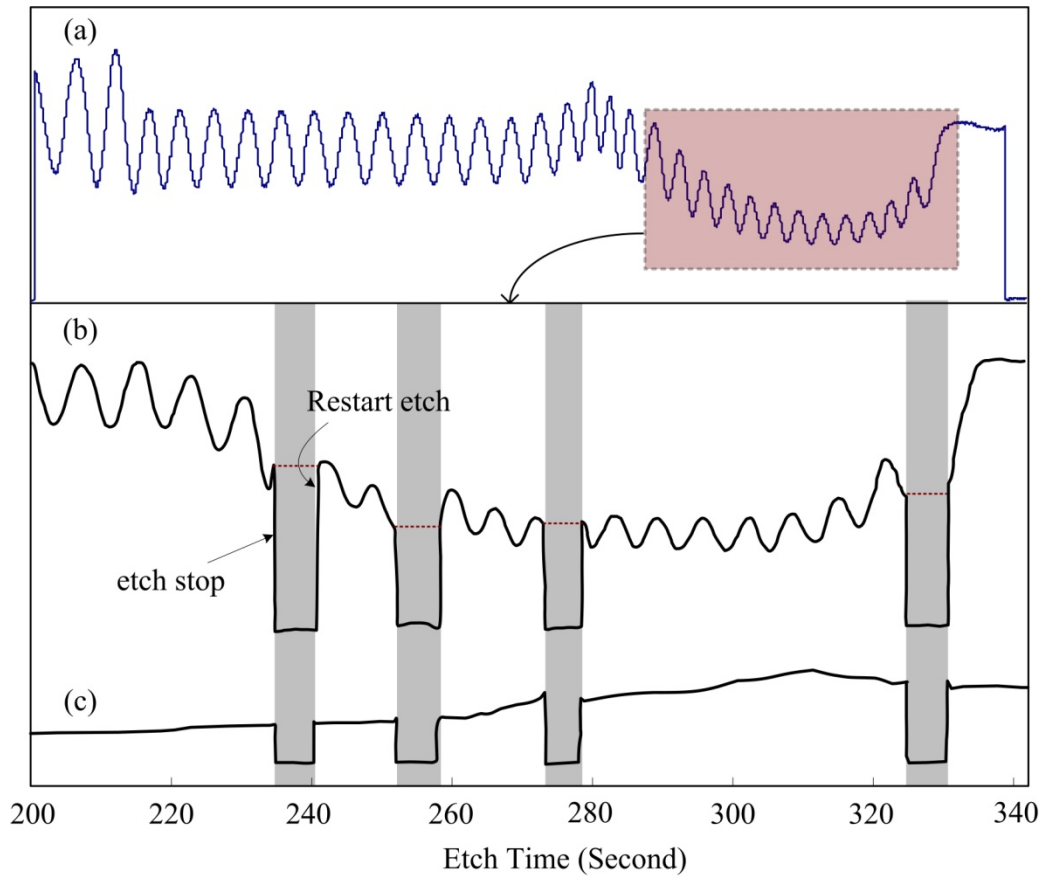


Figure 4.12 (a) Typical reflectometer signal during the laser PAW etching of the M1 sample, (b) reflectometer signal and (c) corresponding photoluminescence intensity in the boxed area from (a) where the anomaly occurs. Etching stops four times for a rinse in DI water during the anomalous behavior of the reflectometer signal. The reflectometer signal returns to the identical level as before the rinse indicating a relatively stable surface layer.

Figure 4.12 shows an example of the anomaly for green laser-PAW etching in the sulfuric acid etchant (volume ratio 4:1:25 of Sulfuric Acid (H_2SO_4), Hydrogen Peroxide (H_2O_2) and DI water (H_2O)). The etching is stopped at several points and rinsed. The reflectometer signal

resumes the same average level and more significantly, the fringe pattern resumes the same height and phase as prior to the rinse (compare fringes across the breaks near 240, 260 and 280 seconds in Figure 4.12b). Apparently, the dissolution has produced a relatively stable surface layer (such as oxide layers as mentioned in Chapter 2,) that forms on the n-type AlGaAs layer only with high power laser illumination.

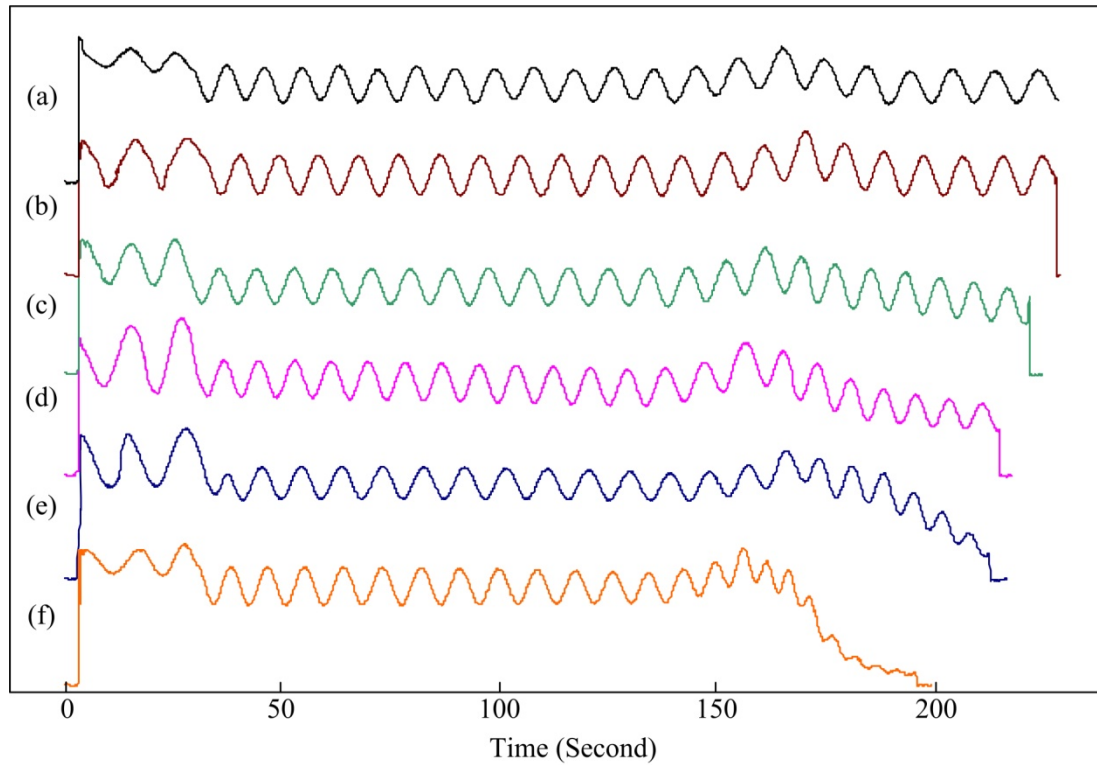


Figure 4.13 Reflectometer signal versus PAW laser power for M1-3: (a) Dark, (b) $P_{PAW} \leq 5\text{mW}$, (c) $P_{PAW} \sim 10\text{mW}$, (d) $P_{PAW} \sim 30\text{mW}$, (e) $P_{PAW} \sim 70\text{mW}$ and (f) $P_{PAW} \sim 100\text{mW}$. The plots have been displaced along the vertical axis and therefore, the absolute magnitude does not correlate with reflectance.

The behavior of the PL signal indicates the carrier concentration within the heterostructure. The $\text{Al}_{0.6}\text{Ga}_{0.4}\text{As}$ layers absorb the green 532nm light within approximately $300\mu\text{m}$ (absorption length). For the p-type semiconductor, the photoelectrons easily recombine with the majority holes. As in Figure 4.11 (c), the PL signal rapidly decreases near the quantum

well at the n-type semiconductor suggesting large photo-hole consumption at the reaction surface as expected for increased etch rates. The PL signal remains relatively constant throughout the time frame of the anomaly. The etch rate increases by 50% in this region compared with the p region. One might conjecture on whether removing the etch-formed transition layer during etching would further increase the etch rate. For both EPI and M1 samples, PL shows higher intensity in the p-type layer than n-type layer. Agitating the solution during the etching does not affect the PL pattern. All the other M1 samples with high power PAW etching show the same pattern.

The reflectometer signal “dip” in the n-AlGaAs layer depends on the PAW laser power. Figure 4.13 shows the reflectometer signals parameterized by the PAW laser power incident on the M1 sample. The dip in the n-AlGaAs layer starts to appear with PAW laser powers of about 10mW (Figure 4.13 (c)) and correlates with the increased etched rate Figure 4.13 (d), (e) and (f)). The reflectometer signal drops by 3db (at the dip) for PAW laser power larger than approximately 30mW (Figure 4.13 (e) and (f)).

4.2.2 EPI samples: Waveguide Etch Tests

Before the actual laser device fabrication, the PAW etching with high power laser as a source is tested with prepared samples (EPI and M1) following the fabrication steps in Figure 4.2 using the Initial-Mask. The laser fabrication uses two PAW etching steps – one for the waveguide and another for the mirrors (Figure 4.2 (b) and (c)). This section tests the waveguide etching step using the EPI sample. The waveguide mask designed in this work has a metal layer for contacts and PR covers the metal contact for reducing lateral etching at the waveguide edge as well as to protect the mirror pattern. From the LED-PAW experiment, etching an EPI sample with the metal-PR mask should provide vertical side profiles with low lateral etching.

Figure 4.14 presents the waveguide etch mask for the laser fabrication. The Initial-Mask for waveguide etching includes serpentine waveguides, ridge-waveguide lasers and TIR (total

internal reflection) laser patterns. The wafers are designed so as to leave approximately 2mm of space at the top part of the surface for the reflectometer probe beam; the device patterns are placed in the lower part of the sample as presented in the Figure 4.14 (a). PR covers part of the blank area to reserve reflectometer probing area for a subsequent mirror. The PR mask protects the mirror pattern. Figure 4.14 (b) shows more details of the ridge-waveguide pattern near the mirror area. To remove lateral etching and possible misalignment, the PR layer overlaps the metal contact by $2\mu\text{m}$.

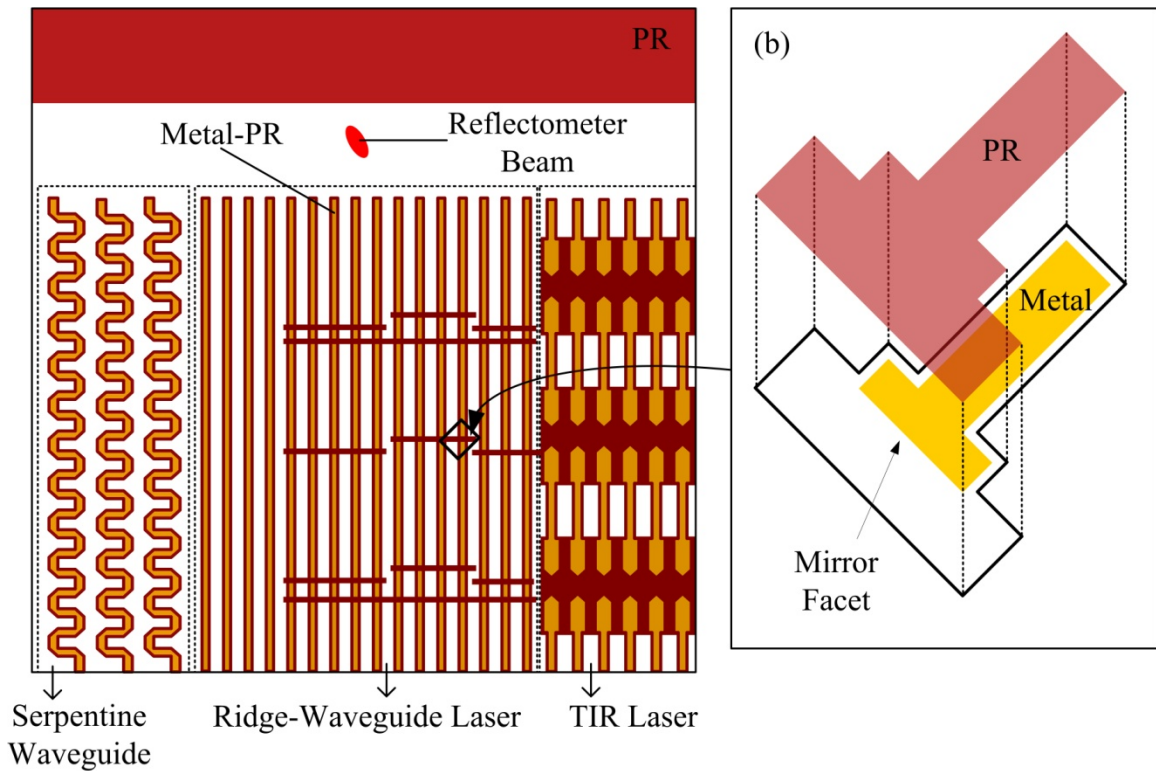


Figure 4.14 Initial-Mask for waveguide: (a) Overall patterned sample and (b) details of ridge-waveguide pattern near the mirror pattern. A sample includes three device patterns; Serpentine waveguide, ridge-waveguide laser and TIR laser. See Appendix E for details of ridge-waveguide pattern.

As a first test, the PAW system etches through the active layer while monitoring the PL (measured from PD and CCD) and surface conditions (using the reflectometer). Figure 4.15

shows the PL measured from the PD and the reflectometer signals for the EPI samples with the corresponding CCD images. The PL remains low in the n-type layers until the etching reaches the n-AlGaAs layer. At the interface, the PL intensity starts to increase at the center of the patterned area and decreases again as it reaches the n-AlGaAs layer (Figure 4.15 (b) and (c) during the period B). At the n-AlGaAs layer, the reflectometer signal intensity drops. The PL starts to increase near the end of the n-AlGaAs layer and reaches the maximum intensity at the interface of the n-AlGaAs and active layer (Figure 4.15 (b) and (c) point C and period D). This time, the blank area also starts to emit PL. After the interface, the PL intensity starts to decrease again (Figure 4.15 (b) and (c) period D).

The reflectometer determines the depth, rate and roughness by reflecting the probe beam from the upper blank area and the results must be extrapolated to apply in the patterned areas. The almost flat signal at the interface of n-GaAs and n-AlGaAs indicates that the etching becomes very slow at the interface (Figure 4.15 (a) between 53sec and 140sec).

The etch is stopped after the active layer which correspond to about $2\text{ }\mu\text{m}$ of etch depth based on the layer structure of the EPI sample (Figure 4.8 (b)). In this case, the etch rate calculates to be about $0.33\text{ }\mu\text{m}/\text{min}$. The profilometer measurement, however, shows a different etch depth at the patterned area. It etches about $4.80\text{ }\mu\text{m}$ at the patterned area (etch rate about $0.71\text{ }\mu\text{m}/\text{min}$). The profilometer measures a deep trench at the edge of the PR layer with a depth of about $4.86\text{ }\mu\text{m}$ which is approximately the same as the etch depth at the patterned area. The reflectometer signal only determines the etch depth at the probed region at the upper blank area of the sample (Figure 4.14 (a)). It is most likely that the etching reaches the active layer when the first bright PL is observed at the center of the patterned area. The PL could be expected to show the maximum intensity at the active layer interface due to efficient carrier recombination at the Quantum Wells (Q.Ws).

In this experiment, the reflectometer signal does not show any fringe patterns after the n-GaAs layer (the first layer). This indicates a rough surface condition during the etching or

misalignment of the reflectometer probe beam. The reflectometer signal in Figure 4.15 (a) does not represent a standard signal of the EPI sample during the high power EPI sample. Some of the EPI samples prepared under the same condition show slightly different signal as shown in the Figure 4.16

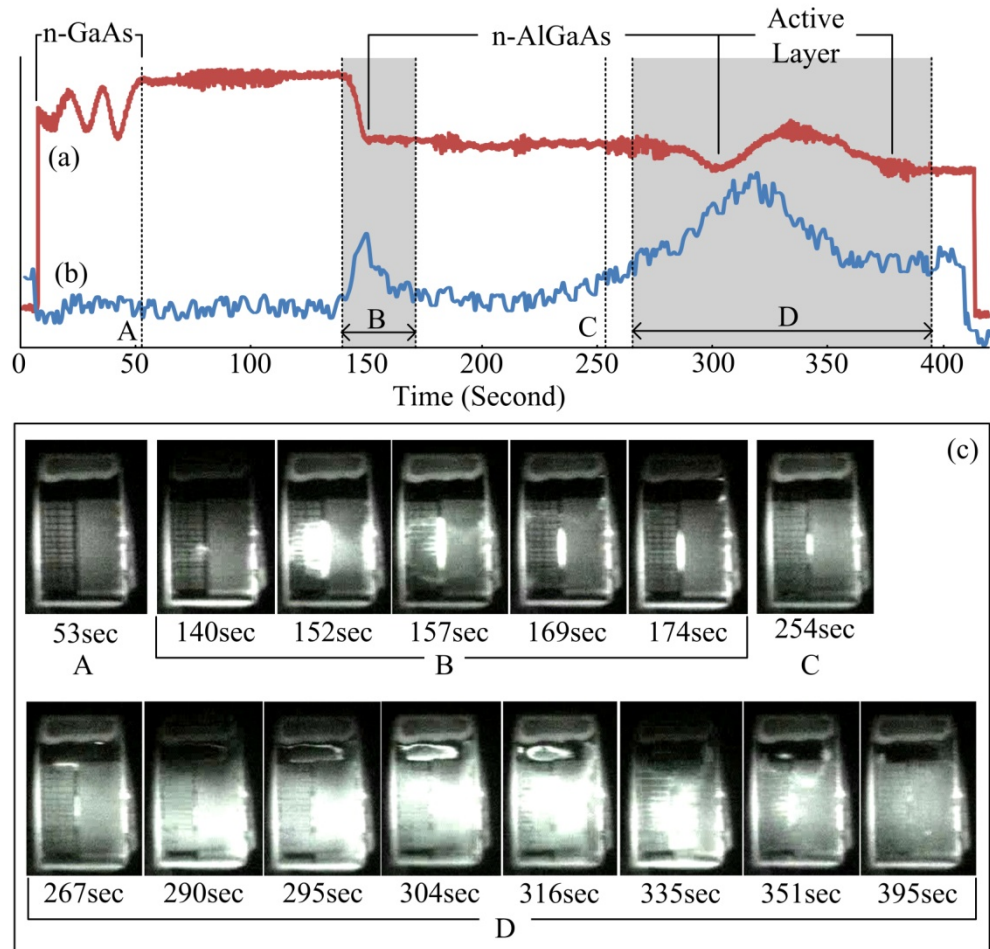


Figure 4.15 (a) Reflectometer and (b) PL signal measured using PD for EPI material etched with high power green laser ($P_{PAW} \sim 100\text{mW}$). (c) shows corresponding CCD images of the sample. For size reference, the thin strip in the center is about $100\mu\text{m}$ wide.

In Figure 4.16, the reflectometer signal shows the fringe patterns in the n-AlGaAs. Unlike to the reflectometer signal in Figure 4.16, the fringe pattern shows an etch delay at the n-GaAs and n-AlGaAs interface not a flat signal. In case the probe beam aligns to the edge of the PR, the

reflectivity becomes very low as the etching continues and does not show any fringes. The etch tests are repeated with same condition and material with the experiments for Figure 4.15 but better alignment of the reflectometer probe beam. Both cases show about same PL signal for the sample from both the PD and CCD camera.

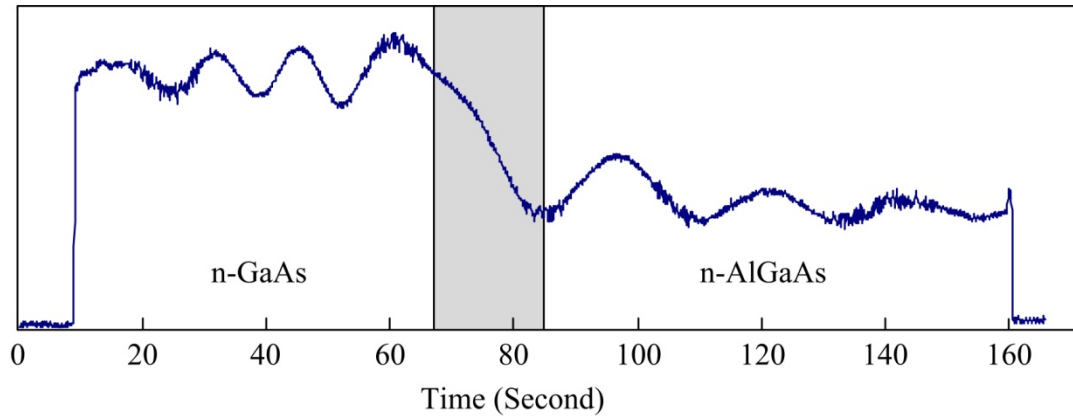


Figure 4.16 Reflectometer signal of waveguide masked EPI sample with high power PAW laser ($P_{PAW} \sim 100\text{mW}$). Gray color boxed region shows etch rate delay at the n-GaAs and n-AlGaAs layer interface.

From both reflectometer signals in Figure 4.15 and 4.16, the etch depth monitored at the blank surface does not match to the actual etch depth of the pattern with high power laser. The reflectometer signal of EPI sample in the Figure 4.16 has only about 7 fringes corresponding to an etch depth of approximately $0.7\mu\text{m}$ until the etch is stopped. However, the profilometer measures about $1.9\mu\text{m}$ at the patterned area that matches the depth of the active layer.

The PAW etched side profile of the waveguide patterns looks as expected from the LED-PAW etching of EPI samples that have small lateral etching and a steep sidewall (Figure 4.17 (a)). High power UV and green LED-PAW etching achieves low lateral etching and steep sidewall using silica-metal-PR (type 3) masked EPI samples (Figure 3.11 (g)). The waveguide mask does not have a silica layer but still achieves steep sidewall and less lateral etching for the EPI sample.

PAW etching improves the side profile using a metal-PR mask (Initial-Mask for waveguide) as expected from LED-PAW etching in Chapter 3.

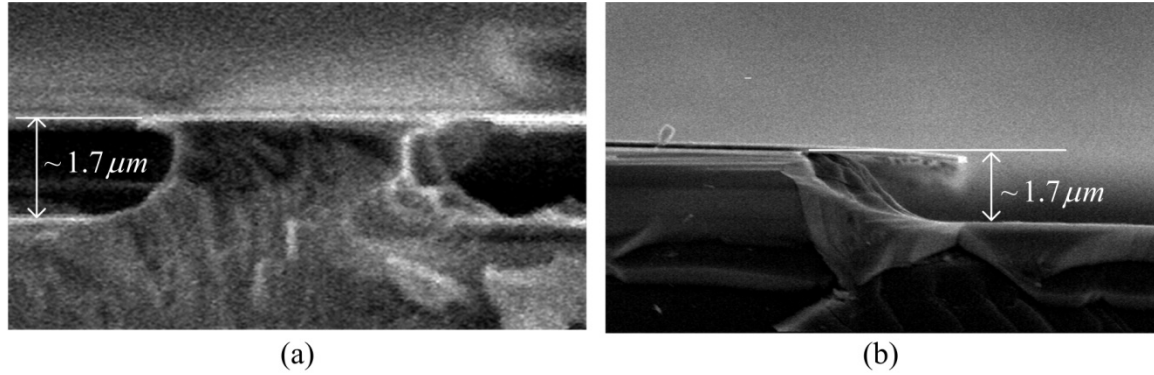


Figure 4.17 Waveguide etched side profile of (a) EPI with high power green laser PAW ($P_{PAW} \sim 100mW$) and (b) dark.

From the previous PAW etching of the EPI sample using the Initial-Mask for the waveguide, one can conclude that the system dissolves the material faster near the metal-PR patterned area than the blank area (reflectometer probed area). In the blank area, the etch rate decreases about 46% while the etch rate increases about 19% in the patterned area (that is, $R_{VR} \sim 46$ for reflectometer probed area and $R_{VR} \sim 19$ for the patterned area). Even though the etch rate shows differences between the reflectometer probed area and the patterned area, the PAW etching of the waveguide patterns present uniform etch rate within in the patterned area. The line patterns in the middle area and serpentine waveguide patterns (Figure 4.14 (a)) at the left side have etch rate differences within 1.4%

The post-etched surface shows clear interference patterns on the EPI sample surface especially near the mask pattern (where it etches faster) as seen in Figure 4.18. These interference patterns more often occur in the n-type material since it has the greater sensitivity to the PAW illumination compared with the p-type material. Once the pattern is generated at the top layer, wet

etching tends to maintain the pattern. These diffraction/interference patterns were found to be primarily due to imperfections and particulates on the clear etch vessel or lenses.

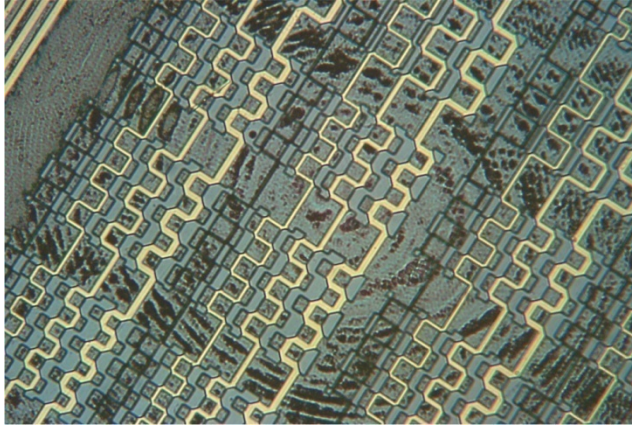


Figure 4.18 Microscope picture of the post-etched serpentine waveguide pattern of EPI sample with laser PAW etching ($P_{PAW} \sim 100\text{mW}$). The width of the figure corresponds to approximately 1.7 mm.

It would not be appropriate to monitor the etch depth using a tightly-focused reflectometer beam due to the non-uniform etch depth shown in above examples (Figure 4.15 and 4.16). One could estimate approximate stopping points for laser fabrication from the PL image since the PL intensity suddenly changes just before the active layer. The PL intensity increases near the active layer during the PAW etching of EPI sample (Figure 4.15). However, PL does not provide as high a resolution as the reflectometer. For more precise control of etch depth, it is necessary to improve the reflectometer signal for PAW etching.

In the waveguide etch test, PAW etching shows non-uniform etch rate over the sample surface. The surface charge or surface currents might cause the etch depth variation. If this is the case, the arrangement of the mask pattern (size and the position of the blank area) and the type of masking materials affects the PAW etching. The present research tests several different mask patterns. As a simple test, the blank regions on the left and right sides of the patterns (serpentine waveguide and TIR laser patterns in the Figure 4.14 (a)) are given different masking conditions: (1) both sides covered with PR (Both-PR), (2) most of the both side left as blank with some PR-

only patterned serpentine waveguide and TIR laser without metal contacts (Both-Blank) and (3) metal deposited on the both side of the sample (Both-Metal).

4.2.2.1 Result from Both-PR Mask for Waveguide Etching

A reflectometer signal derived from a portion of the sample away from the metal structures does not correlate well with the actual etch depth of waveguide pattern. Instead of the reflectometer, the PL image from the CCD camera can be used to estimate etch depth and thereby stop the etching of the waveguide. For EPI samples (n-type layer above the active layer), the etch is stopped when the PL intensity grows based on the CCD image.

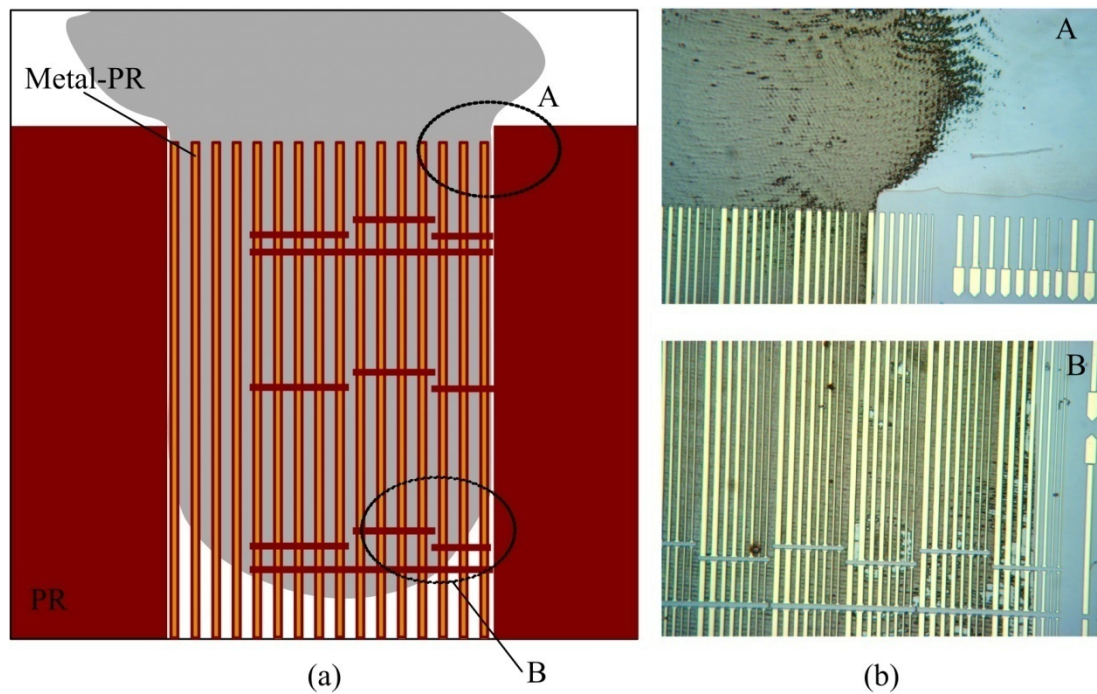


Figure 4.19 (a) Both-PR case surface condition after waveguide etching and (b) corresponding microscope pictures of positions A and B. Pictures A and B span an approximate horizontal distance of 1.3mm.

Figure 4.19 shows (a) the overall post-etched surface condition when both sides of the waveguide mask pattern are covered with the PR-pad and (b) the microscope pictures of two

regions on the sample. Using the Both-PR mask, large un-patterned PR pads covers on both sides of the waveguide pattern. As an insulator, the PR prevents charge from transferring to the solution. Near the center of the wafer, the PAW etching achieves the desired depth at the patterns (gray colored area in the Figure 4.19 (a)) while at the edge of the top blank area and near the PR pads (white colored area in the Figure 4.19 (a)) the etch produces shallow depth. The grey and white colored areas in Figure 4.19 (a) represent deep etching with rough surfaces and shallow etching with clean surfaces, respectively. The microscope pictures of the post-etched surface in Figure 4.19 (b) show interference patterns produced by the laser on the deep etched surface at the top and bottom of the patterned area (position A and B in the Figure 4.19 (a)).

After etching for 177sec, the patterns near the center etch uniformly ($\sim 1.76\mu\text{m}$) but, under optical inspection, the samples have rough surfaces whereas patterns near the edge with the PR-defined mesa regions etched shallower (about $0.32\mu\text{m}$ and $0.35\mu\text{m}$) than the ones in the center area. The etch rate of the patterns in most of the patterned area increase by about 37% for 532nm PAW ($P_{\text{PAW}} \sim 100\text{mW}$) while it decreases by approximately 74% near the PR pad area (that is, $R_{\text{VR}} \sim 37$ for patterned area and $R_{\text{VR}} \sim -74$ for the area near the PR pads on both sides).

For the PAW etch tests with the original waveguide mask (Type IM) shown in Figure 4.14, the etching is inhibited near (but not throughout) the top blank area (reflectometer probe area). With the PR side-strips (Figure 4.19), the PAW etching promotes solid dissolution near the patterned area and some parts of the reflectometer probing area (the center of the reflectometer probing area). In Figure 4.19 (a), the grey area indicates faster etching produced by the high power PAW laser. The deep-etched area with the rough surface in the upper blank area suggests charge flow in direction of waveguide patterns. For the two cases using the Initial-Mask and the Both-PR mask, the PAW etching promotes and inhibits the material dissolution near the patterned and PR covered area, respectively. The excess electron (i.e., photo-electrons) generated under the PR layer diffuse toward the blank area and slows the etching process near the PR area. At the patterned area in the center of the sample, the etch rate increases by transferring the electrons

through the sample surface to the etching solution. The laser intensity at the sample edge is approximately 80% of the peak value at the center (refer to Table 4.2) that can contribute to limited diffusion of electrons to the edges. It is likely that the metal layer of the waveguide pattern promotes the etching by attracting the electron away from the surface exposed to the etching solution. Since photo-generation does not occur under the metal layer (dark area), the patterned layer also has fewer electrons than the PR covered area.

4.2.2.2 Result from Both-Blank Mask for Waveguide Etching

From the previous tests with a sample mostly covered by PR (Both-PR mask for waveguide in Section 4.2.2.1 above), the PAW etching of the EPI sample inhibits near the PR covered side-strips. With the PR mask, photo-carriers can accumulate underneath the mask since the photo-generated charges cannot be consumed by the etching solution there. In the patterned area, the metal layer underneath the PR can dissipate excess electrons from the sample surface and leave more holes to accelerate the dissolution rate. To see the function of the exposed surface to the etching solution, both sides of the sample except the laser patterns in the middle area are left as blank so as to leave most of the sample surface exposed to the etching solution (Both-Blank mask for waveguide, see exposure percentages in Table 4.1). Some of the PR of the serpentine waveguide and TIR laser patterns on the left and right side of the laser patterns are unintentionally deposited due to difficulty with the photolithography process. A portion of the narrow metal pads at the bottom of the wafer do not have PR in order to promote electron consumption in the etching solution. Figure 4.20 shows post-etched sample surfaces for this case. In contrast to the Both-PR mask case shown in Figure 4.19, patterns around the center of the sample produced by the Both-Blank mask have smoother post-etched surfaces and shallower etches than along the edge (Figure 4.20). The dark patterns appear on the edge of the waveguide-patterned area and on the edge of the sample (Figure 4.20 (a)). The dark area has slightly different characteristics from the previous experiments using Both-PR masks. With the Initial-Mask

(Figure 4.14) and Both-PR mask for waveguides (Figure 4.19), the dark area occurs in the region containing the interference pattern on the sample surface but the PAW process does not deposit any other substance there.

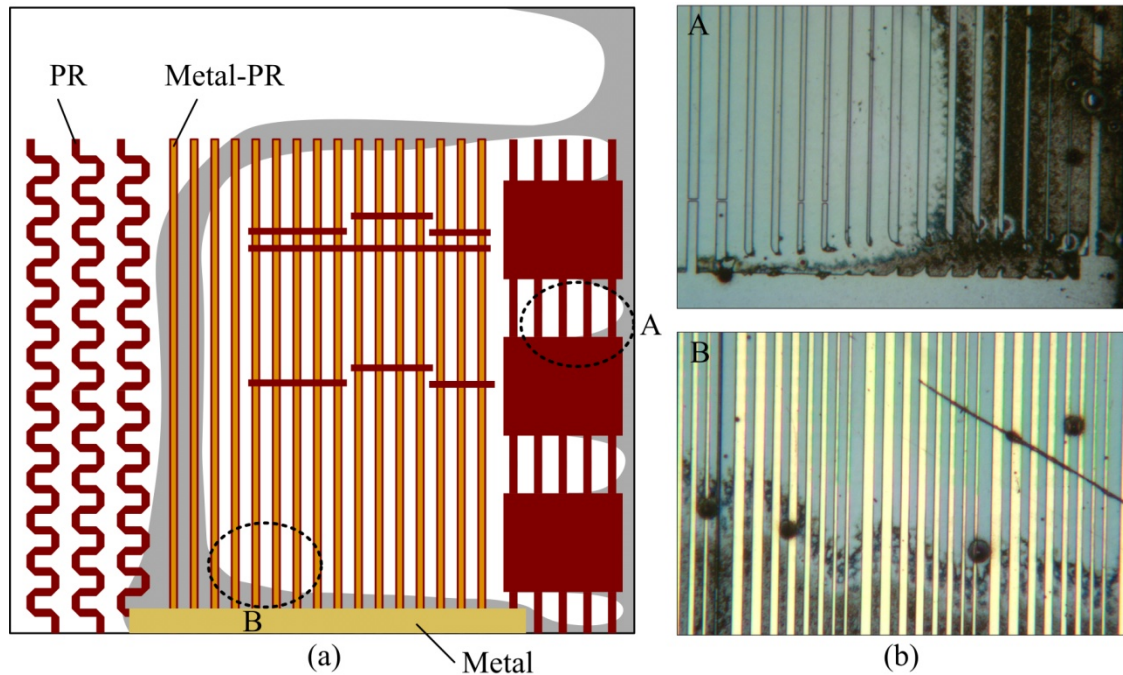


Figure 4.20 (a) overall illustration of the post-etched surface of EPI samples and (b) microscope pictures of area A and B. Both-Blank mask but with some PR patterns in the side strips. The horizontal width of the Figures A and B span approximately 900 μm

In the present Both-Blank case, however, the dark area shows both a rough surface due to the interference patterns and a dark colored material that could only have originated from a PAW deposition process (Figure 4.20 (b) A). The overall etch rate measures higher than for the Both-PR case. The etch rate reduces slightly from the dark rate in the clean surface areas (etch rate about 0.57 $\mu\text{m}/\text{min}$). In the rough surface area, especially for the patterns near the bottom metal pad, the etch rate increases to 1.04 $\mu\text{m}/\text{min}$. The relative vertical etch rate, R_{VR} , calculates to about -5 and 74 at the patterns in the clean and rough surface, respectively. Near the center, the etch rate is slightly lower than dark etched case but shows clean surface condition. The PR-only

area in the both side of the sample has a slower etch rate than the clean surfaced patterned area ($R_{VR} \sim -16$).

The PR patterned area (Both-Blank mask) shows lower etch rate than the dark etching since electrons still accumulate near the PR pattern. In the laser patterned area (with metal-PR mask in the center), the etch rate near the bottom metal pads measures higher than other parts. Electrons drifting to the metal layer can be consumed more effectively by transferring through the metal pad to the etching solution. The electrons transfer to the etching solution directly through the metal layer when produced under the PR on the metal layer (which is exposed to the solution near the bottom of the pattern). From the experiments with different sizes for the blank surface (Both-PR and Both-Blank cases), patterns near the metal-only layer have higher relative etch rate than the masked area (metal-PR mask) and PR prohibits etching in the vicinity of the mask. The results suggest that the metal layer plays an important role to vary the etch rate with high power laser.

4.2.2.3 Result from Both-Metal Mask for Waveguide Etching

From the PAW experiment in Figure 4.19 and 4.20 in the previous two sections (Section 4.2.2.1 and 4.2.2.2), the etch rate decreases near the PR and increases near the metal. For the PAW etching, the holes increase the etch rate. For promoting solid dissolution, it is necessary to increase hole concentration at the surface and remove electrons since excess electrons inhibit solid dissolution. Since the etch rate with high power illumination on the surface depends on the electron consumption on the surface, wide PR layers can be a hurdle for the process since PR, as an insulator, prevents electron transfer from the surface to the etching solution while as a transparent material, the PR covered layer still generates electron-hole pairs under illumination. In contrast, electrons transfer to the etching solution through the metal mask. To see the metal effect in the PAW etching, metal pads are deposited on both sides of the EPI sample as seen in Figure 4.21 (a) (Both-Metal mask). For the present tests, the PR waveguide patterns (serpentine

waveguides and TIR laser patterns on the left and right side of the sample) remain under the metal pads (due to the difficulty of removing the pattern completely) and the metal pad at the bottom connects the metal layers on both sides of the sample (see the lightly shaded pad at the bottom of Figure 4.21 (a)).

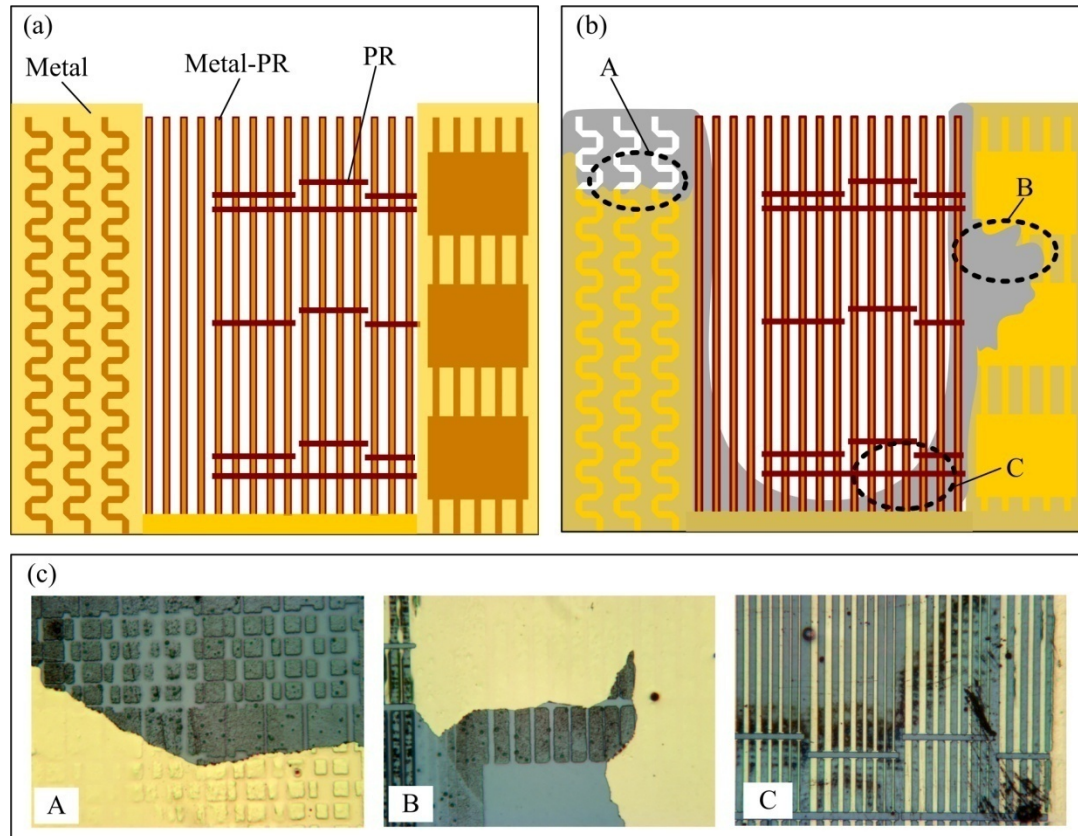


Figure 4.21 Both-Metal sample surface of EPI sample with both side metal covered waveguide pattern (a) before etching, (b) after etching and (c) microscope pictures of corresponding areas. Picture A shows rough surface and rough metal after etching. Figure C spans a horizontal distance of approximately 0.9mm based on the largest width waveguide of 20 μ m.

After etching, a rough surface appears around the edge of the metal pads (Figure 4.21 (b)) with greater etch depth than the smooth area in the center. The etch rate at the clean and rough surfaces measure about 0.5 μ m/min and 1.0 μ m/min, respectively. The relative vertical etch rate

R_{VR} calculates to about -10 and 72 at the patterns in the clean surface area in the center and the rough surface area near the metal pads, respectively. The etch rates are about same as for the Both-Blank case ($R_{VR} \sim -5$ and 74 for the center and edge of the patterned area). From the experiments, it is shown that the etch rate increases only in the vicinity of the metal layer. The etch rate around the center area measures about the same as for the previous experiment when both sides of the sample only have PR patterns and leave most of the sample area blank.

The experiment presents very interesting results for the Both-Metal mask for the waveguides (refer to Figures 4.21(c) A and B). Here the side-strips have waveguide patterns made of photoresist. The patterned PR is left in place and metal is deposited over the side strips. The resulting structure at the side-strips consists of semiconductor underneath patterned PR, which in turn, is underneath a metal layer. Before etching, the metal contour conforms to the PR pattern but the metal forms a smooth continuous sheet. After etching, the pattern of the PR transfers to the metal layer in that the edges become pronounced and metal over unmasked regions becomes rough (see especially Figure 4.21(c) A). The metal surface looks smooth in those regions with PR underneath and it looks rough where there isn't any PR underneath. After etching, some portions of the metal are detached from the surface (see Figures 4.21(c) A and B). The surface underneath the metal looks corroded (i.e., rusty) when viewed through an optical microscope (Figure 4.21 (c)-A). The rusty surface at the metal pad suggests charge transfer through the metal layer from the solid to the etching solution or vice versa when there is no PR layer to block the charge transfer underneath the metal layer.

4.2.2.4 Summary for Waveguide Etch Test of EPI

This section reviews the etch characteristics of EPI samples with waveguide patterns. The laser-PAW etching does not directly agree with LED-PAW etching from Chapter 3. With the Initial-Mask implemented using metal-PR for waveguides (Figure 4.14), the etch depth of the sample is not uniform. The material dissolves faster at the patterned area than at the reflectometer

probed area. It is difficult to determine the actual etch depth at the laser patterns using the reflectometer monitor due to the etch depth difference between the probed-area and the pattern area. As an alternative, PL monitoring can be used as a etch depth monitor since PL intensity increases suddenly at the cladding and active layer interface. The waveguide etching using the Initial-Mask has suitable etch characteristic for optical devices (such as vertical sidewall and suppressed lateral etching as seen in Figure 4.17); however, this mask and corresponding fabrication process does not precisely control the waveguide etch depth due to the non-uniform etch depth. For laser fabrication, not only the side profile but also the etch depth of the waveguide is one of the important factors that determines device performance and related parameters [67]. Further study on the reflectometer and PAW etching is necessary for the practical application.

It is possible that the active layer impedes the transport of charge toward the substrate and causes the PL intensity changes when the etching surface is near the active layer. In addition, the backside insulating glass slide ensures backside electrical isolation. Therefore, most of the photo-charge contributes to the solid dissolution process and it is important to control the charge at the surface to promote or inhibit solid dissolution for laser material. By changing the Initial-Mask slightly, one can test different masks for the effect of surface charge on the PAW etching as follows. First, the left and right side patterns (serpentine waveguide and TIR laser patterns in the Figure 4.14 (a)) are eliminated and then three different surface conditions are applied: (1) PR covers both side strips (Both-PR), (2) most of the side-strips left unmasked (Both-Blank) but with limited PR patterns (3) metal layers deposited on the side strips (Both-Metal) but some PR patterns remain underneath. Figure 4.22 compares the relative vertical etch rate (R_{VR}) at different sample positions (reflectometer monitored area at upper blank, center of the patterned and edge of the patterned area) for different masks (Initial, Both-PR, Both-Blank and Both-Metal mask).

With the Initial-Mask for waveguides, etch inhibition occurs near the reflectometer probed area (near the PR pattern) while the patterned area etches slightly faster than for dark conditions (Figure 4.22(a)). When PR covers the side-strips (Both-PR mask), those regions of the

EPI sample near the side-strips etch slower than the Initial-Mask case while the patterned area near the center etches faster (Figure 4.22 (b)). Compared to the dark etching, the PAW etching increases the etch rate by about 37% in the center while it decreases the rate by about 74% near the PR covered area. Illumination generates electron-hole pairs under the PR covered area and at the bare surface exposed to the etching solution. Since the electrons cannot be consumed in these regions they could diffuse toward the patterned area. The excess electrons inhibit etching around the PR area.

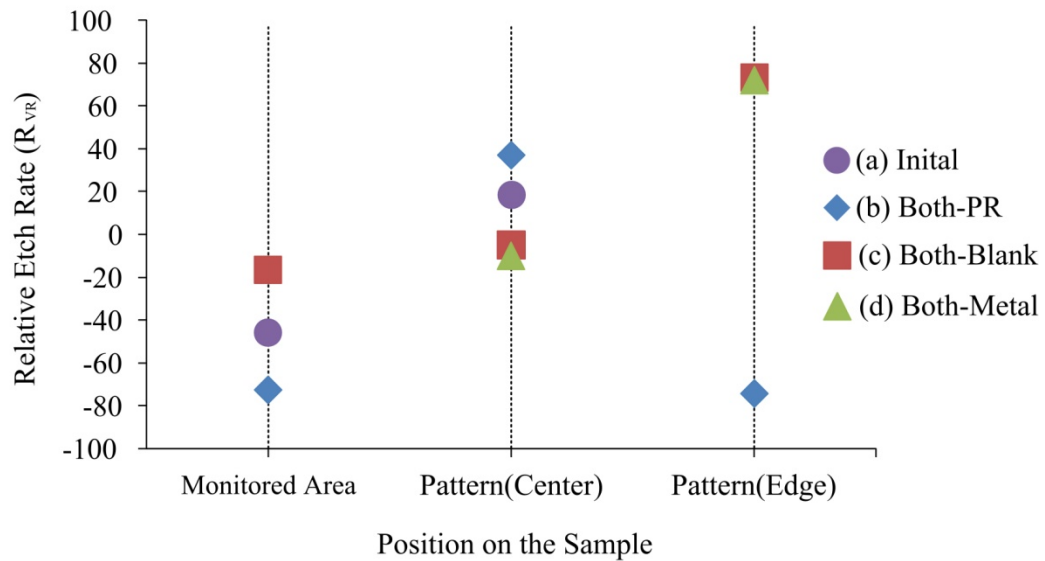


Figure 4.22 Relative vertical etch rate (R_{VR}) variation of the patterns depends on the conditions at the side strips: (a) with Initial-Mask for waveguide, (b) Both-PR (PR covers both sides of the waveguide pattern), (c) Both-Blank (most of the side area leaves as blank) and (d) Both-Metal (metal layers area deposited on the both side of the sample).

Figure 4.22 (c) presents the relative vertical etch rate (R_{VR}) of the EPI sample with the side-strips mostly blank (Both-Blank) as seen in the Figure 4.20. PR-only serpentine waveguides and TIR patterns remain on each side (Figure 4.20) due to the difficulties with the processing. Unmasked metal patterns are exposed to the etching solution at the bottom and along the edge of the sample. In contrast to the case when both sides are covered with PR, the etch rate slightly

decreases at the patterned area in the center ($R_{VR} \sim -5$) and increases at the part of the patterned area near the metal at the bottom and edge of the sample ($R_{VR} \sim 73$). The PR patterns on both sides of the sample show lower etch rate than patterns in the center area with the metal-PR masks ($R_{VR} \sim 16$).

When both side of the sample are covered with metal (Both-Metal), it shows similar etch characteristics to the Both-Blank case (Figure 4.21 (c) and (d)). Patterns in the center etch slower ($R_{VR} \sim -10$) than the ones near the edge ($R_{VR} \sim 72$). The results from Both-Blank and Both-Metal cases suggest that the metal layer on the sample has similar function as the blank surface in the PAW etching system. The electrons can easily transfer from the solid to the etching solution through the metal contact layer. The only difference is that the metal layer blocks the illumination and prevents photo-carrier generation under the mask. For all cases, the enhanced-etching region shows rough surfaces with interference patterns while the inhibited-etching region shows a clean surface.

4.2.3 EPI samples: Mirror Etch Test

For fabricating lasers with etched mirrors, the present process uses two steps. The first step forms the waveguides and the second forms the mirror facet. The mirror etching is the most important step in the fabrication of the laser. From the LED-PAW experiment, it is expected to obtain a vertical sidewall profile by using a silica-metal-PR (type 3) mask for the EPI sample (Figure 3.11 (g)). For the laser-PAW process, metal-PR masks are used for the simplicity of the laser fabrication step. Different light sources and masks may produce variations in the etch characteristics. The waveguide etch experiments in Section 4.2.2 show that the laser-PAW inhibits the etching near the PR mask for the EPI sample. This can be a problem for the mirror etching if the mirror mask is designed to have very small windows to define the mirrors since then most of the sample would be covered with PR. Figure 4.23 shows such an Initial-Mask designed for the mirror.

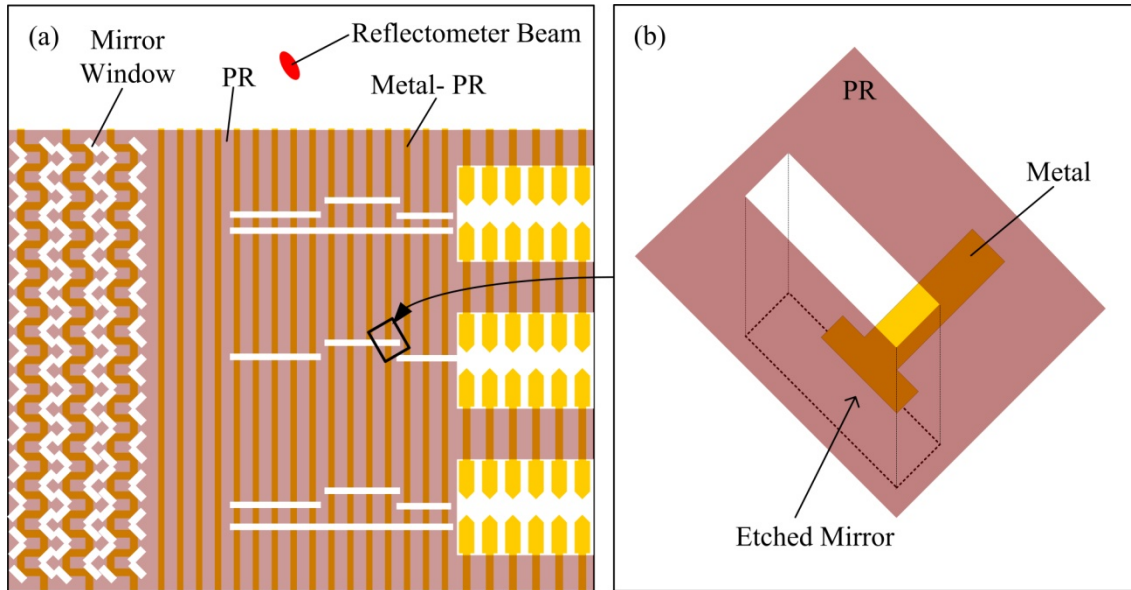


Figure 4.23 Initial-Mask for Mirror etch (a) overall sample illustration and (b) mirror window pattern at the etched mirror side of the ridge-waveguide laser.

The design in Figure 4.23 includes a PR mask to cover the waveguides for protection and it has a small opening for the etched mirrors. The mirror etching is performed after the waveguide etching according to the fabrication steps designed in Figure 4.2. Once the PR patterns for the waveguide are removed (after etching the waveguides) a second set of PR patterns are placed for the mirror window using photolithography. Figure 4.23 (a) and (b) illustrates the overall mirror pattern for the ridge-waveguide lasers. A tightly focused beam from the reflectometer is applied to the blank area in the upper portion of the wafer for etch depth monitoring of the mirror. However, due to the surface charge distribution and the resulting etch variations, the reflectometer signal does not provide the actual etch depth for this present case.

The PAW tests for the mirror patterns also present unexpected results as the waveguide etching in Section 4.2.2. While the reflectometer signal measures more than $1.5\mu\text{m}$ etch depth, most of the mirror wells etch very shallowly and the non-uniformity of the etch depth becomes more serious than for the waveguide etching using the Initial-Mask. The PAW etching conditions for the mirrors are identical to those for the waveguides except for the relative sizes of the

exposed and PR-covered areas of the sample. With the mirror patterns, more etch inhibition occurs near the patterned area than for the region probed by the reflectometer. It is clear that the laser-PAW process for the EPI sample inhibits the etching near the PR pattern and the PR covers most of the sample area for mirror mask.

The SEM pictures in Figure 4.24 shows a close-up view with greater detail on the mirror etching with high power PAW. The SEM picture of the post-etched mirror in Figure 4.24 (a) shows that etching stops at the mirror facet with the metal-PR mask (A in Figure 4.24 (a)) while the etching progresses near those regions covered with PR only (B in Figure 4.24 (a)) such as between the waveguide areas. In most of the sample area, the etching continues along the edge of the etch window and along the waveguide metal contact thereby resulting in large lateral etching and deep vertical etching near the waveguide. Some of the mirror patterns near the blank area (within on the order of $250\mu\text{m}$, although this represents only an average since etch deeper than the ones around the center (up to $3.6\mu\text{m}$ deep) as in Figure 4.24 (b) A; however, there is still large lateral etching ($3\text{-}4\mu\text{m}$) between waveguide patterns as in Figure 4.24 (b) B.

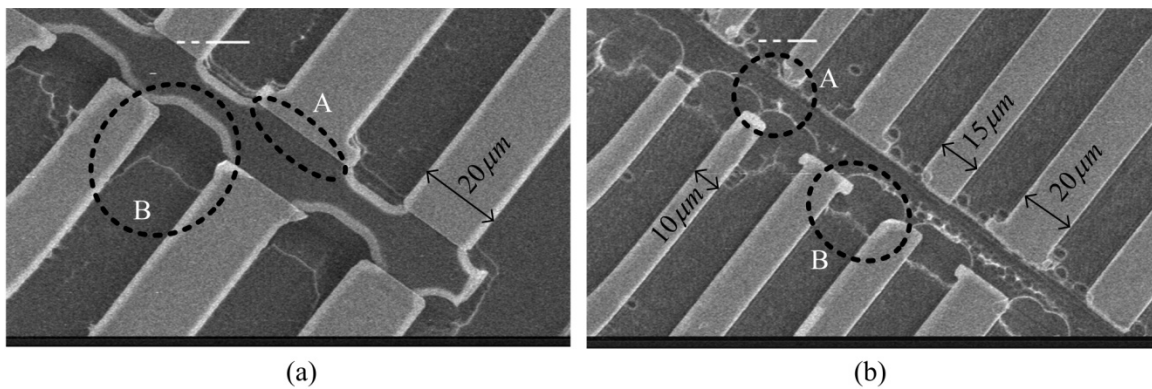


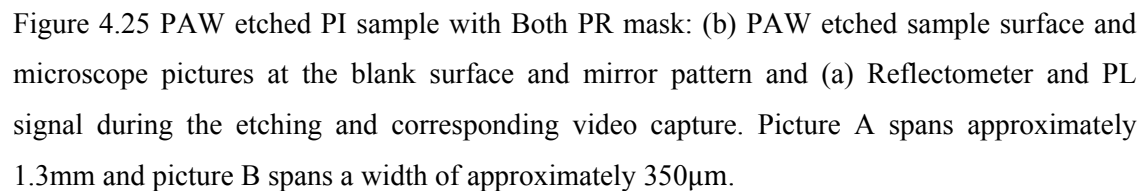
Figure 4.24 SEM pictures of mirror after PAW etching using the Initial-Mask with high power green laser for EPI sample. (a) mirror window pattern on the sample near the center of the sample and (b) patterns near the edge of the sample.

From the PL images, the PL in the center of the sample does not decrease but within roughly 1 mm of the sample edge (at the edge-strips) the PL extinguishes as etching continues which indicates that etching almost stops in the center after the active layer while at the edge-strips, the etch accelerates for the ‘high power’ green laser ($P_{PAW} \geq 70\text{mW}$). Since most of the patterned area is covered with PR, the area does not etch and since the PR is transparent to light, the electron-hole pairs generated under the PR recombined and emit light (PL).

In summary, the semiconductor dissolution stops at the center area of the mirror window near the end of the metal waveguide using the Initial-Mask in Figure 4.23. The etching proceeds for the exposed semiconductor between the PR-covered metal waveguide patterns. As shown in the waveguide etch tests, the non-uniform etching depends on the position of the pattern and the surface conditions near the pattern. For more study on the effects of the size of the blank surface and the material types, the patterns are only deposited in the center of the sample as done for the waveguide etch test in Section 4.2.2. The mirror etching shows different etch characteristics by the surface condition at the non-patterned area: (1) both sides of the sample covered with PR (Both-PR), (2) both sides of the sample left as blank (Both-Blank) and (3) both sides covered with metal (Both-Metal). The next sections detail the results for the three different mask types

4.2.3.1 Results for Mirror Etching Using Both-PR Mask

For the mirror etching using Initial-Mask, most of the surface is covered with PR but some metal patterns are exposed to the etching solution at the both sides of the sample as a part of TIR and serpentine mask design as shown in Figure 4.23. In this case, etch inhibition occurs at most of the mirror windows especially near the center area (Figure 4.23 (a)) and some of the mirror windows near the blank area etch deeper than the ones in the center area. For this reason and based on the results of previous experiments as discussed above, three different alternative masks (Both-Blank, Both-PR, Both-Metal) and the corresponding fabrication procedures are developed. The present section examines the effects of the Both-PR mask.



After the etching, the reflectometer probe area at the center area of the top blank area in Figure 4.25 (a) shows cleaner surface than the edge of the top blank area. At the edge, the sample surface appears to have dark colored substances deposited on it along with an interference pattern (Figure 4.25 (a)-A). The reflectometer probe area only shows interference patterns not the dark substances. With PR covering approximately 1mm on both sides (as measured from the edge of the sample), the mirror wells etched deeper than for previous cases with the Initial-Mask for the mirror shown in the Figure 4.23 (a). Interestingly, etch inhibition does not occur near the metal pattern unlike for the Initial-Mask case shown in the Figure 4.23 (a). Figure 4.25 (a) B shows a microscope picture of the post-etched mirror pattern. In contrast to the waveguide etch test in section 4.2.2, there is no etch inhibition observed near the PR pad when both sides of the sample are covered with PR. Mirror patterns near the center of the sample etch about $2.6\mu\text{m}$ deep ($R_{VR} \sim -5$) while the ones on the right side etch to the greater depth of about $3.4\mu\text{m}$ ($R_{VR} \sim 28$).

Figure 4.25 (b) shows the reflectometer signal, the PL signal and the corresponding CCD images during the etching. The reflectometer signal shows that etch rate decreases as etching continues at the probed area. The fringe height also decreases as etching continues which indicates the surface becomes rougher at the position of the reflectometer probe beam. Due to the poor quality of the fringes, it is difficult to estimate the etch depth from the reflectometer signal. One can assume that the active layer starts to etch near the point B in Figure 4.25 (b) since the reflectometer probe area starts to luminescence at that point based on the CCD image. From the increasing fringe spacing for the reflectometer signal and the PL measurement, the etch rate at the reflectometer monitored area decreases when the PL approaches its maximum intensity (plot I and II in Figure 4.25 (b)).

When both side-strips are covered with PR, the mirror etching conditions improve compared to the original mirror pattern. The profilometer measurement across the mirror well next to the waveguide contact shows a wider opening than the mirror well (see Figure 4.26). While the mirror patterns are designed to be $20\mu\text{m}$ wide, the profilometer measurement shows

etching also occurs just outside the $20\mu\text{m}$ region. It indicates the etching occurs underneath the PR.

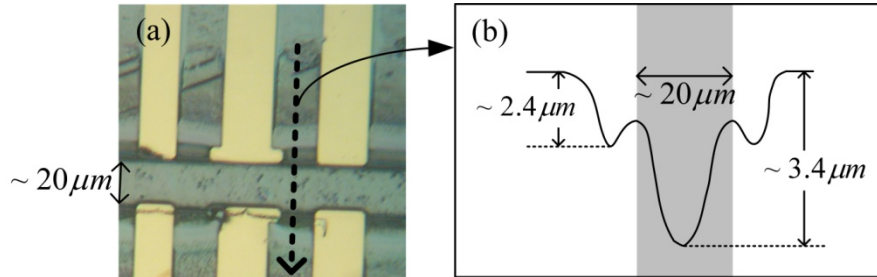


Figure 4.26 Etched-mirror profile for the EPI sample and Both-PR mask using high-power PAW laser. (a) and (b) shows scanning position on the sample and the profile across the mirror pattern, respectively. The arrow in (a) represent profilometer scanning and the grey area ($20\mu\text{m}$ wide) in (b) indicate the actual mirror area.

Both the Initial-Mask and the Both-PR mask cover most of the sample with PR but the Both-PR mask case produces mirror wells. The PAW process inhibits etching at the mirror pattern for the Initial-Mask in Figure 4.23 (a) while the sample with the Both-PR mask promotes mirror etching by 28% for the patterns at the edge and inhibits by 5% for the patterns in the middle area compare to the dark etching. The major difference for the cases is that for Both-PR, the waveguide metal-contacts for the laser are exposed to the etching solution (Figure 4.25 (a)), while the Initial-Mask only has metal exposed at the mirror well (Figure 4.23 (a)). The metal waveguides exposed to the etching solution for the Both-PR mask are also connected to the mirror pattern (as shown in the Figure 4.25 (a)) and can therefore directly affect the mirror etching due to the electron flow through the metal waveguide. There are also metal layers exposed to the etching solution for the original mirror pattern but the metal layers are part of TIR mirror patterns and not connected (through metal) to the mirrors on the laser pattern (Figure 4.23 (a)). For the Initial-Mask, the mirrors for the serpentine waveguides and TIR lasers do show higher etch rate than for the center laser patterns where the metal layer is exposed to the solution.

The fact that part of the metal waveguide pattern is exposed to the etching solution might help to dissipate electrons near the mirror pattern. The excess electron distribution generated near the mirror well can flow through the metal patterns. If electron charging near the mirror well is responsible for the etch inhibition, then exposing the semiconductor surface to the etching solution or having more metal exposed to the etching solution may increase the dissipation of the photo-electrons. By more effectively conducting the electrons away from the mirror pattern, one can expect to see greater etching in the area. The cases for when the semiconductor side-strips are exposed to etching solution and when they are covered with metal will be reviewed in the following sections 4.2.3.2 and 4.2.3.3.

4.2.3.2 Results for Mirror Etching Using the Both-Blank Mask

The Initial-Mask suggests greater exposure of the metal or the bare surface to the solution improves the etching performance. The present section investigates the effects of the bare surface. However, the situation becomes complicated by the fact that the surface layer affects the rate of photo-carrier production (such as for metal) and the ability of the surface to dissipate the charge (for PR) and introduces regions not exposed to the illumination that can increase the photo-electron diffusion to those regions. The work will require the full set of tests to sort out the effects.

To improve the mirror etching, both sides of the sample are exposed to the etching solution. Using the Both-Blank mask, laser patterns are only deposited in the center and most of the surface is left blank except for the PR mask for the mirrors (Figure 4.27 (a)). The reflectometer probe beam is applied to the upper blank area of the sample. Lower parts of the waveguide metal layers are exposed to the etching solution to promote electron consumption from the mirror wells.

Figure 4.27 (a) shows the overall sample outline and related microscope pictures of post etched sample. Rough surface patterns are generated on the blank surface. A dark-colored layer appears to be deposited around the patterned area and divides the blank region into two parts. The

mirror etching characteristics are similar to the Both-PR cases shown in Figure 4.25 except here, the mirror wells etch deeper.

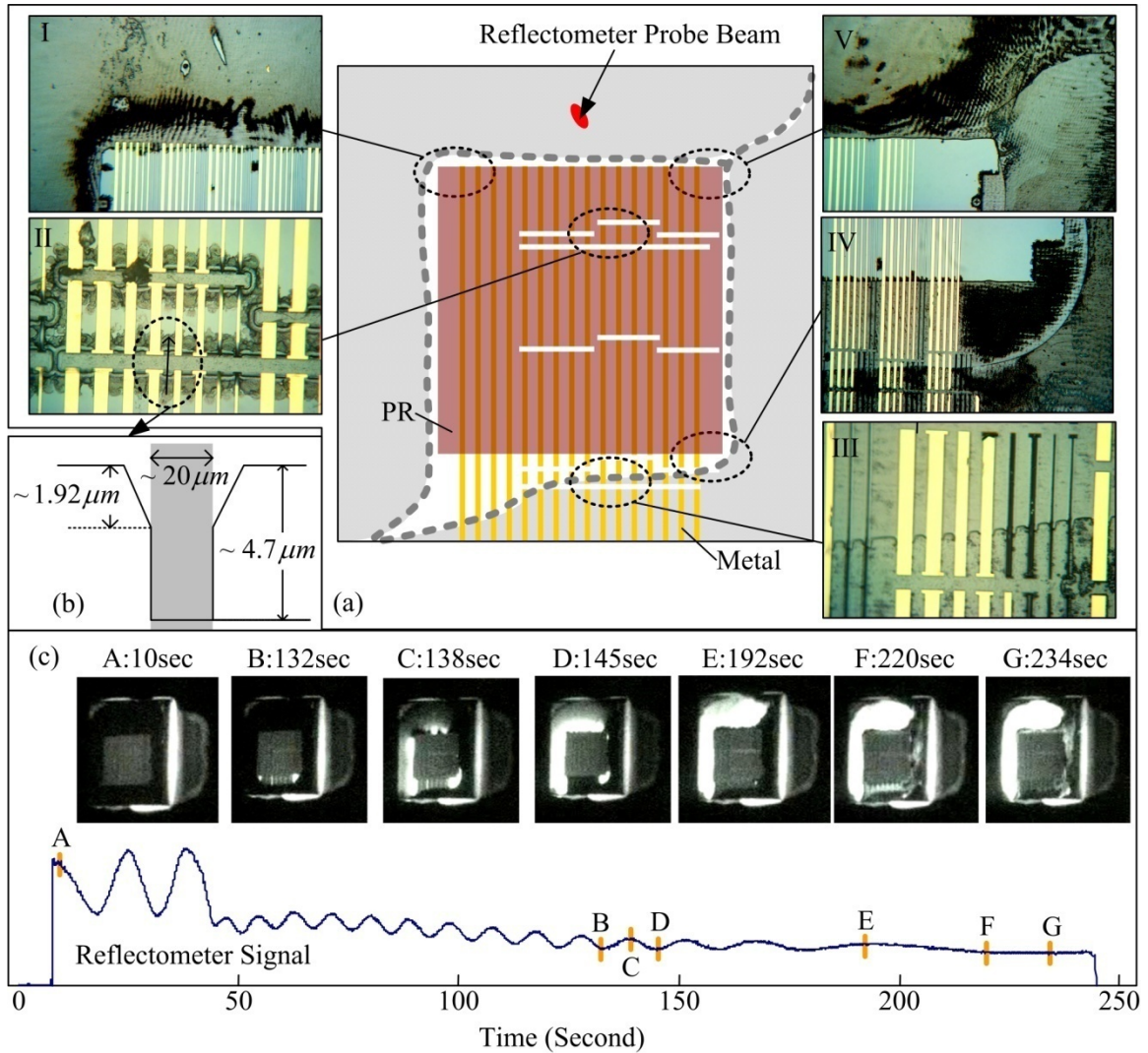


Figure 4.27 PAW etch results for the EPI sample with the Both-Blank mask: (a) Reflectometer signal during the etching and corresponding video capture, (b) PAW etched sample surface and microscope pictures of five different areas on the sample and (c) simplified profilometer profile across the mirror pattern. The grey area in (b) represents the actual mirror area. Pictures I, IV and V span a horizontal distance of approximately 1.3mm and II and III span a horizontal distance of 400 μm .

Most of the mirror patterns deep-etched to about $4.74\text{ }\mu\text{m}$ for these samples that have low PR coverage (etch rate $\sim 1.2\text{ }\mu\text{m}/\text{min}$, $R_{VR} \sim 101$). Similar to the profilometer measurement of the Both-PR case shown in the Figure 4.26 (b), a Dektak profilometer measurement shows the well is wider at the top and that the etching starts outside the designed mirror window (Figure 4.27 (b)). The etching actually occurs underneath of the PR mask to a depth about $1.92\text{ }\mu\text{m}$. The etch rate reduces about 18.7% compared with the dark etching ($R_{VR} \sim -18.7$) at the mirror well. The metal-only lines exposed to the etching solution at the bottom of the pattern (Figure 4.27 (a) III) has about 95% higher etch rate than for dark etching ($R_{VR} \sim 95$).

The reflectometer shows similar signals as for the Both-PR case in Figure 4.25. Based on the reflectometer signals shown in Figure 4.27 (c), the etch rate decreases as the etch depth approaches the active layer (the fringes become wider). However, in the patterned area, the etch rate differs from that in the probed region. The etch rate in the probed region decreases (fringe width increases) when the PL increases there (from Figure 4.27 (c) point C). The mechanical profilometer shows that the actual mirror wells etch much deeper than the depth indicated by the optical monitoring at the edge. From the CCD images, the left side of the sample photoluminance before the right side, which can be interpreted as due to different etch rates. From the previous PAW etching of EPI samples, PL typically starts near the active layer which means that the left side etches faster than right side of the sample. PL measurements from the CCD images agree with the post-etched sample surface condition and etch depth differences.

Figure 4.28 compares high power PAW ($P_{PAW} \geq 70\text{mW}$) and dark etching at the mirrors. After high-power laser-PAW etching with the Both-Blank mask, most of the mirror wells are etched deeper than for dark etching. From the microscope picture shown in Figure 4.28 (a), the high-power PAW etched sample clearly shows that the dark lines follow the waveguide metal contact. The dark lines (for example in Figure 4.28 (a) circled area A) along with deep vertical etching indicate that the etching continues toward the waveguide metal patterns which are

protected by the PR mask (Figure 4.28 (a)). Dark etched mirror pattern shows isotropic etch character with large lateral etching.

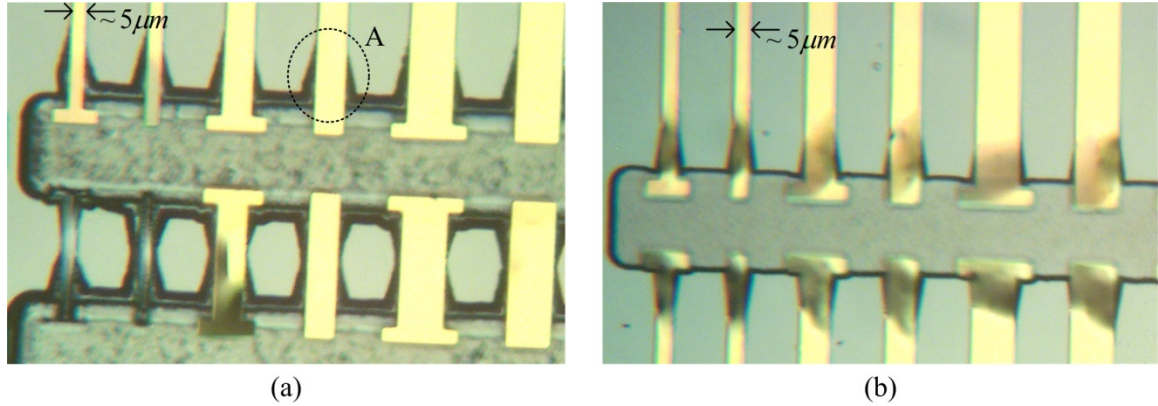


Figure 4.28 Microscope pictures of mirror patterns with mostly exposed EPI sample after (a) PAW etching and (b) dark. ($P_{PAW} \geq 70\text{mW}$). The scale is set by the waveguide width; the widest waveguide is $20\mu\text{m}$.

4.2.3.3 Results for Mirror Etching Using the Both-Metal Mask

Previous experiments show the effect of (i) metal connected to the laser contacts and (ii) PR layers. To more fully investigate the effects on the PAW etching, consider the mirror etching tests with metal pads deposited on the side strips as illustrated in Figure 4.29 (b).

After etching, the metal pads look corroded and some of them peel off (Figure 4.29 (b) D). Rough patterns are generated at the bottom of the etched region and around the edge of the top blank area. From the waveguide etching using the Both-Metal mask in Figure 4.21 (metal pads on the side-strips), the sample also shows the same metal corrosion and the metal peels off. For the present Both-Metal case, the mirrors etch differently depending on the position of the pattern. Most of the mirror wells etch faster with illumination than without it. The etch rate varies from $1.3\mu\text{m}/\text{min}$ to $2.0\mu\text{m}/\text{min}$ (R_{VR} from 115 to 237). Short patterns near the bottom etch slower than others with an etch rate of about $0.9\mu\text{m}/\text{min}$ ($R_{VR} \sim 45$) and some patterns show no etching.

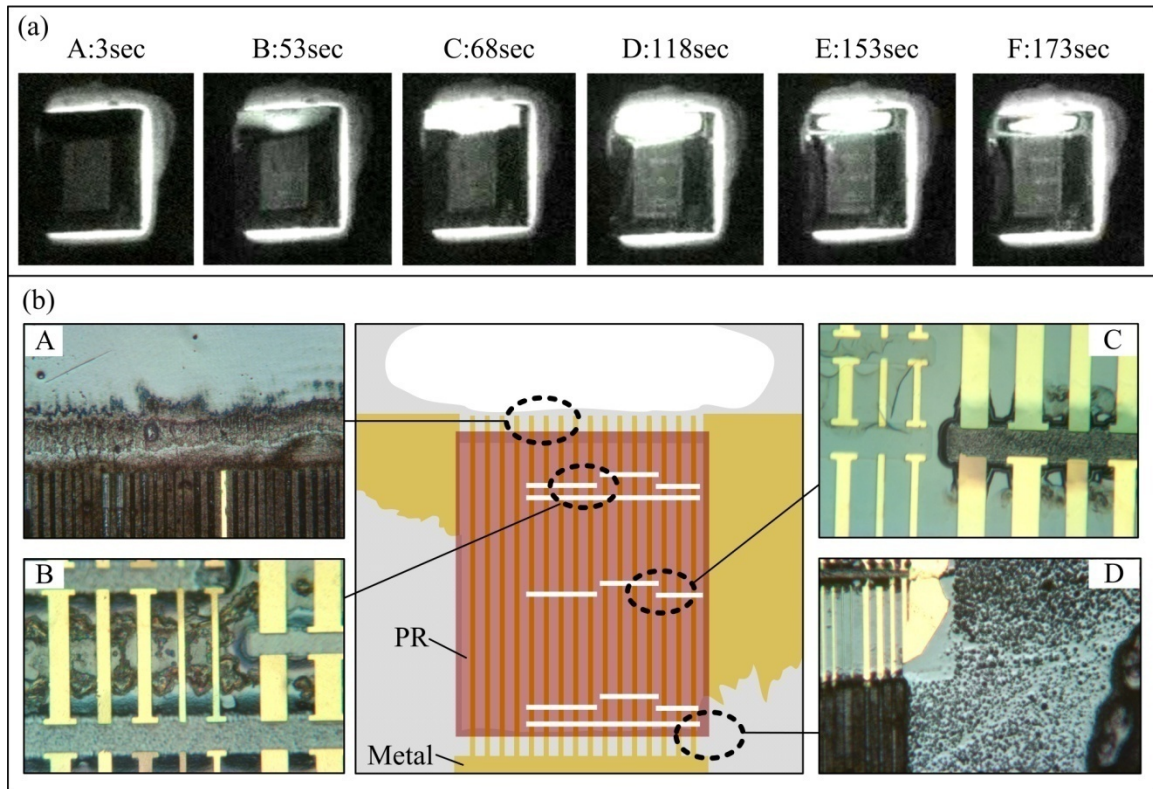


Figure 4.29 Mirror etch test using the Both-Metal mask on the EPI sample: (a) PL monitoring CCD image captured during the PAW etching and (b) post-etched surface illustration and microscope pictures of 4 different positions.

4.2.3.4 Summary for Mirror Etch Test of EPI

In the mirror etch experiments, the mirror regions show deep etching with all three alternative mask conditions (Both-PR, Both-Blank and Both-Metal mask) while the Initial-Mask for mirrors inhibits etching at the mirror facet. The mirror etching increases as the sample has more exposed surface. The metal pads deposited on the sample further promote the etching by exposing more metal to the etching solution.

Figure 4.30 shows how the etch rate at the center area of the sample depends on the masking conditions for high power PAW ($P_{PAW} \geq 70\text{mW}$) mirror etch test. “Both-PR”, “Both-Blank” and “Both-Metal” refer to the cases when the side strips are covered with PR, left blank, or covered with metal, respectively (refer to Table 4.1 above). However, the mirror pattern with

the Both-Metal mask generates more variations of the etch depth in the mirror well than do the other cases; the variation depends on the position and length (shape) of the pattern. For all mirror and waveguide etch tests with high power illumination, the post-etched surface appears very rough where the etching is promoted.

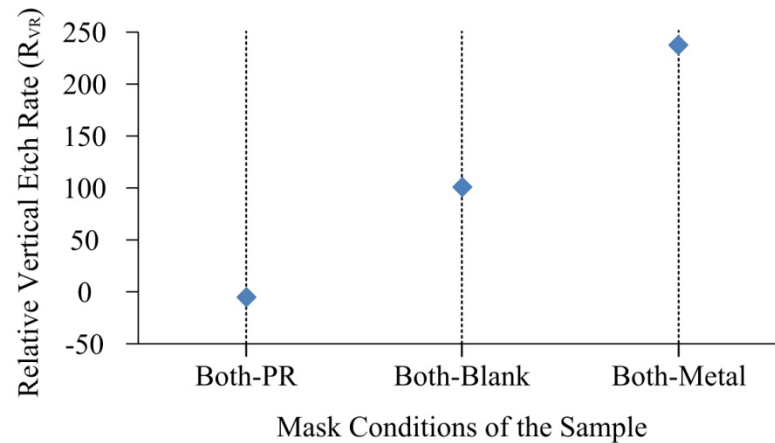


Figure 4.30 Relative vertical etch rate (R_{VR}) of the patterns depends on the conditions at the side strips. Both-PR: PR covers the side-strips straddling the waveguide pattern, Both-Blank: Side-strips expose semiconductor to light and etchant, Both-Metal: metal layers deposited on the side-strips.

The Both-PR mask (with both sides covered with PR) exposes part of the waveguide metal layer to the etching solution while the Initial-Mask for the mirrors covers all of the waveguide pattern in the center area; however, some metal is exposed to the etching solution in the Initial-Mask but the metal constitutes part of TIR mirror pattern and not connected to the laser mirror patterns under inspection. The waveguide structure connects to the mirror patterns through metal and can thereby directly affect the mirror etching. The portions of the metal waveguide patterns exposed to the etching solution may help to dissipate electrons from the mirror pattern. The excess electrons generated near the mirror wells can flow through the metal patterns. Those portions of the semiconductor surface exposed to the etching solution or having more metal on the surface may enhance the dissipation of the photo-electrons. The metal pads deposited on the

both side of the sample also connect to the waveguide pattern to help dissipate the excess electron from the mirror area.

4.2.4 M1 samples: Waveguide and Mirror Etch Test

Sections 4.2.2 and 4.2.3 discuss waveguide and mirror etching of EPI samples using high power PAW ($P_{PAW} \geq 70\text{mW}$). The laser-PAW etch tests shown those two sections do not achieve the expected etch properties for the laser devices. In particular, the mirror etching produces large lateral etching and non-uniform etch depth. Also, since the etch depth depends on the position on the sample, the reflectometer monitor with the tightly focused probe beam does not necessarily detect the correct depth. The mask design and PAW etch system needs to be improved for practical application for device fabrication.

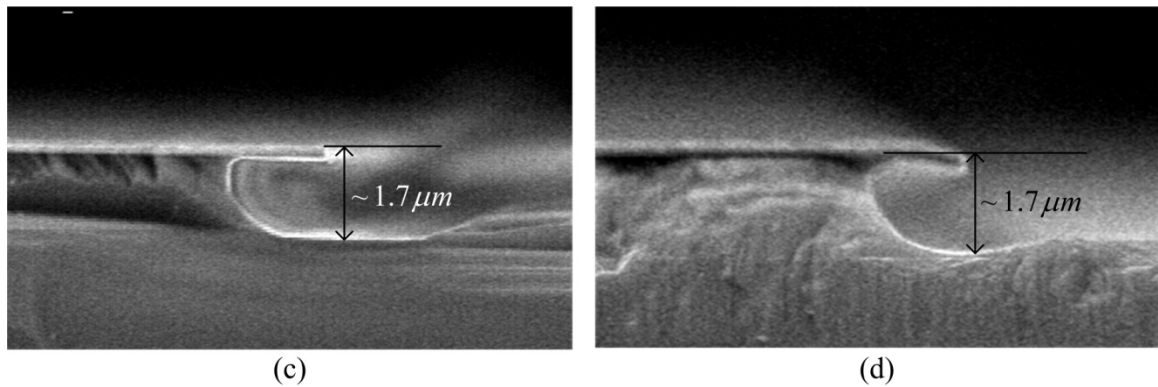


Figure 4.31 Waveguide etched side profile of (a) M1 with green laser PAW and (b) dark. ($P_{PAW} \geq 70\text{mW}$)

This section reviews the waveguide and mirror etching for the M1 sample. The waveguide mask designed in this work (Figure 4.14) has a top metal layer for electrical contact to the devices and it has PR for protection of the mirror pattern (the PR covers the metal on the waveguide and the mirror windows but allows for waveguide etching). From the LED-PAW experiments, this mask would not be the best choice for the M1 samples (Figure 3.10). While

using a silica-metal-PR (type 3) mask for the PAW etching of the EPI sample improves the side profile and decreases the lateral etching, it does not significantly improve the etch characteristic of the M1 sample. The laser-PAW etch test in Section 4.2.2 shows that metal-PR masks also produce vertical sidewall with low lateral etching for EPI samples. From the LED-PAW etching experiments (Figure 3.10 (b)), the M1 sample etching shows the best performance with the metal-only mask (type 1 mask) for the high power green LED. Figure 4.31 compares the laser-PAW ($P_{PAW} \geq 70\text{mW}$) etch profile with that for dark etching of the M1 sample. After PAW etching, the etched pattern has almost same amount of lateral etching as the dark etched one (Figure 4.31 (a) and (b)).

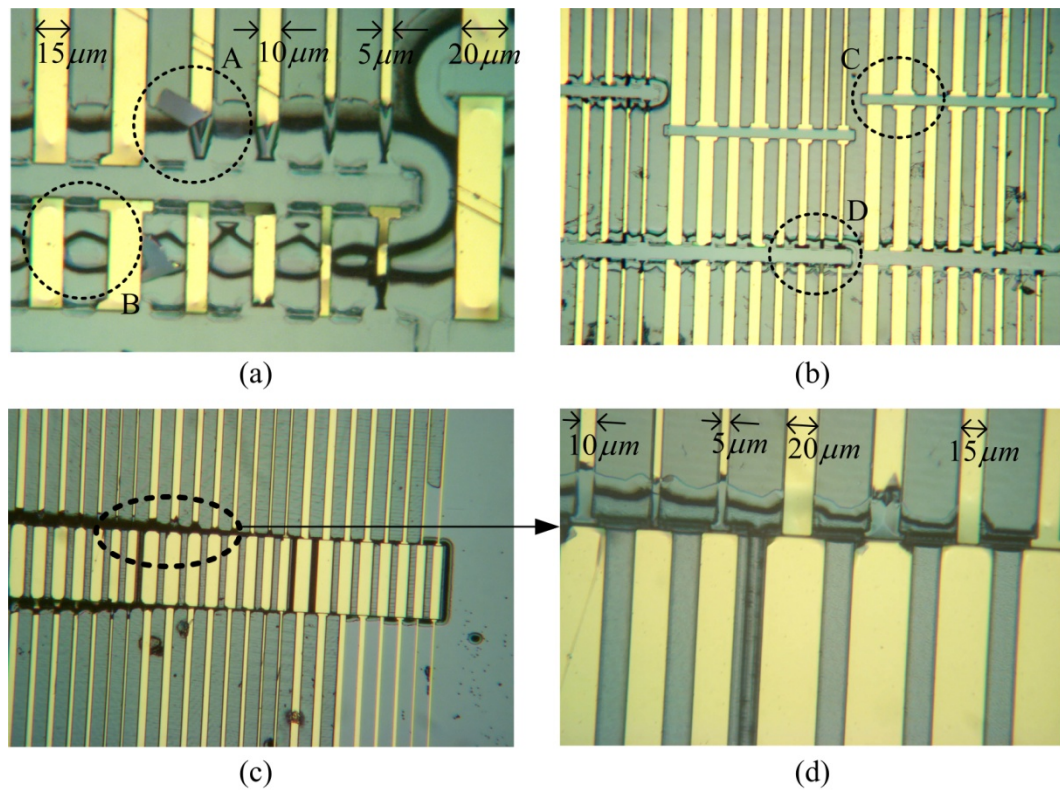


Figure 4.32 Microscope pictures of post-etched M1 samples with high power PAW etching. (a) and (b) shows the pictures of the mirror patterns near the center and edge, respectively. (c) shows laser and PD pattern and (d) present magnified picture of the circled area in the picture. Picture (b) spans a horizontal distance of approximately 640 μm while (c) spans approximately 1.2mm.

The PAW etching of the M1 mirrors shows unique patterns. Figure 4.32 shows microscope pictures of the post-etched M1 sample that used high power PAW etching with the Initial-Mask for mirror. Mirror etching using the high power green laser produces deep lateral etching and leaves a triangular shape at the edge which means the etching proceeds along the material crystal direction as for the dark wet etching (Figure 4.32 (a) area A and B). The etch depth of the mirror pattern varies according to the position of the particular mirror pattern. Those patterns near the edge, etch slower than patterns near the center while the EPI sample works the opposite way. For the M1 sample, some of the pattern does not etch (Figure 4.32 (b) area C). Some patterns stop etching near the middle of the pattern (Figure 4.32 (b) area D). From the profilometer measurement, the mirror well etches at a rate of approximately $0.8\mu\text{m}/\text{min}$ ($R_{VR} \sim 33$) at the center area while it etches at a low rate of about $0.01\mu\text{m}/\text{min}$ ($R_{VR} \sim -98$) at the edge of the sample. The etch depth of the mirror pattern increases toward the center area of the sample as does the lateral etching along the mirror pattern. Figure 4.32 (c) and (d) shows microscope pictures of the high power PAW etched sample surface. Figure 4.32 (d) presents magnified view of the lateral etching at the mirror pattern (circled area in the Figure 4.32 (c)). The lateral etching shown as dark lines near the mirror pattern extends toward the center of the sample.

The SEM pictures of the post-etched sample show the mirror etching condition more clearly. Figure 4.33 compares the post-etched surfaces for the two cases of high power PAW ($P_{PAW} \geq 70\text{mW}$) etching (Figure 4.33 (a) and (b)) and dark wet etching (Figure 4.33 (c) and (d)). The high-power PAW etching produces deep trenches (narrow $\sim 2\mu\text{m}$ wide but deep etch regions) along the mirror well as well as lateral etching that follows the waveguide patterns (Figure 4.33 (a) and (b)). The dark etched sample does not show the trenches along the masks (Figure 4.33 (c) and (d)). Also the pictures show that PAW etching has more lateral etching than the dark wet etching.

The PAW mirror etching does not produce the desired mirror facet for either EPI or the M1 sample. The Initial-Mask inhibits etching at the mirror window for the EPI sample while the M1 sample etches faster using the high power PAW process than it does in the dark. However, the PAW etching forms a deep trench along the mirror window and produces large lateral etching for the M1 sample.

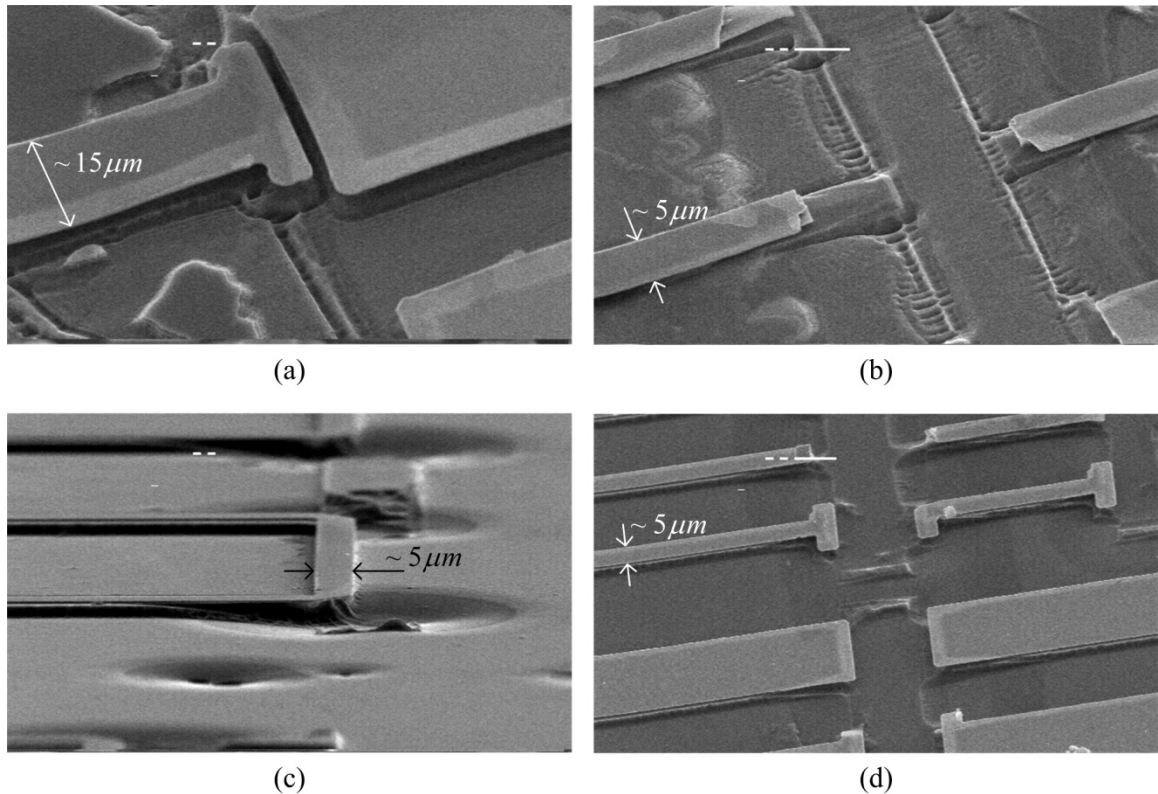


Figure 4.33 SEM pictures of M1 sample with (a) and (b) high power PAW etched, (c) and (d) dark wet etched samples.

For the previous EPI etch tests, the PAW etching characteristics depend on the surface masking conditions. High-power PAW etching is tested for the M1 sample when most of the sample surface remains bare. Photolithography generates mask patterns for which the mirror window is applied to the metal waveguides only near the center of the sample; the other parts (side strips) remain bare (Figure 4.34 (a)). The mask is the same as the Both-Blank mask for

mirror etch tests of the EPI sample in Figure 4.27 (a). The bottom area exposes the metal waveguide layers to the etching solution and the reflectometer probes the upper bare area of the sample. Figure 4.34 shows the mirror test results for the M1 sample with both side strips exposed to the etching solution.

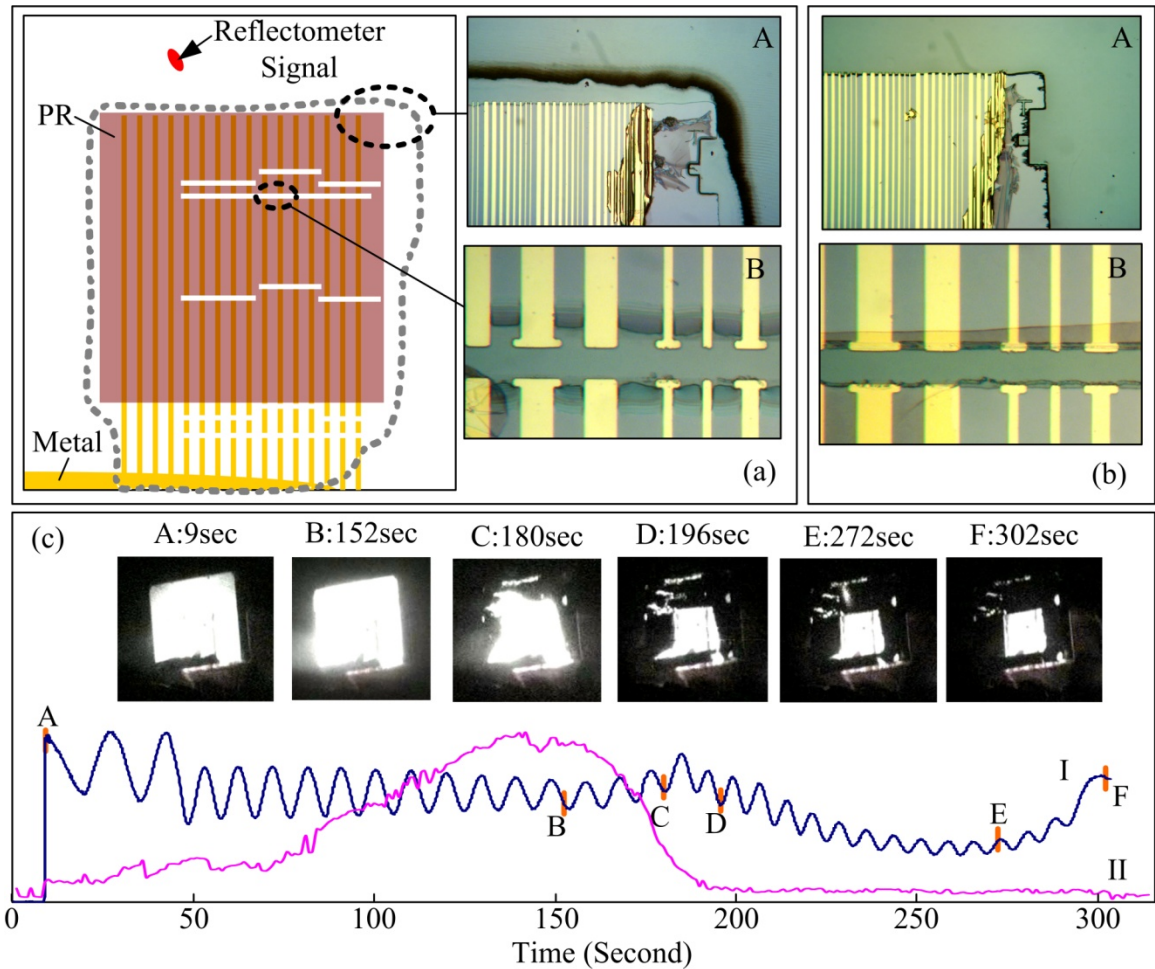


Figure 4.34 M1 mirror etch with the Both-Blank mask (a) post-etched surface under PAW, (b) dark etched sample surface with same mask and (c) Reflectometer and PL signal of the upper blank area of the sample during the high power PAW etching. I and II represent reflectometer and PL signal, respectively in (c). The distance scales in the pictures can be determined based on the widest waveguides of $20\mu\text{m}$.

For the mirror etching of EPI sample with the Both-Blank mask, a dark layer is generated around the patterned area and it covers most of the blank area. For the sample, mirror patterns

etch faster than the blank area that surrounds the patterned area (Figure 4.27 (a)). The M1 samples under the same conditions (Both-Blank mask) show the dark substance deposited around the PR pattern but the substance does not spread to the blank area. The dark substance forms a boundary surrounding the patterned area. The M1 sample etches slower near the center (within the dark boundary) and faster in the blank areas while the mirror pattern etches faster for the EPI sample.

The reflectometer signal for the blank M1 sample under high-power green laser illumination shown in Figure 4.11 also shows the “dip” in the n-AlGaAs layer for mirror etching with the Both-Blank mask (Figure 4.34 (c)). In contrast to the EPI samples, the reflectometer signal shows good fringe patterns for the M1 samples in addition to showing the “dip” in the n-AlGaAs layer. The PL has higher intensity before the etching reaches the active layer since the M1 samples have p-type AlGaAs layer before the active layer. From the reflectometer signal and PL data, the PL emission decreases at the active layer and becomes negligible for the n-type AlGaAs layer at the blank area of the sample including reflectometer-probed area. One can expect to see slower etching at the mirror window since PL emission still remains at the masked area when the blank area does not emit light. Agitating the etchant during the etching does not affect the PL and reflectometer patterns.

As PAW etching continues in the n-AlGaAs, the surface of the layer becomes rough as shown by the reflectometer signal since the fringe height becomes smaller for the layer. The pictures from the video capture correspond to the reflectometer signal in Figure 4.34 (c) and show the PL intensity variation during the etching. The sample produces large photoluminescence from all regions so long as the etching surface remains in the p-type material (Figure 4.34 (c) from point A to B) after which, the PL level quickly reduces near the active layer in the blank region (Figure 4.34 (c) point C). After the active layer, the PL level becomes undetectable from the ‘blank area’ but it remains intense from the PR patterned area (Figure 4.34 (c) from point D to F). The PL primarily emits through the PR masking layer, which prevents material dissolution

underneath, since the PR is transparent to the PAW light source and IR (Infra-Red) light of PL. Under the PR layer, the PAW light generates electron-hole pairs under the PR protected layer and some of these excess carriers recombine. The etching inhibits around the PR layer since the excess electrons diffuse from under the PR mask to the blank area.

The sample surface looks clean and the etch depth measures from $1.8\mu\text{m}$ to $2.0\mu\text{m}$ with an average etch rate of $0.4\mu\text{m}/\text{min}$ ($R_{VR} \sim -43$) at the mirror pattern and the profilometer shows a rectangular shape. However, the etch depth of the mirror well does not match the depth in the blank area as determined from the reflectometer signal. The reflectometer signal (Figure 4.34 (c)), indicates that the etching was stopped near the substrate ($\sim 3.5\mu\text{m}$) but the mirror patterns etched only about $1.8\mu\text{m}$ (50% of the etch rate in the blank area). The reflectometer probe area shows about 10% higher etch rate than dark ($R_{VR} \sim 10$); this behavior is opposite to the etching of the EPI samples under the same conditions (Figure 4.27). Under the same chemical conditions (same etching solution and temperature) without illumination, the mirror wells etch about $3.5\mu\text{m}$ with an etch rate of $0.6\mu\text{m}/\text{min}$ and they do not have deep rounded features (Figure 4.34 (b)) for M1 sample. In the dark, the mirror patterns uniformly etch and the reflectometer signal matches the actual etch depth, without any “dip” in the signal for the n-AlGaAs layer. Also, the post-etched sample surface does not have the dark surface structure that forms on the surface around the PR patterned area under illumination (Figure 4.34 (b)-A and (a)-A).

4.3 Laser Fabrication to Evaluate PAW Etching

The results for the four types of mask are applied to an initial fabrication of heterostructure lasers using principles gained from the previous experiments. Section 4.1 discussed an initial reticle design for ridge-guided quantum well lasers (Initial-Mask). As discussed in Section 4.2, both EPI and M1 samples present issues that need to be addressed to achieve the necessary etch characteristics for optical device fabrication. The etch depth varies by

position and masking conditions on the sample. Also PAW etching of the mirror pattern shows large lateral etching. The high power PAW process produces a dark substance on the surface. From the previous experiments, the PR mask plays an important role in causing non-uniform etch depth and the metal pattern does not inhibit etching. For fabrication of PAW-etched lasers and tests of the etched mirror quality, this section fabricates lasers using M1 material with metal mask only for device test. The next chapter slightly modifies the fabrication process, applies it to heterostructure laser mirrors and waveguides, and tests the performance of the lasers and thereby extracts parameters to qualify the etching.

The fabrication sequence and associated processes have been adjusted for the available equipment, material and etching techniques. To simplify the etching process, both waveguides and mirror facets are simultaneously etched. Since the waveguide etches deeper than the active layer, the resulting highly confining waveguide with air-semiconductor sidewalls will affect the laser threshold. However, by comparing laser properties for cleaved and etched mirrors fabricated with the same conditions, one can determine the etched mirror quality. Integrated lasers are fabricated with different PAW laser powers to see the light intensity effects on waveguide and mirror etching.

Figure 4.35 illustrates simplified etched-mirror laser fabrication steps for a simple metal-only mask. First, p-type metal contacts (Titanium (Ti, 400 Å) –Platinum (Pt, 200 Å) –Gold (Au, 3000 Å)) are deposited on the surface using negative photolithography (Figure 4.35 (a)). The metal contact layer functions as an etch mask for the waveguides and mirrors (Figure 4.35 (b)). The etching is stopped after the active layer of the wafer. For the M1 sample, the waveguides and mirrors etch deeper than 2 μm. The reflectometer and PL sensors monitor the etching to control the depth. After the pattern definition, the substrate of the material is lapped down to about 150 μm thick and then the n-type metal layers (Ni (100 Å) – Ge (400 Å) – Au (800 Å)) are deposited at the back side of the sample (Figure 4.35 (c)). For the PAW laser tests with different

laser power, the integrated lasers are fabricated with four different PAW powers ($P_{PAW} = 0, 5\text{mW}, 70\text{mW}$ and 100mW) for comparison.

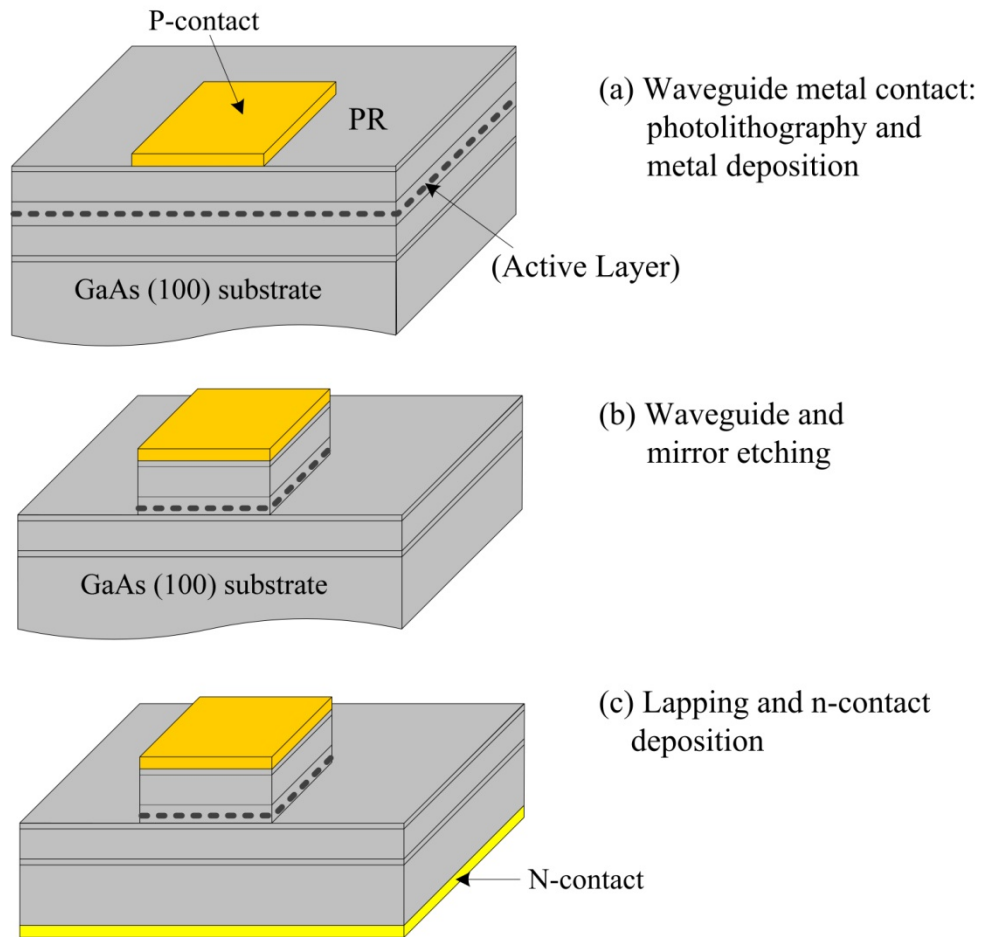


Figure 4.35 Fabrication process for laser devices with metal-only mask.

With the metal-only mask, the reflectometer signal shows similar characteristics with previous experiments in the Section 4.2 in Figure 4.11. As before, the reflectometer signal shows a ‘dip’ corresponding to a surface transition layer. The etch rate also accelerates as laser power increases at the reflectometer probe area. However, the semiconductor does not uniformly etch using the high power laser illumination ($P_{PAW} \geq 70\text{mW}$). The PAW etch depth varies according to the mask pattern and layer structure of the material. For the M1 case, the sample etches slower

near the mask when using the high power laser whereas the EPI sample behaves in a manner opposite to that of M1 (i.e. etch faster at the edge of the sample). Figure 4.36 shows the post-etched sample surface with PAW laser power larger than 70mW for the samples with metal-only mask.

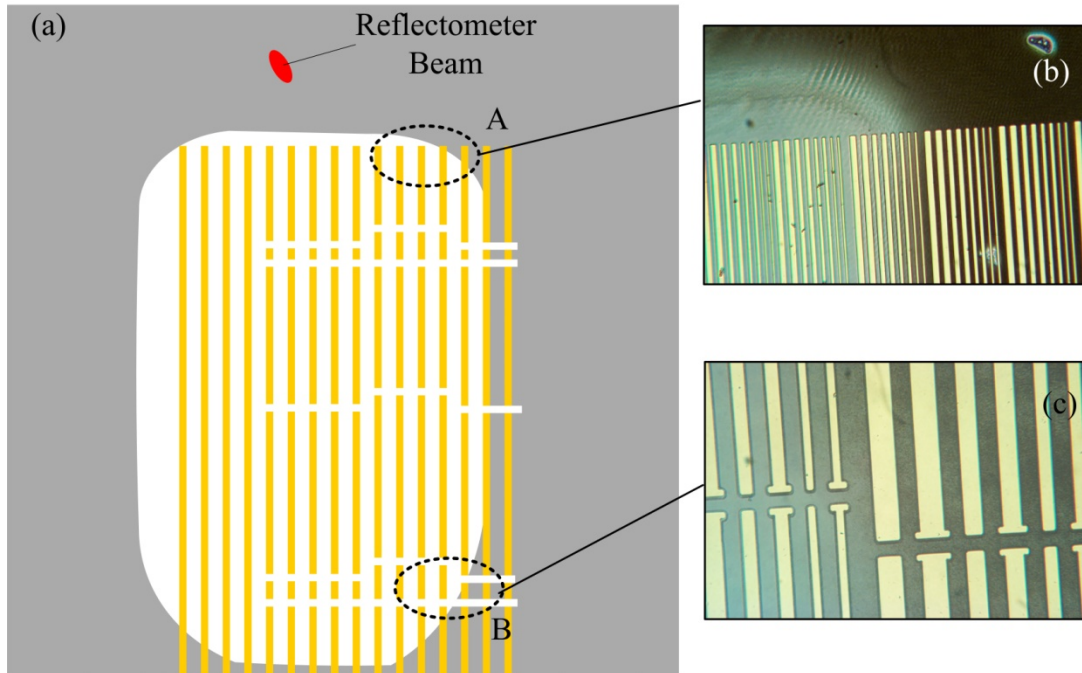


Figure 4.36 High power PAW etched M1 sample with metal-only mask (a) Overall etched sample surface. The gray area represents dark surface, (b) and (c) microscope picture of the sample surface corresponds to the area A and B, respectively. ($P_{PAW} \geq 70\text{mW}$). Picture (b) spans a horizontal distance of approximately $900\mu\text{m}$ while Picture (c) spans $350\mu\text{m}$ based on the widest waveguide of $20\mu\text{m}$.

The sample has metal contacts on the ridge-waveguides lasers in the center; the outer area of the sample is left blank (Both-Blank mask). The metal mask serves as an etch mask and the reflectometer probe beam is applied on the upper bare area of the sample. The etching is stopped at an etch depth of approximately $3\mu\text{m}$ from the reflectometer signal which places the etched surface near the middle of the n-AlGaAs layer by counting fringes. With PAW laser powers less

than 30mW, the post-etched sample did not show any dark-colored substance deposition and the etch depth agrees with the reflectometer monitor. However, for high power PAW etching ($P_{PAW} \geq 70\text{mW}$), a profilometer measurement in the masked area does not agree with the reflectometer etch monitor, and the PAW etch appears to deposit material on the surface which appears dark in an optical microscope. The actual etch depth at the patterned area measures about $2\text{ }\mu\text{m}$ while reflectometer monitor measures about $3\text{ }\mu\text{m}$ at the probe area. The dark pattern follows the mask pattern and where it appears dark, and the etch depth agrees with the reflectometer.

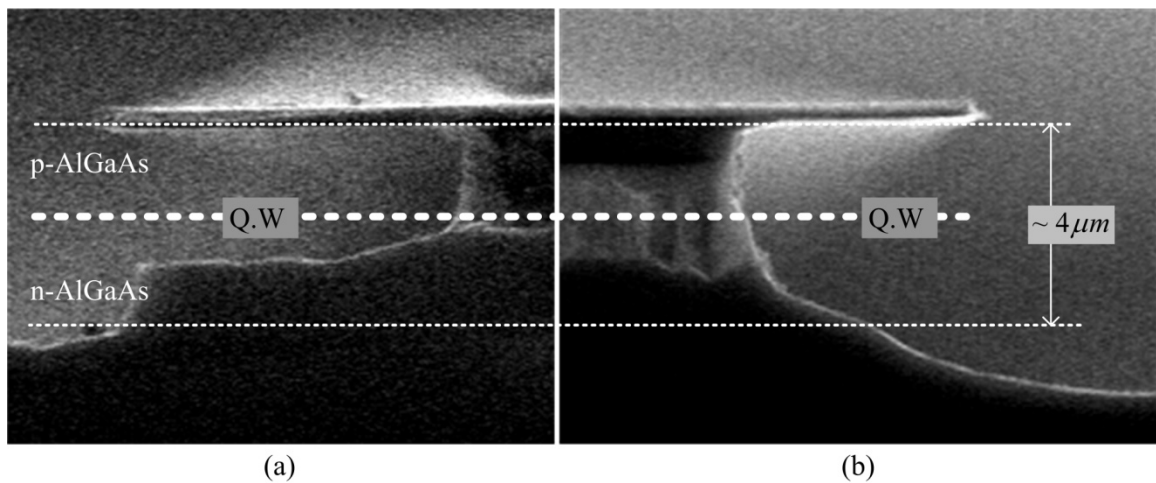


Figure 4.37 Comparison of side profiles of (a) Laser and (b) LED PAW etching. Both have the same masking conditions and same M1 material type. The quantum well (QW) layer has a position above the etch steps.

From the LED-PAW experiments, the M1 samples show the most vertical side profile by using the metal-only mask (type 1 mask) as shown in Figure 3.10 (b). With laser-PAW, the side profile looks different than for the LED-PAW etching as can be seen in the side-by-side profile comparison in Figure 4.37 for the M1 sample with metal masking. The side profile of the LED-PAW shows smooth sidewalls throughout the heterostructure layers (about $4\text{ }\mu\text{m}$). In contrast to the LED-PAW etching, the laser-PAW also shows the vertical sidewall but with a step-like

profile (Figure 4.37 (a)). Until the etching reaches the active layer, the laser-PAW shows vertical sidewalls but with deep lateral etching. After the active layer in the n-AlGaAs layer, the lateral etching reduces to almost zero and still maintains vertical side walls. Since the active layer locates above the ‘step’, this profile can function as a mirror. However, deep lateral etching is not desired for the semiconductor device fabrication.

The laser-PAW also shows different side profile depending on the etch depth. One can see how the side profile variations depend on the etch depth by stopping the etch at several depths and examining each in the SEM. The high power laser-PAW etching ($P_{PAW} \geq 70\text{mW}$) shows different sidewall profiles depending on the etch depth as shown in Figure 4.38. When the etch is stopped just below the active layer (etch depth about $2.16\mu\text{m}$ in Figure 4.38 (a)), PAW etching produces a vertical sidewall with small lateral etching as expected. However, the profile changes as the etching deepens. When the etch depth reaches about $4.33\mu\text{m}$ (Figure 4.38(b)), the sidewall shows clear step-like profile with larger lateral etching but with a vertical angle at both layers. The PAW etching for p and n-type AlGaAs shows a difference. With high power PAW etching, the vertical etch rate increases for both the p and n-type materials while exhibiting less lateral etching. The n-AlGaAs responds more sensitively to the high power PAW laser than p-AlGaAs material. As a result, the n-type etch profile has vertical sidewalls aligned with the mask edge (almost no lateral etching) while the p-AlGaAs layer has more lateral etching. When the sample etches even deeper, however, the top layer (before the active layer) shows the same profile as for the dark etching of the M1 sample (Figure 3.9 (a)) while the n-type layer and substrate show vertical angles with no lateral etching.

The laser-PAW etching with a metal-only mask reduces lateral etching and helps to produce vertical sidewalls for both p and n-type AlGaAs material as shows in the Figure 4.38 (a). However, the PAW etching works better for the n-type material and some lateral etching still exists at the p-type material. When the etching continues to the n-AlGaAs layer, the laser increases the etch rate in the layer without any lateral etching while the already-etched p-type

layers fall in the shadow of the metal mask and have similar etch characteristics to that in the dark. When the metal mask blocks the light, the chemical etching dominates the material dissolution at the area. As a result, samples that etch deeper show more lateral etching and when it etches for a long time, the dark-area etch characteristics become the same as for dark chemical etching.

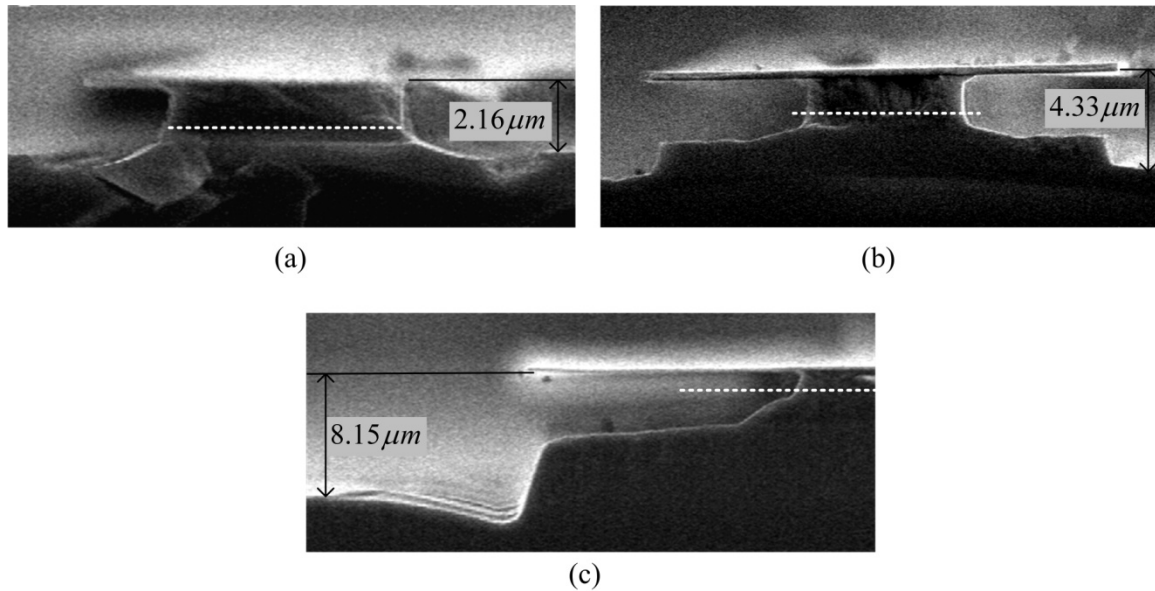


Figure 4.38 High power green laser PAW etched side profile variations on the etch depth of M1 samples with Metal-Only mask; etch depth about (a) $2.16\mu\text{m}$, (b) $4.33\mu\text{m}$ and (c) $8.15\mu\text{m}$. While dotted line indicates the active layer in figure (a), (b) and (c).

The PAW etching achieves an integrated wet-etched laser device by using an M1 sample with a metal pattern. Since the sidewall etch profile varies with the etch depth as shown in Figure 4.38, the etch depth of the mirror also needs to be controlled to maintain vertical sidewalls. The etch depth should not be too deep for laser mirror fabrication even with high power PAW. When it is etched too deep, the side profile becomes almost the same as dark etching due to the shadow under the mask. The laser power, material and wavelength are not the only conditions to fabricate vertical sidewalls. It would be better to stop etching after the active layer to minimize the lateral etching and thereby maintain the vertical sidewall angle. By monitoring the precise etch depth

during the etching using a reflectometer, the etch depth can be controlled. With PAW power higher than 70mW, the reflectometer monitors the etch rate near the edge which does not match the etch depth in the patterned area due to the etch-depth variations on the sample surface. The etch depth varies by the mask material and design. For practical devices and applications, the reflectometer system needs to be changed from having a single photodetector that convolves the probe signal over the probe beam area to one capable of simultaneously mapping the entire surface. To minimize the variations in the etch depth in the patterned area, more study should be done to optimize the PAW laser power and mask conditions for different layers of materials.

4.4 Discussion

One of the important applications of PAW etching would be to integrate optical devices in laser heterostructure material that require vertical sidewalls. The sidewall quality can be determined by fabricating optical devices such as a laser and measuring the device properties. The efficiency of the typical ridge-waveguide laser (and therefore, the threshold current) is closely related to the cavity mirror reflectivity. The laser threshold depends on the optical scattering losses and on the construction of the optical waveguide.

This chapter discussed new laser-PAW apparatus, fabrication processes, and tests for etched laser devices using two different types of laser material, namely the EPI and M1 material. The laser-PAW etch apparatus includes reflectometer and PL systems for real time etch depth and surface condition measurement. The etch tests shows unexpected results from both EPI and M1 samples. The laser-PAW does not agree with the LED results in the Chapter 3, which can be attributed to differences in masking and to differences in the distribution of optical intensity across the surface. The mask material such as PR or metal affects the etch characteristics under illumination.

The reflectometer and PL monitoring system provide information for the PAW etching of the EPI and M1 samples using the high power laser. The reflectometer signal shows very

different signals for PAW illumination than for the dark case depending on the layer structure of the laser material. The EPI and M1 samples show similarity in the characteristics of the reflectometer signal and PL. The reflectometer signal shows the “dip” in the n-AlGaAs layer and PL intensity drops near the n-AlGaAs layer. For both the EPI and M1 samples, the PL intensity correlates with the primary signal of the reflectometer. Since the PL emission does not interfere with the reflectometer signal detection, the reflectometer dip and the reduced fringe height suggests variations of the surface condition produced by the laser at the n-type AlGaAs layer.

The reflectometer and PL signals from the M1 samples are clearer for interpretation than from the EPI sample. Reflectometer signals from M1 sample are consistent for most of the samples and show fringe patterns throughout the layers. Even at the ‘dip’ the reflectometer signal shows fringes that can be counted to estimate etch depth. EPI sample case, the fringe patterns never recover from an anomalous ‘dip’. For the M1 samples, the reflectometer signal shows a dip in the surface reflectance for the n-type AlGaAs layer and the reflectance returns to the initial level at the n GaAs layer (substrate). In the ‘dip’, the reflectometer signal still maintains the same fringe signal height (i.e., secondary signal) as for the etching of the p-type layer which indicates the surface remains smooth in both layers. The PL has high intensity for the p-AlGaAs laser and suddenly drops after the active layer (Q.W) where reflectometer signal shows the ‘dip’ and did not recovered.

Previous work for this dissertation [98] has shown similar anomalous dips for the p-type layer of the GaAs/AlGaAs laser materials in (dark) diffusion rate limited phosphoric acid etches. A camera system shows the dip is due to viscous etch byproduct with mass density larger than that of the etchant. However, for this case, the “dip” in the n-type AlGaAs layer is not affected by agitating the etching solution. In Figure 4.12, stopping the etching at the time of the anomaly, rinsing the surface, and restarting the etching does not bring the reflectometer signal back to the proper level. The reflectance exactly follows the primary reflectometer signal. The PL signal rapidly decreases near the quantum well at the n-type semiconductor suggesting large photo-hole

consumption at the reaction surface as expected. Agitation of the etching solution during the etching does not effect on the PL pattern. The dip appears to correspond to the formation of surface oxides; however, the exact nature of the substance will require further testing.

The reflectometer signal “dip” in the n-AlGaAs layer depends on the PAW laser power. The dip in the n-AlGaAs layer starts to appear with PAW laser power about 10mW and becomes deeper as the laser power increases. It becomes clear with PAW laser power higher than 70mW.

The PAW etching with a high power laser ($P_{PAW} \geq 70\text{mW}$) is tested on prepared samples (EPI and M1) for Initial-Mask for waveguide and mirror (Figure 4.2). From LED-PAW etch tests, the green LED-PAW produces a smooth vertical sidewall suitable for laser mirrors when using a silica-metal-PR (type 3) mask for the EPI material and metal-only (type 1) mask for the M1 samples (Figure 3.10 and 3.11). The designed laser fabrication process in Figure 4.2 would work better for EPI sample and it may need to be modified for the M1 sample. (It is expected to work better with EPI sample since it is metal-PR mask.)

The tests of the laser fabrication process for both EPI and M1 samples show that a couple of issues need to be addressed. With the Initial-Mask for waveguides, the EPI samples etch faster at the patterned area than the edge region with the reflectometer probe area; the situation is reversed for the M1 sample. The surface current due to the different densities of photo-carriers may cause the etch depth variation. The current flow in the many possible paths produces a surface distribution of charge that controls the etch rate at any given point and thereby also controls the variations on the etch depth. Near PR, carriers accumulate while surfaces exposed to the solution have fewer carriers due to the carrier transfer to/from the solution. When a metal layer is on the sample, the current also can flow through the metal layer. If it is the case, the arrangement of the mask pattern (size and the position of the blank area) and material type of the mask affects the PAW etching. As a simple test, the left and right sides of the patterns remain blank while different conditions are applied to the blank area; (1) Both-PR (PR covers both sides

of the waveguide pattern near the sample edges), (2) Both-Blank (both side left as blank) and (3) Both-Metal (metal deposited on the both sides of the sample).

With the Initial-Mask for waveguides, etch inhibition occurs near the reflectometer probed area while patterned area etches slightly faster than dark etching (positive R_{VR}). When PR covers both blank side-strips (Both-PR mask), the EPI sample near the PR-covered area etches even slower while the patterned area near the center etches faster than the original waveguide mask case. Compared to the dark etching, the PAW etching promotes the etch speed to about 37% in the center while it decreases about 74% near the PR covered area. Illumination generates electron and hole pairs at the same surface including under the PR covered area. Since the electrons cannot be consumed in the region, they could transport toward the patterned or blank areas. The excess electrons inhibit etching near the PR area.

In contrast to the Both-PR case, the etch rate decreases at the patterned area slightly in the center ($R_{VR} \sim -5$) and increases at the patterned area near the metal at the bottom and edge of the sample ($R_{VR} \sim 73$) compared with the dark (and both sides blank). The Both-Metal case shows similar etch characteristics to the Both-Blank case. Patterns in the center etch slower ($R_{VR} \sim -10$) than the ones near the edge ($R_{VR} \sim 72$). The results from Both-Blank and Both-Metal cases suggest that the metal layer on the sample has similar function with the blank surface in the PAW etching system. The electrons can easily transfer from the solid to the etching solution through the metal contact layer. The only difference is that the metal layer blocks the illumination and prevents photo-carrier generation under the mask. For all cases, those regions with an increased etch rate (under illumination) show rough surfaces with interference patterns while slower etching areas show clean surfaces.

PAW etch tests using the Initial-Mask for mirror presents some problems for the EPI sample. The PAW illumination inhibits the etch at the mirror pattern while the etching continues to follow the waveguide metal layers under the PR protected area as shown in Figure 4.28 (a). The same set of mask types are applied to the mirror etching as for the waveguide etching: (1)

Both-PR (both sides covered with PR), (2) Both-Blank (both sides left blank) and (b) Both-Metal (both sides covered with metal). The mirror wells show deep etching with all three alternative mask conditions while the Initial-Mask for the mirrors inhibit etching at the mirror facets. The mirror etching increases as the sample has more exposed surface. The metal pad deposited on the sample promotes the etching. However, the mirror patterns on those samples with metal pads deposited on the side-strips generate more variations on the etch depth at the mirror depending on the position and length (shape) of the pattern. For all cases, the post-etched surface appears very rough where the etching is promoted. Same rough surfaces appear on the waveguide etched sample.

For the mirror etch tests, all the alternative masks (Both-PR, Both-Blank and Both-Metal) expose some metal on the waveguide to the etching solution while the Initial-Mask for the mirrors covers the whole waveguide pattern. The waveguides connect through metal to the mirrors which can directly affect the mirror etching. That is, the part of the metal waveguide patterns exposed to the etching solution may help to dissipate electrons near the mirror patterns. The excess electrons generated near the mirror window area flow through the metal patterns. Semiconductor surfaces exposed to the etching solution or having more metal on the surface may dissipate the photo-generated excess electron by more effectively conducting the electrons away from the mirror pattern. The metal pads deposited on the both side of the sample also connect to the waveguide pattern to help transport the excess electrons from the mirror area.

For M1 samples, the Initial-Mask for the mirrors promotes the etching at the mirror side using high power PAW etching while it inhibits etching at the mirror window for EPI sample. However, the etching forms deep trenches along the PR mask and large lateral etching for M1 sample.

From the etch tests in this chapter, the PAW etching needs to be improved to meet the desired etch properties for optical device fabrication with heterostructure laser materials. Unlike the bulk material, the heterostructure sample can block current flow toward the substrate of the

material due to the built-in fields near the p-n junction, changes in the bandgap in the graded index region, and due to recombination at the Q.Ws. In addition, the backside glass slide ensures standard back side conditions (covers backside of the sample) and guarantees to block carrier transport to the solution through the backside. The high power laser generates excess carriers at the surface which affects the dissolution of the material. Since most of the excess carriers are accumulated at the surface for the heterostructure material, it is difficult to remove electrons from the surface and leave holes to promote etching. The mask material affects excess charge flow at the surface. For laser fabrication, it is necessary to modify the mask.

From the previous experiments, evidently the PR mask can (and does) produce unexpected PAW etch characteristics. Lasers are fabricated using the M1 samples with the Metal-Only mask with the PAW etching. To simplify the etch process, both the waveguide and mirror facets are simultaneously etched. Since the waveguide etches deeper than active layer, it will affect the laser threshold. Deep etching of the waveguide may cause high optical loss at the sidewall. However, by comparing laser properties of cleaved and etched mirrors fabricated with same conditions, one can estimate etched mirror quality. Chapter 5 tests PAW fabricated M1 lasers with metal only mask.

Chapter 5 Test of Photo-Assisted Wet (PAW) Etched Mirror Laser

Fabricating a laser without cleaved mirrors represents one of the major tasks to realize integrated optics and optoelectronics. Vertical etches must maintain good control of lateral etching to prevent undercutting of metal contacts and increase the degree of integration. While dry etching is the most widely accepted process to fabricate optoelectronic devices [108], it can be relatively expensive, slow, and most importantly, it can generate rough surfaces which lead to increased optical loss of the device [16]. Wet etching can produce smooth sidewalls as an alternative etching system. However, conventional wet etching has a couple of drawbacks for laser fabrication such as uncontrollable non-vertical sidewall profile and deep lateral etching. The sidewall profiles obtained from wet chemical etching normally depend on the etching solution and the material crystal direction [23].

Wet etching of integrated laser mirrors has been of interest since the first semiconductor lasers with etched mirror facets. Dobkin et al [109] investigate early wet etched sidewalls for GaAs homojunction laser diodes while [110], Merz [111] and Iga [18] have reported experiments for double heterostructure lasers. These works implement either deep vertical etching (over 10 μ m) [18, 111] or selective lateral etching of a thin GaAs active layer [110]. Adachi et al. fabricate facets using crystallographic etching [112]. However, the method limits the device design since the laser has to be aligned along a non-cleavage plane. Bouadma et al. and Yuasa et al. fabricate etched mirror facets using IBE (ion-beam-etching) [113] and RIBE (Reactive Ion Beam Etching) with ECR (Electron Cyclotron Resonance) Cl₂ plasma [114]. However, dry etching produces a rough surface at the mirror facet. “Hybrid” etches have been reported using a nearly vertical dry etch (RIE) and a smoothing wet etch [115, 116]. The method adds complexity and expense to the fabrication process of the device.

Photo-Assisted Wet (PAW) etching provides control of the sidewall while retaining the benefits of wet etching such as smooth surfaces, low cost and fast etch speed for GaAs bulk [64]

and Multi-Quantum-Wall (MQW) laser material [97, 117]. Photo-Assisted Wet (PAW) etching improves the sidewall profile while reducing the lateral etch of the GaAs/AlGaAs heterostructure material.

As an evaluation of the PAW etching, two basic types of lasers are fabricated. The CE type has one cleaved and one etched mirror while the CL2 type has two cleaved mirrors. In order to distinguish between shallow- and deep-etched waveguides, respectively, an S or D is appended to the designator. A shallow etched waveguide (such as CL2-S) forms when the etching stops prior to the active layer whereas a deep-etched waveguide (such as CL2-D and CE-D) forms when the etching extends beyond the active layer. The typical ridge-waveguide laser has a shallow etched waveguide and two cleaved mirrors. However, the waveguide must be etched deeper than the active layers for the PAW etched lasers because of the unexpected etch depth dependence on the sample mask discussed in the previous chapter (Chapter 4). For experiments and tests, the lasers are fabricated under a variety of illumination conditions in order to determine the effect of wavelength and intensity. CL2-S (shallow ridge) waveguides are etched in either dark conditions or with the green laser power of about 60mW. The 894nm laser material is used for CL2-S devices. CL2-D and CE-D devices (deep etched waveguide laser) are fabricated in 852nm and 894nm laser heterostructure using four different PAW powers ($P_{PAW}=0\text{mW}$, 5mW, 70mW and 100mW). All the other fabrication conditions, such as metal contacts and wafer thickness, remain the same. Chapter 4 describes the laser fabrication and PAW etching process (and properties). The present chapter details the tests and compares the laser properties including optical power, bias current relations, and spectrums.

From the experiments shown in Chapter 3, PAW etching improves both mirror and waveguide qualities by reducing the lateral etching and improving the side profile. The distributed losses (due primarily to optical scattering) and the mirror reflectance will be obtained and compared for several cases. The dependence of the threshold and external differential efficiency will be displayed for a range of PAW etch powers ($P_{PAW}=0\text{mW}$, 5mW, 70mW and

100mW). Chapter 4 indicates that PAW laser powers of 70mW and 100mW produce the same etch characteristics. For convenience, the terms ‘high’ and ‘low’ power PAW etching refers to the cases when the PAW laser emits total power more than 70mW and less than 5mW, respectively.

For comparison of the waveguides, shallow-waveguide lasers etched either in the dark or under high power laser are tested. The shallow etched waveguide lasers are compared with deep etched waveguide lasers (CL2-S and CL2-D lasers) with various PAW laser power. When the waveguide is etched deeper than the active layer, the laser performance is more sensitive to the sidewall quality than those with shallowly etched waveguides. The etch properties depend on the PAW laser power and wavelength. This chapter examines the etched-mirror lasers (CE-D) fabricated with different PAW powers. CE-D type lasers are also compared to the CL2-D lasers. Section 5.1 reviews basic equations for calculating laser parameters such as reflectance and efficiency. Section 5.2 presents the laser test setup used for laser optical power versus bias current (P-I) plots and spectrum measurements. The following section (Section 5.3) compares P-I plots of lasers with different etch depths (CL2-S and CL2-D) and mirrors (CL2-D and CE-D) for various PAW etch laser power. The test results are summarized and discussed in Section 5.4

5.1 Basic Equations Used to Compare Laser Operation

The PAW etching quality can be ascertained through SEM micrographs and through operational measurements of the output power versus bias current (PI curves). The PI curves provide a sensitive measure of etching quality through the internal loss $\alpha_i(\text{cm}^{-1})$ and the mirror loss

$$\alpha_m = \frac{1}{L} \ln \left(\frac{1}{R} \right), \quad R = \sqrt{R_1 R_2} \quad (5.1)$$

where R_1 and R_2 denote the mirror reflectance. As can be shown [67, 118], the total optical power ($P_o = P_1 + P_2$) from an ideal laser (without mode hopping) has a linear relation with the bias current (above threshold, $I > I_{th}$)

$$P_o = \eta_i \frac{hc}{e\lambda} \left[\frac{\alpha_m}{\alpha_m + \alpha_i} \right] (I - I_{th}) \quad (5.2)$$

where P_1 and P_2 represent the power from mirror 1 and mirror 2, respectively, and η_i , λ and I_{th} indicates internal quantum efficiency, wavelength of the laser, and threshold current measured from P-I plot.

h: plank constant, $h = 6.626 \times 10^{-34}(\text{J} \cdot \text{s}) = 4.1357 \times 10^{-15}(\text{eV} \cdot \text{s})$

c: speed of light in free space, $c = 3 \times 10^8(\text{m/s})$

e: electron charge, $e = 1.602 \times 10^{-19}(\text{C})$

The optical factor, $hc/e\lambda$ depends on the wavelength of the laser as shown in the Equation (5.3a) and (5.3b). For the emission wavelength of the materials used in this work, the optical factors are as following.

$$\frac{hc}{e\lambda} \sim 1.388 \text{ with } \lambda = 894\text{nm} \quad (5.3a)$$

$$\frac{hc}{e\lambda} \sim 1.456 \text{ with } \lambda = 852\text{nm} \quad (5.3b)$$

From Equation (5.2), the total slope of the P-I plot, $M = M_1 + M_2$ where $M = dP_o/dI$, depends on the laser mirror and internal loss as in the following equation,

$$M = \frac{dP_o}{dI} = \eta_i \frac{hc}{e\lambda} \left[\frac{\alpha_m}{\alpha_m + \alpha_i} \right] \quad (5.4)$$

The external differential quantum efficiency, η_d , can be found from Equation (5.4)

$$\eta_d = M \frac{e\lambda}{hc} \quad (5.5)$$

The external differential efficiency is the slope of Equation (5.4) where under certain conditions, the efficiency can be taken as unity so as to provide an upper bound on the differential efficiency and a lower bound on the internal loss.

The experiments separately measure the power through both mirrors (P_1 and P_2) as a function of the bias current I . From these measurements one easily deduces the threshold current

as the point on the current axis through which the straight line (extrapolated through zero power) would pass.

The mirror loss and internal loss are more complicated in that the reflectance for both mirrors must first be determined for the case of a Fabry-Perot cavity with dissimilar mirrors. One procedure uses transfer matrices [67]. A simpler approach is possible as follows. Consider a cavity of length L , gain g (cm^{-1}), and having two mirrors at either end as shown in Figure 5.1.

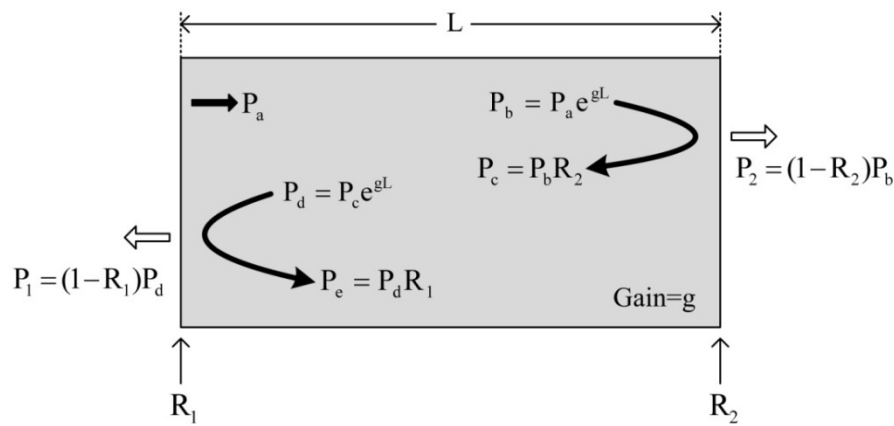


Figure 5.1 Fabre-Perot cavity with length, L and gain, g with two different mirrors 1 and 2. R_1 and R_2 denote the reflectance of mirror 1 and 2. P_1 and P_2 indicates power output from mirror 1 and 2.

Assume that the increase in optical power of initial power P_a for a one-way trip across the cavity is $P_b = P_a e^{gL}$ and that a mirror of reflectance R_2 produces the reflected power P_c based on the incident power P_b to mirror 2 as $P_c = P_b R_2$. The power P_2 transmitted through the mirror can be expressed as $P_2 = (1 - R_2)P_b$. The return trip along the cavity increases P_c to $P_d = P_c e^{gL}$ and mirror R_1 provides reflected power $P_e = P_d R_1$ and transmitted power $P_1 = (1 - R_1)P_d$. Combining these equations and assuming the starting power, P_a must be the same as the ending power $P_a = P_e$ at steady state yields

$$\frac{\sqrt{R_1}}{(1 - R_1)} P_1 = \frac{\sqrt{R_2}}{(1 - R_2)} P_2 \quad (5.6)$$

By using the total power $P_o = P_1 + P_2$, one can also show the power through R_1 (and a similar one for R_2) is

$$P_1 = \frac{(1 - R_1)\sqrt{R_2}}{(\sqrt{R_1} + \sqrt{R_2})(1 - \sqrt{R_1 R_2})} P_o \quad (5.7a)$$

$$P_2 = \frac{(1 - R_2)\sqrt{R_1}}{(\sqrt{R_1} + \sqrt{R_2})(1 - \sqrt{R_1 R_2})} P_o \quad (5.7b)$$

Once the power through the mirrors P_1 and P_2 as a function of bias current I has been determined, the slopes $M_1 = dP_1/dI$ and $M_2 = dP_2/dI$ can be determined. Defining the ratio $z = M_2/M_1$ allows one to find R_2 given that one knows R_1 (such as for a cleaved mirror)

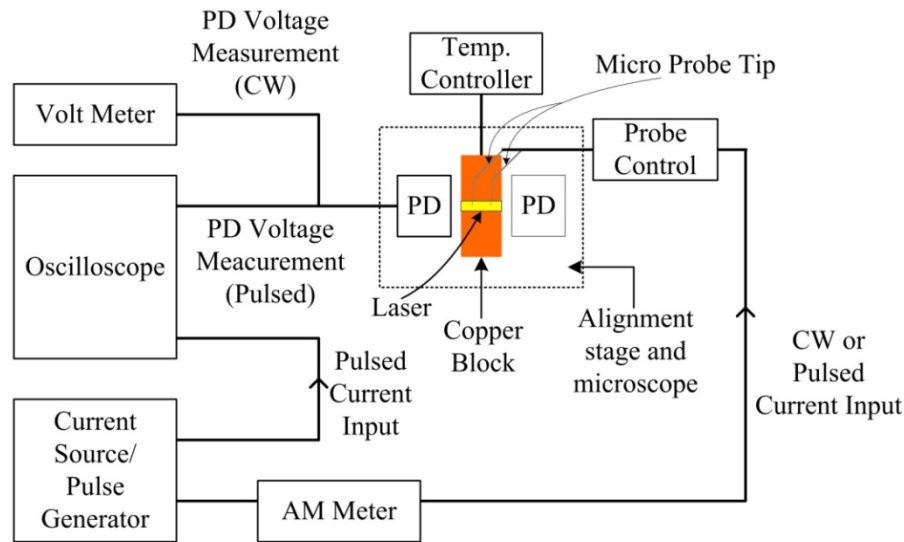
$$R_2 = \left[1 + \frac{z^2(1 - R_1)^2}{2R_1} \right] - \left\{ \left[1 + \frac{z^2(1 - R_1)^2}{2R_1} \right]^2 - 1 \right\}^{1/2} \quad (5.8)$$

Finally then one can deduce the mirror loss α_m , and then the internal loss α_i from knowledge of the slope of the PI curve.

5.2 Laser Test Setup

The optical power versus input current relation is measured for CW (Continuous Wave) and pulsed operation. From the PI measured value, laser parameters such as mirror reflectance and optical loss can be determined using equations reviewed in Section 5.1. Figure 5.2 illustrates the laser test set-up. Cleaved lasers are mounted on a copper block with temperature regulated to 20°C using an ILX 5910 temperature controller and a thermoelectric (TE) cooler. For CW operation, an ILX LDX-3620 current source applies bias current through a micro-tip to the p-type Ohmic contact of the laser. Electrically-actuated flexure stages (designed by JDS Uniphase) provide submicron control of the microtips. Two Hamamatsu S5107 photodetectors (PDs), with active areas of 1 cm², independently measure the light output from both sides of the devices. They are placed close to the laser mirrors (within 2-5mm) in order to collect all of the emitted light. The PDs are reverse biased and placed in-series with a dropping resistor so as to produce a

voltage signal. The devices and probes are aligned and monitored using a MicroZoom II microscope with CCD camera and custom software to measure distance and angles.



*PD: Photo-Detector

Figure 5.2 P-I test set-up for CW and pulsed current operations. CW: Continuous Wave, PD: Photo Detector.

For pulsed operation of the laser, a pulse generator (HP8015A) applies pulsed bias to the p-contact. Digital oscilloscopes (HP 54111D) measure the PD signal (similar to the CW case) and the bias current as determined by a Pearson Electromagnetic Current Torroid (model 2877). The laser operates with pulsed bias of 20 μ sec per 1msec period. The oscilloscope also monitors the bias current pulse. For CW operation, a DC source (Circuit specialist 3645A) supplies bias current flowing through the micro-probe tip and the PDs connect to the voltage meters (Keithley 175) to measure output powers from both sides of the lasers. Rather than use a single microprobe tip to carry bias current to the laser p-contact, two microprobe tips (connected in parallel) were used to reduce the effects of contact distributed impedance and improve the uniformity of the bias current flow to the device. For spectrum measurements, an optical fiber replaces the front PD to measure the optical spectrum of light from the front mirror. An HP Optical Spectrum Analyzer

(HP 71950A) measures the laser spectrum from the target device connected through the optical fiber and transfers and saves to a computer.

The apparatus in Figure 5.2 tests lasers with either pulsed or CW (Continuous Wave) bias. For both cases, the P-I plots show similar slope and similar threshold (Figure 5.3). For the CW operational case, heating of the device shifts the threshold current slightly higher than for pulsed operation [67]. Also for CW operation, the bias current is limited to 20mA (Figure 5.3 (b),(d)) to prevent possible device break down. The P-I curves for pulsed and CW operation appears about same. Therefore, it is sufficient to examine the pulsed P-I plot for the laser characteristics.

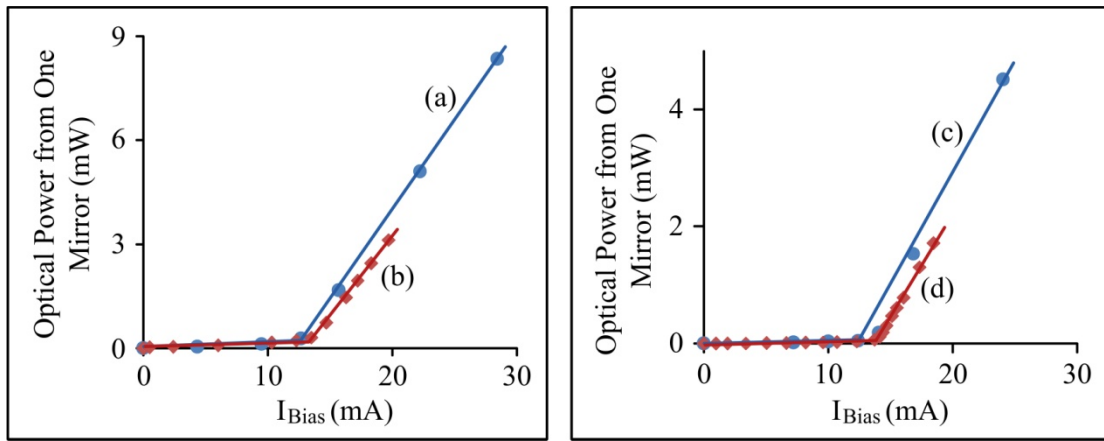


Figure 5.3 Optical power measured from one mirror versus bias current (P-I plots): (a) and (b) present pulsed and CW operation of shallow etched 10 μ m wide laser etched in low power PAW etching, respectively, (c) and (d) show P-I of pulsed and CW operation of deep etched 5 μ m wide laser etched in 70mW PAW, respectively.

5.3 Evaluation of the PAW Etched Laser

The fabrication methods affect the laser characteristics especially as concerns the etching of the waveguide and mirror of the laser. The etching controls the surface roughness and the angle of the side profiles both of which control the mirror reflectance and loss of the devices. Optical power and bias current (P-I) relations characterize the laser devices including mirror reflectance and internal loss of the device which can be directly correlated with the etch

properties. The tests of the laser fabrication and operation evaluate the application of PAW etching to optical devices. For the waveguide, etch depth and surface smoothness of the sidewall can be important while etched facet angle can be the most critical element for the mirror.

In this work, three different designs of lasers (CL2-S, CLS2-D and CE-D) are fabricated and compared. Figure 5.4 illustrates the shallow and deep etched lasers. Figure 5.4 (a) depicts a laser (CL2-S) with conventional shallow-etched ridge-waveguide (etch stopped just before the active layer) and with cleaved mirrors on both ends of the cavity. The waveguide etch depth measures about $1.5\mu\text{m}$. The laser waveguides are etched with and without applying optical energy from the PAW etch laser. Usually, for ridge-waveguide lasers, the waveguide etch stops just before the active layer since otherwise, exposing the active layer to the air increases optical scattering [119] and also increases the surface recombination [67] at the side of the waveguide which causes decrease of the optical efficiency of the laser.

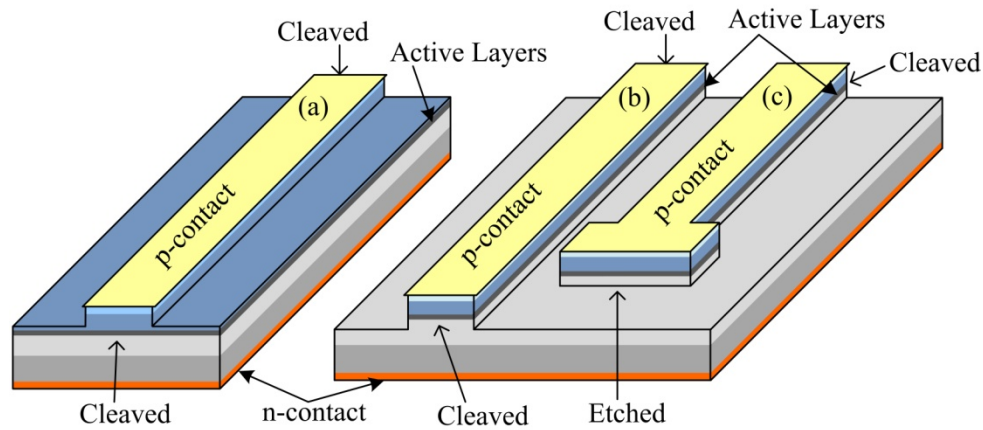


Figure 5.4 Ridged Waveguide Lasers with either two cleaved mirrors (CL2) or one cleaved and one etched mirror (CE). (a) The CL2-S laser has a shallow ridge that does not extend to the active region. (b), (c) The CL2-D and CE-D lasers have deep etched waveguides that have ridge depths past the active layer.

Lasers of the type CL2-D and CE-D depicted in Figures 5.4 (b) and (c) are fabricated with different PAW laser powers that produce the same depth at the waveguide (etch depth from

2 μm to 2.5 μm) and the mirror sides. Some of the lasers have two cleaved mirrors (Figure 5.4 (b)) and some have one etched mirror (Figure 5.4(c)). The deep etched lasers (Figure 5.4 (b) and (c)) are fabricated with two slightly different laser materials, i.e. 894nm (M1-5) and 852nm (M1-3) lasers. Lasers illustrated in Figure 5.4 (a), (b) and (c) are denoted as device CL2-S, CL2-D and CE-D, respectively.

The next section evaluates lasers with two cleaved mirrors but having different waveguides. For comparison of the waveguide, shallow etched waveguide lasers with and without illumination are tested. CL2-S lasers are compared with CL2-D devices fabricated with various PAW laser power. The lasers have two cleaved mirrors to rule out mirror effects on the laser properties (laser (a) and (b) in Figure 5.4). PAW-etched laser mirrors are evaluated with various PAW powers in Section 5.3.2. The etched mirror CE-D lasers are compared to the lasers with cleaved mirrors CL2-D fabricated with PAW etching (laser (b) and (c) in Figure 5.4). Lasers fabricated with high power PAW show various etch depths depending on the position of the device. Also, some of the lasers have another laser aligned to the etched mirror side causing unique P-I characteristics. Section 5.3.3 discusses CE-D type lasers (one etched mirror) fabricated with high power PAW etching. Deep etched 852nm lasers are reviewed in Section 5.2.4 presenting P-I plots and spectrums of lasers etched with various PAW laser powers.

5.3.1 Comparison of Lasers with Various Etched-Ridge Heights

The laser properties are sensitive to the waveguide etch depth and sidewall profiles – too shallow etching can cause large laser threshold (and failure) due to low optical confinement while deep waveguide etching can alter the laser properties that depend on the sidewall. For deep etching, the carriers in the active layers have increased non-radiative recombination at the air-semiconductor interface which lowers the laser efficiency. In addition, the optical scattering at the sidewall increases for strongly confining waveguides as obtained from the deep etching [119]. As

a result, the properties of the lasers with deep etched waveguides are more sensitive to the sidewall conditions [67].

First consider the effects of the dark versus PAW etching for shallow waveguides with approximately the same etched-ridge depth. Figure 5.5 presents the P-I curve (optical power measured from one mirror versus bias current) for the pulsed operation of lasers with shallow etched waveguides. Both lasers have approximately the same waveguide etch depth ($1.5\mu\text{m}$) (i.e. etch stopped just above the active layers and mirrors are both cleaved, see the heterostructure layer structure in Figure 4.9).

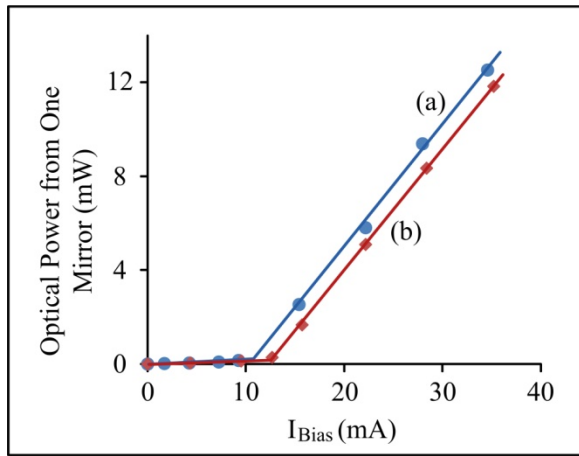


Figure 5.5 Optical power measured from one mirror versus pulsed bias current for shallowly etched waveguide lasers (CL2-S); (a) and (b) present P-I plots corresponding to the waveguide etched using PAW etch powers of about 60mW and 0mW, respectively.

One waveguide was etched with a PAW (532nm) optical power of approximately 60mW and the other in dark. These lasers etched with different PAW powers exhibited about 10mA and 12mA of threshold current, respectively. In general, all PAW-etched waveguide lasers present lower threshold current than those dark etched. Table 5.1 later in this section shows that the PAW etched laser has lower internal loss α_i than the dark etched one. Based on the P-I curve in Figure 5.5 and the parameter calculations listed later in Table 5.1, the PAW etching does improve laser characteristics due to the reduced sidewall angle and lateral etching in the waveguide of the laser. The improvements of the laser P-I curves, however, are not pronounced for the shallow-etched

waveguide lasers since (i) the etch method does not directly affect the active layer and (ii) the optical mode has less sensitivity to the surface roughness in those regions where the effective index produces weak confinement (i.e., where the ridge sidewall meets the horizontal etch plane). With deep etched waveguide lasers, the PAW etching brings clear differences to the laser P-I curve.

Next consider the effects of the dark versus PAW etching for shallow and deep etched waveguides lasers with two cleaved mirrors (CL2-S and CL2-D). For the deep-etched ridges, the difference in threshold can be attributed to the difference in sidewall conditions (angle, profile contour and sidewall angle). Figure 5.6 compares the shallow etched waveguide lasers (CL2-S) and the deep etched waveguide lasers (CL2-D). Figures 5.6 (a) and (b) show the laser properties for CLS-2 and Figures 5.6 (c), (d) and (e)) show the CL2-D lasers. The deep etched waveguide lasers (Figure 5.6 (c), (d) and (e)) are etched under the various PAW powers (from 0mW to 100mW). As shown in Figure 5.6 (a) and (b), the P-I does not show much difference by the etch methods for the shallow etched waveguide lasers. When the waveguide is etched deeper than the active layers, the sidewall profile and roughness at the waveguide affect the laser performance (Figure 5.6 (c), (d) and (e)) through larger threshold and decreased external differential efficiency (i.e., slope, since the slope is proportional to the ratio of mirror loss to total loss).

For deep-etched-waveguide (CL2-D) lasers, the PAW laser power affects the laser P-I characteristics (Figure 5.6 (c), (d), and (e)). For high-power PAW-etching ($P_{PAW} \geq 70\text{mW}$) in Figure 5.6 (e)), the CL2-D lasers have similar characteristics to shallowly etched waveguide lasers ($I_{th} \sim 14.7\text{mA}$). From the P-I plot, CL2 lasers etched in dark (Figure 5.6 (c)) also have about same threshold current (or little larger) as the high power etched ones. Low-power PAW-etched lasers ($P_{PAW} \leq 5\text{mW}$) in Figure 5.6 (d)) show higher threshold current than high-power PAW-etched lasers primarily because they have twice the length of the dark etched ones. The slopes of the P-I curve measures lower than that for high-power PAW-etched lasers so as to indicate higher internal loss and lower efficiency for the low-power PAW lasers (Table 5.1 #3-6 and #7-10). The

laser parameters calculated using equations in Section 5.1 shows that the internal loss of high power PAW etched CL2-D laser calculates to be in the range 16.2~23.1 (Table 5.1 #7-10) while dark or low-power PAW-etched CL2-D laser shows higher values in the range 40.7~56.4 (Table 5.1 #3-6). High-power PAW etched CL2-D lasers also present lower differential quantum efficiency than dark etched ones. In both P-I plots, CL2-D lasers etched with low-power PAW have higher threshold than dark-etched lasers since lower power PAW-etched lasers have about twice of the length of the dark etched one.

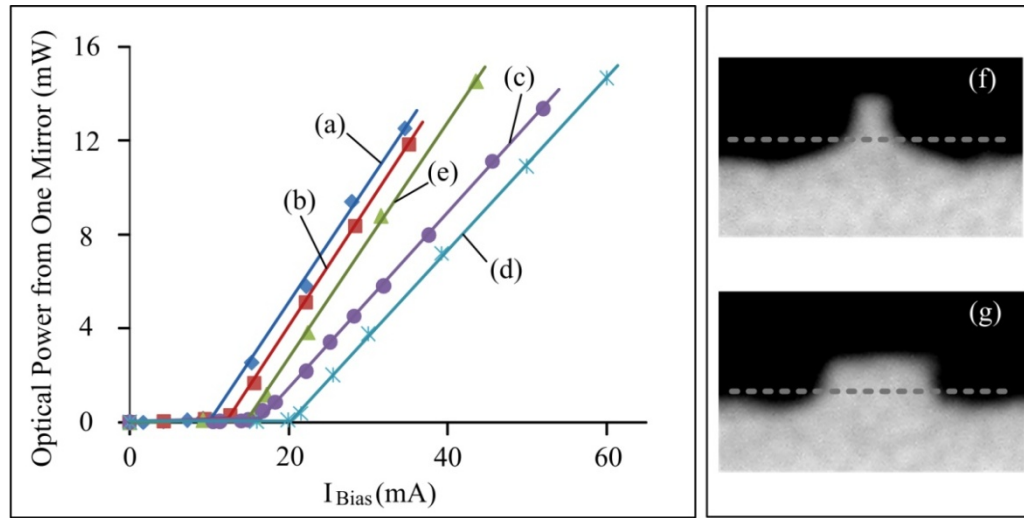


Figure 5.6 Optical Power measured from one mirror versus bias current (P-I) plot of shallow and deep etched waveguide lasers with mask width of $10\mu\text{m}$ and sidewall pictures; (a) and (b) presents P-I plots of the shallow etched waveguide laser with two cleaved mirrors (CL2-S) using PAW etch laser powers of approximately 60mW and 0mW, respectively. (c), (d) and (e) present P-I plots of deep etched waveguide lasers (CL2-D) with PAW powers of 0mW, 5mW and 70mW, respectively. Laser operation measured with pulsed input bias current. (f) and (g) shows the microscope pictures of side profile correspond to the dark and low PAW power etched laser (plot (c) and (d)) and high PAW power etched laser. (e), respectively. Gray dotted line in Figure (f) and (g) indicates the active layer.

The difference in the deep etched waveguides are clear from the microscope pictures shown in Figure 5.6 (f) and (g). The pictures show post-etched sidewall profiles for the same mask width (laser width $\sim 5\mu\text{m}$). From the picture, the high-power PAW-etched lasers show

much less lateral etching than for the low-power etched ones. The $5\mu\text{m}$ wide, low-power PAW-etched lasers have post etched widths of about $1.46\mu\text{m}$ while high-power PAW etching produces about $4.3\mu\text{m}$ wide lasers. The post-etched laser width affects the threshold current density. The high-power PAW-etched laser has threshold current density (J_{th}) of approximately 1.2 KA/cm^2 while dark-etched laser shows about five times higher threshold current density ($J_{\text{th}} \sim 5.3\text{ KA/cm}^2$) for the lasers with same mask width ($W \sim 5\mu\text{m}$). In addition to the lateral etch considerations, the sidewall profile is flatter and at more nearly vertical angles for high-power PAW-etched lasers than for low-power PAW-etched ones. The sidewall conditions at the active layer play an important role to decide laser characteristics especially for the deep etched lasers.

The lasers compared in the Figure 5.6 slightly differ in length and width. It is well known that different lengths of the laser produce different threshold current [67]. The etching method also produces size variations of the laser due to the lateral etch rate dependency on the PAW power as shown in Table 5.1. Figure 5.7 shows optical power measured from one mirror of the laser versus input current density. The use of current density helps to remove the length dependence (except for the mirror term).

The optical power measured from one side of the mirror versus bias current density plot (P-J) in Figure 5.7 shows similar characteristics to the lasers with the P-I plots in Figure 5.6 except the dark and low power PAW etched ($P_{\text{PAW}} \sim 5\text{mW}$) lasers (Figure 5.7 (c) and (d)). In the P-I plot, dark etched laser has lower threshold current than low power PAW etched laser due to the longer laser length of low power etched laser ($\sim 400\mu\text{m}$) than other lasers ($200 \sim 240\mu\text{m}$). P-J plot shows the threshold current density of the lasers decrease as PAW power increase by removing laser length dependence (Figure 5.7 (c), (d) and (e)). P-I CL2-D lasers etched with high power PAW have slightly higher threshold current density compared with shallowly etched lasers and about same slope as shown in the optical power versus bias current plot (P-I). Further CL2-D lasers etched in dark and low-power PAW (Figure 5.7 (c) and (d)) show higher threshold

current density than (1) CL2-S lasers etched either in the dark or with a high-power laser (Figure 5.7 (a) and (b)) and (2) CL2-D laser etched with high-power PAW ($P_{PAW} \geq 70\text{mW}$) (Figure 5.7 (e)).

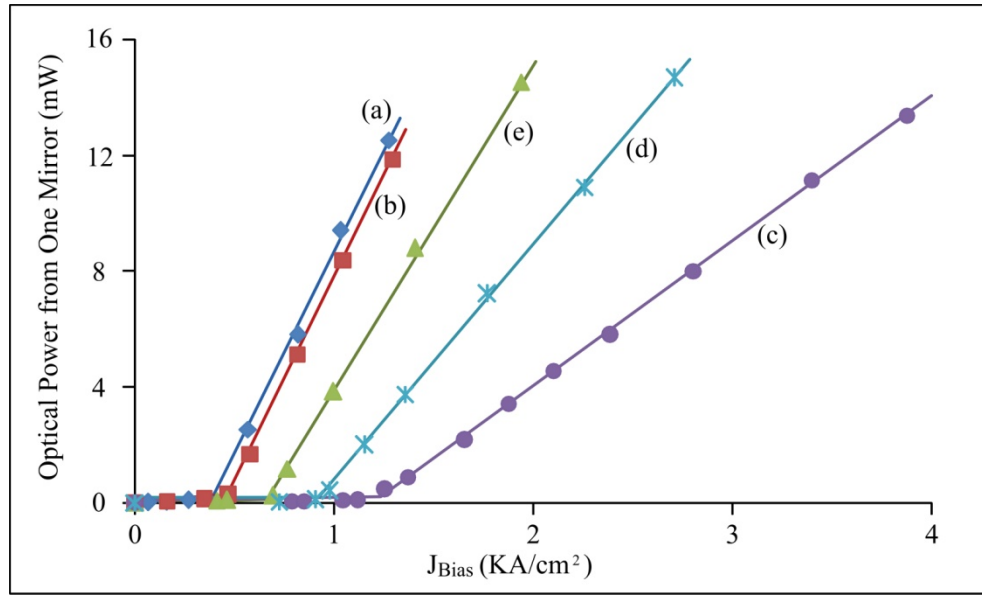


Figure 5.7 Optical Power measured from one mirror versus bias current density (P-J) plot of shallow and deep etched laser waveguides ($10\mu\text{m}$ wide); (a) and (b) presents P-J plots of the shallow etched waveguide laser with two cleaved mirrors (CL2-S) using PAW etch powers of about 60mW and 0mW, respectively. (c), (d) and (e) present P-J plots of deep-etched waveguide lasers (CL2-D) with PAW laser powers of 0mW, 5mW and 70mW, respectively. Laser operation measured with pulsed bias current.

From both P-I and P-J plots, the etching method does not much affect the laser characteristics (Table 5.1 #1 and 2) until the etching reaches the active region where the actual light generation occurs. When the etching passes through the active layer, the quality of the side wall including the geometrical profile and roughness becomes one of the major elements to determine the device characteristics [119]. From the optical inspection of the post-etched device, the sidewall profile varies by the PAW laser power. For low power PAW illumination (less than 5mW), the etched sidewall looks almost the same as for dark etching which produces the larger

lateral etching with angled side walls. For the high power PAW etched devices, the sidewall looks very different than the low power PAW etched ones – less lateral etching and flatter sidewall (Figure 5.6 (f) and (g), Figure 5.8). The difference correlates with the P-I and P-J plots of the devices in Figure 5.6 and 5.7.

Table 5.1 Laser Parameter of CL2-S and CL2-D Lasers

#	Type	P_{PAW}	L	W_m	W_e	I_{th}	J_{th}	M	α_i	η_d
1	A	60	400	10	6.8	9.7	0.36	1.00	11.7	0.72
2	A	0	400	10	6.8	12.43	0.46	1.05	19.46	0.76
3	B	0	222	5	1.36	15.9	5.29	0.68	56.4	0.49
4				10	6.04	15.7	1.17	0.73	40.5	0.53
5				15	10.59	20.8	0.89	0.79	40.5	0.57
6				20	15.19	21.4	0.64	0.75	46.7	0.54
7	B	70	243	5	4.3	10.3	0.99	0.95	23.1	0.68
8				10	9.26	14.7	0.66	0.97	21.3	0.70
9				15	14.23	18.7	0.54	0.93	16.2	0.67
10				20	19.14	24	0.52	1.05	16.2	0.75

CL2-S: Shallow etched waveguide, CL2-D: Deep etched waveguide laser, P_{PAW} (mW): PAW laser power, L(μm): Cavity length, W_m (μm): Laser width from mask, W_e (μm): Actual device width after etching, I_{th} (mA): Threshold current, J_{th} (KA/cm²): Threshold current density, M: total slope of the P-I plot, α_i (cm⁻¹): Internal loss, η_d : Differential quantum efficiency.

Table 5.1 summarizes the parameters determined from Equation (5.1) to (5.8) in Section 5.1 for lasers with two cleaved mirrors and two different types of waveguides (CL2-S and CL2-D). From the table, CL2-S (two cleaved mirrors, shallow etched waveguide) lasers have lower

internal loss than CL2-D lasers (two cleaved mirrors, deep etched waveguide). The surface recombination and optical scattering at the sidewall of the active layer decreases the efficiency of the device which corresponds to higher internal loss. For the same CL2-D lasers, high power PAW etching produces lower internal loss than the dark etched one which proves that the high power PAW etching improves waveguide sidewall properties.

The etched sidewall becomes more important for the mirror facet. For lasers with two cleaved mirrors, problematic waveguide etching may cause threshold shifts due to the larger scattering loss, surface recombination and poor confinement at the waveguide. For the etched mirror lasers, however, poor etching of the mirrors will cause the device to fail. The following section presents results for lasers with one etched and one cleaved mirror (CE-D) and compares the results with lasers having two cleaved mirrors (CL2-D).

5.3.2 Comparison of Deep-Etched Lasers

The threshold current obtained from the cleaved-mirror cases can be compared to the PAW etched mirror case as a matrix of the photo-dissolved sidewall quality (angle and surface condition). Deep etched lasers with cleaved and etched mirror facets (CL2-D and CE-D) are compared for various PAW laser powers. For all the lasers, the waveguides have the same etch depth as the mirror (etched deeper than the active layers) although the etch depth between lasers slightly varies. The laser properties present two different characteristics depending on the PAW laser power used during etching of the waveguide and mirror. With PAW laser power less than 5mW, the PAW etching produces about the same profile as for dark etching, i.e. non-planar sidewall and deep lateral etching. In contrast, PAW etching with laser power higher than 70mW decreases the lateral etching and fabricates flatter sidewalls. The etch properties appear the same for PAW powers of 70mW and 100mW. Figure 5.8 presents sidewall profiles of PAW etched devices for high ($P_{PAW} \geq 70\text{mW}$) and low ($P_{PAW} \leq 5\text{mW}$) PAW laser powers.

Smaller lateral etching and improved planarity make it possible to increase the degree of integration and improve mirror quality of the laser. As a result, the optical power versus bias current plot (P-I) shows clear dependency on the PAW laser power used on the etching process. For convenience of terminology in this work, PAW laser power higher than 70mW and lower than 5mW classifies as high and low power PAW etching, respectively.

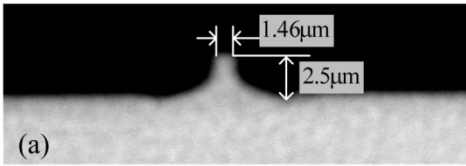
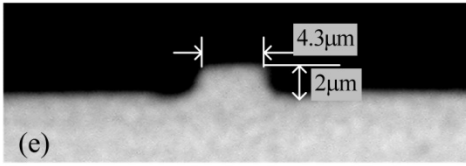
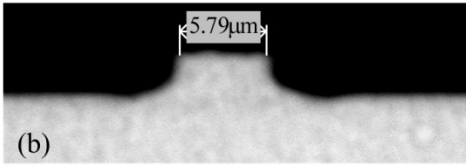
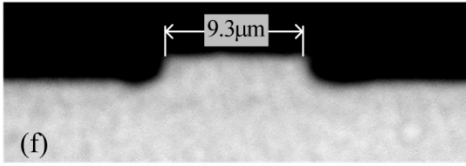
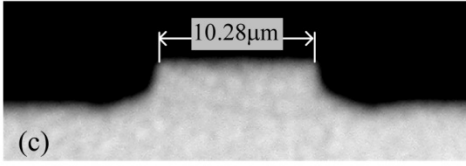
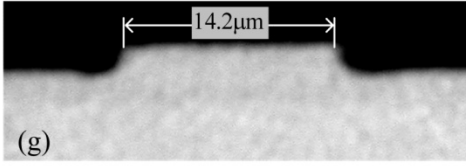
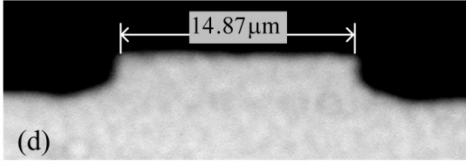
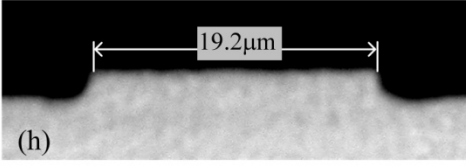
	PAW laser power <5mW	PAW laser power >70mW
5 μ m	 (a)	 (e)
10 μ m	 (b)	 (f)
15 μ m	 (c)	 (g)
20 μ m	 (d)	 (h)

Figure 5.8 Sidewall profile versus PAW laser power. (a), (b), (c) and (d) show microscope pictures of the etched sidewall of 5 μ m, 10 μ m, 15 μ m and 20 μ m wide metal contacted pattern with low power (i.e. lower than 5mW) PAW etching, respectively. (e), (f), (g), and (h) shows etched sidewall of 5 μ m, 10 μ m, 15 μ m and 20 μ m wide metal contacted pattern with high power (i.e. higher than 70mW) PAW etching, respectively. The post-etched widths and depths written on the figures are average values.

All of the CE-D laser devices etched with PAW power less than 5mW did not show any lasing characteristics in P-I measurement. The 5mW of PAW illumination could be too low to modify the etch characteristics of the material. The required PAW power and wavelength can be expected to vary by the material types based on the work presented in Chapters 4 and 5. For dark etching (and low power PAW laser), the lateral etch distance of the chemical etching is about the same as the vertical etch. From the microscope picture of the side profile (Figure 5.8 (a)), the 5 μ m metal contact reduces to about 1.46 μ m after the etching of the laser devices which makes it difficult to use these contacts due to mechanical breakage and electrical burn-out during the P-I tests. For those 5 μ m lasers that survive the probes, the narrow width increases the laser threshold and the heating. However, heating problems are compounded for the deep etched lasers as the thermal resistance to the wafer increases with increasing ridge depth. In addition, calculations of threshold for narrower lasers need to account for relatively smaller pump efficiency due to (i) sidewall recombination, (ii) variations in optical scattering as the sidewall is positioned closer to the high-intensity center of the optical mode, and (iii) transitions from multimode to single mode behavior. Not only the lateral etching but also the etched sidewall profile affects the optical output of the laser devices.

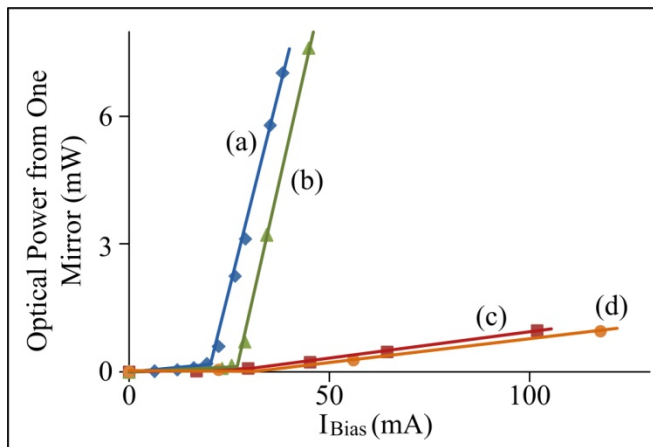


Figure 5.9 Optical Power measured from one mirror versus bias current (P-I) plot for deep-etched 15 μ m wide laser using low power PAW etching. P-I measured in pulsed operation: (a) and (b) show both CL2-D lasers etched in dark and low power PAW etch laser, respectively. (c) and (d) shows CE-D laser etched in dark and with low power PAW, respectively.

Under low-power etching, the designed laser widths of 10 μm , 15 μm , 20 μm wide lasers reduce to 5.79 μm , 10.28 μm , 14.87 μm after etching. Figure 5.9 compares P-I plots of laser fabricated in dark and with low power PAW etching for CL2-D and CE-D lasers. Lasers with two cleaved mirrors (CL2-D) can still lase even with inefficient waveguides (Figure 5.9 (a) and (b)). However, due to the non-planar profile of the etched mirror as shown in the Figure 5.8 (b), (c) and (d), none of the Low-Power PAW-etched etched-mirror devices (CE-D) work as a laser (Figure 5.9 (c) and (d)).

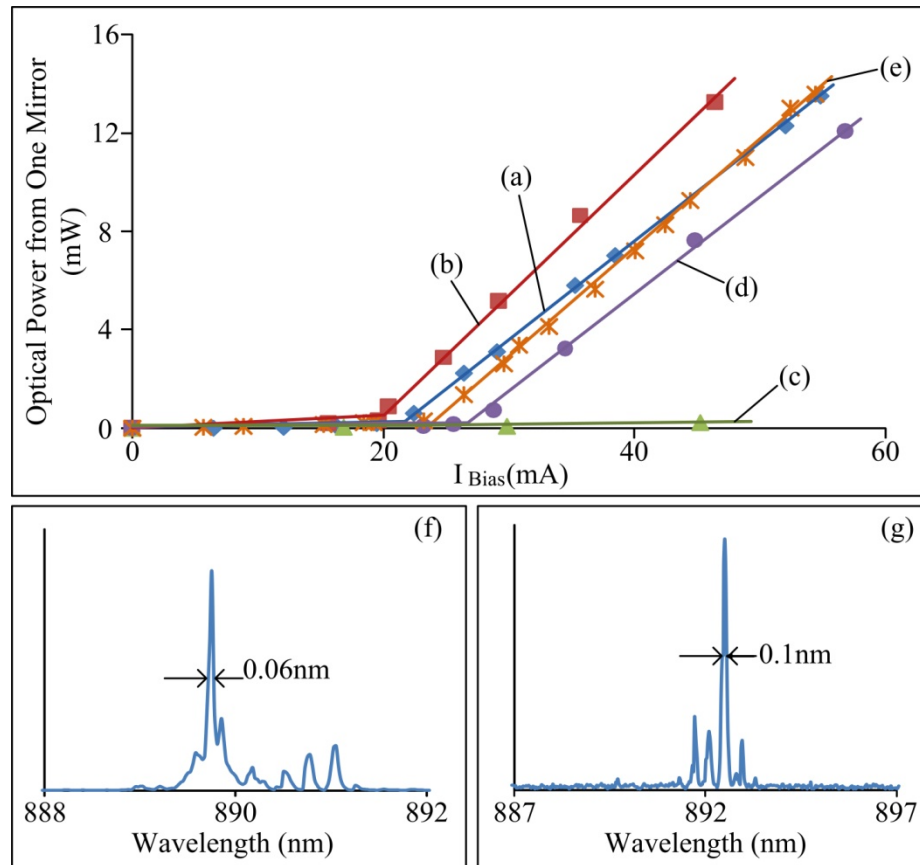


Figure 5.10 Optical power measured from one mirror versus input bias current from (a) CL2-D etched in dark, (b) CL2-D etched with high-power PAW, (c) etched-mirror on CE-D etched in low power PAW, (d) etched-mirror on CE-D etched in high power PAW, (e) cleaved-mirror on CE-D etched in high-power PAW. Example optical spectrums of CE-D lasers: (f) $P_{\text{PAW}} \sim 100\text{mW}$, CE-D laser, 5 μm Wide, $I_{\text{Bias}} = 39.2\text{mA}$, $P_{\text{out}} = 8.97\text{mW}$, (g) $P_{\text{PAW}} \sim 100\text{mW}$, CE-D laser, 20 μm Wide, $I_{\text{Bias}} = 36.8\text{mA}$, $P_{\text{out}} = 3.24\text{mW}$.

Contrary to the low-power PAW cases in Figure 5.9, CE lasers fabricated using high power PAW have comparable threshold current with CL2-D devices (Figure 5.10). The better performance of the laser indicates the etched sidewall is improved with higher power PAW illumination. From Figure 5.8, the lateral etch decreases and maintains nearly vertical sidewalls with high power ($P_{PAW} \geq 70\text{mW}$) PAW illumination. The post-etch widths measure approximately $4.3\mu\text{m}$, $9.3\mu\text{m}$, $14.2\mu\text{m}$, and $19.2\mu\text{m}$ for $5\mu\text{m}$, $10\mu\text{m}$, $15\mu\text{m}$ and $20\mu\text{m}$ wide metal contact lasers, respectively. Figure 5.10 compares the P-I (optical power measured from one mirror versus bias current) plots for $15\mu\text{m}$ wide metal contact lasers with different types of mirrors (CL2-D and C lasers) and PAW power (dark, low and high power PAW). Lengths of the lasers range from 220 to $250\mu\text{m}$.

For CE-D lasers, the etched mirror reflectance can be calculated from the P-I relation of the laser. For lasers with different mirrors for example, one etched and one cleaved mirror in Figure 5.11, the reflectance of the mirrors differ, and therefore the emitted powers differ although they can be related through the reflectance as described in Section 5.1 and Equations (5.7a) and (5.7b) [118].

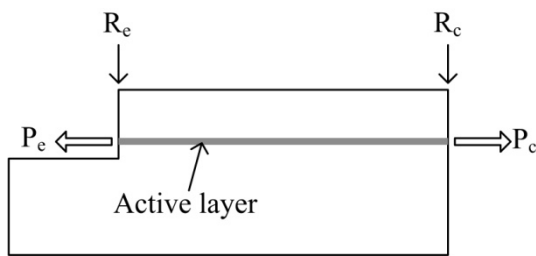


Figure 5.11 Schematics of CE-D laser. R_e and R_c indicate etched and cleaved mirror reflectance. P_e and P_c represent power output from etched and cleaved mirror side.

Similar to the Equations (5.7a) and (5.7b) in Section 5.1, power from cleaved, P_e , and etched mirror, P_c , can be expressed as Equation (5.9) and (5.10).

$$P_e = \frac{(1 - R_e)\sqrt{R_c}}{(\sqrt{R_e} + \sqrt{R_c})(1 - \sqrt{R_e R_c})} P_o \quad (5.9)$$

$$P_c = \frac{(1 - R_c)\sqrt{R_e}}{(\sqrt{R_e} + \sqrt{R_c})(1 - \sqrt{R_e R_c})} P_o \quad (5.10)$$

where $P_o = P_e + P_c$, the total power from the laser. And optical power from etched and cleaved mirror can be expressed as follow

$$\frac{\sqrt{R_e}}{(1 - R_e)} P_e = \frac{\sqrt{R_c}}{(1 - R_c)} P_c \quad (5.11)$$

Similar to the calculations in Section 5.1, reflectance of etched mirror can be determined from the cleaved and etched mirrors (P_c and P_e) as a function of bias current I and the slopes $M_c = dP_c/dI$ and $M_e = dP_e/dI$ measured from P-I plot from cleaved and etched mirror. Defining the ratio $z = M_e/M_c$ allows one to find R_e (etched mirror reflectance) given that one knows R_c (cleaved mirror reflectance) using Equation (5.12). In this work, cleaved mirror reflectance R_e is assumed to be 0.3[67, 118].

$$R_e = \left[1 + \frac{z^2(1 - R_c)^2}{2R_c} \right] - \left\{ \left[1 + \frac{z^2(1 - R_c)^2}{2R_c} \right]^2 - 1 \right\}^{1/2} \quad (5.12)$$

From knowledge of the total slope of the PI curve $M = M_c + M_e$ and reflectance of both mirrors, one can deduce the mirror loss α_m and then the internal loss α_i from Equation (5.1) and (5.4). The external differential quantum efficiency η_d can be determined from Equation (5.5). Table 5.2 shows the parameters of CL2-D and CE-D lasers.

For lasers with two cleaved mirrors (CL2-D), those etched with high-power PAW have lower threshold currents than dark etched ones (Figure 5.10 (a) and (b)) as discussed in the previous section. The better waveguides obtained from the high-power PAW etching improves the laser properties with same mirror conditions. The high-power PAW-fabricated etched mirror for the CE-D laser (Figure 5.10 (d) and (e)) have threshold currents of 23mA while the dark PAW-etched CE-D lasers do not lase (Figure 5.10 (c)). The P-I curves separately measured from the cleaved and etched mirrors show the same threshold current but the etched mirror has the

larger slope since it has the smaller reflectance (compare Figures 5.10 (d) and (e)). The slopes are $M_e = 0.44$ and $M_c = 0.38$.

The set of CE-D lasers (laser #1-6 in Table 5.2) produced an average R_e (etched mirror reflectance) of 87% of R_c (cleaved mirror reflectance). The high power PAW process produced the largest observed reflectance of 93% of R_c for a 216 μm long laser (laser #5 in Table 5.1). Based on a search of the literature, the 93% is the highest observed value for any etched mirror without special coatings. The (high-power PAW) CE-D lasers have 22% higher average threshold compared with similarly etched CL2-D lasers and they have 9.5% higher average threshold than dark-etched CL2-D. The P-I curves (Figure 5.10) and the profiles (Figure 5.8) make it clear that the high-power PAW improves mirror quality by reducing sidewall angle, non-planarity and roughness, and the lateral etching. Figure 5.10 (f) and (g) show example spectrums obtained from the cleaved facet of a high-power PAW-etched ($P=100\text{mW}$). Figure 5.10 (f) shows the spectrum for the 5 μm wide, CE-D laser with bias current $1.5I_{th} = 39.2\text{ mA}$ and Figure 5.10 (g) shows the one for the 20 μm wide, CE-D lasers with bias current $1.4I_{th} = 36.8\text{ mA}$. The full-width half-maximum (FWHM) of the peak measures approximately 0.06nm and 0.1nm, for 5 and 20 μm wide lasers.

As discussed, the etch characteristics affect the waveguide of the laser device and hence the internal distributed optical loss. The waveguides with the sidewalls etched deeper than the active region expose the optical mode to the air-semiconductor interface and increase the optical scattering compared with the more typical shallow etched ones [120]. Figure 5.10 provides a comparison of CL2-D lasers with dark-etched waveguides (Figure 5.10 (a)) and high-power PAW etched waveguides ($P=70\text{mW}$, Figure 5.10 (b)). These two lasers have the same cleaved-mirror conditions but the high-power PAW etched lasers show lower threshold current and lower internal loss than the dark etched ones as a result of improved sidewalls (see Table 5.2). The table

shows that the CL2-D laser optical loss ranged from 16 to 25cm^{-1} for contact widths of 20 to $5\mu\text{m}$, respectively. However, CE-D laser #5 showed the smallest optical loss of 13.8cm^{-1} .

Table 5.2 Parameters of CL2-D and CE-D lasers

#	Type	P_{PAW}	L	W_m	W_e	I_{th}	J_{th}	M	α_i	η_d	R_e/R_c
1	CE-D	100	230	5	4.1	16.3	1.72	0.94	26.6	0.68	0.87
2	CE-D			10	9.2	25.1	1.18	0.69	56.7	0.50	0.80
3	CE-D			15	14.2	23.3	0.72	0.81	39.7	0.59	0.83
4	CE-D			20	19.1	26.3	0.60	0.82	38.9	0.59	0.87
5	CE-D	70	216	15	14.2	33.3	1.02	1.12	13.8	0.67	0.93
6	CE-D			20	19.1	30.9	0.76	0.93	28.3	0.81	0.90
7	CL2-D	70	243	5	4.3	10.3	0.99	0.95	23.1	0.68	--
8	CL2-D			10	9.3	14.7	0.66	0.97	21.3	0.70	--
9	CL2-D			15	14.2	18.7	0.54	0.93	16.2	0.67	--
10	CL2-D			20	19.1	24.0	0.52	1.05	16.2	0.75	--
11	CL2-D	0	222	5	1.5	16	5.3	0.68	56.4	0.49	--
12	CL2-D			10	5.6	15.7	1.19	0.73	40.5	0.53	--
13	CL2-D			15	10.3	20.8	0.89	0.79	40.5	0.57	--
14	CL2-D			20	15.2	21.4	0.68	0.75	46.7	0.54	--

P_{PAW} (mW): PAW laser power, L (μm): Cavity length, W_m (μm): Laser width from mask, W_e (μm): Actual device width after etching, I_{th} (mA): Threshold current, J_{th} (KA/ cm^2): Threshold current density, M: total slope of the P-I plot, α_i (cm^{-1}): Internal loss, η_d : Differential quantum efficiency and R_e/R_c : Ratio of etched vs. cleaved mirror reflectance.

An estimate for a lower bound on the pumping efficiency η can be obtained from Equation (5.4) if one assumes the values α_i for CL2-D #7-10 apply to the CE-D lasers #1-6. The average value is found to be $\eta = 80\%$ while CE-D laser #1 shows the highest value of $\eta = 96\%$ presumably due to the large overlap between the mode and pump current for the narrow 4.1 μm width. The value η is not strongly dependent on the exact value for α_i near 20cm^{-1} since the fractional deviation is on the order of $\pm d\eta/\eta \sim \pm 6\%$. The actual threshold current is reduced from Table 5.2 values by the fraction η . The average upper bound on the normalized external differential efficiency can be estimated as $\eta_d = M/1.388 \eta = 73\%$.

Table 5.2 shows a general trend for the threshold current density J_{th} to increase as laser width decreases [121]. The sidewall recombination plays a role in the bias current efficiency η but the relative contribution decreases with increasing width [67]. Similarly, the threshold current and internal losses can be expected to decrease for wider lasers since the sidewall will be further away from low-order modes propagating primarily near the center of the waveguide [120].

The Photo-Assisted Wet (PAW) etching can produce nearly vertical sidewalls independent of the crystal orientation [117]. It produces the largest known reflectance of 93% of R_c (reflectance of a cleaved mirror) for etched mirrors (without coatings, and independent of crystal direction) in heterostructure lasers. However, the process has not been optimized and there were variations among devices. The average R_e (etched mirror reflectance) is 86% of R_c while the current pump efficiency η was estimated larger than 80%, the external differential efficiency η_d in the range 64% to 73% , and an internal optical loss α_i as low as approximately 14cm^{-1} .

5.3.3 Deep Etched Lasers: One Side Etched Mirror

Three different types of lasers (CL2-S, CL2-D and CE-D) are compared in Sections 5.3.1 and 5.3.2. It is clear that the high-power PAW etching improves the waveguide and mirror facet compared with dark. However, as discussed in Chapter 4, the high-power PAW etch depth

depends on the masking material and position of the patterns. As a result, the laser performance varies by the position of the devices on the sample. This section discusses the operation of the lasers.

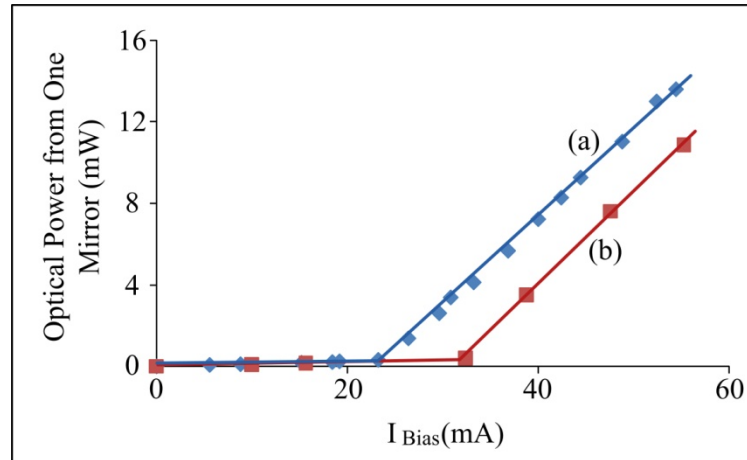


Figure 5.12 P-I plot of CE-D lasers with high power PAW etching ($P_{PAW} \geq 70\text{mW}$) placed (a) near the edge and (b) center of the sample.

Figure 5.12 present CE-D lasers etched with high power PAW from different positions on the sample. Threshold current measures higher for the devices placed near the center area of the samples (Figure 5.12 (b)) than for the ones placed toward the edge of the patterned area (Figure 5.12 (a)) due to the etch depth difference at two areas. From the profilometer measurement, etch depth measures about $1.7\mu\text{m}$ near the center while it measures about $2\mu\text{m}$ for the patterns at the outer area. Most of the good samples presented in the Section 5.3.2 are taken from the edge area of the sample. The uniformity of etch depth needs to be controlled for practical applications of the PAW etching. Excessive electron charging near the metal mask can reduce the etch rate at the center. The PAW etching can be improved by finding a way to discharge the excess electrons at the center area or by finding an optimum PAW power. Also, it is observed that some of the CE-D high-power PAW-etched lasers have more than one slope in the P-I plot as shown in Figure 5.13 (b).

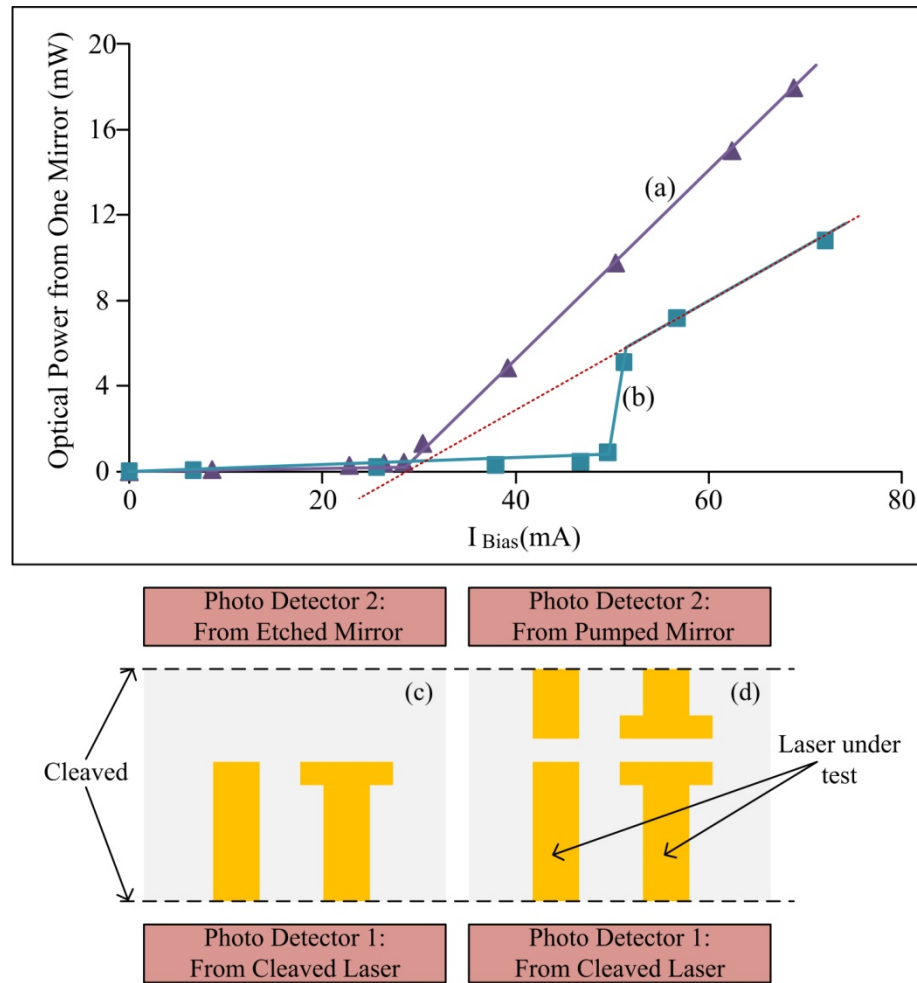


Figure 5.13 Optical power measured from one mirror versus bias current (P-I) plot for CE-D type lasers: (a) single laser without a second laser optically coupled through etched mirrors, and (b) two lasers optically coupled through the etched mirrors. (c) and (d) illustrate lasers measured (a) and (b), respectively. The laser (a) is about $230\mu\text{m}$ long and (b) is approximately $249\mu\text{m}$ long with same width.

The CE-D lasers have two different designs as shown in the Figure 5.13 (c) and (d). In Figure 5.13, The CE-D laser with two slopes in the P-I plot is butt-coupled to another short laser through two etched mirrors as shown in Figure 5.13 (d). For the type in Figure 5.13 (d), the ‘main’ laser (i.e., the one providing the P-I curve) has a ‘secondary’ laser optically coupled through etched mirrors. The separation between the main and secondary laser is approximately $20\mu\text{m}$. The beam from the main laser couples into the secondary laser (unbiased) where it is

absorbed to produce carrier pairs and thereby alters the optical absorption. That is, the secondary laser can operate as a saturable absorber. Increasing the optical beam from the main laser reduces the (differential) optical absorption until the waveguide reaches transparency at which point, the combination of two lasers behave as a single laser and produce the P-I curve shown in the figure. Due to the absorption, the secondary laser brings the threshold current higher than that expected for the main laser and causes a sudden increase of the laser power and generates a step-like P-I plot. For the lasers with an absorber on the etched mirror side as in the Figure 5.13 (b) and (d), extending the straight line passing through the upper data points to the x-axis produces approximately the same threshold current as the laser shown in Figure 5.13 (a) (dashed line in the Figure 5.13 (b)).

5.3.4 Fabrication and Tests of 852nm Lasers

As discussed in previous sections, PAW etching using illumination power greater than approximately 70mW successfully fabricates optical devices using 894 nm laser heterostructure materials. In this section, high power PAW etching fabricates etched-mirror lasers using different heterostructure (852nm laser heterostructure). In Chapter 4, both 894nm and 852nm material shows identical etch properties with high power PAW denoted as M1 sample. The etched lasers show good lasing properties for high-power PAW but with different laser parameters (such as threshold current) which can be caused by the active layer structure differences from two materials. Detailed layer structures are illustrated in Figure 4.9 in Chapter 4.

PAW etching with various illumination powers fabricates 852nm lasers with identical geometry to those using the 894nm material. For the comparison, two different types of devices can be classified as CL2-D for two cleaved mirrors and as CE-D for one etched and one cleaved mirror. The lasers are etched with different PAW powers. Figure 5.14 displays the P-I characteristic and spectrums of CL2-D and CE-D lasers etched with different PAW powers.

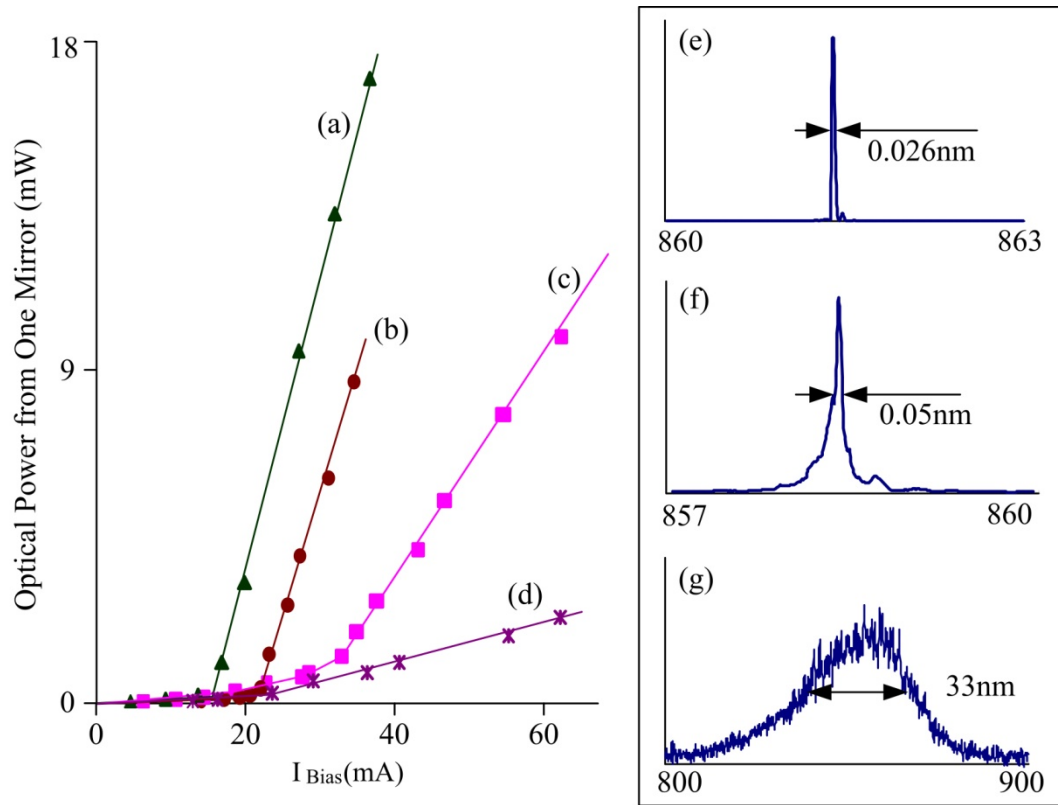


Figure 5.14 Optical power measured from one mirror versus bias current (P-I) plot of 852nm lasers. (a) and (b) presents both cleaved mirror laser (CL2-D) etched in high power PAW and Dark. (c) and (d) shows one etched (CE-D) lasers fabricated with high power PAW and Dark. (e), (f) and (g) shows laser spectrum of CE-D lasers; (e) high power PAW Etched 5 μ m wide and 256.9 μ m long, I_{Bias} =18.2mA, (f) high power PAW Etched 20 μ m wide and 256.9 μ m long, I_{Bias} =38.8mA and (g) with Dark Etched 15 μ m wide and 273.6 μ m long, I_{Bias} =60mA.

The lasers have width of 20 μ m and length of approximately 250 μ m. Figures 5.14 (d) and (g) show the laser devices with dark etched CE-D lasers present LED-like characteristics, which indicate the importance of the mirror quality for lasing. Figure 5.14 (c) shows an example P-I curve of high power PAW etched CE-D laser that is comparable to a laser with CL2-D laser in Figure 5.14 (a). High-power PAW-etched CE-D lasers (Figure 5.14 (c)) show clear lasing patterns in the PI curves with threshold currents about 28mA and sharp peaks in the spectrum with bias current $I_{Bias} \sim 1.4I_{th} = 38.8$ mA (Figure 5.14 (f)) while a dark wet-etched CE-D laser produces broad output spectrum as shown in Figure 5.14 (g). Threshold current as low as 14mA

and narrow single-mode spectrum (FWHM as narrow as 0.026nm) have been achieved from 5 μ m wide and 250 μ m long high-power PAW etched CE-D laser with bias current $I_{\text{Bias}} \sim 1.3I_{\text{th}} = 18.2\text{mA}$ (Figure 5.14 (e)). In this example, the laser threshold is about twice that for a laser with two cleaved mirrors fabricated under the same condition (Figure 5.14 (a)).

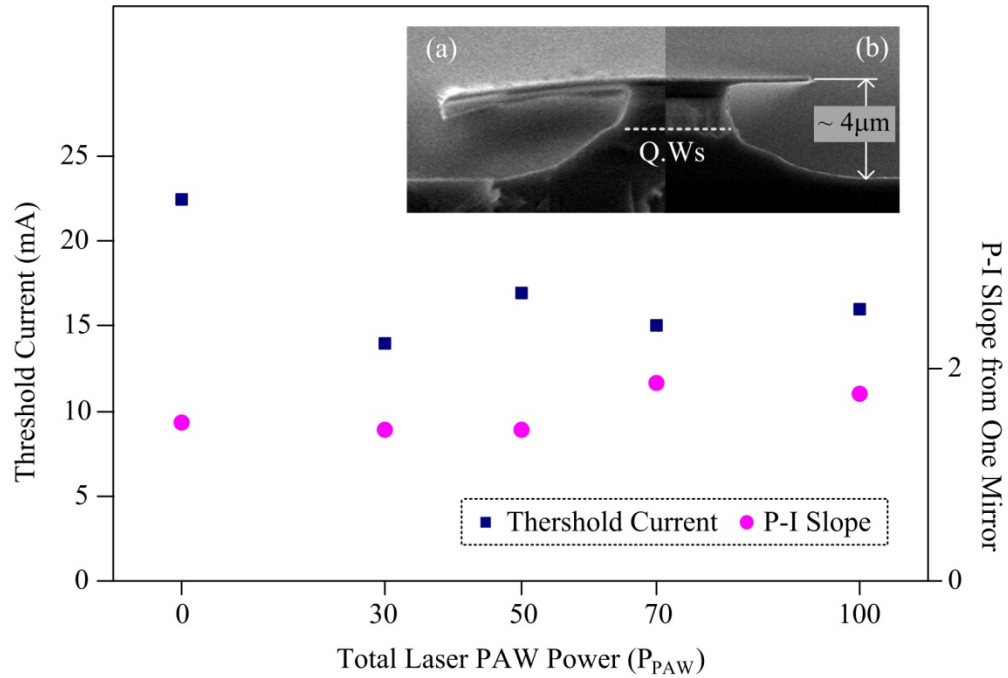


Figure 5.15 Threshold current and slope versus etching power for lasers with two cleaved mirrors and deep-etched waveguides (CL2-D). Pictures show typical (a) Dark Wet etched and (b) PAW etched side profiles.

The waveguide profile also affects the threshold current of the laser as shown in the 894nm lasers in the Figure 5.8 and 5.10. From Figure 5.14 (a) and (b), the PAW-etched laser has lower threshold current than a dark-etched laser with the same geometry of two cleaved mirrors. The differences in Figure 5.14 (a) and (b) indicate the PAW-etched waveguide works significantly better than the dark wet etched case. Figure 5.15 compares threshold currents and P-I slopes from laser devices with different PAW powers and the figure also shows SEM pictures of the PAW and dark etched side profile. For lasers with two cleaved mirrors, the dark etched

waveguides show higher threshold current. The threshold does not vary much for PAW power ranging from 30mW to 100mW which indicates the side profiles are about the same in this region of PAW light source.

Figure 5.15 (a) and (b) respectively present typical SEM pictures of dark and PAW etched sidewall for the MQW laser material used in this work. The dark etched device shows large lateral etching and angled side profiles. The angle changes for different layers. On the contrary, the PAW-etched side profile has less lateral etching and flatter sidewall angle. The PAW-etched side profile does not show crystal direction dependencies [97] unlike with the dark wet etching. The mirror angle is one of the very important factors for lasing as evidence by the fact that the dark-etched mirrors with various facet angles do not lase while the PAW-etched ones with nearly vertical profiles do lase.

5.4 Multimode Behavior of CE-D and CL2-D Lasers

For the wide lasers, lateral modes might affect the deduced reflectance of the laser mirrors since the light can reflect at an angle other than normal incidence [118, 122]. In the cases that the PI curves in Section 5.3 depart from straight-line behavior, the threshold and internal losses are deduced from the low power (linear) portion of the curve. However, the multimode behavior of CE-D and CL2-D is briefly checked. Some lasers exhibited multimode behavior at larger (pulsed) bias current. The present section illustrates the behavior.

5.4.1 Modes Observations

The CL2-D lasers are mounted on copper blocks as describe in Figure 5.2. Pulsed bias is applied (20μsec on, 1msec off) but there is little difference for longer pulse widths. Figure 5.16 (a) shows the samples (20μm wide, 256μm long) under the optical microscope with two 12μm probe tips touching the laser. The figure also shows the copper block around the laser which

reflects the optical mode up into the microscope camera. The Figure 5.2 (b)-(h) span an areas of $1000 \times 718\mu\text{m}^2$ and $647 \times 462\mu\text{m}^2$ for Figure 5.2 (a).

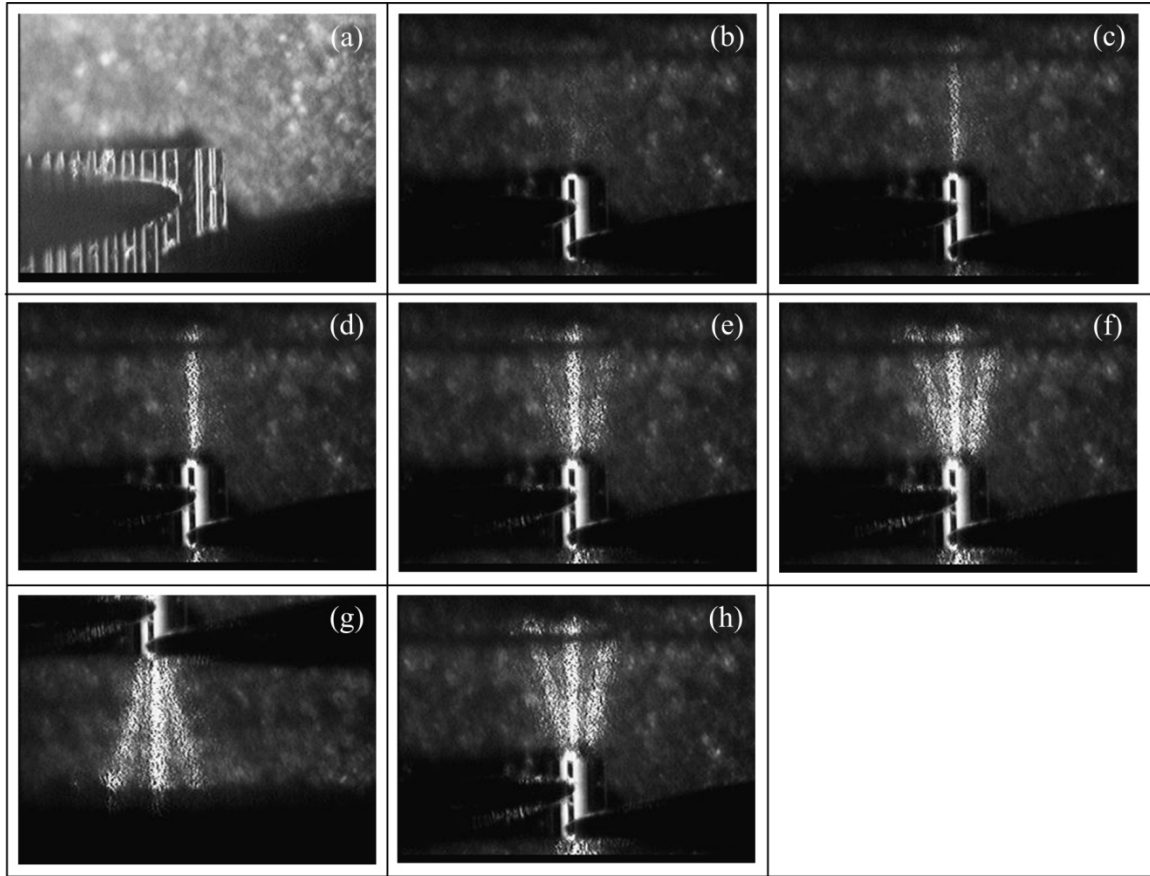


Figure 5.16 Microscope pictures of CL2-D laser ($20\mu\text{m}$ wide, $256\mu\text{m}$ long) with two $12\mu\text{m}$ probe tips. (a) shows overall device picture with $I_{\text{Bias}} = 0\text{mA}$. Microscope pictures of one laser device with different bias current (b) $I_{\text{Bias}} = 15\text{mA}$, (c) $I_{\text{Bias}} = 16\text{mA}$, (d) $I_{\text{Bias}} = 17.6\text{mA}$, (e) $I_{\text{Bias}} = 20\text{mA}$, (f) $I_{\text{Bias}} = 24\text{mA}$, (g) $I_{\text{Bias}} = 25.8\text{mA}$, front mirror and (h) $I_{\text{Bias}} = 25.8\text{mA}$, back mirror.

The images appear in Figures 5.16 (b) to (h) shows the results for increasing bias current. The threshold appears to be near 30mA as indicated by the increase of a well defined beam. Near 40mA , one can see a side mode which further clarifies for 48mA . One should note that the large photodetectors used in Figure 5.2 will also collect these side modes; therefore the photocurrent

from the photodetectors will not decrease for the multimode behavior. Both mirrors had the same behavior (Figures 5.16 (g) and (h)).

Custom camera software was used to measure the sizes and angles. In the present case, the side beams make an angle of 18° with respect to the center line. Using Snells law, this translates to about 5° angles of incidence within the cavity of the laser. The multimode path within the laser suggests higher optical scattering loss at the waveguides while the mirror loss can decrease.

One might speculate as to whether the laser might lase totally internally within the cavity by following a zig-zag path and not exit the mirror. In such a case, the angle of incidence at the mirror would need to exceed the critical angle of approximately 17° for this material. An initial model incorporating sidewall roughness [119] shows there will be a minimum in the gain required for such a mode but it is not the absolute minimum. For these lasers with the deep-etched sidewalls, the primary mode appears to be the center mode with multimode behavior for higher currents. Based on the model, the optical losses at the sidewalls are believed responsible for this behavior.

5.4.2 End View of the Single Mode

The present section shows the results for end-on viewing of the laser emission. The samples mirrors make a 45° angle with the line of viewing in the microscope similar to that shown in Figure 5.17. The microprobes make contact with the laser from the open side. The bias current is pulsed same with the previous experiments in Section 5.3. The image is diffraction limited but one can see the emission from the laser in the center mode. The outer modes might not properly enter the microscope objective for viewing, but there is some indication of the side modes. The laser does not emit directly into the lens, but instead the object collects light diffracted from the narrow laser aperture (on the order of 200nm).

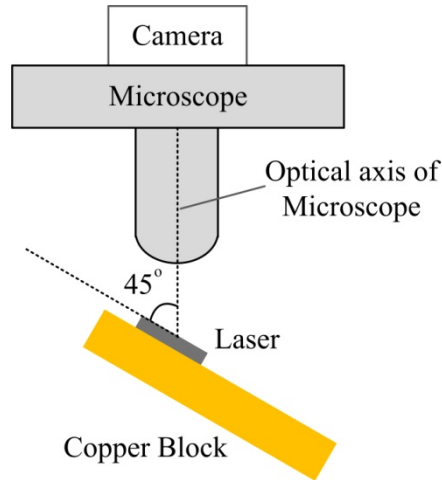


Figure 5.17 Microscope picture taking set up for laser emits at a 45° angle with respect to the optical axis of the microscope.

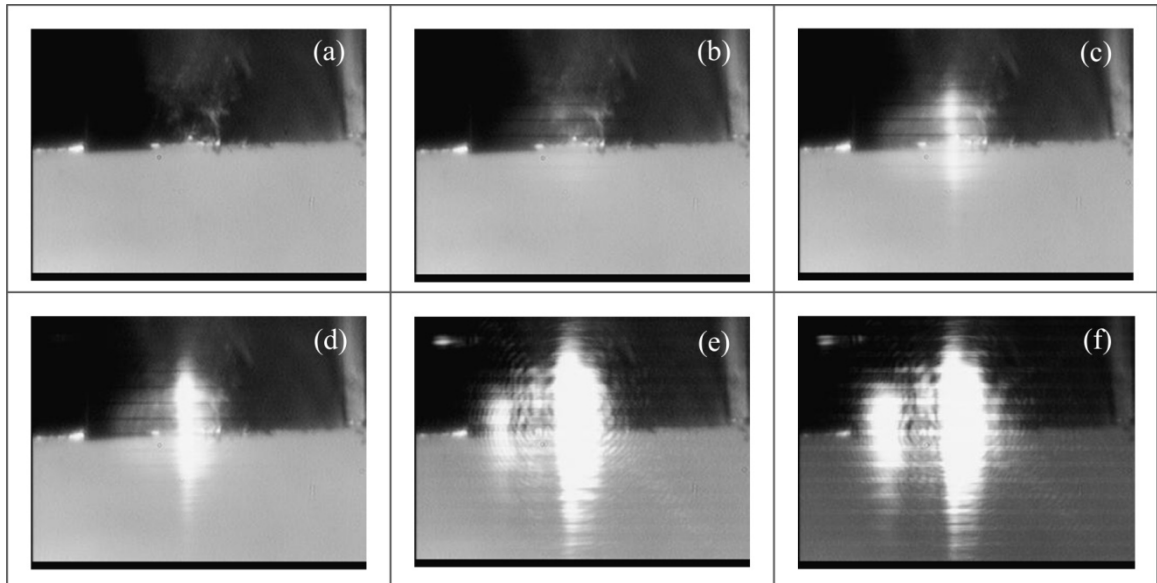


Figure 5.18 Microscope pictures of CL2-D laser front with different bias current (a) $I_{\text{Bias}} = 0\text{mA}$, (b) $I_{\text{Bias}} = 11.2\text{mA}$, (c) $I_{\text{Bias}} = 15.2\text{mA}$, (d) $I_{\text{Bias}} = 15.6\text{mA}$, (e) $I_{\text{Bias}} = 20.2\text{mA}$ and (f) $I_{\text{Bias}} = 27\text{mA}$.

The Figure 5.18 (a) to (g) shows mirror end view of the laser with different bias current ($I_{\text{Bias}} = 0$ to 27mA). The figures indicate that the modes emanate from one side of the laser by drawing the rays back to the laser body. However, this appears to be a remnant of the optical

focus of the microscope although it would need further investigation. The size of the picture can be ascertained by comparison with the $20\mu\text{m}$ width of the laser. One can discern only a slight shift in mode position (on the order a $3\text{-}5\mu\text{m}$) over the range of currents.

5.5 Discussion

Etched lasers have been successfully fabricated using GaAs/AlGaAs MQW material and the PAW etching technique; these lasers have been compared to the dark-etched and cleaved mirror lasers. The PAW etched lasers show similar quality to the cleaved mirrored devices since the R_e (etched mirror reflectance) are as large as 93% of R_c (reflectance of a cleaved mirror) without coatings and independent of crystal direction. However, the process has not been optimized and there were variations among devices. The average R_e was 86% of R_c while the current pump efficiency η was estimated larger than 80%, the external differential efficiency η_d was found to be in the range 64% to 73%, and the internal optical loss was as low as approximately $14(\text{cm}^{-1})$.

The reflectance exceeds the previous reports of wet and dry etched mirror facets. Deep etched mirror facets have been reported with reflectance of 84 and 81% by Merz and Iga, respectively [111, 123]. Ito et al achieves high reflectance (94% of the cleaved mirror reflectance) selectively wet etching of thin active layer after deep etching of the single quantum wall (SQW) laser structure [124]. However, the method does not applicable for the integrated device fabrication due to the high later etchin. Using Dry etching, Yuasa and Bouadma report 75 and 78% of R_c from RIE (Reactive Ion Etching) and IBE (ion-beam-etched) mirror facet [113, 114]. Dry etched mirror facets tend to have lower reflectance than wet etched ones due to the rough surfaces often produced by dry etches. Coldren [115] reduces the surface roughness by wet etching the mirror facet followed by RIE etching. However, the mirror measures lower

reflectance than dry etched mirrors as 58% of R_c . Table 5.3 compares ratio of reflectance of etched and cleaved mirror.

Table 5.3 Comparison of Etched Mirror Reflectance [111, 113- 115, 123-125]

Author (year)	Laser	Etch method	R_e/R_c
Yi	GaAs/AlGaAs MQW	PAW	0.93
Merz (1976)	GaAs/AlGaAs DH	Deep Wet Etching	0.84
Iga (1982)	GaAs/AlGaAs DH	Deep Wet Etching	0.81
Coldren (1982)	InGaAsP-InP DH	RIE and XWEC	0.58
Bouadma (1985)	GaAs/GaAlAs BH	IBE	0.78
Yuasa (1986)	GaAs/AlGaAs MQW	RIBE	0.75
Vawter (1987)	GaAs/AlGaAs DH	RIE	0.52
Ito (1988)	InGaAsP/GaAs SQW	Selective Wet Etching of thin active layer after deep Br-Methanol etching	0.94

* DH: Double Heterostructure, BH: Buried Heterostructure, MQW: Multi-Quantum Wall, SQW: Single Quantum Wall, IBE: ion-beam-etched, RIBE: Reactive Ion Beam Etching, XWEC: Crystallographic Wet Chemical Etching.

Table 5.4 Summaries of Etched TIR mirrors [14, 126-128]

Author (year)	Laser	Etch method	R_{TIR}
Appelman (1990)	GaAs/AlGaAs	CAIBE	0.32
Shimokawa (1990)	GaAs/AlGaAs Single QW	RFABE	0.80
Han (1995)	InGaAs/GaAs/AlGaAs strained-layer QW heterostructure laser	RIE	0.90
Swanson (1995)	GaAs/AlGaAs MQW	ECR	0.81

*CAIBE: Chemically Assisted Ion-Beam-Etching, RFABE: Reactive Fast Atom Beam Etching, RIE: Reactive Ion Etching, ECR: Electron Cyclotron Resonance, R_{TIR} : Reflectance of TIR mirror.

Swanson et. al. reduced roughness by a quick (couple of seconds) wet etch after an ECR etch. The TIR (total internal reflection) mirror reflectance was as high as 81% [14]. Appleman, Shimokawa and Han et al. also reported etched TIR mirror lasers using various dry etching [126-128]. Table 5.4 summarizes the reflectance of the dry etched TIR mirror lasers. Since the ideal TIR mirror has reflectance of 1, reported dry etched TIR mirror shows as high as 90% of the idea reflectance.

Various levels of optical powers are tested for PAW etching techniques. With laser power higher than 70mW (and present wafer topology and mounting), non-uniform etch depth and poor surface conditions start to appear for the PAW etching. From the experiment, reducing the laser power could solve the problem. However, PAW laser power less than 5mW does not modify the etch characteristics. The minimum required laser power to produce an effect on the heterostructure material varies by the layer structure. The surface roughness caused by diffraction patterns can also be removed by improving the optical design of the system or using LED as a light source. For typical GaAs/AlGaAs heterostructure materials evaluated in this research, the laser power needs to be maintained higher than 70mW (refer to Table 4.2 in Chapter 4) to produce good sidewall profile and low lateral etching.

With high powers of PAW illumination, heterostructure near the metal patterned area etches slower than blank areas on the sample. Mass charge flow of the excess photo-generated carriers on the surface may cause the regional non-uniformity of the etch depth. Detailed research on this matter will be continued. For device fabrication, use of a reflectometer can solve the problem by monitoring the etch depth at the patterned layer during the etch process. Further research on the surface current flow might lead to the solution of the etch depth problem in the high power PAW etching.

Chapter 6 Summary and Conclusions

Fabricating a laser without cleaved mirrors constitutes one of the major tasks to realize integrated optics and optoelectronics. Vertical etches must maintain good control of lateral etching to prevent undercutting of metal contacts and increase the degree of integration. In addition to the vertical side wall for integrated laser mirrors, other integrated optical devices also require many other etch characteristics including various etched-sidewall profiles and angles ranging from shallow etched-slopes for electrical contacts to vertical flat smooth surfaces for integrated laser mirrors.

Generally, device fabrication requires either dry or wet etching processes. Dry etching is the most widely accepted process to fabricate optoelectronic devices [4-9] since it can easily produce vertical mirror facets for active optical elements. However, it is expensive, slow, and most importantly, generates rough surfaces which lead to increased optical loss of the device [10-16].

On the contrary, wet etching has potential advantages over dry etching [11, 12, 14, 17] including lower cost, smoother surfaces, and faster etch speed. However, conventional wet etching has a couple of drawbacks for laser fabrication such as uncontrollable non-vertical sidewall profile and deep lateral etching. The sidewall profiles from wet chemical etching normally depend on the etching solution and the material crystal direction which makes it difficult to produce angles other than that corresponding to the natural crystal direction [21-25].

This work develops a new etch process, Photo-Assisted Wet (PAW) etching, that uses light directed perpendicular to the surface of an etching wafer in order to break the typical crystal-plane etching and thereby control the sidewall profile. The research explores the PAW etching process using both coherent (Laser) and non-coherent (LED) optical sources for different types of material. Samples with different masking materials are investigated with various wavelengths and intensities of light source. Specific combinations control the sidewall profile and etching

characteristics to produce on-demand etch-stop layers and sidewall angles ranging from approximately 0 to 90° without depending on the crystal orientation of the sample. Laser heterostructure materials (EPI and M1 samples) show particularly interesting results due to the complicated layer structures and Quantum Walls. The laser material shows non-uniform etch depth depending on the masking material. Charge flow at the surface contributes to the etch depth variations.

New apparatus for laser-PAW was designed and applied to the PAW etching process for the fabrication of III-V devices. The laser-PAW etch apparatus includes the reflectometer and PL systems for real time etch depth and surface condition measurement. The new techniques fabricate integrated laser mirrors in III-V quantum-well laser heterostructure. These mirror facets do not depend on the crystal orientation. Etched laser mirrors fabricated in this work achieve as high as 93% of the reflectance of the cleaved mirror.

In summary, this work achieves the following:

- Develops new Photo-Assisted Wet (PAW) etching using both incoherent and coherent illumination sources for the fabrication of integrated optical devices.
- Investigates LED-PAW etching for bulk and multilayer materials using non-coherent light sources under various masking conditions, wavelengths and intensity.
- Develops an initial model for bulk material.
- Develops a reflectometer for wet etching using a pulsed laser and capable of determining the etch rate, depth, and the formation of surface microstructure and transition layers in real time.
- Designs and tests new PAW etching apparatus incorporating the reflectometer etch monitor and photoluminescence measurement unit.
- Investigates Laser-PAW etching for multilayer materials under various masking conditions using coherent illumination from a 532nm laser with various emission powers.

- Discovers that exposing metal layers on the heterostructure to the etching solution in specific regions of the sample during laser-PAW etching enhances the etched-sidewall quality.
- Explains the role of insulated, metalized and bare surfaces during the PAW etching.
- Develops diffraction-limited optical measurement of micron-level features, software to measure distance and angle, and a CCD based reflectometer.
- Fabricates and compares heterostructure lasers having two cleaved mirrors with those having one cleaved and one etched mirror.
- Achieves etched mirror reflectance as high as 93% of the cleaved mirror reflectance. These are the first wet-etched heterostructure mirrors with reflectance independent of the crystal orientation.

For understanding the etch mechanism, Chapter 2 presents the theoretical background of semiconductor dissolution in an etching solution; the background includes electrochemistry, wet etch mechanisms and an introduction to photo-chemical etching. Wet etching can be described as electrochemical dissolution of the solid in the etching solution (i.e., electrolyte). Such dissolution occurs via electrochemical reactions between the solid (semiconductor) and the electrolyte (etching solution). At the solid/etching solution interface, the solid dissolution occurs by consuming holes [31-35], which is related to the current flow at the semiconductor/solution interface. Holes at the surface of the solid remove electrons from the bonds and thereby reduce the bonding energy of the surface atoms, which weakens the bonds [36, 37]. Consequently, the accessibility of holes and electrons at the surface can be a determining factor of the solid dissolution rate. The charge transfer and associated current flow represent important factors to determine the etch rate. The Gerischer model explains charge transfer at the interface.

According to the Gerischer model [27], the solid/electrolyte contact has analogy to the

solid-to-solid contact such as for a PN junction. Equilibrium at the solid-etchant interface occurs when the electrochemical potential of a redox system (i.e., the Fermi level of the electrolyte) coincides with that for the solid [27, 33]. However, the charge transfer theories are for very simple redox systems and not directly applicable to the general etching system. Also, the Gerishcer theory assumes that there are no surface states at the solid (semiconductor) surfaces and the material has only one layer (bulk semiconductor material). At the semiconductor/electrolyte interface, electron transfer across the interface occurs via the energy bands [32]. Therefore any variation in the energy bands, such as band bending or shifting, plays very important role in the charge transfer process. The energy band diagram at the interface depends on various factors such as doping type of the semiconductor and Fermi energy level of the redox system, ion concentration in the redox system, and any electrical potential or light applied to the solid.

Applying electrical potential or light to the etching system can lead to variations of the electrochemical parameters for the two phases (semiconductor and electrolyte) [31, 32, 54]. The experiments for the present work indicate that the photo-assisted semiconductor dissolution is more readily applicable to the semiconductor fabrication since the system does not require the complicated apparatus normally required by electro-chemical etching systems with external potential application [54].

Chapters 3 and 4 explore PAW etching using incoherent light from an LED (LED-PAW) and coherent light from a laser (Laser-PAW) with different materials under various conditions. Chapter 4 discusses the fabrication of PAW-etched heterostructure lasers while Chapter 5 presents tests and determined-properties of the etched mirror lasers. The PAW-etching properties depend on the etch conditions including the layer structure of the material, wavelength of light and the masking materials.

The LED-PAW etch is performed with three different wavelengths with an intensity of $64 \pm 10 \text{ mW/cm}^2$. The experiments investigate the LED-PAW etching of various types of multi-layered GaAs/AlGaAs materials using four types of masks (Type 0, 1, 2 and 3) and three different

wavelengths (UV (395nm, 3.14eV), green (530nm, 2.33eV) and red (625nm, 2.00eV)). Type 0 and 1 masks consist solely of photoresist (AZ 5214-E) and e-beam evaporated metal, respectively. Type 2 masks consist of silica in direct contact with the semiconductor, which is then covered with metal layers. To study the Photo-Assisted Wet (PAW) etching with “non-metallic” light-blocking masks, a Type 3 mask employs three layers in the order of silica (on the semiconductor), followed by metal and then topped with photoresist (AZ 5214-E).

From the experiment, it is obvious that the electrochemical reaction of the semiconductor and the etching solution (redox system) under illumination can be influenced by many factors in the system such as light source, layer structure of the target material and the masking material deposited on the sample. Bulk GaAs material produces rather straight forward results. Both UV and green LEDs increase the etch rate of n-type GaAs with Type 1 and 2 masks. N-type GaAs material with Type 2 masks shows vertical sidewalls using the UV LED. The etch profile of the PAW etching depends not only on the light wavelength and intensity, but also on the electrical type of the mask and layer structure of the material. For the n-GaAs, the excess holes move to the etching solution/semiconductor interface to increase the oxidation rate and thereby increase the vertical etching rate. On the other hand, some of the photogenerated electrons transport to the dark region such as under the mask or etched sidewall while others move to the backside of the sample or recombine with holes. The data for the present work suggests that the Type 1 metal-only mask removes excess electrons from the solid by collecting the electrons from the same surface. However, the silica-metal (Type 2) mask blocks the flow through the metal and appears to increase the electron density at the etching sidewall which inhibits oxidation, alters the horizontal etch rate, and thereby changes the etch profile.

In p-type GaAs bulk case, metal only (Type 1) masked samples show slight increases of etch rate under illumination but samples with silica-metal (Type 2) mask shows lower etch rate under illumination than dark wet-chemical etching. With p-GaAs material, photo-generated electrons interfere with the etching in the illuminated areas and cause lower vertical etch rate. The

dark area (under the mask) can still show deep etching. The model of the sidewall angle dependency of the Photo-Assisted Wet (PAW) semiconductor etching for bulk GaAs is suggested. Improvement of the model is necessary for the multi-layered material and includes various photo-dissolution characteristics observed in the experiments.

The PAW etching of multi-layered samples adds complexity to the system and according to the experiments, the results do not directly correlate with the relative etch rate and the type of mask. The experiments show that not only the electrical properties of the mask, but also doping type and concentration, and the energy gap of each layer, and the band bending may have an effect on the photo-carrier dynamics to control the photo-dissolution characteristics of multi-layered materials.

The LED-PAW experiments in Chapter 3 suggest possible applications for the PAW etching of the GaAs and GaAs/AlGaAs multilayer material to device fabrication and can be summarized as follows: (1) Control over the sidewall angles in n-GaAs bulk material requires an oxide layer and the etch mask plays an important role in the photo-dissolution. (2) The experiments show that the aluminum concentration, illumination wavelength and layer structure of the multi-layered affect the PAW etching of a heterostructure (vertical and horizontal etch rate and sidewall angle). For example, applying red (625nm) LED illumination to semi-insulating laser heterostructure, which has a top n-type GaAs layer next to a silica-metal-PR or silica-metal contact, almost completely stops the etching on an $n - \text{Al}_{0.5}\text{Ga}_{0.5}\text{As}$ layer just under the n-GaAs. (3) The photo-dissolution using (i) green (532nm) and UV (395nm) LED illumination on semi-insulating laser heterostructure with silica-metal-PR mask for EPI (laser heterostructure with n-type layers on top) and (ii) green (532nm) LED illumination with a metal mask for M1 samples (laser heterostructure with p-type layers on top) produce a smooth vertical sidewall suitable for integrated semiconductor lasers.

The LED-PAW etch setup has a drawback for practical application to the optical device fabrication. In the etch setup, the distance between target sample and the LED light source has to

be maintained within 5mm to maximize the optical intensity at the target. Laser fabrication requires delicate control of the etch depth for the waveguides. With typical wet chemical etching, it is difficult to control the etch depth since the chemical reaction and the dissolution rate are very sensitive to the etching conditions. The reflectometer etch monitor developed for this research can be utilized for etch depth control. Also, using the reflectometer, the dissolution rate and the surface condition variations can be observed in real time. However, this requirement on the maximum separation distance makes it difficult to incorporate the reflectometer monitoring system into the LED-PAW setup.

The dissolution system for device fabrication uses semiconductor lasers rather than a high-power LED. The intensity of a semiconductor laser can be easily adjusted through the bias current. The low divergence laser beam allows the laser to be backed away from the sample, and thereby provide additional space for optics to combine multiple laser beams and to facilitate the installation of the etch monitor. The laser provides good control over the wavelength, polarization and coherence. Unlike the LED however, the laser cannot uniformly cover large sample areas as a result of the intrinsically low divergence of the beam and in addition, the laser can produce a speckle pattern in the etching surface.

Chapter 4 discusses the new laser PAW apparatus, fabrication processes, and tests for etched laser devices using two different types of laser material, namely the EPI and M1 material. New apparatus was designed and applied to the PAW etching process for the fabrication of III-V devices. The etching apparatus has in-situ, real-time systems including (i) an optical system to expand, filter and dither the etching beam, (ii) a pulsed-laser wet-etch monitor to determine the etch depth, rate, formation of surface microstructure and transition layers in a preselected region of the sample, (iii) a steady-state photoluminescence (PL) monitor using a CCD array that provides 2-D measurements across the etching surface, and (iv) a Photo Detector (PD) and data logging circuit that determines the spatially-integrated steady-state PL during the etching. The etch tests show unexpected result from both EPI and M1 samples. The laser PAW does not agree

with the LED results in Chapter 3. The mask material such as PR or metal affects the etch characteristics under illumination.

The reflectometer and PL monitoring system provide information for the PAW etching of the EPI and M1 samples using the high power laser (total PAW laser power higher than 70mW). The reflectometer signal shows very different signals for PAW illumination than for the dark case. The EPI and M1 samples show some similarity in the characteristics of the reflectometer signal and PL. The reflectometer signal shows a “dip” in the n-AlGaAs layer and the PL intensity drops near the n-AlGaAs layer (before and after the active layer for EPI and M1 sample, respectively). For both EPI and M1 samples, the PL intensity correlates with the primary signal (i.e., average signal) of the reflectometer. Since the PL emission does not interfere with the reflectometer signal detection, the reflectometer dip and reducing fringe height only suggests variations of the surface condition by the laser at the n-type AlGaAs layer.

The “dip” in the n-type AlGaAs layer has different characteristics than previously observed anomalous dip [98], which was due to viscous etch byproduct with mass density larger than that of the etchant that did not bond to the etching surface. There, the reflectometer signal showed the anomalous dips for the p-type layer of the GaAs/AlGaAs laser materials in diffusion-rate-limited phosphoric acid etches without illumination. For the present case, the “dip” for the n-type AlGaAs layer indicates the formation of surface layers (possibly oxide layer) as stable compounds on the etching surface. The reflectance exactly follows the primary reflectometer signal. The PL signal rapidly decreases near the active layer at the n-type semiconductor suggesting large photo-hole consumption at the reaction surface as expected. The reflectometer signal “dip” in the n-AlGaAs layer depends on the PAW laser intensity. The dip in the n-AlGaAs layer starts to appear with average PAW laser intensity of about $10\text{mW}/\text{cm}^2$ and becomes deeper as the laser power increases. It becomes clear with an average PAW laser intensity larger than $70\text{mW}/\text{cm}^2$.

The PAW etching with a high power laser (total $P_{PAW} \geq 70\text{mW}$) is tested on prepared EPI and M1 samples with various masks summarized in the Table 6.1. The tests of the laser fabrication process for both sample types show that a couple of issues need to be addressed. With the Initial Mask for the waveguide, one issue concerns the coverage and arrangement of the mask across the sample surface during etching. The experiments show that the arrangement of the mask pattern (size and the position of the blank area) and material type of the mask affects the PAW etching.

Table 6.1 Definitions for the Etching Masks.

Mask	Description			
Initial-Mask	Uniformly distributed patterns across the sample surface with a 2mm blank region for the reflectometer probe. Processing steps detailed in Section 4.1.1. Appendix E shows detailed mask designs.			
	Waveguide	PR covers metal waveguide patterns. 60% of the surface exposed. (See Section 4.2.2 for detail)		
	Mirror	PR covers the entire sample surface except mirror window. 30% of the surface exposed. (See Section 4.2.3 for detail)		
Modified	Defines two regions “side strips” approximately 1mm wide on either side of the sample at the edge. These strips can be given PR or Metal coatings, or left blank as necessary. The specific configurations are denoted by Both-PR, Both-Blank, and Both-Metal.			
	Both-PR	The side-strips are covered with PR. Light can be absorbed but the PR provides electrical isolation and masks the surface from the etchant.	Waveguide	40% exposure, (See Section 4.2.2.1)
			Mirror	20% exposure, (See Section 4.2.3.1)
	Both-Blank	The side-strips are left blank and surface exposed to etchant and light. Charge can transfer between solid and etchant.	Waveguide	70% exposure, PR-only patterns are still on the blank area. (See Section 4.2.2.2)
			Mirror	50% exposure, (See Section 4.2.3.2)
	Both-Metal	The side-strips are covered with metal. Charge can flow through the metal but the mask isolates the surface from light and etchant.	Waveguide	40% exposure, PR patterns are under the metal covered area. (See Section 4.2.2.3)
			Mirror	20% exposure, PR patterns are under the metal covered area. (See Section 4.2.3.3)

For EPI samples with the Initial-Mask for waveguides, etch inhibition occurs near the reflectometer probed area (near the PR pattern) while the patterned area etches slightly faster than dark etching (positive R_{VR}). From the chapters, R_{VR} is defined as the ratio of ‘the etch rate due solely to photo dissolution’ to ‘the etch rate due solely to dark chemical dissolution’.). When PR covers the side-strips (Both-PR case), the EPI sample near the side-strips etches even slower while the patterned area near the center etches faster than the original waveguide mask case. Compared to the dark etching, the PAW etching increases the etch speed to about 37% (i.e., $R_{VR} = 37$, enhanced) in the center while it decreases about 74% (i.e., $R_{VR} = -74$, inhibited) near the PR covered area. Illumination generates electron-hole pairs at the same surface including under the PR covered area. Since the electrons cannot be consumed in the PR-covered side-strips, they could transport toward the patterned area or blank areas. The excess electron inhibits etching around the PR area.

In contrast to the Both-PR case, the etch rate for the Both-Blank case slightly decreases at the patterned area in the center ($R_{VR} = -5$) and increases ($R_{VR} = 73$) at the part of the patterned area near the side-strips and the metal at the bottom. The Both-Metal case shows similar etch characteristics to the Both-Blank case even with much less surface exposure than Both-PR case. Patterns in the center etch slower ($R_{VR} = -10$) than the ones near the edge ($R_{VR} = 72$). The results from the Both-Blank and Both-Metal cases suggest that the metal layer on the sample has similar function with the blank surface for the PAW etching. The electrons can easily transfer from the solid to the etching solution through the metal contact layer. The only difference is that the metal layer blocks the illumination and prevents photo-carrier generation under the mask. For all cases, those regions with an increased etch area (under illumination) show rough surfaces with interference patterns while slower etching areas show clean surfaces.

PAW etch tests using the Initial-Mask for mirrors also presents unexpected etch result for the EPI sample. The PAW illumination inhibits the etching at the mirror pattern while the etching continues along the waveguide metal. The mirror walls, which consist of a region at the end of

the laser cavity and form an air-semiconductor interface for the mirrors, show deep etching with all three alternative mask conditions (Both-PR, Both-Blank and Both-Metal) while the Initial Mask for mirrors inhibits etching at the mirror facets. The mirror etching increases as the sample has more exposed surface or metal layer. Particularly, the etching of the mirror wall becomes inhibited for the Initial-Masked sample while Both-PR mask promotes etching at the mirror wall even with about the same PR coverage for Initial Mask and Both-PR mask.

The alternative masks (Both-PR, Both-Blank and Both-Metal) expose the metal layer part of the waveguide to the etching solution while the Initial Mask for the mirror covers the whole waveguide pattern and exposes only the mirror well for etching. The waveguides connect through metal to the mirrors which can directly affect the mirror etching. That is, the part of the waveguide metal exposed to the etching solution may help to remove electrons near the mirror patterns. The excess electrons generated near the mirror window area flow through the metal patterns. Semiconductor surfaces exposed to the etching solution or having more metal on the surface may dissipate the photo-electrons. The metal pads deposited on the side-strips also connect to the waveguide pattern to help conduct the excess electrons from the mirror area. However, the mirror patterns on Both-Metal masked samples have more variations in etch depth at the mirror depending on the position and length (shape) of the pattern. For all cases, the post-etched surface appears very rough where the etching is promoted. Same rough surfaces appear on the waveguide etched sample.

In contrast to the EPI sample, the waveguide etch rate is lower at the patterned area than at the edge of the sample using Initial Mask. Opposite layer structures of the wafers can cause the differences of PAW etch properties. Also, for mirror etching, the Initial-Mask for mirrors promotes the etching at the mirror side using high power PAW etching while it inhibits etching at the mirror window for EPI samples. However, the etching forms deep trenches along the PR mask and large lateral etching for M1 sample. Attention can be focused on the application of the etching to fabrication especially for laser mirrors once completing the experiments on the effects

of coherent and incoherent illumination, wafer types and masking materials. Lasers are PAW fabricated using the M1 samples with metal-only masking. To simplify the etch process, both the waveguide and mirror facets are simultaneously etched. Since the waveguide etches deeper than active layer, it will affect the laser threshold. Deep etching of the waveguide may cause high optical loss at the sidewall. However, by comparing laser properties of cleaved and etched mirrors fabricated with the same conditions, one can determine the etched-mirror quality.

Measurements of the optical power versus bias current (P-I) and spectra of ridge-waveguide lasers provide values for the etched-mirror reflectance, the internal optical loss, and the efficiency. As an evaluation of the PAW etching, tests are performed on three different types of ridge-waveguide lasers including those with (i) shallow-etched waveguides (the ridge height is smaller than the depth of the active region) (CL2-S), (ii) deep-etched waveguide and two cleaved mirrors (CL2-D), and (iii) one etched mirror (CE-D) using one-step-etching of the waveguide and mirrors. Laser parameters including mirror reflectivity, internal loss and differential quantum efficiencies are calculated from PI curve to compare cleaved and etched mirror quality.

The PAW etching has been shown to improve both mirror and waveguide quality by reducing the lateral etching and improving the side profile. The distributed losses (due primarily to optical scattering) and the mirror reflectance were obtained and compared. The dependence of the threshold and external differential efficiency were displayed for various PAW etch powers. For comparison of the waveguides, shallow-etched waveguides etched with high power PAW and in dark were tested. The shallow-etched waveguide lasers were compared with deep etched waveguide lasers (CL2-S and CL2-D lasers) with various PAW laser power. When the waveguides were etched deeper than the active layer, the laser performance became more sensitive to the sidewall quality. The etch properties depend on the PAW laser power and wavelength. The etched mirror lasers (CE-D) were examined with different powers of PAW lasers. CE-D lasers (etched mirror with deep etched waveguide) were compared to the CL2-D type lasers (two cleaved mirrors with deep-etched waveguides).

The PAW etched lasers show comparable quality to the cleaved mirrored devices with R_e (etched mirror reflectance) as large as 93% of R_c (reflectance of a cleaved mirror) independent of crystal direction and without coatings. However, the process has not been optimized and there were variations among devices. The average reflectance was 86% of R_c while the current pump efficiency η was estimated larger than 80%, the external differential efficiency η_d was found to be in the range 64% to 73%, and an internal optical loss was as low as 14cm^{-1} . The reflectance exceeds the previous reports of wet and dry etched mirror facets.

As previously mentioned with respect to the etch setup, several issues should be addressed for more general application of the PAW etching to the optical device fabrication. From the experiment, reducing the laser power could remove the etch depth variations. However, PAW laser power less than 5mW does not modify the etch characteristics. The minimum required laser power to produce an effect on the heterostructure material varies by the layer structure. For the GaAs/AlGaAs heterostructure materials evaluated in this research, the average laser intensity needs to be maintained higher than approximately $70\text{mW}/\text{cm}^2$ to produce good sidewall profile and low lateral etching. However, mass charge flow of the excess photo-generated carriers on the surface may cause the regional non-uniformity of the etch depth.

In order to improve the etching, experiments must focus on the charge distributions on the surface of the sample and also, therefore, the conduction paths and voltage distributions within the material. Unlike the bulk material, the heterostructure sample can block current flow toward the substrate of the material due to the built-in fields near the p-n junction, changes in the bandgap in the graded index region, and due to recombination at the Q.Ws. The PAW laser generates excess carriers at the surface which affects the dissolution of the material. For surface absorbed illumination, most of the excess carriers are produced at the surface and it is difficult to remove electrons from the surface and leave holes to promote etching. The mask material affects excess charge flow at the surface.

Exposing select portions of metal to etching solution sufficiently improves the etch characteristics over approximately 75% of the wafer to produce integrated laser mirrors. However, further improvement will be necessary to extend the range of clean uniform etching across the entire sample. Two of the main issues concerns uniform illumination and a mechanism to remove excess electrons near the etching surface while maintaining relatively large electron density near vertical facets (so as to inhibit the etching there). The PAW laser needs a lens arrangement that changes the Gaussian profile to a uniform distribution across the sample. In such a case, the etching might be expected to produce more uniform etching across the entire surface. However, the PAW laser coherence produces surface structure on size-scales smaller than 100 μ m in the form of interference patterns. In this regard, the incoherent illumination from broad-area LEDs produces cleaner surfaces. One additional point concerns the deposition of material under PAW laser illumination not observed for LEDs. Further experimentation will be needed to determine the cause and best resolution of the issue. Regarding the issue of controlling the charge distribution across the surface, one solution might be to integrate electrode patterns and develop methods to electrically remove the charge. However, unless metals and materials with etching properties distinct from the device structures, these metals and materials might not be easily removed and might interfere with the device performance. However, the experiments to fabricate the mirrors were successful and it might be possible to adjust the PAW beam characteristics (uniformity, power and wavelength) to improve results across the entire surface.

Using a reflectometer that monitors the etch depth of the sample can improve device fabrication. To minimize errors from possible etch depth variation, it is necessary to use a reflectometer capable of monitoring the entire surface of the sample in real-time. The most recent version of the etch monitor (to be published) uses a CCD array to map the reflections from the entire surface as it etches. This provides real-time etch depth, rate and roughness monitoring at each point on the surface.

Appendix A: $\text{Al}_x\text{Ga}_{1-x}\text{As}$ Complex Refractive Index

Table A.1 Refractive Index of $\text{Al}_x\text{Ga}_{1-x}\text{As}$ (Real Part) [107]

$\begin{matrix} x \\ E \end{matrix}$	0	0.1	0.2	0.3	0.4	0.5	0.6	0.7	0.8	0.9	1
0.4	3.322	3.277	3.235	3.193	3.151	3.107	3.060	3.008	2.951	2.889	2.819
0.6	3.347	3.300	3.256	3.213	3.170	3.125	3.077	3.024	2.967	2.903	2.833
0.8	3.383	3.333	3.287	3.242	3.198	3.151	3.102	3.048	2.989	2.924	2.852
1.0	3.432	3.378	3.328	3.281	3.234	3.186	3.134	3.079	3.018	2.952	2.878
1.2	3.501	3.437	3.382	3.331	3.281	3.230	3.176	3.118	3.056	2.987	2.911
1.4	3.614	3.518	3.452	3.395	3.340	3.285	3.228	3.167	3.101	3.030	2.951
1.6	3.684	3.641	3.548	3.476	3.414	3.353	3.292	3.227	3.157	3.082	3.000
1.8	3.765	3.704	3.654	3.600	3.508	3.438	3.370	3.299	3.225	3.144	3.058
2.0	3.851	3.805	3.752	3.691	3.639	3.547	3.466	3.387	3.306	3.220	3.127
2.2	3.993	3.933	3.873	3.815	3.744	3.681	3.592	3.497	3.405	3.311	3.211
2.4	4.204	4.121	4.040	3.963	3.889	3.811	3.733	3.645	3.528	3.421	3.312
2.6	4.518	4.389	4.274	4.168	4.070	3.978	3.892	3.792	3.704	3.560	3.434
2.8	4.955	4.729	4.574	4.436	4.309	4.190	4.079	3.975	3.858	3.751	3.589
3.0	4.666	4.783	4.874	4.741	4.564	4.444	4.317	4.190	4.066	3.930	3.799
3.2	4.052	4.185	4.335	4.487	4.638	4.718	4.570	4.434	4.306	4.166	4.007
3.4	3.696	3.763	3.855	3.980	4.144	4.332	4.513	4.644	4.554	4.419	4.274
3.6	3.550	3.575	3.612	3.673	3.770	3.912	4.098	4.312	4.503	4.614	4.532
3.8	3.563	3.563	3.565	3.578	3.614	3.686	3.804	3.972	4.182	4.404	4.579
4.0	3.688	3.682	3.668	3.653	3.647	3.663	3.713	3.810	3.960	4.157	4.380
4.2	3.877	3.883	3.874	3.855	3.833	3.817	3.817	3.849	3.927	4.061	4.247
4.4	4.029	4.066	4.084	4.088	4.080	4.064	4.050	4.046	4.071	4.140	4.268
4.6	3.896	3.955	4.000	4.033	4.054	4.067	4.075	4.085	4.108	4.162	4.268
4.8	3.291	3.310	3.316	3.312	3.303	3.292	3.285	3.290	3.324	3.409	3.572
5.0	2.549	2.519	2.475	2.424	2.370	2.319	2.279	2.262	2.290	2.395	2.619
5.2	2.011	1.968	1.914	1.854	1.795	1.740	1.698	1.681	1.713	1.835	2.103
5.4	1.678	1.639	1.591	1.538	1.485	1.437	1.400	1.385	1.418	1.542	1.828
5.6	1.469	1.438	1.397	1.352	1.307	1.266	1.232	1.218	1.245	1.362	1.647
5.8	1.329	1.305	1.270	1.232	1.193	1.157	1.126	1.110	1.129	1.232	1.506
6.0	1.228	1.208	1.179	1.146	1.112	1.080	1.052	1.034	1.044	1.130	1.383

Table A.2 Refractive Index of $\text{Al}_x\text{Ga}_{1-x}\text{As}$ (Imaginary Part) [107]

$\begin{matrix} x \\ E \end{matrix}$	0	0.1	0.2	0.3	0.4	0.5	0.6	0.7	0.8	0.9	1
0.4	0	0	0	0	0	0	0	0	0	0	0
0.6	0	0	0	0	0	0	0	0	0	0	0
0.8	0	0	0	0	0	0	0	0	0	0	0
1.0	0	0	0	0	0	0	0	0	0	0	0
1.2	0	0	0	0	0	0	0	0	0	0	0
1.4	0	0	0	0	0	0	0	0	0	0	0
1.6	0.097	0.050	0	0	0	0	0	0	0	0	0
1.8	0.180	0.130	0.057	0	0	0	0	0	0	0	0
2.0	0.260	0.206	0.145	0.111	0.075	0	0	0	0	0	0
2.2	0.352	0.305	0.255	0.202	0.150	0.108	0.051	0.041	0	0	0
2.4	0.444	0.409	0.365	0.315	0.261	0.199	0.150	0.077	0.056	0.043	0.036
2.6	0.540	0.514	0.474	0.425	0.371	0.313	0.246	0.187	0.115	0.069	0.047
2.8	0.940	0.618	0.585	0.539	0.484	0.423	0.358	0.286	0.213	0.137	0.068
3.0	1.980	1.767	1.474	1.070	0.599	0.532	0.462	0.389	0.312	0.231	0.154
3.2	2.224	2.171	2.076	1.913	1.671	1.313	0.817	0.486	0.403	0.320	0.235
3.4	2.216	2.194	2.161	2.112	2.036	1.906	1.687	1.337	0.806	0.400	0.312
3.6	2.112	2.103	2.090	2.080	2.069	2.047	1.993	1.874	1.639	1.240	0.630
3.8	2.044	2.029	2.012	2.002	2.004	2.019	2.036	2.035	1.984	1.837	1.537
4.0	2.066	2.038	2.005	1.980	1.969	1.979	2.011	2.057	2.098	2.099	2.013
4.2	2.241	2.201	2.152	2.105	2.069	2.053	2.064	2.106	2.175	2.250	2.294
4.4	2.652	2.616	2.566	2.509	2.454	2.408	2.381	2.386	2.428	2.508	2.605
4.6	3.291	3.302	3.295	3.273	3.242	3.205	3.169	3.144	3.143	3.178	3.253
4.8	3.804	3.865	3.909	3.939	3.955	3.960	3.955	3.947	3.947	3.969	4.030
5.0	3.856	3.904	3.934	3.950	3.951	3.940	3.920	3.899	3.890	3.917	4.013
5.2	3.625	3.644	3.646	3.634	3.610	3.576	3.537	3.502	3.489	3.533	3.691
5.4	3.338	3.339	3.325	3.299	3.262	3.219	3.173	3.135	3.127	3.195	3.420
5.6	3.076	3.068	3.047	3.015	2.975	2.929	2.882	2.844	2.842	2.933	3.223
5.8	2.853	2.841	2.817	2.784	2.744	2.698	2.651	2.615	2.618	2.728	3.080
6.0	2.665	2.652	2.628	2.595	2.556	2.511	2.466	2.432	2.439	2.565	2.975

* x = aluminum mole fraction of $\text{Al}_x\text{Ga}_{1-x}\text{As}$, ** $E = h\nu$ (Photon energy of incident light)

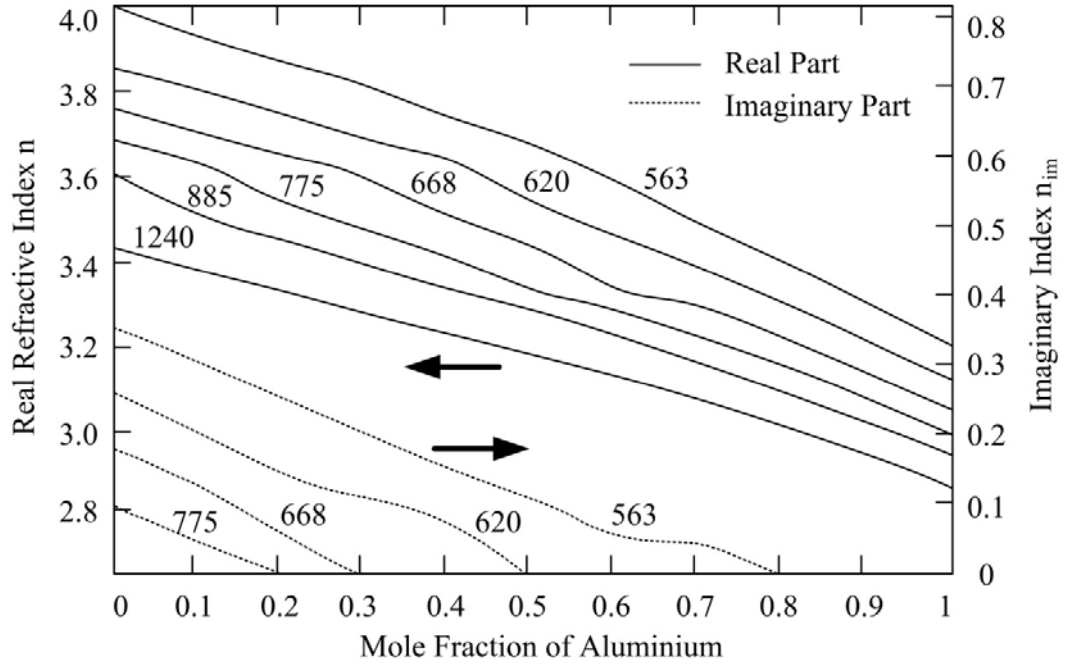


Figure A.1 Real and imaginary refractive index versus aluminum mole fraction [107].

Calculation of absorption length

Equation (A.1) presents an absorption length of the light (for Electric Field) with wavelength λ

$$L_E = \frac{\lambda}{2\pi n_{im}} \quad (\text{A. 1})$$

where $n_{im}(\lambda)$ denotes imaginary refractive index of the material. Absorption length for power L_P is half of the length of L_E .

$$L_P = \frac{L_E}{2} \quad (\text{A. 2})$$

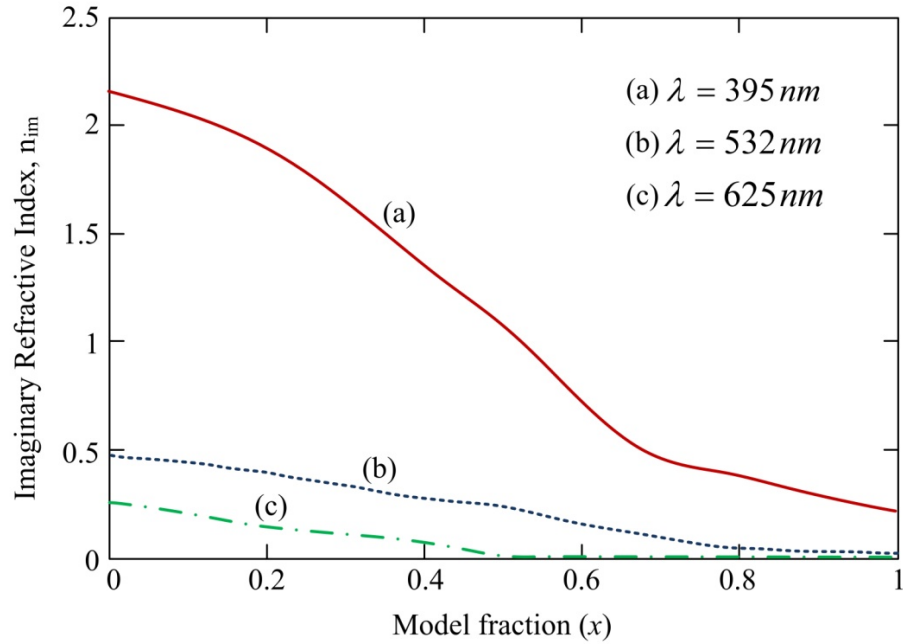


Figure A.2 Imaginary refractive index versus aluminum mole fraction for incident light wavelengths of (a) $\lambda = 395$, (b) $\lambda = 532 \text{ nm}$ and (c) $\lambda = 625 \text{ nm}$.

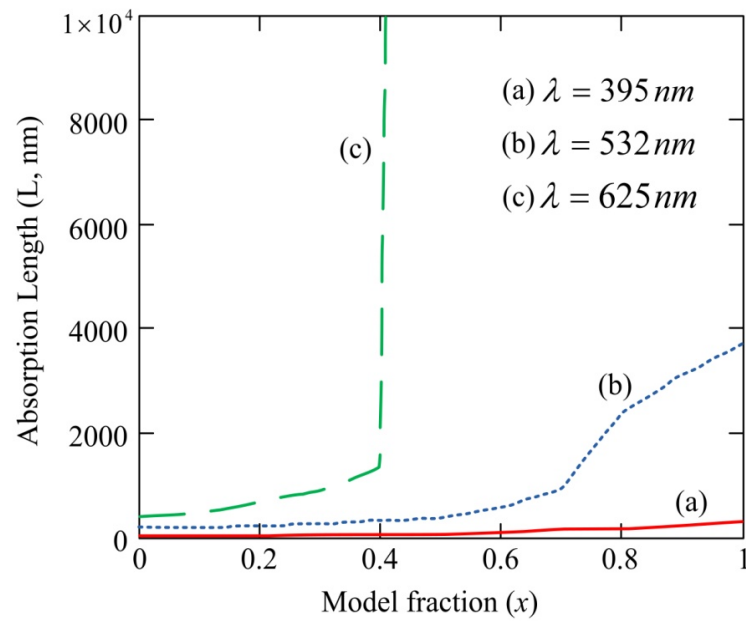


Figure A.3 Absorption length for the $\text{Al}_x\text{Ga}_{1-x}\text{As}$ with incident wavelength (a) $\lambda = 395$, (b) $\lambda = 532 \text{ nm}$ and (c) $\lambda = 625 \text{ nm}$. (y scale from 0 to $10 \mu\text{m}$)

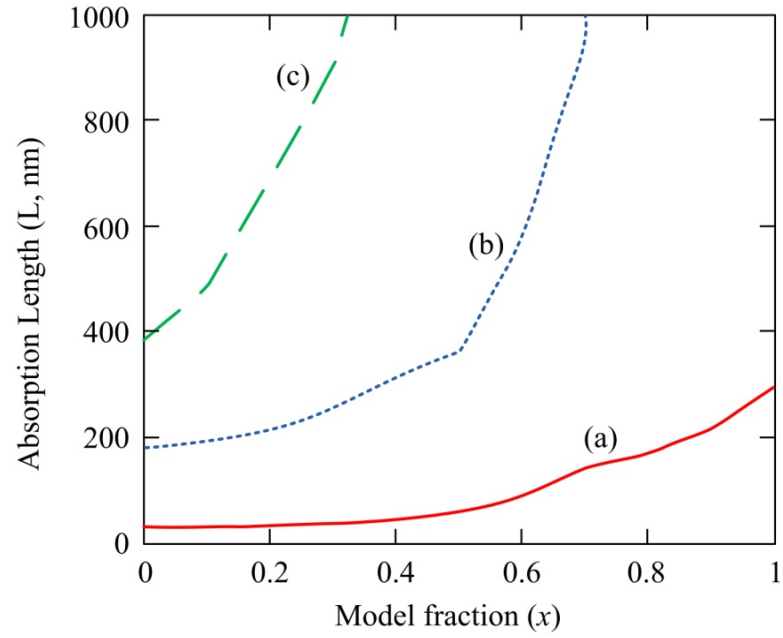


Figure A.4 Absorption length for the $\text{Al}_x\text{Ga}_{1-x}\text{As}$ with incident wavelength (a) $\lambda = 395$, (b) $\lambda = 532$ nm and (c) $\lambda = 625$ nm. (y scale from 0 to $1\mu\text{m}$)

Appendix B: GaAs/AlGaAs Heterostructure Wafer Specs

Table B.1 EPI-1179 Wafer Specs

Material Specifications for AlGaAs Int. FET/laser structure

Additional specifications on separate page

Additional Specifications

Thickness uniformity	± 5.0% over inner 40 mm diameter of 2" wafer
Thickness at wafer centre	Within ± 10% of specified value
Doping level uniformity	± 10.0% over inner 40 mm diameter of 2" wafer
Doping level at wafer centre	Within ± 20% of specified value
Relaxed cubic lattice mismatch	N/A
Peak Photoluminescence wavelength	* Peak emission to be 857±3nm
Defect density	< 10 cm-2

Substrate Specification 0014-1050

Material	GaAs-u/d	Major flat	16 ± 2 mm
Technique	LEC / VGF	Minor flat	7 ± 1 mm
Size	50.8±0.4mm	Edge rounding	0.25 Rmm
Carrier conc.	-	Orientation	(100) (110) 2±0.5
EPD	< 5 E+4 cm-2	Flat spec.	EJ
Thickness	500 ± 25 µm	Surface finish	P/P

[illegible]

Table B.4 M1-5 Wafer Layer Structure

Bandwidth Semiconductor

Structure: Generic 894nm laser structure

Proprietary

6/1/2004

Layer #	Material	x value	y value	Thickness	Doping	Density	Dopant
		%	%	(μm)	Type	(cm^{-3})	
12	Al(x)GaAs	0		0.2	p+	>2e19	Zn
11	Al(x)GaAs	0		0.05	p	1.E+18	Zn
10	Al(x)GaAs	60		1.2	p	1.E+18	Zn
9	Al(x)GaAs	30-60		0.5	p	5.E+17	Zn
8	Al(x)GaAs	8		0.02		None	
7	In(y)Al(x)GaAs	5	~12	0.008		None	
6	Al(x)GaAs	8		0.02		None	
5	In(y)Al(x)GaAs	5	~12	0.008		None	
4	Al(x)GaAs	8		0.02		None	
3	Al(x)GaAs	30-60		0.5	n	5.E+17	Si
2	Al(x)GaAs	60		1.2	n	4.E+17	Si
1	Al(x)GaAs	0		0.3	n	2.E+18	Si
Substrate	GaAs N+, (100)						
Notes: PL target to be between 884 and 886nm. For lasing at 894nm							

Table B.5 M1-3 Wafer Layer Structure

Bandwidth Semiconductor Proprietary

Date: 6/1/2004

Structure ID:

852 Generic Structure (3QW)

Layer	AlGaAs (x=Al)	Thick (μm)	Dop	Doping cm^{-3}	Comments
14	0	0.15	Zn	8E19	
13	0	0.05	Zn	1E19	Subcontact
12	0.6	1.2	Zn	1E18	Clad
11	0.3>0.6	0.2	Zn	lowE17	Graded
10	0.3	100A	None		Confinement
9	0	70A	None		GaAs QW
8	0.3	100A	None		Confinement
7	0	70A	None		GaAs QW
6	0.3	100A	None		Confinement
5	0	70A	None		GaAs QW
4	0.3	100A	None		Confinement
3	0.6->0.3	0.2	None	None	Graded
2	0.6	1.2	Si	4.00E+17	Clad
1	0	0.2	Si	2E18	Buffer
Sub	0		Si	N+	(100)

Note: PL target to be between 842 and 846nm for lasing at 852nm.

Appendix C: R_e/R_c Versus R_c Plot

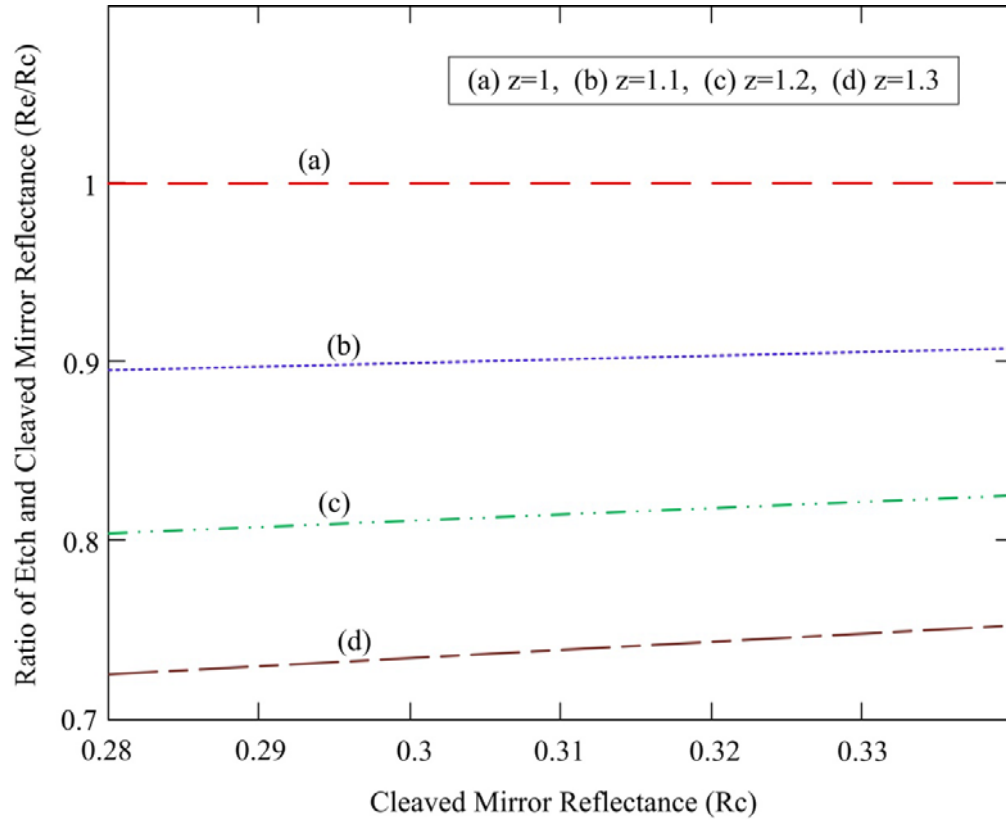


Figure C.1 Simulation of R_e/R_c (Ratio of etched and cleaved mirror reflectance) versus R_c (Cleaved mirror reflectance) for different P-I slope. z represents ratio of slopes of P-I (optical power versus bias current) from etched and cleaved mirror (M_e/M_c) above threshold current. R_e : reflectance of etched mirror and R_c : reflectance of cleaved mirror.

R_e/R_c changes by at most 3% over the entire range from 0.28 to 0.33. So a change from $R_c = 0.3$ to 0.31 is negligible.

Appendix D: Pictures of Experimental Set-up

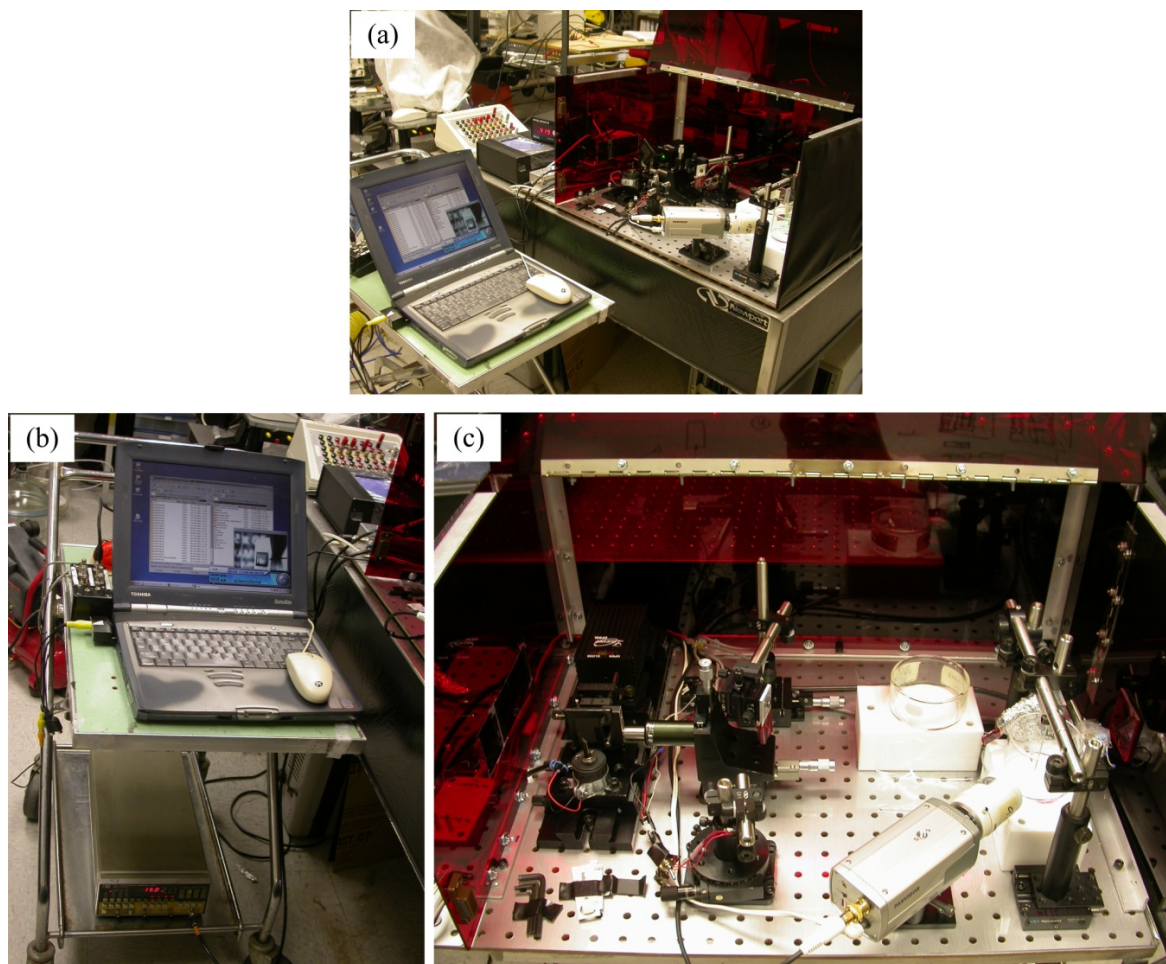


Figure D.1 Laser PAW etch set up: (a) overall set up, (b) control part and (c) optical elements and detectors.

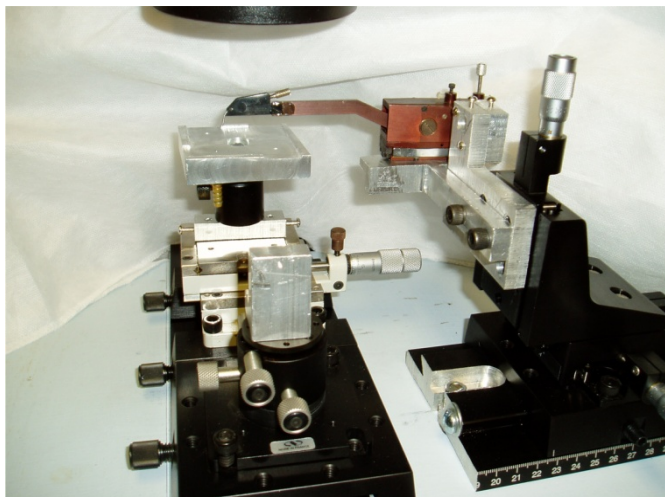


Figure D.2 Cleaving stage

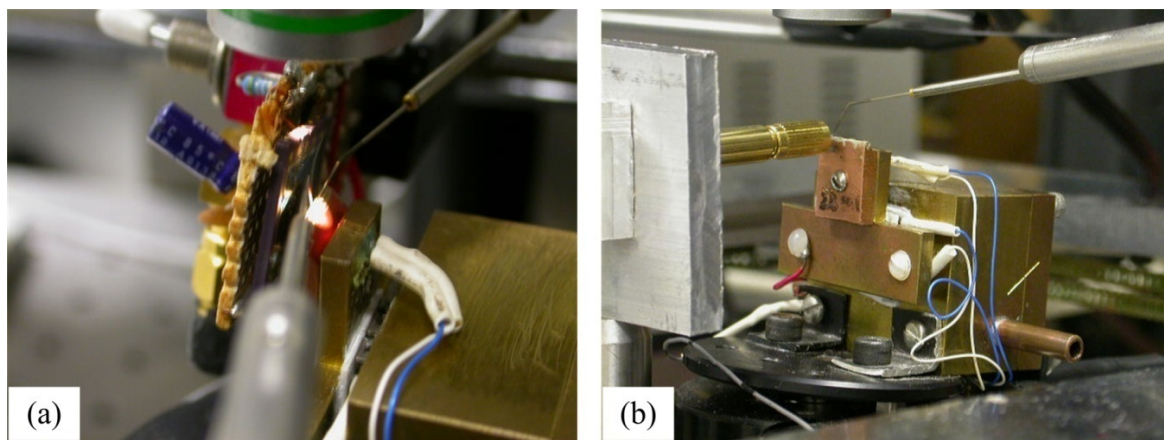


Figure D.3 Laser test set up: (a) Laser power versus current test set up and (b) Optical spectrum measurement set up.

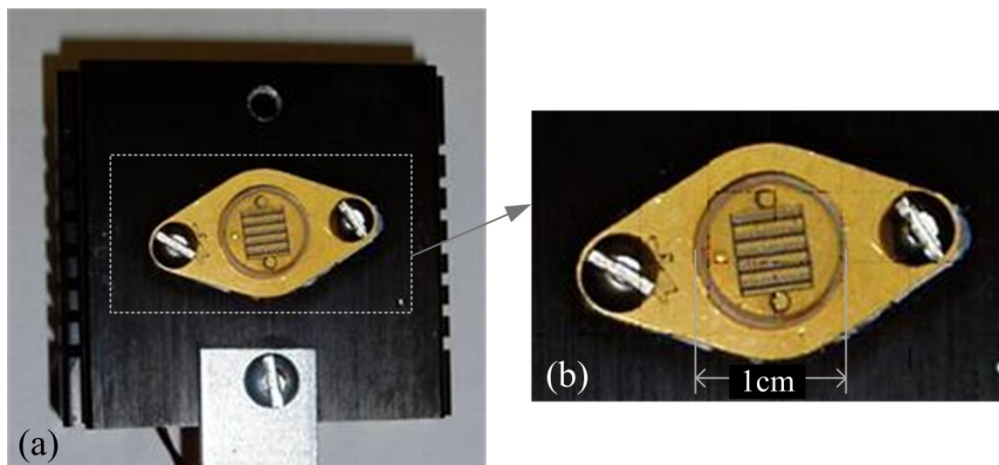


Figure D.4 High power LED for LED PAW etch test: (a) high power LED mounted on the cooling fan and (b) magnified picture of the LED.

Appendix E: Ridge-Waveguide Laser Masks

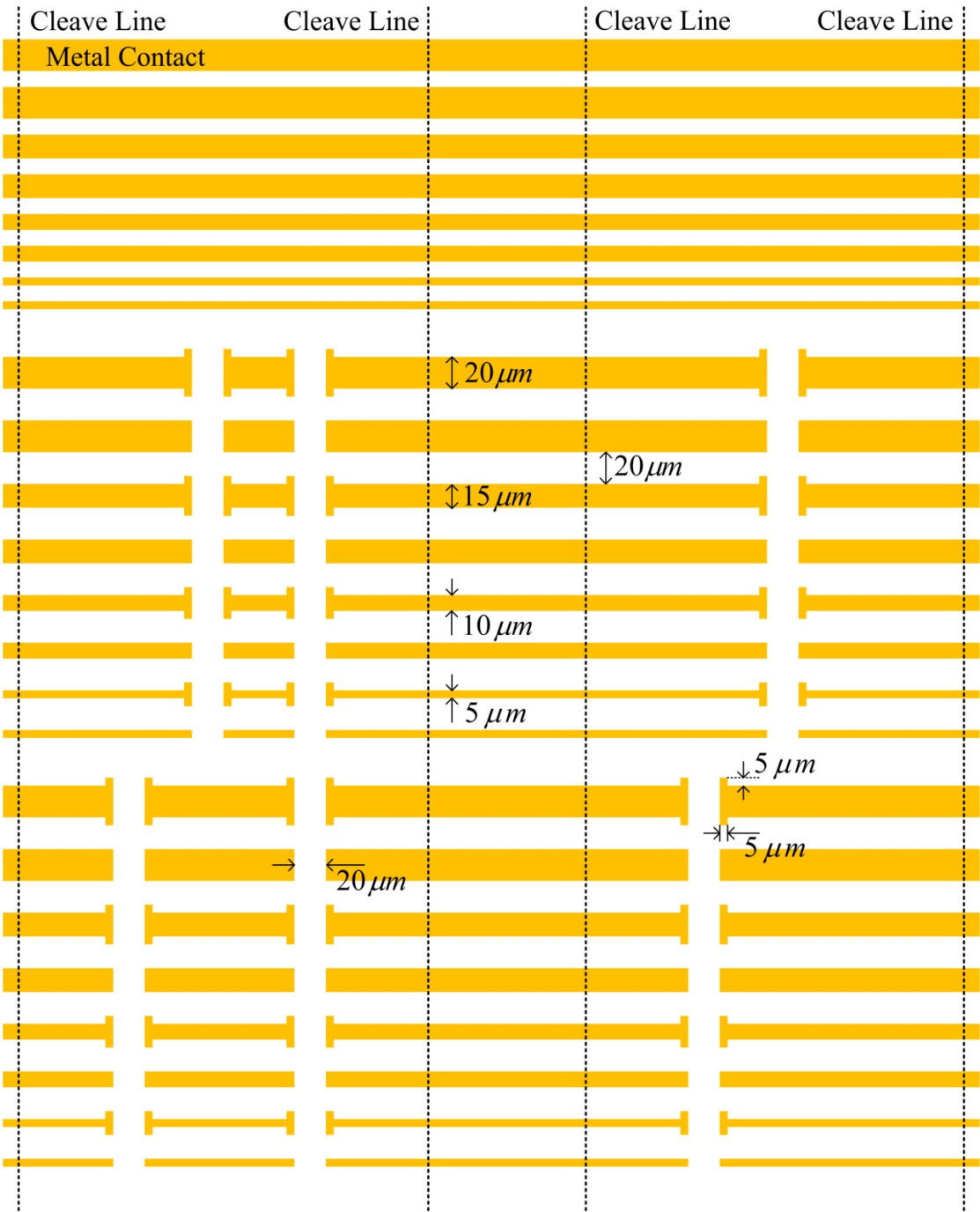


Figure E.1 Ridge-Waveguide Laser Mask: Metal Layer

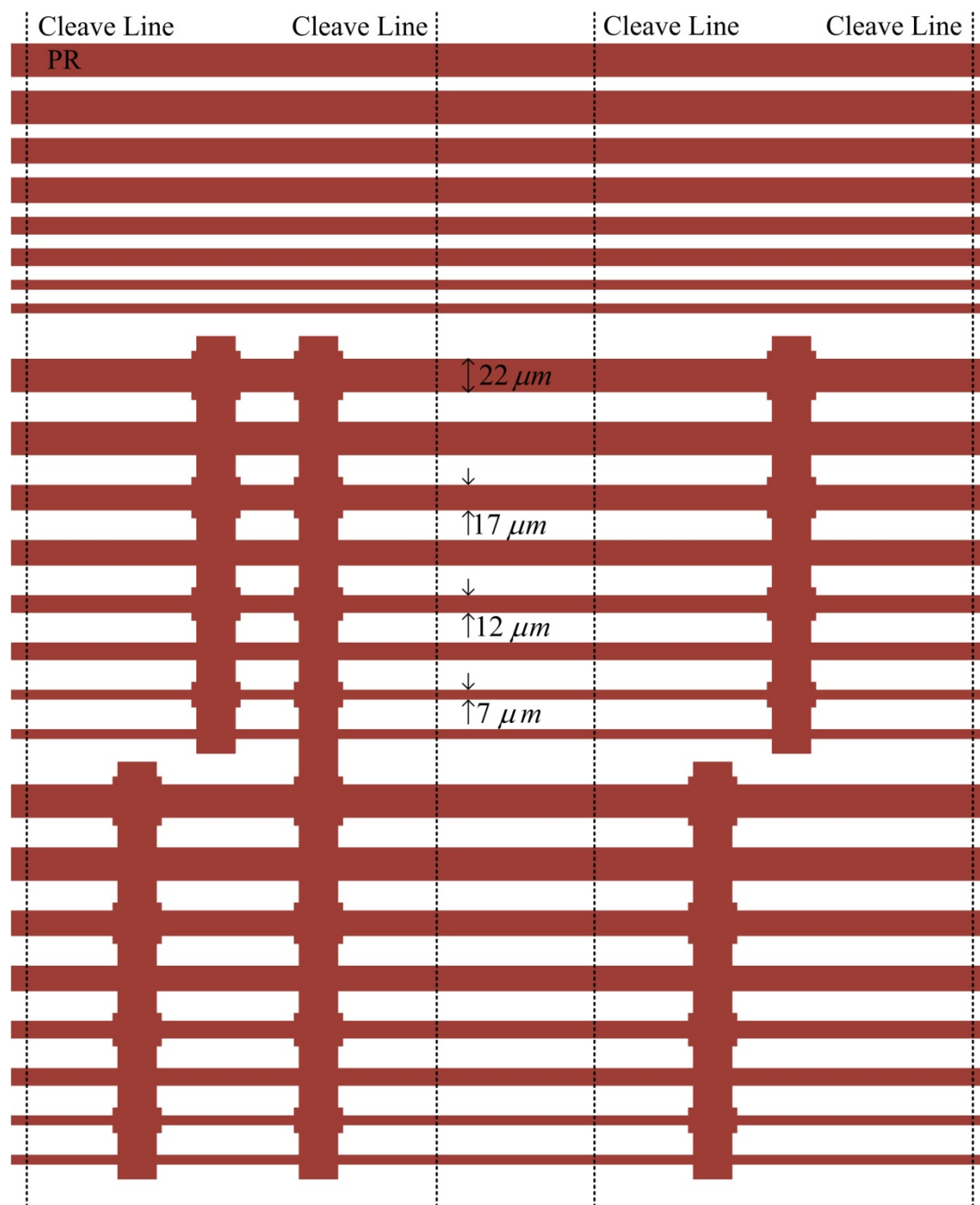


Figure E.2 Ridge-Waveguide Laser Mask: PR Layer

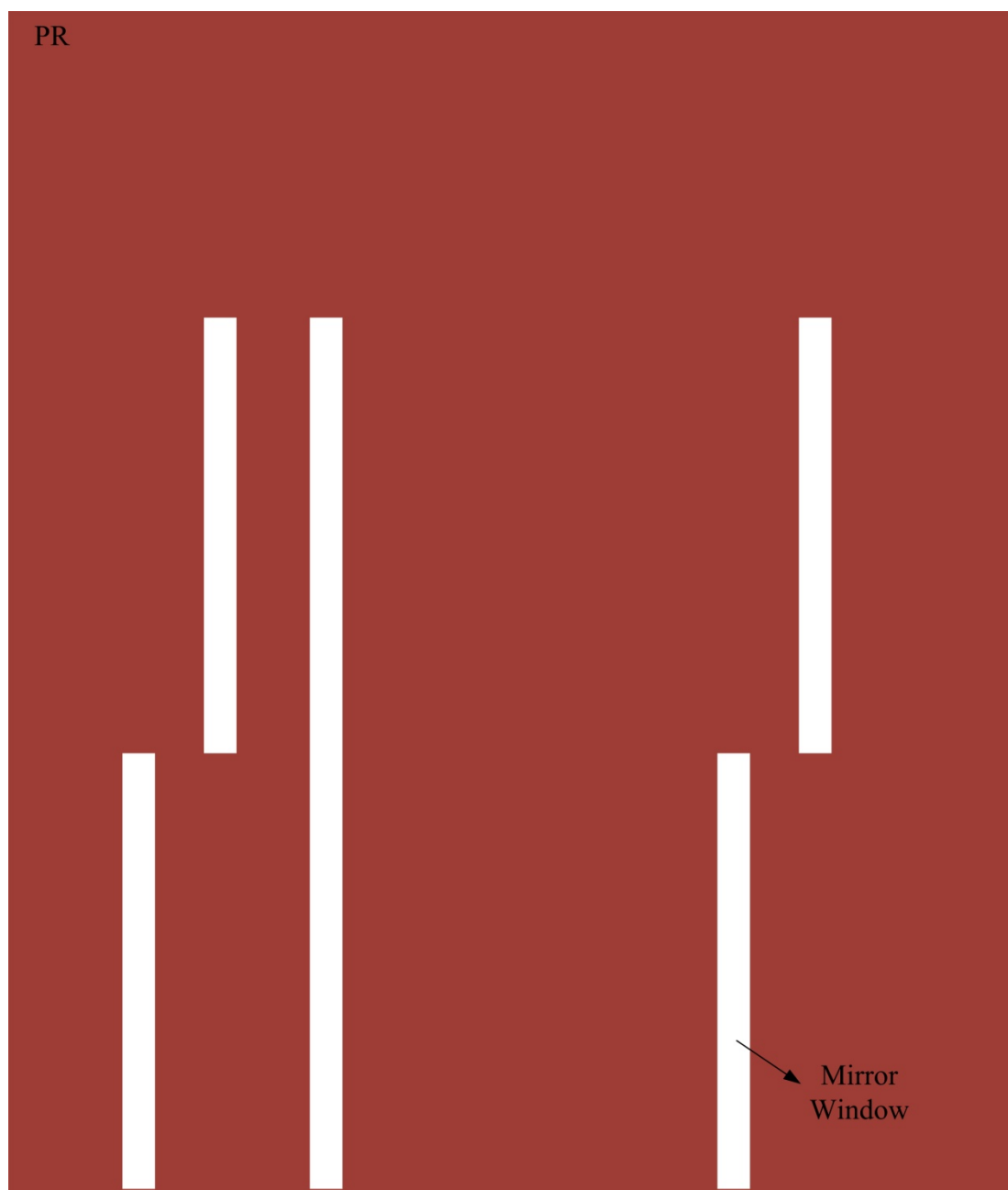


Figure E.3 Ridge-Waveguide Laser Mask: Mirror Windows

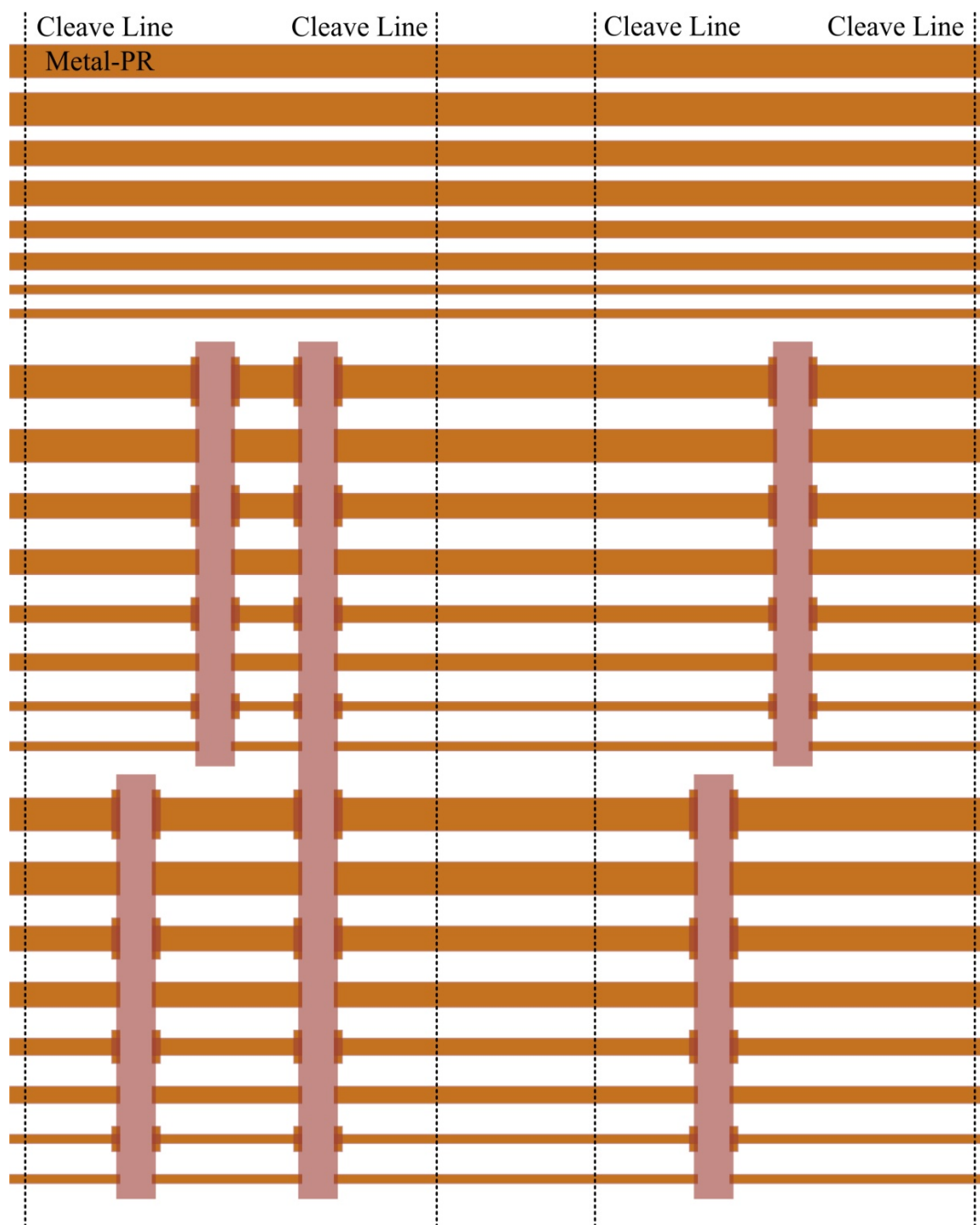


Figure E.4 Masks for Ridge-Waveguide Etching: PR layer (Figure E.2) covers Metal waveguide patterns (Figure E.1) for minimizing lateral etching and protect mirror wells.

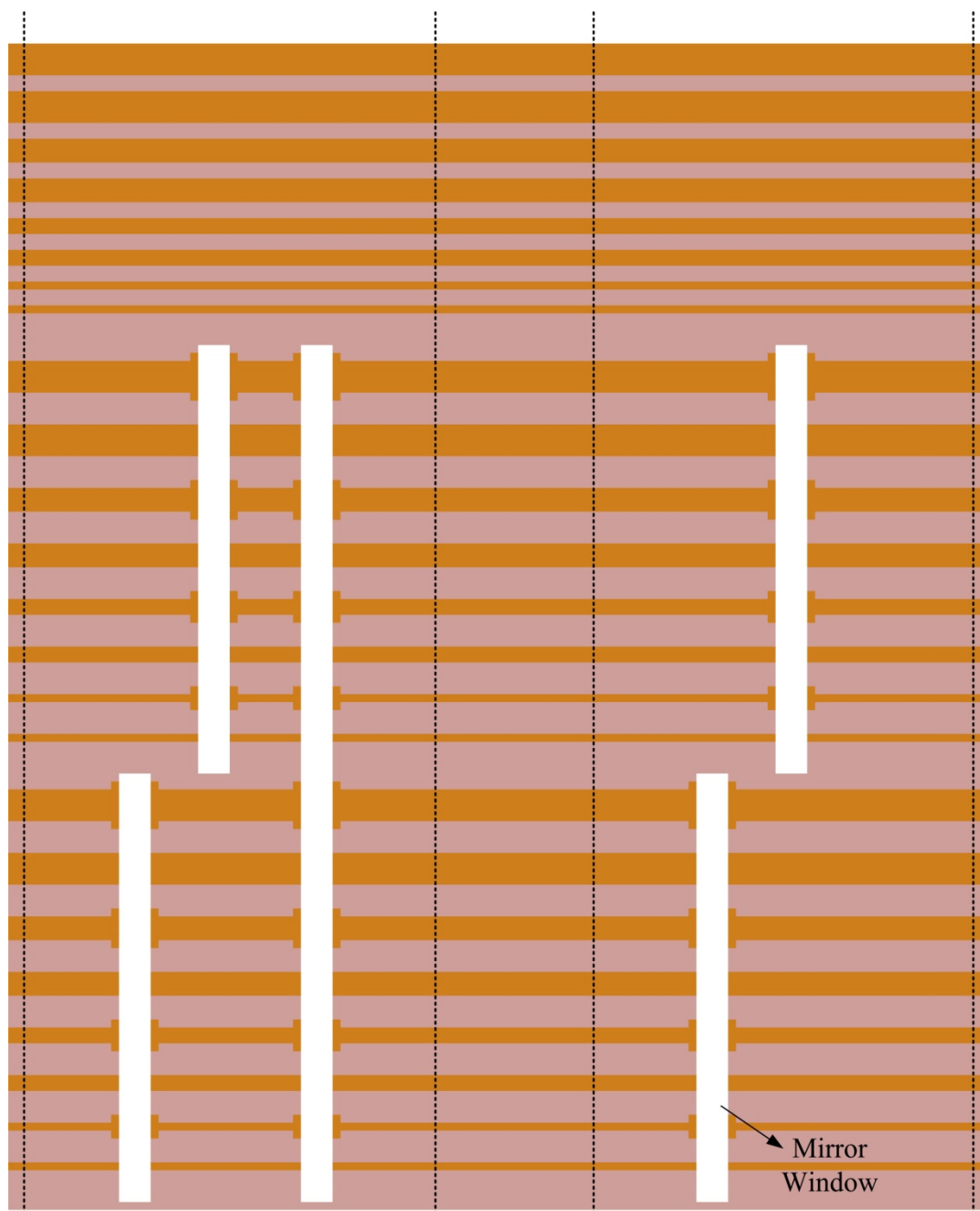


Figure E.5 Masks for Mirror Etching: Mirror window pattern (Figure E.3) is deposited over waveguides.

Appendix F: CCD-Based Holographic Etch Monitor

F.1 Introduction

The fabrication of integrated circuitry requires the chemistry of dissolution processes in order to remove semiconductor material from a wafer in select regions to produce a desired topography. For III-V semiconductors, as an important material for optical emitters and high mobility devices, the dry etching process uses chlorine decomposed from a gas in a plasma reaction, while the wet etching process typically uses an oxidizer (hydrogen peroxide) in combination with an acid such as sulfuric or phosphoric. For dry etching, the topography of the etching semiconductor is determined by both a mechanical (ion bombardment) and a chemical (reactive) component determined by the configuration of the etching unit. Etching to a specific depth in either case, often requires that a layer immune to the dissolution (etch-stop layer) be designed into the material; this added layer can lower the performance of an otherwise optimized material and allows the etch to be stopped at only one particular depth; however, the layer provides immunity to variations in etch rate across the surface. An in-situ Etch Monitor and Controller (EMC) can provide active control over the process without the need for special geometry and material composition.

The wet etch presented in this dissertation uses instrumentation to monitor and control the process. The etching parameters including temperature, solution concentration and fluid motion have an impact on the post-etched surface on scales ranging from microns to many centimeters. Without using an etch-stop layer, the etching can be controlled by popular methods such as timing the etch to obtain an average etch depth and afterwards, using a mechanical profilometer to find the depth. The procedure has obvious drawbacks such as making after-the-fact measurements, and using a tip with a size smaller than several microns to scan an area exceeding 1cm^2 . Methods of in-situ monitoring have been developed such as the pulsed-laser reflectometer presented in Chapter 3. The laser reflectometer uses a single photodetector that

provides a real-time etch depth, rate, and surface roughness measurement with interferometric accuracy.

Rather than use techniques that determine an average of the etch parameters, it would be better to resolve the entire surface during the actual dissolution process without making physical contact and without altering the surface state to be determined. Potentially, the most convenient method would be to optically image the etching surface to provide in-situ real-time monitoring and control. The technique would need to return information on the etch depth, rate, and surface microstructure (roughness). A suitably dense CCD array with optical lens system would be able to map the 2-D surface into a topographical map [99, 119]. In order to achieve nano-scale depth and rate resolution, one needs to incorporate holographic techniques and be able to interpret the resulting interference patterns. A suitably fast computer can interface with the dissolution apparatus, provide the real-time decoding of the interference patterns, and exert control over the process. A non-contact optical probe does not alter the device design (electrical contacts and mesa) nor does it require any alteration of the material composition. With recent progress in micro-processing techniques and circuits, the CCD array and the associated dedicated microprocessor can be incorporated into a small portable unit.

Although a Holographic Etch Monitor and Controller HEMC has immediate applications to semiconductor device research and fabrication, and especially for Photo-Assisted Wet (PAW) etching. As discussed in Chapter 2, the PAW technique uses light to break the typical crystal-plane etching and produce a range of sidewall profiles depending on the intensity and wavelength of the illumination. To achieve its potential, the PAW technique must overcome difficulties with controlling the many etching parameters. The HEMC provides a full 2-D map of the etching process both in real time and as saved data that can be examined at a later time.

F.2 Background Review

The CCD-based reflectometer (i.e., Holographic Etch Monitor and Controller, HEMC) has many characteristics of a holographic instrument. For typical holograms, an optical beam reflects from an object, carrying with it the intensity and phase information, and then superposes with a coherent reference beam to produce the interference signals at photographic film. One obvious method for the HEMC would be to substitute an etching surface for the object in the typical hologram setup. Such an approach would be appropriate for etching bulk materials that don't incorporate a reference plane for the reference beam. Another method utilizes the internal interfaces in modern heterostructure materials as the reference plane.

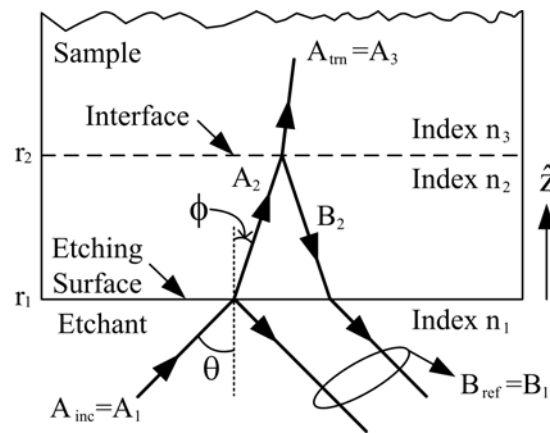


Figure F.1 Electromagnetic Fields in a multi-layer structure.

The optical signal reflected from the surface interferes with that from the internal interface (assumed to be flat) and the superposed beam illuminates a photosensor. The internal reference plane adds some complexity compared with the typical hologram in that the reference beam must first propagate across a potentially rough surface that alters the phase relations. For previous experiments with AlGaAs heterostructure however, the use of an internal reference plane provides resolutions on the order of 10 – 20 nm as a result of the higher refractive indices

on the order of 3.5. Furthermore, with the internal reference interface, one does not need to worry about critical alignment and vibration issues.

As discussed Chapter 3, Figure F.1 shows the relevant electromagnetic fields for the case of a planar surface with reflectivity r_1 and an internal interface with reflectivity r_2 . A two layer model suffices for typical III-V laser heterostructure, otherwise transfer and scattering matrices should be used. The incident field A_1 splits at the surface to provide a modified reference field B_2 (by partially reflecting from the internal interface). The two reflected beams carry phase information and combine into the signal beam represented by B_1 . It is actually the reference signal in this geometry that carries the greatest sensitivity to any surface microstructure owing to the greater optical path lengths (larger refractive index) in the material.

The primary signal consists of the surface reflected light based on the surface reflectance R_s while the secondary signal consists of the interference between the primary signal and a field reflected from an internal reference plane. As discussed in Chapter 3, the effective reflection coefficient $R_{\text{eff}} = P_o/P_{\text{inc}}$ (where P_{inc} is the incident power and $P_o = B_1^2$ is the ‘reflected’ power) can be written as

$$R_{\text{eff}} \cong R_s + 2r_1r_2\cos(2k_2z) \quad (\text{F.1})$$

where the surface reflectance is $R_s = r_1^2 = (n_2 - n_1)^2/(n_2 + n_1)^2$, n_2 denotes the refractive index of the $\text{Al}_x\text{Ga}_{1-x}\text{As}$ undergoing dissolution, and n_1 represents the refractive index of the gas plasma ($n \sim 1$) or of the etchant. The absorption length L_{abs} for a material with mole fraction x can be calculated from the imaginary index n_{im} using $L = \lambda_o/(2\pi n_{\text{im}})$. The Cosine term in Equation (F.1) produces oscillations centered on the average indicated by R_s . The surface reflectance R_s maps out the composition of the material during the etch while the internally reflected beam and the resulting oscillations provide the interferometric accuracy for the etch monitor. Equation (F.1) produces fringes in the data plotted versus time with peaks corresponding to distances

$$z(t)|_{\text{max}} = m\pi/k_2 = m\lambda_2/2 \quad (\text{F.2})$$

where $m=0, 1, 2, \dots$ and $\lambda_2 = \lambda_0/n_2$.

Surface roughness due to the formation of nanostructures during the etching necessarily decreases the coherence between the surface and internally reflected signals and therefore decreases the fringe amplitude. However, it does not necessarily significantly affect the surface reflected signal R_s [104]. The coherence effects are embodied in the Secondary Modulation Ratio (SMR) defined as the ratio of the peak-to-peak Fabry-Perot interference signal (Cosine in Equation (F.1)) to its average value (surface reflectance R_s). As discussed in Chapter 3, the SMR can be correlated with the surface nanostructure and the consequential roughness. For an EMC with a single photodetector, the beam can be expanded to cover the entire surface which makes the SMR sensitive to gradual changes in thickness (uneven etches). However, this single number cannot represent variations in etch depth versus position on the wafer surface.

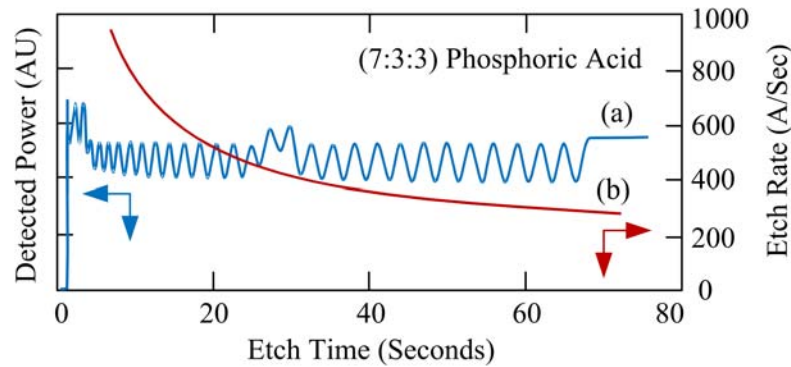


Figure F.2 Interference pattern and etch rate for a diffusion limited wet etch. (a) and (b) denotes reflectometer signal and etch rate, respectively. The spacing between fringes corresponds to approximately 100 nm.

Figure F.2 shows time resolved data from $\text{Al}_x\text{Ga}_{1-x}\text{As}$ laser heterostructure. The experimental apparatus used a single photodetector (2mm diameter beam), a laser pulsed at approximately 7Hz, and an etchant composed of phosphoric acid, hydrogen peroxide and water in the volumetric ratio of 7:3:3 which produced a diffusion limited etch [98]. Two consecutive fringes correspond to an etch depth of 100nm. The etch rate clearly decreases with etching time.

During the etching, one can stop the etching with a resolution of rough 1/10 fringe (or better for a slower etch) which corresponds to roughly 10nm. The average displacement of the fringe above horizontal determines the type of material based on the reflectance. The higher mole fraction (1-x) of Ga produces larger reflectivity. The small ‘bump’ in the center corresponds to a graded index region centered on the quantum wells for the laser heterostructure. One can also see that the diffusion limited etch ‘cleans up’ (i.e., reduces the roughness) since the peak-to-peak fringe height increases with the etching time.

For wet etching, the monitor probe laser can induce or inhibit etching that will interfere with the measurement accuracy. The problem can be corrected by pulsing the probe laser with relatively low duty cycle to reduce the energy delivered to the etching surface [98]. The photodetector will produce a corresponding photocurrent pulse with large signal-to-noise levels suitable for an analog-to-digital converter ADC (as opposed to using low light levels with slow lock-in amplifiers). For CCD arrays in cameras with full manual control, the laser pulses can be synchronized with the camera framing operation. However, cameras incorporating a CCD array without internal color filtering have excellent intensity response. The power in a steady state probe beam can be reduced so as to have negligible affect on the etching – this is especially true for the newer Photo-Assisted Wet (PAW) processes that apply relatively high intensity illumination to the etching surface.

F.3 HEMC System Overview

The wet etch environment presents the most demanding requirements on the HEMC as a result of the variation of etching conditions across the wafer and its sensitivity to optical energy. The unit is designed to provide 2-D real-time etch maps for III-V AlGaAs heterostructure (with interchangeable probe lasers for other materials). In principal, one can obtain interference patterns from bulk materials (without internal interfaces) by using a probe beam with photon energy smaller than the band gap so that the light reflects from both the front and the back surfaces. The

use of the backside reference plane would provide the highest resolution for the bulk material. The other possibility consists of using an external reference beam similar to typical holographic setups, using surface absorbed light, and monitoring the superposition of the reflected surface light and the reference beam. A pulsed probe beam lowers the energy delivered to the surface and helps eliminate unwanted photo-induced etching that would alter the surface state and render inaccurate measurements. However, a CCD array can be very sensitive which allows a steady state probe beam to be reduced in intensity so as to have negligible effect on the etching.

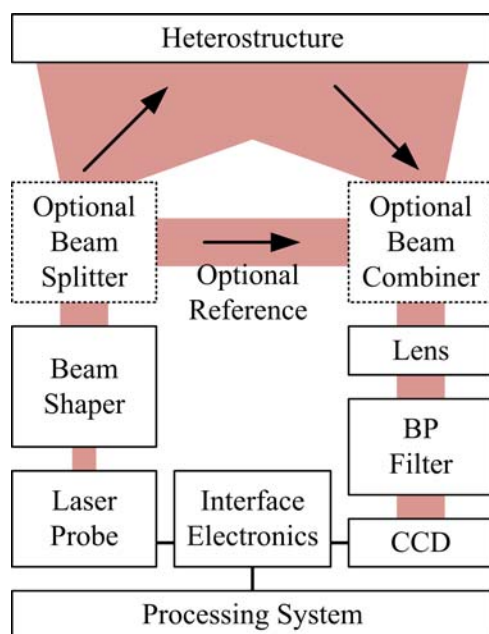


Figure F.3 Block diagram for the HECM. BP: Band Pass

The apparatus has three basic components (represented in Figure F.3). The optical unit has a 670 nm low power laser, beam shaping, a CCD array (in an inexpensive commercial camera with full manual control), interference band pass filter, lens system, and an optional beam splitter for an external reference beam. An electronics hardware unit provides laser drive and interfaces the optical unit with the processing unit. In the case of a pulsed laser system, one needs to synchronize the pulses with the CCD image capture event preferably using a sync pulse directly

from the camera. While the experimental HEMC can be miniaturized, the present unit uses a laptop PC with a video adapter and custom software. Previous work with the single detector system indicates that a frame rate of 7 FPS will provide sufficient temporal resolution for the wet etching systems (slower rates for the dry etches). For comparison, typical video systems have rates of 30 FPS and CCD cameras can be found with rates exceeding 200 FPS. A fourth unit (Figure F.4), although not strictly part of the HEMC, consists of a calibration system for the CCD array. In a fully manual mode for the CCD imager, the ‘brightness’ response of the CCD to optical power can be quite nonlinear which cannot be modeled by a simple power law. As such, one must convert from the ‘brightness’ reported by an analog to digital converter (video adapter) to an actual unit of optical power. Most importantly, one must find a functional map from brightness to a linear scale. The conversion must be applied to each pixel of data from the CCD prior to integrating over any portion of the optical image.

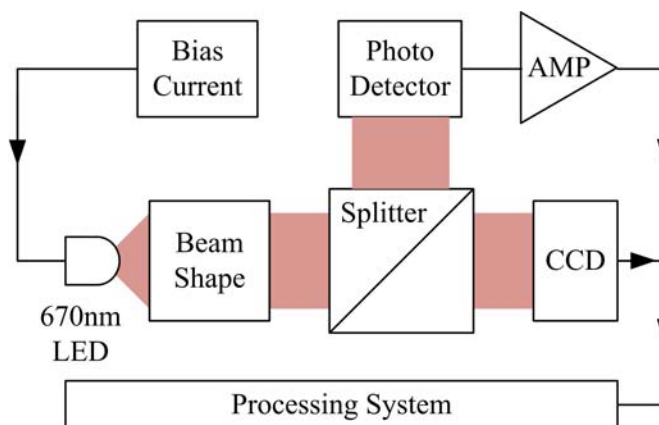


Figure F.4 A CCD calibration system. AMP: Amplifier

The block diagram of the HEMC appears in Figure F.3. The interface electronics interfaces the CCD array to the processor and applies any applicable timing pulses to the 670nm laser probe. The emission from the laser must be expanded across the surface of the etching semiconductor wafer by the beam shaper. Preferably, the beam shaper would convert a nearly

Gaussian beam profile into one uniformly distributed across the surface. As discussed previously, an optional reference beam can be extracted for experiments with bulk wafers and external reference planes. The beam incident on the surface of the etching wafer returns phase and intensity information to the CCD. Note the interference band pass filter placed next to the CCD array. The HEMC is specifically designed to be used in conjunction with Photo-Assisted Wet (PAW) experiments that uses high intensity laser illumination at wavelengths other than 670nm and for which, the etching wafers also emit photoluminescence at wavelengths of 800nm and larger depending on the type of heterostructure. The interference filter has narrow bandwidth of approximately 10nm to ensure these other sources do not affect the measurements from the CCD.

The manufacturer must either supply linearity data or one must explicitly make measurements to determine the functional relation between the ‘optical power per pixel’ versus the ‘brightness’ reported by that pixel. A single value (such as ‘gamma’ used in a power law) does not sufficiently characterize the CCD array for the purposes of the HEMC. The fully manual cameras such as the Cohu 1300 or 2200 series have more than 640×480 pixels arranged in the standard ratio of 4/3 in $6.4\text{mm} \times 4.8\text{mm}$. The units have fully manual gain control, color balance, shutter speed, and integration times. As such one needs to set the controls prior to calibration. The calibration method (Figure F.4) consists of uniformly illuminating the surface of the CCD while simultaneously making a measurement on the photodetector using the 50-50 beam splitter. Knowing the area of the photodetector and the fact that the illumination is uniform allows one to calculate power per pixel. The power incident on the CCD array is independent of pixel position and also therefore of the number of pixels selected to determine ‘brightness’. The illumination source for the calibration has 670nm wavelength to match the probe beam used with the HEMC. The calibration process needs to use custom software similar to that used for the HEMC.

The primary analysis tool for the proposed system consists of custom software written in Microsoft Visual C++/Basic. Figure F.5 shows the flow chart for the planned software. The software provides the capability of selecting regions of the video for analysis in real time. The

user selects rectangular regions (arbitrary size) of the image which map to the etching sample. At a rate of approximately 7 frames per second (FPS), the software calculates the average and total optical power in each of the selected regions for each frame event. The software uses a look-up style table for the conversion from 'brightness' to optical power. Each frame is saved to a video file (*.avi) in chronological order and with proper time duration (so as to reconstruct the original video stream) along with the results from the real-time rectangle results. The software is capable of reloading the video at a later time for analysis on an as needed basis.

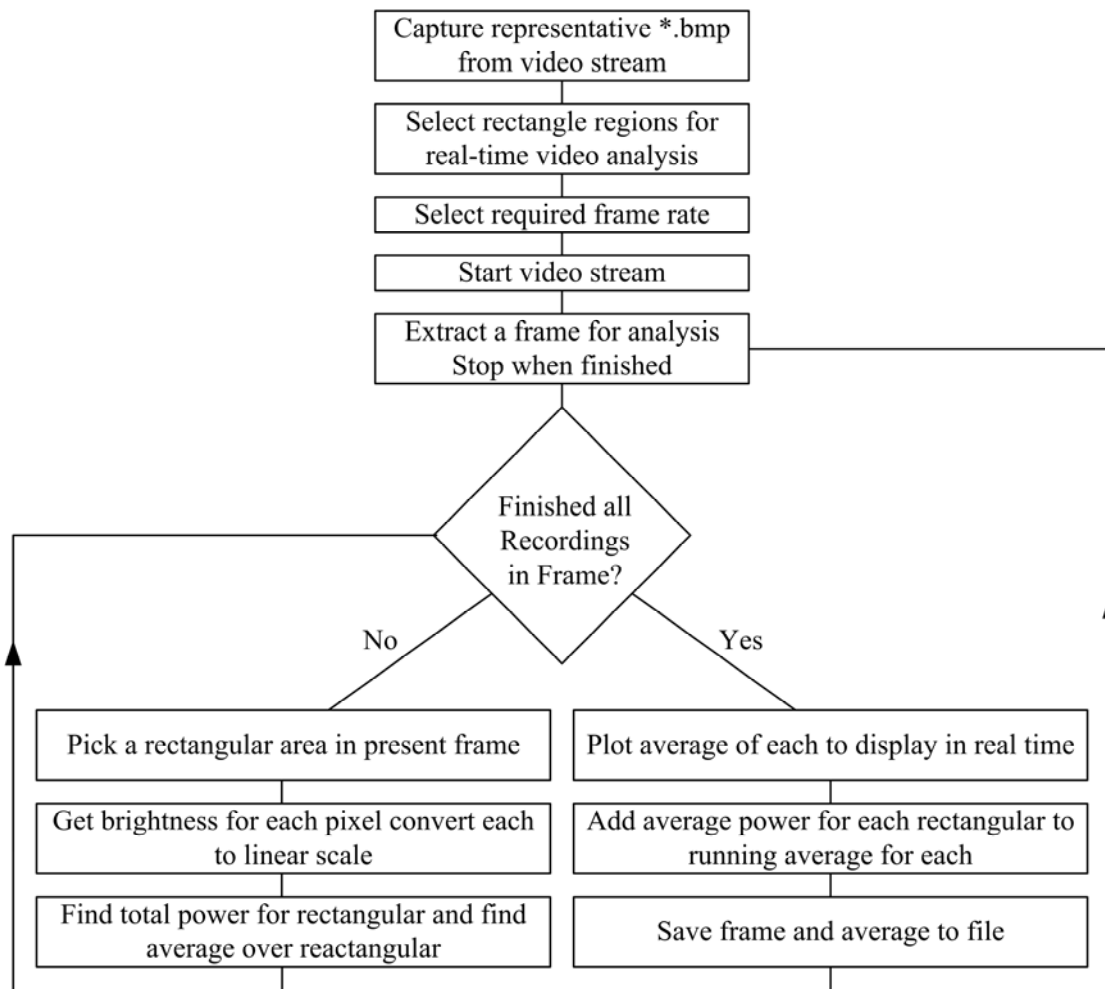


Figure F.5 Basic flow chart for custom EMC analysis software.

Such post etch analysis is important in order to correlate device tests results (such as threshold current) with the geometry or microstructure of the device. An important aspect of the software is the ability to control the etching in real time. For example, semiconductor laser waveguides need to be stopped within about 100nm of the active region for optimum performance of some waveguides. The number is well within the 10-20nm resolution of the EMC instrument. The software can be modified to plot the actual layer structure of the material rather than solely showing the interference plots. In some cases, it is necessary to do additional computation to extract an actual depth. For example, the distributed Bragg layers used for the VCSEL mirrors often have a resonance tuned for 850nm (for AlGaAs heterostructure) that causes a type of ‘beat’ phenomena with the 670nm probe beam. As such, one cannot use the rule-of-thumb of 100nm per fringe. The etch depth is determined by a transfer/scattering matrix approach that must include the complex index of refraction.

F.4 Example Calibration Plot

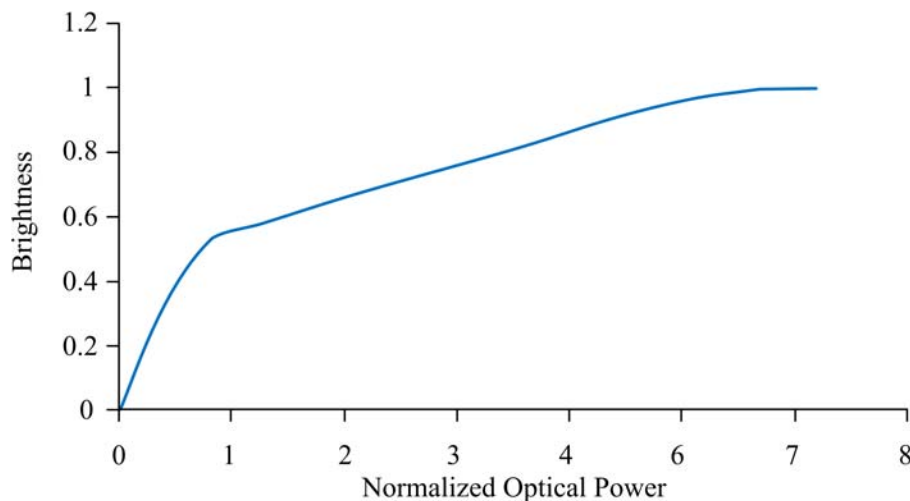


Figure F.6 Example calibration plot for the CCD array. Vertical: brightness, horizontal: Optical power in arbitrary units.

The CCD camera has controls for manual gain and shutter speed settings. For the digital camera, the shutter speed refers to the digital capture time rather than a mechanical shutter. The gain curve for the specific cohu camera for these trials is relatively independent of the control settings to levels of microwatts. It is clear from Figure F.6 that the correction is not a simple power law. To use the CCD array to detect optical power, one determines the brightness of a pixel and converts to a value on the horizontal scale.

F.5 Example Results

Proof-of-concept measurements have been made on laser heterostructure but without the calibrations. An example sample (approximately $2 \times 5\text{mm}^2$) appears in Figure F.7. The sample appears red as a result of 670nm incoherent illumination used. In this case, three small regions around the sample are chosen for which to examine the etch depth, rate and roughness. The software tracks each individual rectangle during the etching process. It calculates an average value of the brightness in each rectangle and plots it in real time, and then saves the video and rectangle information to file. It is possible to average over the same rectangle from frame-to-frame as a type of running average. The video saved in file can be re-examined at any time to find etch depth, rate and roughness.

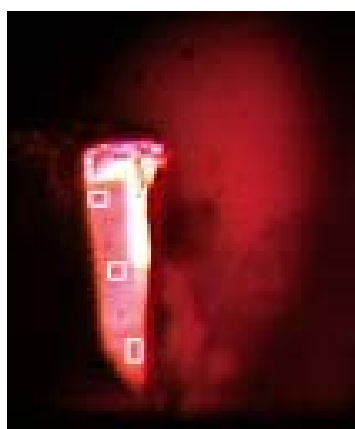


Figure F.7 Example sample with three small white selection rectangles for software analysis.

The sample in Figure F.7 and similar ones produce familiar fringe patterns for each rectangular region. These first test average the brightness rather than the proper intensity since the calibrations were not applied. In actual operation, one must convert brightness for each pixel prior to finding an average. In general, the interpretation of the surface roughness depends on the viewing area as described in [104], and on a convolution between signals from neighboring surface elements. For example one rectangle will receive some phase and intensity information from neighboring cells, which must then be properly interpreted.

Example fringe patterns appear in Figure F.8. Using the 'brightness' scale, one can determine neither the primary signal nor the surface roughness because of the nonlinear dependence of 'brightness' on optical power. However, the etch depth and rate can be determined. The figure shows that the two areas corresponding to the top two fringe patterns produce similar etch rates and similar surfaces. The lower plot corresponds to a region overlapping an edge and shows lower reflected signal.

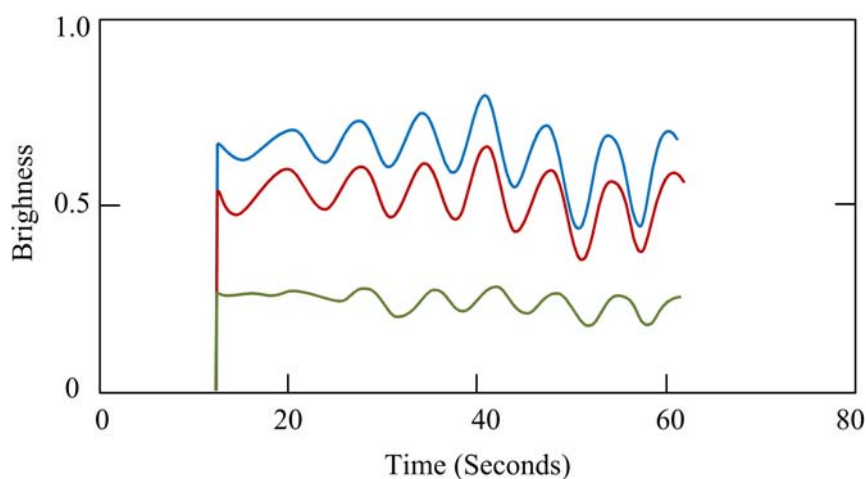


Figure F.8 Fringe patterns for 3 small regions on an etching sample.

Figure F.9 shows a second example for the entire etch. By the end of the etch, one can see that the depth between the two selected areas differs by approximately $1/4$ fringe which corresponds to approximately 25nm (since one fringe is approximately $0.1\mu\text{m}$).

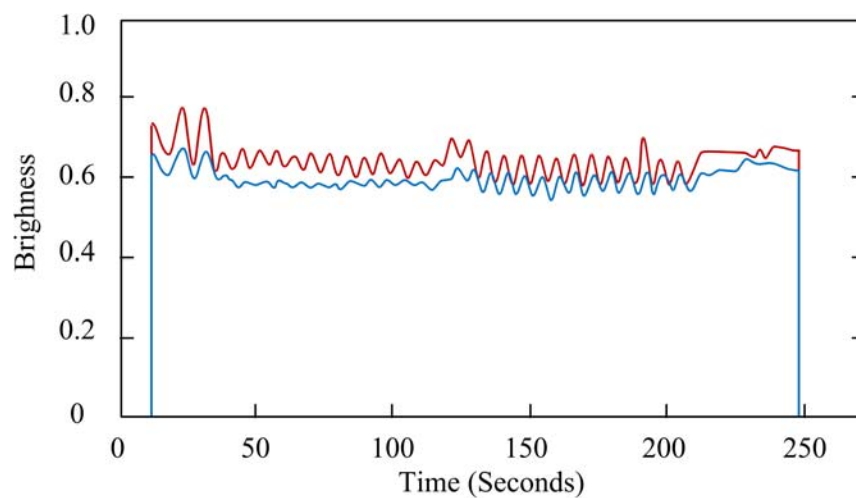


Figure F.9 Example full fringe patterns using the CCD array.

Appendix G: 1-D Lens Calculations for Transforming a Gaussian Beam into a Uniform Intensity Profile

The PAW etching system requires illumination uniformly distributed across the surface of the etching wafer. Chapter 4 shows the use of a diverging lens to increase the waist of the laser beam to roughly 1.5 cm in order to produce a relatively uniform beam across the 5 mm sample. The diverging lens produced illumination 80% uniform across the wafer according to Table 4.2. However, the total power striking the sample decreases by 75%. In order to improve the efficiency of the system, one can investigate a method for converting the Gaussian beam into one with uniformly distributed intensity profile. Several possibilities can be imagined including adjusting the refractive index in a glass slab as a function of radius and adjusting the thickness of a lens. The present appendix develops the equations to design the appropriate lens contour which can then be coded into ray tracing software. The lens operates by contouring the surface in such a way that those rays corresponding to high-intensity illumination are ‘fanned out’ into regions with lower intensity as suggested by Figure G.1. The objective becomes one of calculating the required lens contour.

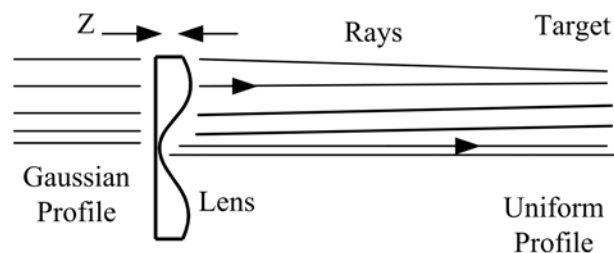


Figure G.1 Concept diagram for beam shaping lens. Z represents the thickness of the lens at any vertical point y .

G.1 Lens Equations

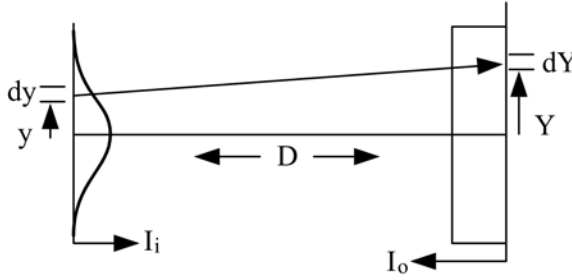


Figure G.2 Ray trajectory and definition of parameters.

Assume intensities (W/m) $I_i(y)$ and $I_o(Y)$ symbolize the input and output profiles respectively. If P_{tot} represents the total power in the input beam then the input intensity profile has the form

$$I_i(y) = \frac{P_{\text{tot}}}{\sqrt{2\pi}\sigma} e^{-\frac{y^2}{2\sigma^2}} \quad (\text{G. 1a})$$

(where σ represents the standard deviation) as can be verified by integrating. Further assume that I_o is constant from $Y = -a_o$ to $Y = a_o$ for which the intensity and power must be related by $P_{\text{tot}} = 2a_o I_o$. The intensity in Equation (G.1a) becomes

$$\frac{I_i(y)}{I_o} = \frac{2a_o}{\sqrt{2\pi}\sigma} e^{-\frac{y^2}{2\sigma^2}} \quad (\text{G. 1b})$$

First determine the required trajectory for the rays. Consider a ray starting at height y and ending at height Y at the target. Relate Y and y by

$$Y = g(y)y \quad (\text{G. 2})$$

The Gaussian is symmetrical across the center line and so Equation (G.1) does not require an offset constant.

Conservation of energy produces the slope $g(y)$ which ultimately produces the desired contour $z(y)$ for the lens. Require the input power in dy to be the same as the output power in dY .

$$I_i(y)dy = I_o dY \quad (\text{G. 3})$$

Combining Equations (G.2) and (G.3) provides

$$\frac{d}{dy}[yg(y)] = \frac{I_i(y)}{I_o} \quad (G.4a)$$

Integrating across the center line starting at $y = 0$ produces

$$g(y) = \frac{1}{y} \int_0^y \frac{I_i(y')}{I_o} dy' \quad (G.4b)$$

which has the form of an average. For small y , the value of $g(y)$ can be seen to be well defined as $I_i(0)/I_o$ (and does not diverge as $1/y$)

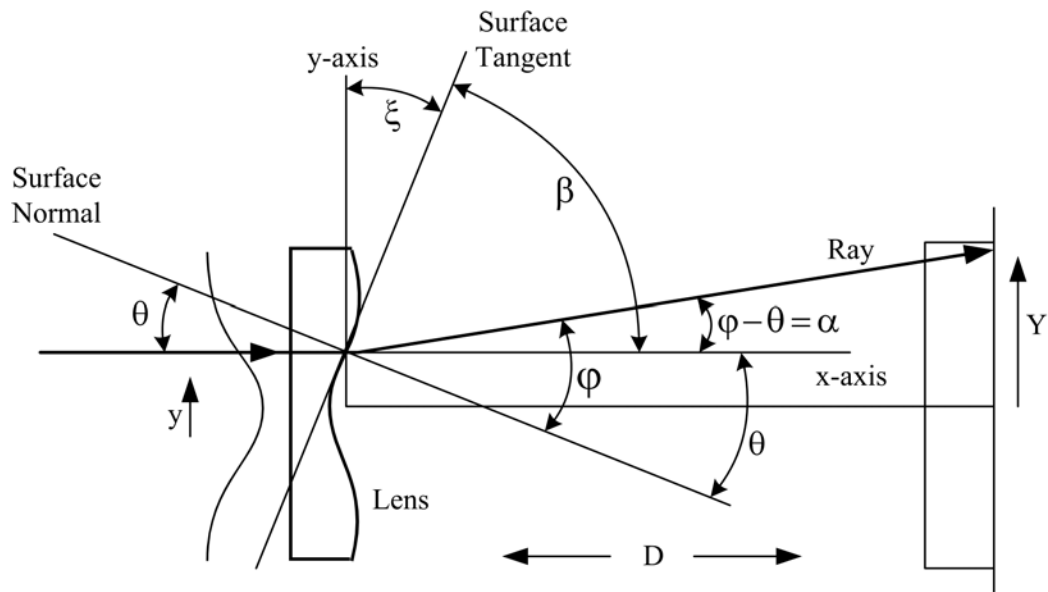


Figure G.3 Definition of angles for the lens surface.

The contour of the lens at any point y determines the propagation direction for the ray defined by $g(y)$. Let $z(y)$ represent the equation for the lens surface and consider the following relations. The slope of the lens surface can be written as

$$\frac{dz}{dy} = \tan \xi = \tan[90^\circ - \beta] = \tan[90^\circ - (90^\circ - \theta)] = \tan \theta \quad (\text{Lens Slope}) \quad (G.5)$$

However, the ray trajectory requires the angle $\alpha = \phi - \theta$ for the slope

$$\text{Tan}\alpha = \text{Tan}(\phi - \theta) = \frac{Y - y}{D} = \frac{[g(y) - 1]y}{D} \quad (\text{Line Slope}) \quad (\text{G. 6})$$

Snell's law provides

$$n_{\text{pl}} \sin \theta = n_{\text{air}} \sin \phi \quad (\text{Snell's Law}) \quad (\text{G. 7})$$

where n_{pl} and n_{air} symbolize the refractive indices of the lens (plastic) and air. Using the trigonometric relation for the sine of the difference of angles, and then squaring, Snell's law can be written as

$$\sin^2 \theta \left\{ \left(1 - \frac{n_{\text{air}} \cos \alpha}{n_{\text{pl}}} \right)^2 + \left(\frac{n_{\text{air}}}{n_{\text{pl}}} \right)^2 \sin^2 \alpha \right\} = \left(\frac{n_{\text{air}}}{n_{\text{pl}}} \right)^2 \sin^2 \alpha \quad (\text{G. 8})$$

Squaring terms in the braces and simplifying provides

$$\sin \theta = \left[\frac{(n_{\text{air}} \sin \alpha)}{n_{\text{pl}}^2 - 2n_{\text{air}}n_{\text{pl}} \cos \alpha + n_{\text{air}}^2} \right]^{1/2} \quad (\text{G. 9})$$

Combine equations to restate the lens slope in Equation (G.5), which is

$$\frac{dz}{dy} = \frac{\sin \theta}{\sqrt{1 - \sin^2 \theta}} \quad (\text{G. 10})$$

The expression for $\sin \theta$ in Equation (G.9) provides the following expression

$$1 - \sin^2 \theta = \frac{n_{\text{pl}}^2 - 2n_{\text{air}}n_{\text{pl}} \cos \alpha + n_{\text{air}}^2 - n_{\text{air}} \sin \alpha}{n_{\text{pl}}^2 - 2n_{\text{air}}n_{\text{pl}} \cos \alpha + n_{\text{air}}^2} \quad (\text{G. 11})$$

Combining the last three equations yields

$$\frac{dz}{dy} = \frac{n_{\text{air}} \sin \alpha}{[n_{\text{pl}}^2 - 2n_{\text{air}}n_{\text{pl}} \cos \alpha + n_{\text{air}}^2 - n_{\text{air}} \sin \alpha]^{1/2}} \quad (\text{G. 12})$$

where the Sine and Cosine can be written as

$$\sin \alpha = \frac{Y - y}{\sqrt{(Y - y)^2 + D^2}} = \frac{[g(y) - 1]y}{\sqrt{(g(y) - 1)^2 y^2 + D^2}} \quad (\text{G. 13a})$$

$$\cos \alpha = \frac{D}{\sqrt{(Y - y)^2 + D^2}} = \frac{D}{\sqrt{(g(y) - 1)^2 y^2 + D^2}} \quad (\text{G. 13b})$$

Equation (G.12) can be integrated since the right hand side involves only y . Equation (G.12) then provides the lens contour starting at $y=0$.

G.2 Example Results

Initial computer simulation shows that the shape of the lens is similar to that shown for example in Figure G.4 where distances are measured in mm.

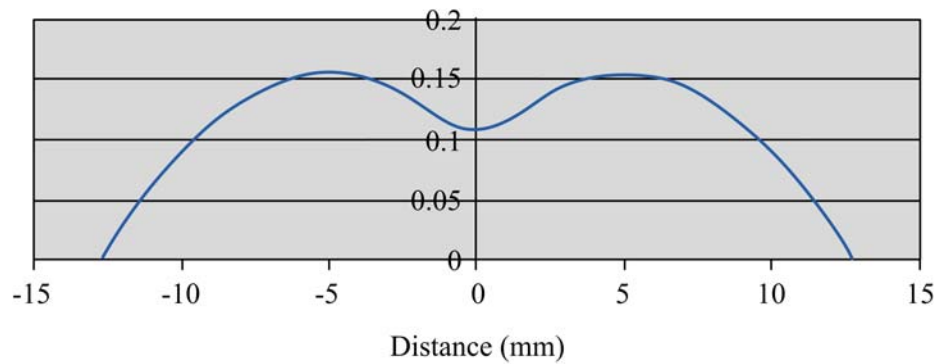


Figure G.4 Example lens contour for transforming a Gaussian beam into a uniform one.

The contour is sensitive to the distance from the lens to the target, lens index and beam waist. In some cases, the contour near $x=0$ is more 'pointed' so as to form a v-shape. Those rays falling near the origin are spread out by the lens (consider Snell's law). Near the thickest portion of the lens, rays essentially pass through unaltered as they represent light with the average power falling on the target. The wings of the lens cause the rays to be compacted as required to bring their intensity up to the average falling on the target.

The present dissertation did not fabricate or purchase such a lens as the lower intensity beams had sufficient power to distinguish between the dark etching and the PAW etching. However, more uniform illumination would likely have helped to eliminate some of the variation in charge density across the surface and improve the etch profile.

Appendix H: Vibrating Mirror for the PAW etching

The Laser-PAW uses coherent illumination to control the wet etching characteristics. However, the coherent illumination tends to cause interference patterns to be etched into the wafer surface. Small rapid motion of the illumination across the surface helps to reduce the interference patterns.

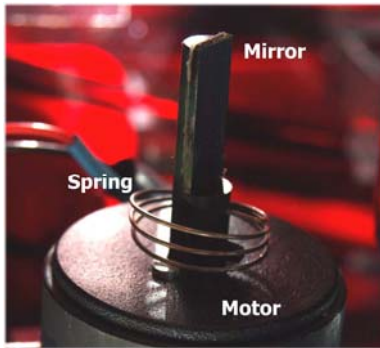


Figure H.1 Small mirror attached to the axle of a motor with a spring return.

The etching system discussed in Chapter 4 uses an electrically controlled mirror arrangement. A Maxton motor with a return spring has a mirror attached to the rotation axle (Figure H.1). By applying a small sinusoidal voltage, the mirror oscillates back and forth sweeping about 10%-20% of the 1.5 cm waist diameter. This appendix provides information on the mirror assembly.

H.1 Simple Mirror Model

The performance of the mirror can be characterized in terms of the circuit elements. Figure H.2 shows the setup as a simple trial model. Resistor R_2 was used during the experiments. One is primarily interested in the deflection of the beam α as a function of driving voltage V and frequency f . The deflection angle is related to the angular position of the mirror through $\alpha = 2\theta$. The mirror assembly has internal series resistance R_s and inductance L . The rotor, axle and

mirror produce moment of inertia I . The shaft has a spring with constant K and there must be a frictional force B . V_m represents the emf induced by the moving magnet.

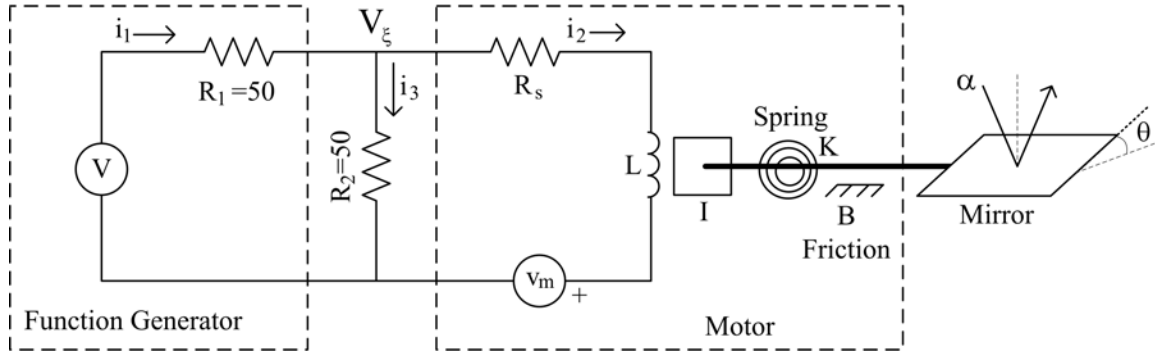


Figure H.2 A function generator drives a shunt resistor R_2 and the mirror motor. The symbols are defined in the table at the back.

H.2 The Transfer Function for the Mirror Angle and Beam Deflection

The parameters in the figure are defined in Table H.1. The assumed component model in Figure H.2 provides the following set of equations. “Twiddle” indicates Laplace transform with variable s .

$$\frac{\tilde{V} - \tilde{V}_\xi}{R_1} = \frac{\tilde{V}_\xi - \tilde{v}_m}{R_s + sL} + \frac{\tilde{V}_\xi}{R_2} \quad (\text{H. 1})$$

$$\tilde{i}_2 = \frac{\tilde{V}_\xi - \tilde{v}_m}{R_s + sL} \quad (\text{H. 2})$$

$$v_m = k_m \dot{\theta} \rightarrow \tilde{v}_m = s k_m \tilde{\theta} \quad (\text{H. 3})$$

$$\tau_\theta = k_T i_2 = K\theta + B\dot{\theta} + I\ddot{\theta} \rightarrow k_T \tilde{i}_2 = K\tilde{\theta} + sB\tilde{\theta} + s^2 I\tilde{\theta} \quad (\text{H. 4})$$

One can combine the previous equations into the transfer function of interest.

$$\frac{\tilde{\theta}}{\tilde{V}} = \frac{k_T R_\parallel}{k_T k_m s + (R_T + sL)(K + Bs + Is^2)} \quad (\text{H. 5})$$

where as shown in Table H.1, R_\parallel is the parallel combination of R_1 and R_2 and $R_T = R_\parallel + R_s$.

The inverse Laplace transform can be found without substituting the values for the variables

using MathCad software; however, it does not return a solution for non-zero L . The assumption of $L=0$ is reasonable since separate experiments indicated below show that the time constants associated with L are significantly smaller than the others. Equation (V.5) has the form

$$\theta(t) = \frac{R_{\parallel}}{\omega_r R_1 R_T} \left(\frac{k_T}{I} \right) V(t) \odot e^{-t/\tau} \sin(\omega_r t) \quad (\text{H. 6})$$

where \odot denotes convolution, k_T represents a constant for the torque and where MathCad provides

$$\omega_r = \left[\frac{K}{I} - \frac{1}{4} \left(\frac{k_m}{R_T} \right)^2 \left(\frac{k_T}{I} \right)^2 - \left(\frac{B}{2I} \right) \left(\frac{k_m}{R_T} \right) \left(\frac{k_T}{I} \right) - \left(\frac{B}{2I} \right)^2 \right]^{1/2} \quad (\text{H. 7})$$

$$\frac{1}{\tau} = \frac{1}{2} \frac{k_m}{R_T} \left(\frac{k_T}{I} \right) + \frac{B}{2I} \quad (\text{H. 8})$$

H.3 Open-Terminal Transfer Functions

Some of the parameters for the simple model are found from the ‘open terminal’ behavior of the mirror assembly. In this case, the function generator and resistor R_2 are removed (Figure H.2). Assume the mirror has zero angular velocity at $t=0$ but starts at angle θ_o (the mirror will be displaced by hand, and the relaxing oscillations will be observed). Using zero external torque produces

$$I\ddot{\theta} + B\dot{\theta} + K\theta = 0 \quad \rightarrow \quad \frac{\ddot{\theta}}{\theta_o} = \frac{Is + B}{Is^2 + Bs + K} \quad (\text{H. 9})$$

This is easy to solve and provides

$$\frac{\theta(t)}{\theta_o} = \left(\frac{B}{2I} \right) \frac{e^{-t(B/2I)}}{\omega_{OT}} \sin(\omega_{OT}t) + e^{-t(B/2I)} \sin(\omega_{OT}t) \quad (\text{H. 10})$$

where the open-terminal resonant frequency is

$$\omega_{OT}^2 = \frac{K}{I} - \left(\frac{B}{2I} \right)^2 \quad \text{and} \quad \omega_o = \sqrt{K/I} \quad (\text{H. 11})$$

and where ω_o represents the resonant frequency for the spring and rotational mass alone. Now one can calculate the voltage v_m , which will be measured,

$$v_m = k_m \dot{\theta} = -\theta_o \frac{k_m \omega_o^2}{\omega_{OT}} e^{-t(B/2I)} \sin(\omega_{OT} t) \quad (H.12)$$

where the open-terminal time constant is

$$\tau_{OT} = \left(\frac{B}{2I} \right)^{-1} \quad (H.13)$$

which is related to the closed-terminal constant in Equation (H.8).

H.4 Determine the Parameters

Resistance is measured on meters ($R_1 = 50$, $R_2 = 50$). The motor parameters are measured using an HP4274A RCL unit. The value of the series resistance is $R_s = 18.8$. The value of the inductance depended on the frequency and ranged from 0.613mH (1kHz) to 0.8mH (100Hz) and might have some component of the voltage v_m . Measured with a handheld meter, $L=0.614$ mH which will be the one for the equations.

The natural resonant frequency $\omega_o = \sqrt{K/I}$ was found by displacing the mirror through a fixed angle and then measuring the frequency as recorded by a high speed chart recorder (the mirror was open-terminal, $R_{chart} = 1M$ Ohm). Figure H.3 shows an example for a starting angle of approximately 45° . For several measurements, the resonant frequency was found to be $\omega_o = 234$ rad/sec. In addition, connecting the mirror to a function generator with R_2 replaced by a high impedance oscilloscope showed the resonant frequency the resonant frequency was $\omega_o = 220$ rad/sec. Holding the axel eliminated the resonance for the oscilloscope. These numbers produce a resonant frequency of approximately 36 Hertz.

The open-terminal time constant in Equation (H.13) can be found from the relaxation oscillations in the chart records. The average time constant was found to be $\tau_{OT} = 113$ msec.

$$\tau_{OT} = \left(\frac{B}{2I}\right)^{-1} = 113\text{msec} \quad (\text{H. 14})$$

which provides the ratio $B/2I$ required in other equations.

The open-terminal resonant frequency (Equation (H.11)) can now be found as

$$\omega_{OT} = \left[\frac{K}{I} - \left(\frac{B}{2I}\right)^2\right]^{1/2} \cong 234 \cong \omega_o \quad (\text{H. 15})$$

The parameter k_T is the constant of proportionality for the torque in the motor produced by the current i_2 . The value is estimated by bouncing a light beam off the mirror, applying a DC current to the mirror assembly and estimating the deflection of the beam on a target approximately 2 meters away. The value of k_T/K was determined to be approximately

$$k_T/K = 1.39 \quad \text{and} \quad k_T/I = (k_T/K)(K/I) = 1.39 \quad (\text{H. 16})$$

where the K/I comes from the open-terminal resonant frequency.

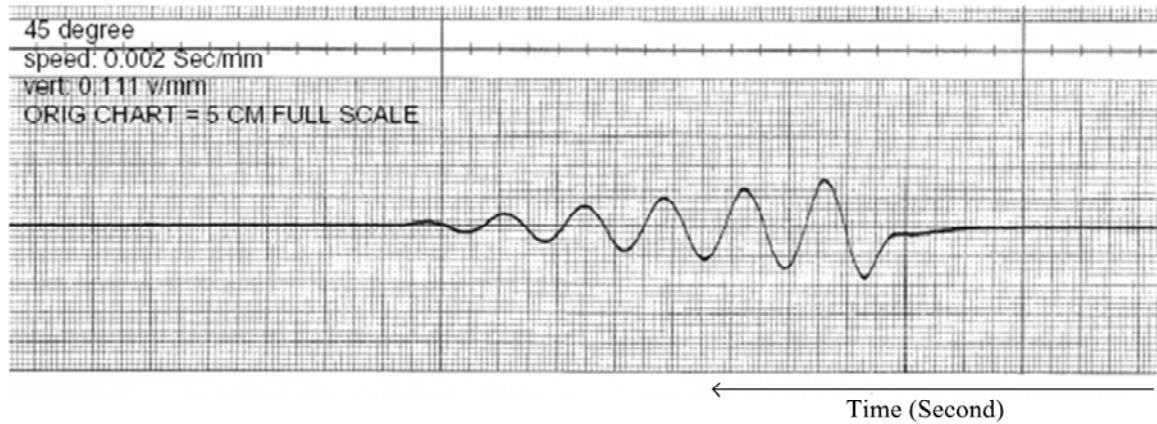


Figure H.3 Relaxation oscillations for open-terminal mirror assembly

The value of k_m is obtained from v_m in Equation (H.12) and the chart strip in Figure H.3 by measuring the peak of the oscillation at the particular time of the first peak in the oscillation (measured from the start). The result is $k_m = 5.5 \times 10^{-3}$.

The resonant frequency ω_r can be determined from Equation (H.7). It is found to be relatively independent of B and other constants to give

$$\omega_r \sim \omega_{OT} \sim \omega_o \sim 234 \quad \text{or} \quad \text{Frequency} \sim 37\text{Hz} \quad (\text{H. 17})$$

The fully damped time constant is now found

$$\tau_{\text{full}}^{-1} = \frac{1}{2} \frac{k_m}{R_T} \left(\frac{k_T}{I} \right) + \frac{B}{2I} \sim 13.3 \quad (\text{H. 18})$$

H.5 Mirror Response

Many of the etching experiments were performed using a driving frequency of 15Hz with no more than 1 volt p-p triangle wave. The angular function has the form of approximately

$$\theta(t) = 198^\circ V(t) e^{-13.3t} \odot \sin(234t) \quad (\text{H. 19})$$

The plot from MathCad below shows the mirror deflection angle for a driving frequency of 15Hz as an example. The beam deflection angle will be double that shown. For the practical situation, the voltage applied by a general laboratory function generator only agrees with the display for 50 Ohm loads. It must be recalculated for the mirror assembly.

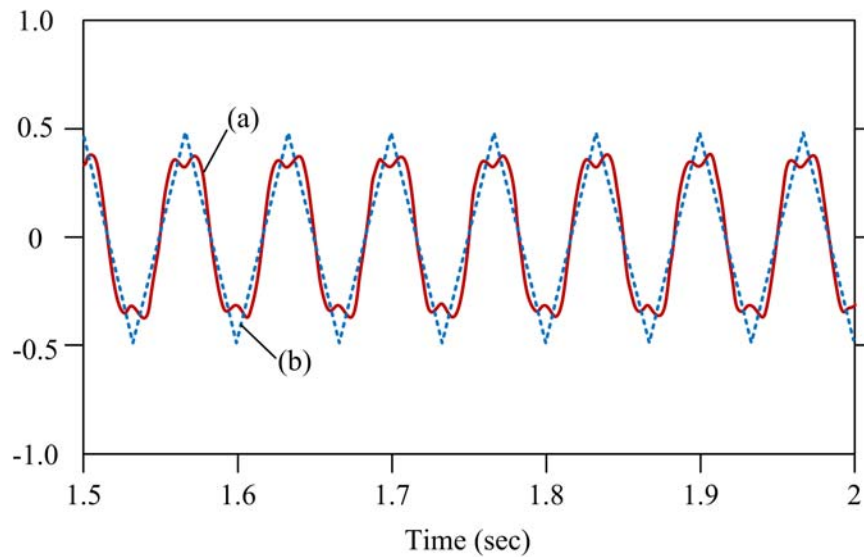


Figure H.4 (a) response of mirror for 15Hz and (b) voltage input signal.

Table H.1 Partial List of symbols

$V(t)$	External voltage from a function generator
R_1	Output resistance of the function generator
R_2	External resistor added to the circuit
L	Inductance of the mirror coil. Neglected to first order ... see text.
$v_m = k_m \dot{\theta}$	Voltage due to motion of mirror due to motion of internal magnet.
θ	Angle of mirror with respect to its rest position
$\alpha = 2\theta$	Deflection angle of light beam
B	Damping coefficient: Torque $\tau = B\dot{\theta}$ (opposes motion)
I	Moment of inertia of mirror, shaft, rotor $\tau = I\ddot{\theta}$
$\omega_o = \sqrt{K/I}$	An oscillation frequency
K	Spring constant
$\tau_\theta = k_T i_2$	Torque of mirror shaft is proportional to current
$R_{ }$	Parallel combination of R_1 and R_2
$R_T = R_{ } + R_s$	Total Resistance
$\widetilde{V}, \widetilde{V}_\xi$	‘Twiddle’ indicates Laplace Transform
S	Laplace transform variable
ω_r	Resonant frequency with all damping effects
$B/2I$	(relaxation time) ⁻¹ for mirror with open terminals
ω_{OT}	Resonant frequency for open motor terminals

Reference

- [1] E. H. Li and B. L. Weiss, "Bandgap engineering and quantum wells in optoelectronic devices", *Electronics & Communication Engineering Journal*, vol. 3, pp. 63-79, 1991.
- [2] M. Maeda and H. Nakano, "Integrated optoelectronics for optical transmission systems", *IEEE Communications Magazine*, vol. 26, pp. 45-51, 1988.
- [3] P. S. J. Zory, "Multiquantum Well Lasers: Threshold Considerations", in *Quantum Well Lasers* San Diego, CA: Academic Press, Inc., 1993.
- [4] L. A. Coldren, K. Iga, B. I. Miller, and J. A. Rentschler, "GaInAsP/InP stripe-geometry laser with a reactive-ion-etched facet", *Applied Physics Letters*, vol. 37, pp. 681-683, 1980.
- [5] N. Bouadma, P. Correc, and F. Brillouet, "GaAs:GaAlAs ridge waveguide lasers and their monolithic integration using the ion beam etching process", *IEEE Journal of Quantum Electronics*, vol.25, no.11, Nov. 1989, pp.2219-28, vol. 25, pp. 2219-2228, 1989.
- [6] D. Remiens, L. Menigaux, G. Ben Assayag, J. Gierak, and P. Sudraud, "GaAs/AlGaAs double heterostructure laser monolithically integrated with passive waveguide using focused ion beam etching", *Electronics Letters*, vol. 25, pp. 1400-1402, 28 Sept. 1989.
- [7] S. C. Horst, S. Agarwala, O. King, J. L. Fitz, and S. D. Smith, "GaAs/AlGaAs ridge lasers with etched mirrors formed by an inductively coupled plasma reactor", *Applied Physics Letters*, vol. 71, pp. 1444-1445, 1997.
- [8] A. Paraskevopoulos, H.-J. Hensel, W.-D. Molzow, K. Janiak, E. Suryaputra, H. Roehle, P. Wolfram, and W. Ebert, "Fabrication of InGaAsP/InP ridge waveguide lasers with dry etched facets using chemically assisted ion beam etching and a simple photoresist mask.", in *LEOS 2001. 14th Annual Meeting of the IEEE Lasers and Electro-Optics Society*, San Diego, CA, USA, 2001, pp. 173-174.
- [9] W. W. Chow and S. W. Koch, *Semiconductor-laser fundamentals*, Springer, 1999.
- [10] M. Kawabe, N. Kanzaki, K. Masuda, and S. Namba, "Effects of ion etching on the properties of GaAs", *Applied Optics*, vol. 17, pp. 2556-2561, 15 August 1978.
- [11] J. R. Lothian, J. M. Kuo, S. J. Pearton, and F. Ren, "Wet and dry etching of InGaP", *Advanced III-V Compound Semiconductor Growth, Processing and Devices Symposium*, Boston, MA, USA, 1992, pp. 307-13.
- [12] W. J. Grande, J. E. Johnson, and C. L. Tang, "GaAs/AlGaAs photonic integrated circuits fabricated using chemically assisted ion beam etching", *Applied Physics Letters*, vol. 57, pp. 2537-2539, 1990.
- [13] S. Salimian, C. Yuen, C. Shih, and C. B. Cooper, "Damage studies of dry etched GaAs recessed gates for field effect transistors", *Journal of Vacuum Science Technology B*, vol. 9, pp. 114-119, 1991.

- [14] P. D. Swanson, D. B. Shire, C. L. Tang, M. A. Parker, J. S. Kimmet, and R. J. Michalak, "Electron-cyclotron resonance etching of mirrors for ridge-guided lasers", *IEEE Photonics Technology Letters*, vol. 7, pp. 605-607, 1995.
- [15] B. C. Qiu, B. S. Ooi, A. C. Bryce, S. E. Hicks, C. D. W. Wilkinson, R. M. De La Rue, and J. H. Marsh, "Reduced damage reactive ion etching process for fabrication of InGaAsP/InGaAs multiple quantum well ridge waveguide lasers", *Journal of Vacuum Science & Technology B*, vol. 16, pp. 1818-1822, 1998.
- [16] T. Rivera, J.-P. Debray, J. M. Gerard, B. Legrand, L. Manin-Ferlazzo, and J. L. Oudar, "Optical losses in plasma-etched AlGaAs microresonators using reflection spectroscopy", *Applied Physics Letters*, vol. 74, pp. 911-913, 1999.
- [17] M. Tong, D. G. Ballegeer, A. Ketterson, E. J. Roan, K. Y. Cheng, and I. Adesida, "A comparative study of wet and dry selective etching processes for GaAs/AlGaAs/InGaAs pseudomorphic MODFETs", *Journal of Electronic Materials*, Boulder, CO, USA, 1992, pp. 9-15.
- [18] K. Iga, M. Pollack, B. Miller, and R. Martin, "GaInAsP/InP DH lasers with a chemically etched facet", *Quantum Electronics, IEEE Journal of*, vol. 16, pp. 1044-1047, 1980.
- [19] N. Bouadma, J. Riou, and J. C. Bouley, "Short-cavity GaAlAs laser by wet chemical etching", *Electronics Letters*, vol. 18, pp. 879-880, 1982.
- [20] B. Cakmak, "Fabrication and characterization of dry and wet etched InGaAs/InGaAsP/InP long wavelength semiconductor lasers", *Optics Express*, vol. 10, pp. 530-535, 2002.
- [21] S. Iida and K. Ito, "Selective Etching of Gallium Arsenide Crystals in System", *Journal of Electrochemical Society*, vol. 118, pp. 768-771, 1971.
- [22] D. W. Shaw, "Localized GaAs Etching with Acidic Hydrogen Peroxide Solutions", *Journal of Electrochemical Society*, vol. 128, pp. 874-880, 1981.
- [23] S. Adachi and K. Oe, "Chemical Etching of GaAs", *Journal of Electrochemical Society: Solid-State Science and Technology*, vol. 131, pp. 126-130, January 1984.
- [24] M. J. Howes and D. V. Morgan, *Gallium Arsenide: Materials, Devices, and Circuits (Wiley Series in Solid State Devices & Circuits)*, New York: John Wiley & Sons, 1985.
- [25] R. E. Williams, *Gallium Arsenide Processing Techniques*, Artech House, 1984.
- [26] R. Memming, "Charge transfer kinetics at semiconductor electrodes", *Berichte der Bunsengesellschaft für Physikalische Chemie*, vol. 91, pp. 353-61, 1987.
- [27] H. Gerischer and W. Ekardt, "Fermi levels in electrolytes and the absolute scale of redox potentials", *Applied Physics Letters*, vol. 43, pp. 393-5, 1983.
- [28] V. G. Levich, *Advances in Electrochemistry and Electrochemical Engineering*, P. Delahay and C. W. Tobias, eds., Wiley Interscience, pp. 249, 1966.

- [29] R. R. Dogonadze, A. M. Kuznetsov, and S. C. Chizmadzhev, "Kinetics of Some Heterogeneous Reactions at a Semiconductor-Electrolyte Interface", *Russian Journal of Physical Chemistry*, vol. 38, p. 652, 1964.
- [30] H. Gerischer, "Electron-Transfer Kinetics of Redox Reactions at the Semiconductor/Electrolyte Contact. A New Approach", *Journal of Physical Chemistry*, vol. 95, pp. 1356-1359, 1991.
- [31] S. R. Morrison, *The Chemical Physics of Surface*, Plenum Press, 1977.
- [32] R. Memming, *Semiconductor Electrochemistry*, Wiley-VCH, 2001.
- [33] H. Gerischer, D. M. Kolb, and J. K. Sass, "The study of solid surfaces by electrochemical methods", *Advances in Physics*, vol. 27, pp. 437-98, 1978.
- [34] H. Gerischer, "On the role of electrons and holes in surface reactions on semiconductors", in Proceedings of the symposium on adsorption and catalysis on semiconducting materials, 2-4 April 1969, Surface Science, San Francisco, CA, USA, 1969, pp. 265-78.
- [35] H. Gerischer, "Charge transfer processes at semiconductor-electrolyte interfaces in connection with problems of catalysis", in Electrocatalysis, Nov. 1969, *Surface Science*, Eindhoven, Netherlands, 1969, pp. 97-122.
- [36] C. A. Coulson, *Valence*, Oxford University Press, Amen House, 1952.
- [37] K. S. Pitzer, *Quantum chemistry*, Prentice-Hall, 1953.
- [38] W. W. Harvey, "Carrier-Limited Currents in Germanium Electrodes", *Electrochimica Acta*, vol. 13, pp. 1263-1277, 1968.
- [39] H. Gerischer, "Electrolytic decomposition and photodecomposition of compound semiconductors in contact with electrolytes", in Proceedings of the 5th Annual Conference on the Physics of Compound Semiconductor Interfaces, 17-20 Jan. 1978, *Journal of Vacuum Science and Technology*, Los Angeles, CA, USA, 1978, pp. 1422-8.
- [40] F. K. Christensen and M. Mullenborn, "Improved laser processing of Lithium Niobate", in *Ultrasonics Symposium*, 1994, pp. 391-396.
- [41] D. J. Ehrlich, J. R. M. Osgood, and T. F. Deutsch, "Laser-induced microscopic etching of GaAs and InP", *Applied Physics Letters*, vol. 36, pp. 698-700, 1980.
- [42] C. Lee, H. Sayama, and M. Takai, "Comparison of laser-induced etching behavior of III-V compound semiconductors", *Applied Physics A*, vol. 56, pp. 343-348, 1993.
- [43] H. Lu, Z. Wu, and I. Bhat, "Photoassisted anodic etching of gallium nitride", *Journal of the Electrochemical Society*, vol. 144, pp. 8-11, 1997.

- [44] L.-H. Peng, C.-W. Chuang, Y.-C. Hsu, J.-K. Ho, C.-N. Huang, and C.-Y. Chen, "Deep ultraviolet enhanced wet chemical oxidation and etching of gallium nitride", in *Technical Digest. Summaries of Papers Presented at the Conference on Lasers and Electro-Optics*, Washington, DC, USA, p. 153, 1998.
- [45] T. Rotter, J. Aderhold, D. Mistele, O. Semchinova, J. Stemmer, D. Uffmann, and J. Graul, "Smooth GaN surfaces by photoinduced electro-chemical etching", *Material Science and Engineering B*, vol. 59, pp. 350-354, 1999.
- [46] J. Zhang, K. Sugioka, S. Wada, H. Tashiro, and K. Toyoda, "Direct photoetching of single crystal SiC by VUV-266 nm multiwavelength laser ablation", *Applied Physics A*, vol. 64, pp. 367-371, 1997.
- [47] Moutonnet, "Photochemical Pattern on p-Type GaAs", *Material Letters*, vol. 6, pp. 34-36, 1987.
- [48] R. M. Osgood, Jr., A. Sanchez-Rubio, D. J. Ehrlich, and V. Daneu, "Localized laser etching of compound semiconductors in aqueous solution", *Applied Physics Letters*, vol. 40, pp. 391-3, 1982/03/01 1982.
- [49] J. F. W. Ostermayer and P. A. Kohl, "Photoelectrochemical Etching of P-GaAs", *Applied Physics Letters*, vol. 39, pp. 76-78, 1981.
- [50] D. V. Podlesnik, H. H. Gilgen, and O. J. R. M., "Maskless, chemical etching of submicrometer gratings in single-crystalline GaAs", *Applied Physics Letters*, vol. 43, pp. 1083-1085, 1983.
- [51] D. V. Podlesnik, H. H. Gilgen, and J. R. M. Osgood, "Deep-Ultraviolet induced wet etching of GaAs", *Applied Physics Letters*, vol. 45, pp. 563-565, 1984.
- [52] D. V. Podlesnik, H. H. Gilgen, and J. R. M. Osgood, "Deep-UV, Light-Assisted, Wet Etching of Compound Semiconductors", in *Materials Research Society Symposium Proceedings*, 1984, pp. 161 - 165.
- [53] J. van de Ven and H. J. P. Nabben, "Contour Photoetching of N-Type Semiconductors", *Applied Physics Letters*, vol. 58, pp. 831-833, 1991.
- [54] P. H. L. Notten, J. E. A. M. van den Meerakker, and J. J. Kelly, *Etching of III-V Semiconductors: An Electrochemical Approach*, Elsevier Advanced Technology, 1991.
- [55] H. H. Gilgen, D. Podlensnik, C. C.J., and J. R. M. Osgood, "Direct Holographic Processing Using Laser Chemistry", in *Material Research Society Symposium Proceedings*, 1984.
- [56] E. J. Twyford, C. A. Carter, P. A. Kohl, and N. M. Jokerst, "The influence of aluminum concentration on photoelectrochemical etching of first order gratings in GaAs/AlGaAs", *Applied Physics Letters*, vol. 67, pp. 1182-1184, 28 August 1995.
- [57] T. C. Chong, Y. F. Lu, and A. Lee, "Laser-Controlled Etching of (Al,Ga)As Epitaxial Layers", in *Material Research Society Symposium Proceedings*, 1996, pp. 491- 496.

- [58] C. Lee, M. Takai, T. Yada, K. Kato, and S. Namba, "Laser-induced trench etching of GaAs in aqueous KOH solution", *Applied Physics A*, vol. 51, pp. 340-343, 1990.
- [59] M. N. Ruberto, X. Zhang, R. Scarmozzinno, A. E. Willner, D. V. Podlesnik, and J. R. M. Osgood, "The laser-controlled micrometer-scale photoelectrochemical etching of III-V semiconductors", *Journal of the Electrochemical Society*, vol. 138, pp. 1174-1185, 1991.
- [60] J. van de Ven and H. J. P. Nabben, "Anisotropic photoetching of III-V semiconductors I. Electrochemistry", *Journal of Electrochemical Society*, vol. 137, pp. 1603-1610, 1990.
- [61] J. van de Ven and H. J. P. Nabben, "Anisotropic Photoetching of III-V Semiconductor, II. Kinetics and Structural Factors", *Journal of Electrochemical Society*, vol. 138, pp. 144-152, 1991.
- [62] R. Khare, D. B. Young, and E. L. Hu, "The Bandgap-selective photoelectrochemical etching of GaAs/Al_xGa_{1-x}As heterostructures with varying mole fraction", *Journal of Electrochemical Society*, vol. 140, pp. L117-L118, 1993.
- [63] R. Khare, D. B. Young, G. L. Snider, and E. L. Hu, "Effect of Band Structure on Etch-Stop Layers in the Photoelectrochemical Etching of GaAs/AlGaAs Semiconductor Structures", *Applied Physics Letters*, vol. 62, pp. 1809-1811, 1993.
- [64] H. T. Yi, M. Thakurdesai, and M. A. Parker, "Control of sidewall angles using UV LEDs during wet etching of GaAs", *Electrochemical & Solid-State Letters*, vol. 7, pp. C137-139, 2004.
- [65] D. V. Podlesnik, H. H. Gilgen, A. E. Willner, and O. J. R. M., "Interaction of deep-ultraviolet laser light with GaAs surfaces in aqueous solutions", *Journal of Optical Society in America B*, vol. 3, pp. 775 - 784, 1986.
- [66] T. Fink and J. R. M. Osgood, "Light-induced selective etching of GaAs in AlGaAs/GaAs Heterostructures", *Journal of Electrochemical Society*, vol. 140, pp. L73-L74, April 1993.
- [67] L. A. Coldren and S. W. Corzine, *Diode Lasers and Photonic Integrated Circuits*, John Wiley & Sons, Inc, 1995.
- [68] I. N. Levine, *Physical Chemistry*, McGraw-Hill, 2002.
- [69] V. S. Bagotsky, *Fundamentals of Electrochemistry*, John Wiley & Sons, Inc., 2005.
- [70] R. Memming, "The role of energy levels in charge transfer processes at semiconductor-electrolyte interfaces", in Electrochemical Society Meeting. (Abstracts only), 12-17 May 1974, *Journal of the Electrochemical Society*, San Francisco, CA, USA, 1974, p. 119C.
- [71] S. R. Morrison, "Study of Semiconductors Using Electrochemical Techniques", *Journal of Vacuum Science and Technology*, vol. 15, pp. 1417-1421, 1978.
- [72] K. W. Frese, M. J. Madou, and S. R. Morrison, "Investigation of photoelectrochemical corrosion of semiconductors. II. Kinetic analysis of corrosion-competition reactions on n-GaAs", *Journal of the Electrochemical Society*, vol. 128, pp. 1527-31, 1981.

- [73] P. E. Gregory, W. E. Spicer, S. Ciraci, and W. A. Harrison, "Surface state band on GaAs (110) face", *Applied Physics Letters*, vol. 25, pp. 511-14, 1974.
- [74] R. Memming, "Surface chemistry and charge transfer kinetics at semiconductor-liquid interfaces", in *Electrochemistry: Solid vs. Liquid State. International Workshop*, 4-8 March 1996, Solid State Ionics, Diffusion & Reactions, Schloss Ringberg, Germany, 1997, pp. 131-40.
- [75] A. J. Nozik and R. Memming, "Physical chemistry of semiconductor-liquid interfaces", *Journal of Physical Chemistry*, vol. 100, pp. 13061-78, 1996.
- [76] B. B. Smith and A. J. Nozik, "Theoretical studies of electron transfer and electron localization at the semiconductor-liquid interface", *Journal of Physical Chemistry B*, vol. 101, pp. 2459-75, 1997.
- [77] R. A. Marcus, "Analytical of chemical reactions. III. Natural collision coordinates", *Journal of Chemical Physics*, vol. 49, pp. 2610-16, 15 Sept. 1968.
- [78] R. A. Marcus, "Analytical mechanics of chemical reactions. IV. Classical mechanics of reactions in two dimensions", *Journal of Chemical Physics*, vol. 49, pp. 2617-31, 15 Sept. 1968.
- [79] J. J. Kelly and P. H. L. Notten, "Surface charging effects during photoanodic dissolution of n-GaAs electrodes", *Journal of the Electrochemical Society*, vol. 130, pp. 2452-9, 1983.
- [80] S. M. Sze, *Physics of Semiconductor Devices*, John Wiley & Sons, Inc., 1969.
- [81] C. F. Yu, M. T. Schmidt, D. V. Podlesnik, and J. R. M. Osgood, "Wavelength Dependence of Optically Induced Oxidation of GaAs(100)", *Journal of Vacuum Science and Technology B*, vol. 5, pp. 1087-1091, 1987.
- [82] J. J. Kelly, J. van de Ven, and J. E. A. M. van den Meerakker, "The mechanism of GaAs etching in CrO_3 -HF solutions. II. Model and discussion", *Journal of the Electrochemical Society*, vol. 132, pp. 3026-33, 1985.
- [83] R. Memming, "The role of energy levels in semiconductor-electrolyte solar cells", *Journal of the Electrochemical Society*, vol. 125, pp. 117-23, 1978.
- [84] S.-M. Park and M. E. Barber, "Thermodynamic stabilities of semiconductor electrodes", *Journal of Electroanalytical Chemistry*, vol. 99, pp. 67-75, 1979.
- [85] B. P. Minks, D. Vanmaekelbergh, and J. J. Kelly, "Current-doubling, Chemical Etching and The Mechanism of Two-electron Reduction Reactions at GaAs, Part 1. Experimental results for H_2O_2 and Br_2 ", *Journal of Electroanalytical Chemistry*, vol. 273, pp. 119-131, 1989.
- [86] K. J. Vetter, *Electrochemical kinetics; theoretical and experimental aspects*, Academic Press, 1967.

- [87] V. F. Kovalenko, F. P. Kesamanly, I. E. Maronchuk, B. P. Masenko, G. P. Peka, and L. G. Shepel, "Photoluminescence and photoconductivity of high-resistivity chromium-doped films", *Soviet Physics - Semiconductors*, vol. 11, pp. 1303-5, 1977.
- [88] J. F. W. Ostermayer, P. A. Kohl, and R. H. Burton, "Photoelectrochemical etching of integral lenses on InGaAsP/InP light-emitting diodes", *Applied Physics Letters*, vol. 43, pp. 642-644, 1983.
- [89] A. E. Willner, M. N. Ruberto, D. J. Blumenthal, D. V. Podlesnik, and J. Osgood, R. M., "Laser fabricated GaAs waveguiding structures", *Applied Physics Letters*, vol. 54, pp. 1839-1841, 1989.
- [90] R. T. Brown, "Laser-assisted selective chemical etching for active trimming of GaAs waveguide devices", *Photonics Technology Letters, IEEE*, vol. 2, pp. 346-348, 1990.
- [91] U. Drodofsky, J. Stuhler, T. Schulze, M. Drewsen, B. Brezger, T. Pfau, and J. Mlynek, "Hexagonal Nanostructures Generated by Light Masks for Neutral Atoms", *Applied Physics B*, vol. 65, pp. 755-759, 1997.
- [92] J. van de Ven and J. J. Kelly, "Galvanic effects in the etching of semiconductor p/n structures", *Journal of the Electrochemical Society*, vol. 148, pp. 10-15, 2001.
- [93] J. J. Kelly and A. C. Reynders, "A Study of GaAs Etching in Alkaline H₂O₂ Solutions", *Applied Surface Science*, vol. 29, pp. 149-164, 1987.
- [94] V. Cracium and D. Cracium, "Thermal mechanisms in laser ablation of GaAs", *Applied Surface Science*, vol. 109, pp. 312-316, 1997 1997.
- [95] J. L. Weyher, P. D. Brown, J. L. Rouviere, T. Wosinski, A. R. A. Zauner, and I. Grzegory, "Recent advances in defect-selective etching of GaN", *Journal of Crystal Growth*, vol. 210, pp. 151-156, 2000.
- [96] L. Hollan, J. C. Tranchart, and R. Memming, "Interpretation of selective etching of III-V compounds on the basis of semiconductor electrochemistry", *Journal of the Electrochemical Society*, vol. 126, pp. 855-9, 1979.
- [97] E. H. Yi and M. A. Parker, "Fabricating vertical sidewalls in GaAs/AlGaAs heterostructure using light-induced wet etching", *Journal of the Electrochemical Society*, vol. 153, pp. 496-501, 2006.
- [98] E. H. Yi, I. G. Akdogan, and M. A. Parker, "Measurements of wet etch dynamics using an in situ optical monitor", *Electrochemical and Solid-State Letters*, vol. 6, pp. 75-7, 2003.
- [99] M. A. Parker and E. H. Yi, Publication and patent in progress
- [100] J. van de Ven and H. J. P. Nabben, "Analysis of determining factors in the kinetics of anisotropic photoetching of GaAs", *Journal of Applied Physics*, vol. 67, pp. 7572-7575, 1990.
- [101] E.-H. Yi and M. Parker, "Photo-Assisted Wet-Etched III-V Heterostructure Laser Mirrors and Waveguides", Summited to *IEEE Photonics Technology Letters*, 2008.

- [102] J. L. Merz and R. A. Logan, "GaAs integrated optical circuits by wet chemical etching", *IEEE Journal of Quantum Electronics*, vol. QE-15, pp. 72-82, 1979.
- [103] M. A. Parker, J. S. Kimmet, R. J. Michalak, H. S. Wang, D. B. Shire, C. L. Tang, and J. P. Drumheller, "Accurate electron-cyclotron-resonance etching of semiconductor laser heterostructures using a simple laser reflectometer", *IEEE Photonics Technology Letters*, vol. 8, pp. 818-20, 1996.
- [104] M. A. Parker, R. J. Michalak, J. S. Kimmet, A. R. Pirich, and D. B. Shire, "Etched-surface roughness measurements from an in situ laser reflectometer", *Applied Physics Letters*, vol. 69, pp. 1459-61, 2 Sept. 1996.
- [105] F. P. Kesamanly, V. F. Kovalenko, and I. E. Maronchuk, "Photoluminescence of aluminium-doped gallium arsenide", *Soviet Physics - Semiconductors*, vol. 8, p. 1292, 1975.
- [106] M. S. Thakurdesai and M. A. Parker, "A hand-held smart wet etch monitor: design, theory, and test", *IEEE Transactions on Instrumentation and Measurement*, vol. 55, pp. 1814-22, 2006.
- [107] E. D. Palik and G. Ghosh, *Gallium Arsenide (GaAs) in Handbook of Optical Constants of Solids*, Academic Press Inc., 1985, pp. 429-443.
- [108] S. Semura, T. Ohta, T. Kuroda, and H. Nakashima, "AlGaAs/GaAs buried multiquantum well lasers with a reactive ion etched window facet", *Japanese Journal of Applied Physics*, Part 2 (Letters), vol. 24, pp. 463-5, 1985.
- [109] A. Dobkin, V. Kokorev, G. Lapitskaya, A. Pleshkov, O. Prozorov, L. Rivin, G. Sukhareva, V. Shil'dyaev, and S. Yakubovich, "Semiconductor laser with local mirrors", *Soviet Physics: Semiconductors*, vol. 4, pp. 515-16, 1970.
- [110] C. E. Hurwitz, J. A. Rossi, J. J. Hsieh, and C. M. Wolfe, "Integrated GaAs-AlGaAs double-heterostructure lasers", *Applied Physics Letters*, vol. 27, pp. 241-243, 1975.
- [111] J. L. Merz and R. A. Logan, "GaAs double heterostructure lasers fabricated by wet chemical etching", *Journal of Applied Physics*, vol. 47, pp. 3503-9, 1976.
- [112] S. Adachi, H. Kawaguchi, K. Takahei, and Y. Noguchi, "InGaAsP/InP buried-heterostructure lasers ($\lambda = 1.5\mu\text{m}$) with chemically etched mirrors", *Journal of Applied Physics*, vol. 52, pp. 5843-5, 1981.
- [113] N. Bouadma, J. Riou, and A. Kampfer, "Low threshold GaAs/GaAlAs BH lasers with ion-beam-etched mirrors", *Electronics Letters*, vol. 21, pp. 566-8, 1985.
- [114] T. Yuasa, M. Mannoh, K. Asakawa, K. Shinozaki, and M. Ishii, "Dry-etched-cavity pair-groove-substrate GaAs/AlGaAs multiquantum well lasers", *Applied Physics Letters*, vol. 48, pp. 748-50, 1986.
- [115] L. A. Coldren, K. Furuya, B. I. Miller, and J. A. Rentschler, "Etched mirror and groove-coupled GaInAsP/InP laser devices for integrated optics", *IEEE Transactions on Microwave*

- Theory and Techniques*, vol. MTT-30, pp. 1667-76, 1982.
- [116] M. Wada, K. Hamada, T. Shibutani, H. Shimizu, M. Kume, K. Itoh, G. Kano, and I. Teramoto, "A new chemical etching technique for formation of cavity facets of (GaAl)As lasers", *IEEE Journal of Quantum Electronics*, vol. QE-21, pp. 658-62, 1985.
 - [117] E. H. Yi and M. Parker, "Photo-Dynamics of Al_xGa_{1-x}As Heterostructure Dissolution: Experiments and Applications", *ECS Transactions*, vol. 6, pp. 525-534, 2007.
 - [118] M. A. Parker, *Physics of Optoelectronics (Optical Engineering)*, CRC, 2005.
 - [119] R. G. Hunsperger, *Integrated Optics: Theory and Technology*, Springer-Verlag, 1984.
 - [120] P. K. Tien, "Light waves in thin films and integrated optics", *Applied Optics*, vol. 10, pp. 2395-13, 1971.
 - [121] J. S. Osinski, K. M. Dzurko, S. G. Hummel, and P. D. Dapkus, "Optimization of stripe width for low-threshold operation of quantum well laser diodes", *Applied Physics Letters*, vol. 56, pp. 2487-9, 1990.
 - [122] G. R. Fowles, *Introduction to Modern Optics*, Dover Press, 1989.
 - [123] K. Iga and B. I. Miller, "Chemically etched-mirror GaInAsP/InP lasers-review", *IEEE Journal of Quantum Electronics*, vol. QE-18, pp. 22-9, 1982.
 - [124] T. Ito, J. Ishikawa, T. Aramaki, T. Machida, N. S. Takahashi, and S. Kurita, "A simple method for monolithic fabrication of InGaAsP/GaAs lasers", *Journal of Applied Physics*, vol. 64, pp. 2770-2, 1988.
 - [125] G. A. Vawter, L. A. Coldren, J. L. Merz, and E. L. Hu, "Nonselective etching of GaAs/AlGaAs double heterostructure laser facets by Cl₂ reactive ion etching in a load-locked system", *Applied Physics Letters*, vol. 51, pp. 719-21, 1987.
 - [126] H. Appelman, J. Levy, M. Pion, D. Krebs, C. Harding, and M. Zediker, "Self-aligned chemically assisted ion-beam-etched GaAs/(Al,Ga)As turning mirrors for photonic applications", *Journal of Lightwave Technology*, vol. 8, pp. 39-41, 1990.
 - [127] F. Shimokawa, H. Tanaka, R. Sawada, and S. Hara, "Continuous-wave operation and mirror loss of a U-shaped GaAs/AlGaAs laser diode with two totally reflecting mirrors", *Applied Physics Letters*, vol. 56, pp. 1617-19, 1990.
 - [128] H. Han, D. V. Forbes, and J. J. Coleman, "Self-aligned high-quality total internal reflection mirrors", *IEEE Photonics Technology Letters*, vol. 7, pp. 899-901, 1995.

Curriculum Vita

Eun-Hyeong Yi

- 1996 B.S. Degree, Electronic Engineering, Yeungnam University, Kyungsan, KOREA(R.O.K.)
- 1999 M.S. Degree, Electronics, Kyungpook National University, Taegu, KOREA (R.O.K.)
- 2003 M.S. degree, Electrical and Computer Engineering, Rutgers, The State University of New Jersey, New Brunswick, New Jersey, Developing Etch Monitor in Semiconductor Research Group
- 2004-present Graduate Student, Fabrication Process Developing in Semiconductor Research Group, Electrical and Computer Engineering, Rutgers-The State University of New Jersey, New Brunswick, New Jersey
- 2002-2006 Teaching Assistant, Electrical and Computer Engineering, Rutgers-The State University of New Jersey
- 2006-2008 Part Time Lecturer, Electrical and Computer Engineering, Rutgers-The State University of New Jersey
- 2000-present Research Assistant, Fabrication Process Developing, Nanolab of Electrical and Computer Engineering,
- 2003 E. H. Yi, I. G. Akdogan, and M. A. Parker, Measurements of wet etch dynamics using an in situ optical monitor. *Electrochemical & Solid-State Letters* 6 (5), G75, 2003.
- 2006 E. H. Yi and M.A. Parker, Fabricating vertical sidewalls in GaAs/AlGaAs heterostructure using light-induced wet etching. *Journal of the Electrochemical Society* 153 (7), 496 2006.
- 2007 Eun-Hyeong Yi and Michael Parker, Photo-Dynamics of Al_xGa_{1-x}As Heterostructure Dissolution. 16th KSEA North East Regional Conference Woodloch Springs, Hawley, PA, 2007.
- 2007 E. H. Yi and M. Parker, Photo-Dynamics of Al_xGa_{1-x}As Heterostructure Dissolution: Experiments and Applications. 211th ECS Conference at Chicago, IL, May 2007.
- 2007 Eun-Hyeong Yi and Michael Parker, "Photo-Dynamics of Al_xGa_{1-x}As Heterostructure Dissolution: Experiments and Applications", *ECS Transactions* 6 (2), 525, 2007.
- 2009 Eun-Hyeong Yi and Michael Parker, Photo-Assisted Wet-Etched III-V Heterostructure Laser Mirrors and Waveguides. *IEEE Photonics Technology Letters*, 21 (10), 663, 2009.